AN ACOUSTIC COUNTERMEASURE TO SUPERCAVITATING TORPEDOES

A Thesis
Presented to
The Academic Faculty

by

Peter J. K. Cameron

In Partial Fulfillment
of the Requirements for the Degree
Doctor of Philosophy in the
School of Mechanical Engineering

Georgia Institute of Technology
May 2009

Copyright © 2009 by Peter J. K. Cameron

AN ACOUSTIC COUNTERMEASURE TO SUPERCAVITATING TORPEDOES

Approved by:

Dr. P. H. Rogers, Committee Chair
School of Mechanical Engineering
Georgia Institute of Technology

Dr. A. A. Ferri
School of Mechanical Engineering
Georgia Institute of Technology

Dr. M. Ruzzene
School of Aerospace Engineering
Georgia Institute of Technology

Dr. M. K. Smith
School of Mechanical Engineering
Georgia Institute of Technology

D. Trivett
School of Mechanical Engineering
Georgia Institute of Technology

Dr. B. T. Zinn
School of Aerospace Engineering
Georgia Institute of Technology

Date Approved: May 11, 2009

ACKNOWLEDGEMENTS

I would like to express my gratitude to Professor Peter H. Rogers, who, as my advisor, has guided me through and supported my research work. It has been a privilege to be his student and to be able to benefit from his expertise, experience, and insight.

I would also like to thank my other committee members, Dr. Aldo A. Ferri, Dr. Massimo Ruzzene, Dr. Marc K. Smith, Dave Trivett, and Dr. Ben T. Zinn for their input and suggestions.

I wish a special thanks to John Doane for countless and invaluable discussions, advice, and ideas throughout the duration of my dissertation work.

Many thanks also go to Dave Gifford for his input, advice, help, and experience with various aspects of my experimental work.

I am also very grateful to others in our research group for their interest in my work and the resulting discussions: Jayme Caspall, Jim Martin, Gregg Larson, Francois Guillot, and Michael Gray.

I would like to thank my friends for support in all aspects of life as a graduate student: James Hamlin, Suzanna Sayre, Melissa Deen Hallow, Rebecca Burnos, Kacey-Jane Ivey, Stephen Steinmann, Laura Stiltz, Nick Krizan, Eric Stockwell, Shai Birmaher, Gerald Lopez, Mike Leclerc, Mark Kiefert, Mark Gertrudes, and Neil Ferrier.

I can not thank my family enough for their love and support: my parents, of course, Kenneth and Marie, and my three brothers, Kim, Jamie, and Michael.

This work was entirely supported by Professor Peter H. Rogers through the Rae and Frank H. Neely Chair.

TABLE OF CONTENTS

LIST OF TABLES

LIST OF FIGURES

LIST OF SYMBOLS OR ABBREVIATIONS

a	A grouping of constants in Logvinovich's model.
a_p	Projectile acceleration.
A	Acoustic pressure amplitude.
B	Bulk modulus.
c	Sound speed.
c_{eq}	Equivalent sound speed.
c_l	Sound speed in a liquid.
C	Point at the projectile center of mass.
C_D	Drag coefficient.
C_F	Lift coefficient.
C_H	Hydrophone capacitance.
C_{OC}	capacitance of hyrdophone extension cable.
d	Ellipse semi-minor axis in the context of supercavitation. Distance between transducers for hydrophone calibrations.
d_c	Cavitator disk diameter.
E_{PH}	Output voltage from hydrophone H when driving projector P.
E_{PT}	Output voltage from transducer T when driving projector P.
E_{TH}	Output voltage from hydrophone H when driving transducer T.
E_{TP}	Output voltage from projector P when driving transducer T.
F_D	Drag force.
f	Frequency.
f_0	Natural frequency.
F_L	Lift force.

F_{pn}	Planing force normal to the axis of the planing body.
F_x	x component of force vector.
F_y	y component of force vector.
F_z	z component of force vector.
Fr	Froude number.
g	Acceleration due to gravity.
h	Ellipse semi-major axis.
h_p	Immersion depth at the projectile transom measured normal to the cavity centerline.
$\mathcal{I}$	Represents inertial space.
I_{xx}^C	Moment of inertia of mass of β about x axis through C.
I_{yy}^C	Moment of inertia of mass of β about y axis through C.
I_{zz}^C	Moment of inertia of mass of β about z axis through C.
I_P	Current driving projector P.
I_T	Current driving transducer T.
J	Reciprocity parameter.
K_{eq}	Equivalent compressibility.
K_g	Compressibility of gas.
K_l	Compressibility of liquid.
L	Source length.
m	Mass.
M_C	Hydrophone sensitivity (overall system).
M_H	Hydrophone receiving sensitivity.
M_O	Hydrophone sensitivity (open circuit).
M_{Cx}	x component of the moment about point C.
M_{Cy}	y component of the moment about point C.
M_{Cz}	z component of the moment about point C.

M_{pp}	Moment about the transom of a planing body.
n	Number of data points in statistical calculations.
n_b	Number of bubbles per cubic meter.
N	Number of turns of wire in Faraday's Law.
O	Origin of coordinate system XYZ.
P	Pressure in a physical context. Probability in a statistical context.
P_c	Cavity pressure.
P_{ac}	Acoustic pressure.
P_{hs}	Hydrostatic Pressure.
P_v	Liquid vapor pressure.
ΔP	Change in pressure.
P_T	Cavitation threshold pressure.
$\bar{r}_{OC}$	Vector from point O which is the origin of XYZ to the center of mass of the body at point C with components $(r_{OC})_x$, $(r_{OC})_y$, $(r_{OC})_z$.
r_c	Cavitator disk radius.
r_i	The radius of an ellipse fitted to the troughs of the supercavity wall measured at the projectile tail location.
r_o	The radius of an ellipse fitted to the troughs of the supercavity wall measured at the projectile tail location.
r_t	Projectile tail radius.
R	Cavity radius.
R_0	Mean radius of bubbles in a bubbly liquid.
R_t	Cavity radius at the projectile tail.
s	Path length in a dynamics context. Sample standard deviation in a statistics context.
S	Cavity cross-section area.
S_0	Initial cavity cross-section area.

$\dot{S}_0$	Initial cavity cross-section area expansion rate.
t	Time. t-value for a student t distribution.
T	Kinetic energy.
U	Potential energy.
v	Speed.
$\bar{v}$	Velocity vector with components v_x, v_y, and v_z in coordinate system XYZ.
v_∞	Flow velocity as the distance from the body tends to infinity.
v_x	x component of the velocity vector.
v_r	Radial component of the velocity vector.
x_1 *through* x_{12}	State variables.
$\bar{Y}$	Point estimate for the sample mean.
XYZ	An inertial reference frame in fixed space $\mathcal{I}$ with associated unit vectors $\bar{I}, \bar{J}$ and $\bar{K}$.
xyz	A coordinate system fixed to body β.
$x_1y_1z_1$	A coordinate system resulting from rotation θ about the Y - axis of XYZ.
$x_2y_2z_2$	A coordinate system resulting from rotation ψ about the z_1 - axis of $x_1y_1z_1$.
α	Angle of attack in projectile dynamics context. Probability chosen for calculating confidence interval in statistics context.
α_p	Angle of attack between the body axis and the cavity axis.
β	Represents the rigid projectile body.
δ	Dampling factor for a resonant bubble.
Δ	The difference between the cavity and hull radii, $\Delta = (R_t - r_t)$.
ϵ	Electromotice force (emf).
γ	Specific heat ratio.

κ	A grouping of constants in Logvinovich's model.
λ	Acoustic wavelength.
μ	Surface tension in a fluid mechanics context. Population mean in a statistics context.
ν	Vapor of gas fraction.
ω	Circular frequency.
ω_0	Natural circular frequency.
$\vec{\omega}_{\beta/\mathcal{I}}$	Angular velocity of body β relative to the inertial space $\mathcal{I}$ with components ω_x, ω_y, and ω_z in the XYZ coordinate system.
ω_M	Minnaert resonance frequency.
ϕ	Velocity potential in a fluid mechanics context. Rotation about the x_2 - axis in a dynamics context.
Φ_B	Magnetic flux.
ψ	Rotation about the z_1 - axis.
ρ	Mass density.
ρ_{eq}	Equivalent density.
ρ_g	Gas density.
ρ_l	Liquid density.
σ	Cavitation number and population standard deviation.
θ	Rotation about the Y - axis in a dynamics context. Phase angle in an acoustic context.
BEM	Boundary Element Method.
B&K	Brüel & Kjær.
CEP	Circular error probable.
CFD	Computational fluid dynamics.
CI	Confidence interval.
GUI	Graphical user interface.
HIFU	High Intensity Focused Ultrasound.

ITC	International Transducer Corporation.
LED	Light emitting diode.
SBT	Slender body theory.
SN	Serial number.
SRA	Source-receive array.
TVR	Transmitting voltage response.

SUMMARY

Supercavitating torpedoes pose new threats to submarines, surface ships, and shore targets whose current countermeasures are inadequate against this technology. These torpedoes have the advantage over their predecessors and companion weapons of dramatically increased speed, which reduces the reaction time available for deploying a countermeasure heightening the threat to their intended target. Proliferation of supercavitating torpedoes has motivated research on countermeasures against them as well as on the fluid phenomenon which makes them possible.

The goal of this research was to investigate an envisaged countermeasure; an acoustic field capable of slowing or diverting the weapon by disrupting the cavitation envelope. The research focused on the interactions between high-level sound signals and a supercavity produced by a small free-flying projectile. In order to conduct this study it was necessary to achieve three preliminary accomplishments involving the design of: 1) experimental apparatus that allowed for the study of a small-scale supercavitating projectile in the laboratory environment; 2) apparatus and software for measuring and recording information about projectile dynamics and supercavity geometry; and 3) an acoustic array and power source capable of focusing the desired sound signal in the path of the supercavitating object.

Positive results have been found which show that the accuracy of a supercavitating projectile can indeed be adversely affected by the sound signal. This research concludes with results that indicate that it is acoustic cavitation in the medium surrounding the supercavity that is responsible for the reduced accuracy. A hypothesis has been presented addressing the means by which the acoustic cavitation could cause

this effect. Additionally, corrugations on the cavity/water interface imposed by the pressure signal have been observed and characterized.

CHAPTER I

INTRODUCTION

1.1 Background and Motivation

Supercavitating torpedoes pose new threats to submarines, surface ships and shore targets whose current countermeasures are inadequate against this new technology. The main advantage that these torpedos have over their predecessors and companion weapons is their dramatically increased speed which reduces the reaction time available for deploying a countermeasure, heightening the threat to their intended target. This has prompted the relatively recent addition of this technology to the underwater warfare arsenal for several nations. Proliferation of supercavitating torpedoes has motivated research on countermeasures against them as well as on the fluid phenomenon which makes them possible.

A supercavity is a cavitation bubble that is large compared to the dimensions of the body that causes it and is generally formed due to hydrodynamic pressure reduction. The realization that cavitation could be used to reduce drag on an underwater vehicle occured some time ago, but it is only recently that a number of applications for projectiles and vehicles that may or may not be powered or controlled have emerged. An appropriately designed vehicle body can utilize the phenomenon of supercavitation to achieve global stability a reduction in overall hydrodynamic drag. Research involving supercavitating vehicles has attracted significantly increased attention over the past decade. Military applications of supercavitating research include torpedoes and underwater bullets, as well as projectiles which have already been used for mine

neutralization [49] and proposed for use as defense against torpedos [85].

Obviously the details of the current state of the art military weapons are unknown to the general public, however, it is known that Russia has had an operational weapon (the "Shkval") since the 1980s and is now developing a far more sophisticated version ("Shkval II") [6, 48]. Germany also has an in-development weapon and made it known in 2004 that they have produced a prototype called the "Barracuda" [25]. Iran has a working weapon named the "Hoot", thought to be based on the early Russian Shkvall. It is also thought that China has purchased Shkvall weapons. The United States has in-development weapons and may be fielding operational models secretly.

These new supercavitating torpedoes have been rumored to travel between 230 and 500 mph (100 and 224 m/s). Previous weapons were only capable of reaching speeds of up to around 90 mph (40 m/s) in the water [72, 67], and most are considerably slower. Much smaller unpowered free flying projectiles have been shown to reach speeds of hundreds of miles per hour and in several cases reaching and exceeding the speed of sound in water (approximately 3355 mph or 1500 m/s) [51]. Other practical applications mentioned in the literature include tension-leg platform mooring and geotechnical exploration [46], big game hunting [39], and high-speed vehicles [53, 96].

The driving motivation behind this research is the potential use of underwater sound as a countermeasure to these emerging weapons.

1.2 Introduction to Cavitation and Supercavitation

Cavitation can be defined as the breakdown of a liquid medium under low pressures, whether due to dynamic pressure reduction, acoustic pressure, or rapid accelerations [34]. This breakdown results in the formation of saturated vapor bubbles in the liquid. However, in most cases when cavitation is discussed, the word refers to the

entire sequence of events from bubble formation to cavity collapse. Cavitation is a liquid phenomenon and does not occur under any normal circumstances in either solids or gases.

Supercavities can be formed either naturally or artificially. A natural supercavity is the result of hydrodynamic pressure reduction in the liquid surrounding a solid body. An artificial supercavity is formed with the help of ventilated gas from other sources. This gas can help a small natural cavity grow or can form a cavity in a low pressure liquid region enabling supercavitation at much lower speeds. The ventilation gas can come from a variety of sources including propulsion exhaust gases, compressed gas carried onboard the projectile or entrained air from above the water surface.

Cavitating flows are generally characterized by the non-dimensional number known as the cavitation number, usually denoted by the Greek letter sigma (σ). This number quantifies how susceptible a flow situation is to cavitation. For external flows with a given flow (or object) speed (v), sigma is a ratio of the pressure difference between the ambient pressure and the vapor pressure to the dynamic pressure of the flow,

$$\sigma = \frac{P - P_v}{\frac{1}{2}\rho v^2} \tag{1}$$

where P is the reference (hydrostatic) pressure, P_v is the liquid vapor pressure, and ρ is the mass density of the fluid. In cavitating flows the numerator in equation (1) may not, however, represent the actual pressure difference seen in the flow since the cavity pressure may not equal the vapor pressure. The true scaling parameter is referred to as the relative underpressure of the cavity where P_v in equation (1) is replaced by the cavity pressure P_c. Under most conditions, for vaporous cavity flows, the cavity pressure is approximately equal to the vapor pressure (P_v) at the bulk temperature of the ambient liquid [34, 52]. If the concentration of gas in the liquid is large, then this

may not be the case because the presence of gas in a vaporous cavity is due to diffusion through the cavity interface of gases dissolved in the liquid. Vasin (2001) notes that in most cases it can be considered that the thermodynamic processes within the cavity are isothermal and it can be assumed that the gas temperature in the cavity is equal to the surrounding temperature [99].

Supercavitation is generally associated with $\sigma < 0.1$ for flow over a blunt body. The body can be shaped such that the supercavity is formed at its foremost part and thus envelops it entirely as depicted in figure 1. Some authors also refer to a projectile in this state as "cavity running" or "riding on its nose".

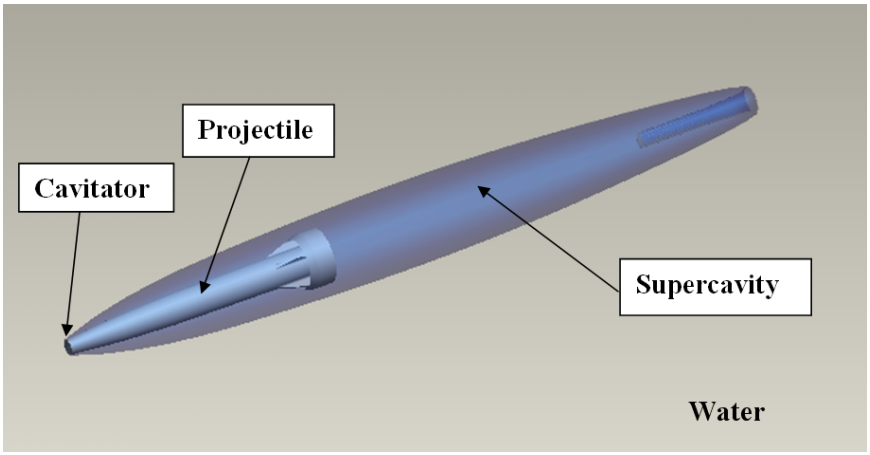

Figure 1: Schematic of a projectile traveling in water showing the cavitator and the supercavity enveloping the body.

The density and viscosity of water vapor, or injected gasses, in a cavity are much lower than that of liquid water which results in reduced skin friction drag on the enveloped body. In fact, stresses on the projectile surface due to the flow of vapor inside the cavity are negligible except at extremely high speeds (Vlasenko (2003) suggests $v > 1000\ m/s$ [102]). Tangential shear stress on the cavity interface is due to friction between the gas in the cavity and the external flow is usually negligible [34]. With correct design the pressure drag can be maintained at a low value by making the

cavitator (see figure 1) as small as possible so that the overall body drag is reduced. Cavitation inception can be enhanced by various changes from ideal conditions such as the amount of gasses absorbed in the liquid, contamination by other liquids or solids, or the presence of bubbles.

For additional information about cavitation, Knapp, Daily and Hammitt 1970 [55], and Franc and Michel 2004 [34] are two notable textbooks which present detailed and more specific discussion of the topic. Good reviews of the present state of cavitation study are presented in references [18] and [42] by Herbert et al 2006. Excellent discussions of supercavitating projectiles are presented in May (1975) [65] and Knapp, Daily and Hammitt 1970 [55].

1.3 Current Torpedo Countermeasures

Traditional defense against torpedos typically involves either maneuvering out of the weapon trajectory or confusing the acoustic homing device on the weapon by deploying additional sources of noise into the ocean environment. With advancing technology and innovations in compact processing power and signal processing algorithms, weapon speeds are increasing and acoustic detection devices are improving. This is decreasing the effectiveness of existing countermeasures even against conventional torpedos. The Applied Research Laboratory (ARL) at Pennsylvania State University, in collaboration with other U.S. government facilities, has been developing an anti-torpedo torpedo over the past several years that addresses these issues, and takes advantage of the very developments that are improving the weapons [66]. This development may improve defense against conventional torpedos and may have application against supercavitating torpedos, however the feasibility of using the ARL countermeasure against supercavitating torpedos is unknown to the author at this time.

1.4 Thesis Hypothesis: An Acoustic Countermeasure

The countermeasure envisaged and investigated in this work is an acoustic field capable of slowing or diverting the weapon by disrupting the cavitation envelope. It is proposed that an acoustic pressure can be used to remotely interfere with the cavitation envelope. An external acoustic pressure will change the cavitation number and have an effect on the inception and subsequent growth of the cavity. The effect that this has on the body dynamics will depend on the projectile design and the intended mode of flight. As is mentioned in Knapp, Daily and Hammitt (1970) [55], if a growing cavitation bubble is subject to a pressure increase its growth will be arrested and reversed, and vice versa, a reduction in pressure would assist cavity growth. Change in the reference pressure is seen by equation (1) to change the cavitation number and thus the characteristics of the flow. Since the supercavitating body interacts with the cavity/water interface as an integral part of its dynamics (see section 2.1.3 on projectile dynamics), disruption of this surface could be used to affect the dynamics.

1.5 Research Questions and Objectives

The questions addressed in this dissertation are of a fundamental nature. They cover basic inquiries that need to be answered to form a ground work for future investigation into the practical development of an acoustic countermeasure. The following list of questions form the basis of this work. They focus on investigating interactions between acoustic pressure signals and the supercavity surrounding a free-flying projectile, and the consequences of this interaction on the body dynamics:

- What effect does an external acoustic pressure signal have on a supercavity?

- Can a realizable cavity alteration disrupt the stability of the cavity or the stability of the supercavitating projectile?
- Can a realizable cavity alteration divert a supercavitating projectile?
- If research concludes that the acoustic pressure does cause an effect, what pressure level and frequency range is desirable?

In order to begin to answer the above list of questions, there are three primary tasks that must be completed: Firstly, design, fabrication and development of an experimental apparatus that allows for the study of a small-scale supercavitating projectile in the laboratory environment. Secondly, design, fabrication, and development of apparatus and software for measuring and recording information about projectile dynamics and supercavity geometry. Lastly, design, fabrication, and characterization of an acoustic array and power source capable of focusing the desired sound pressure levels in the path of the supercavitating object.

After satisfactory completion of these three tasks, the research questions can be addressed through a series of experiments which involve imposing high pressure-amplitude focused sound on the projectiles. The flight dynamics and cavity geometry measurements can then be compared to control experiments, in quiescent water.

1.6 Research Summary

A synopsis of the research is given here as a precursor to chapters 4 and 5. This serves to familiarize the reader with the work so as to put the review of literature in chapter 2, and the simulations discussed in chapter 3 into context.

In the experiments, small projectiles (63.5 mm (2.5") in length) were fired vertically

downward in water from a submerged firing mechanism along a trajectory of approximately 1.1 m. Various measurements were made allowing for characterization of the supercavity shape and the projectile dynamics. Shots were fired both in the absence of any sound signal (control shots) and with an acoustic signal focused at the the midpoint of the projectile's trajectory. The amplitude and the frequency of the sound signals were varied constituting different experiment cases.

Analysis of the observations furnished information on the effects on supercavity shape, projectile accuracy, and the drag force on the body. The models discussed in chapter 3 were used in interpreting and explaining the results, and ultimately led to hypotheses regarding the physics behind the observations and gave insight into use of the method as a countermeasure.

CHAPTER II

BACKGROUND AND SURVEY OF RELEVANT WORK

This chapter presents the necessary background for understanding the main body of work in chapters 3, 4, and 5. In section 2.1, the idea of a free supercavitating projectile will be built upon from the introduction, introducing models for the supercavity shape and the physics of projectile dynamics. Existing experiments involving free naturally supercavitating projectiles will also be reviewed. In section 2.2, the problem of acoustic focusing will be addressed in order to complete the necessary background to begin discussing the design of an experiment in chapter 4.

2.1 Supercavitation of Free Projectiles

Research on cavitating and supercavitating fluid flows has been going on for some time now. The phenomenon is well understood and has been addressed to a great extent in the literature including textbooks devoted to it, for example Knapp, Daily and Hammitt (1970) [55] and Franc and Michel (2004) [34]. Tulins valuable insight into supercavitation is the result of fifty years of his personal research activities [96]. Kirschner et al. (2001) [53] provide a brief overview of research and development on supercavitation, including results on selected experiments with supercavitating projectiles in water and several topics in computational and simulation efforts. They discuss work carried out at the Naval Undersea Warfare Center (NUWC) Newport Division, the Applied Research Laboratory at Pennsylvania State University (ALR/PSU) and the Engineering Technology Center Division of Anteon Corporation (Anteon/ETC). A result of some of this work is presented as a practical application by Jenkins and Evans [49]; They outline the utilization of supercavitating projectiles for mine neutralization using the Rapid Airborne Mine Clearance System (RAMICS) developed by the U.S. Navy.

Section 2.1.1 presents Garabedian's analytical model, Logvinovich's model, and then reviews several other models used in the literature for predicting cavity shape. Several models have been developed over the last 60 - 70 years for supercavity calculations as it has probably been of interest since the productive utilization of supercavitation came under study. Supercavitation can be modeled more accurately using more sophisticated numerical approaches based on boundary element methods, slender body theory and CFD along with various cavity closure models. Although these methods are not used in this work, to provide a more complete review of the current state of knowledge some of the models and work of key authors have been briefly presented in section 2.1.2. Mention of these methods gives indication of possible directions for

more elaborate techniques of predicting the interaction of an external acoustic pressure with a supercavity. Study of the literature has served to show that the simpler analytical models serve adequately for the purposes of this work and with much less computational effort. Section 2.1.3 presents relevant models that describe the forces on a supercavitating projectile as it interacts with the supercavity and a discussion on general projectile dynamics. Section 2.1.4 reviews relevant experimental work on supercavitating projectiles in the literature.

2.1.1 Analytical Models for Cavity Prediction

Cavity shape prediction is used in the design of the supercavitating projectile, verification of the attainment of supercavitation in the experiments, and in the development of a projectile dynamics simulation. A model that can include the effects of an acoustic pressure variation in the surrounding medium is also useful for explaining the effects seen on the cavity shape during experiments.

Two dimensional steady cavity models, both axisymmetric and "plain strain" type, prevail in the literature and are useful for practical treatment of cavity flows. Although it is rare, Knapp, Daily and Hammitt [55] do mention some contributions to mathematical treatment of three dimensional cavities.

The concept of a steady cavity is based entirely on practical considerations and relates to practice only when the shape is sufficiently stable to permit measurement of dimensions. Unsteady and asymmetrical cavities will not be considered in this section. It is also assumed that the size of the cavity is not dependent on the "dry" after body of the projectile. Therefore the shape and size of the cavitator are the only consideration that is made of the projectile dimensions in calculation of the cavity geometry. A major shortcoming of these models is the lack of any consideration of the

complex nature of the cavity closure point. In this work however, the cavity closure has no impact on the projectile dynamics and the wall shape is only of interest in the very front portion of the cavity which can be well described by the simple analytical models.

Gravity affects supercavities in two ways: 1) Buoyancy body forces on the cavity, and 2) Arrested or assisted growth with increase or decrease in depth due to hydrostatic pressure change. The cavity Froude number ($Fr = v/\sqrt{gd_c}$) characterizes the distorting effect of gravity on the cavity shape, where g is the acceleration due to gravity and d_c is the diameter of the disc cavitator. Semenenko (2001) [89] referring to Logvinovitch (1973) states that the effect of gravity can be significant if $\sigma Fr < 2$. The present application does not require the inclusion of gravity effects. Buoyancy generally causes horizontal cavities to bend upward but has little effect on the vertically oriented cavities considered in this work. The change in hydrostatic pressure over the experimental trajectory is approximately 0.1 atmospheres. This is small in comparison to the generated acoustic pressures so can be neglected. It is noted, however, that active torpedoes move primarily horizontally and at depths much greater than in this research effort.

May (1975) [65], referring to Self and Ripken (1955) [88], mentions that the cavity can indeed be significantly influenced by the diameter of the after body occupying the cavity, with smaller cavities for larger bodies. This assertion is based on experimental measurements. Most authors, however, do not consider any dependence. It is also noted here that in this work the measured cavity width agrees favorably with that predicted by Garabedian's model but the measured length is consistently around 20% greater than that predicted by the same model (see figure 29 in section 4.3.4).

2.1.1.1 Garabedian's Supercavity Shape Prediction Model

The formulae describing Garabedian's model were known to Reichardt in 1946 but he was only able to give an empirical derivation. A full theoretical derivation from first principles is given by Garabedian in a 1956 paper [35]. His study deals with axially symmetric, irrotational, incompressible flows (potential flow). Garabedian's model is used frequently in more recent literature and its predictions have been extensively verified. Two examples relevant to this thesis are Kulkarni and Pratap (2000) [57] where it is used in a projectile dynamics model, and Varghese, Uhlman and Kirschner (2005) [97] where the model is compared to a numerical boundary element cavity prediction.

The specific model used in this work applies exclusively to axially symmetric cavities. The formulas are derived by Garabedian [35] as asymptotic expressions for small cavitation number. The cavity is assumed to be ellipsoidal in shape which is quite accurate for large cavities as is concluded by many authors from theoretical, numerical and experimental results [35, 98, 99]. The equations describing cavity shape formed by a disk cavitator at zero angle of attack are the following:

$$\frac{h^2}{r_c^2} \sim \frac{C_D}{\sigma^2} ln \frac{1}{\sigma} \tag{2}$$

$$\frac{h^2}{d^2} \sim \frac{1}{\sigma} ln \frac{1}{\sigma} \tag{3}$$

$$\frac{d^2}{r_c^2} \sim \frac{C_D}{\sigma} \tag{4}$$

where h is the ellipse semi-major axis (half of the cavity length), d is the ellipse semi-minor axis (half of the cavity maximum diameter), r_c is the cavitator radius, and C_D is the drag coefficient of the cavitator. Figure 2 shows a schematic of the assumed elliptical shape. The cavitator drag coefficient will be discussed in detail in section 2.1.3.1.

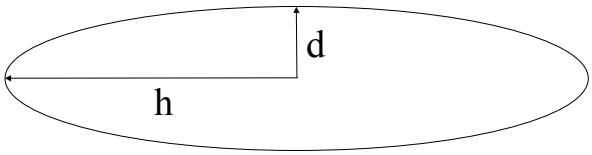

Figure 2: Elliptical cavity dimensions schematic - h is the ellipse semi-major axis (half of the cavity length) and d is the ellipse semi-minor axis (half of the cavity maximum diameter)

Early verification of this simple model is given by Garabedian himself in a comparison of his results to those of Levinson (1946). Also, Knapp, Daily and Hammitt (1970) [55] mention that experiment and theory both indicate that the cavity shape is nearly ellipsoidal and the drag variation with cavitation number is nearly linear. Extensive subsequent use in the literature has made this model a standard for supercavity size estimates.

2.1.1.2 Logvinovich's Supercavity Prediction Model

Logvinovich's principle of independent cavity section expansion is an analytical method of predicting a supercavity shape (*"Hydrodynamics of Flows with Free Boundaries"*, 1969 (in Russian)). The principle is based on the assumption that each cross-section of a cavity expands and contracts independently of adjacent sections and is dependent on the conditions at the moment that the cavitator passes the plane of the section. This assumption implies that the water is modeled as having no shear modulus. The advantage of this model over Garabedian's model for the purposes of the current work

is that it allows for inclusion of a time dependent cavity underpressure and thus the prediction of the resulting cavity shape in the presence of external acoustic pressure fluctuations. The assumption of an axis symmetry is still enforced for individual cross-sections but the individual sections can originate at different orientations or directions of the cavitator velocity vector. This allows for a much more realistic and useful shape prediction for a projectile dynamics model (see section 3.2).

The equation describing cavity cross-section evolution is usually derived from energy considerations and is outlined as such in the literature by Russian colleagues in several English written publications [99, 74, 85]. This approach inherently puts the solution in a Lagrangian frame of reference following the fluid particles, so in this case following the cavity cross section. Franc and Michel (2004) [34] present a somewhat different derivation starting with the general differential fluid equations of continuity and momentum. This approach provides different insight into the result as is the case with the Newtonian versus energy viewpoints in many areas of dynamics and fluid mechanics. Some details of the derivation of each approach is given in appendix A to provide more insight into the assumptions of the model.

The differential equation describing the cavity cross-section area, S, as a function of time and location on the cavitator trajectory is given by

$$\ddot{S}(s,t) = -\frac{\kappa \Delta P(s,t)}{\rho} \tag{5}$$

where ρ is the density of the liquid outside the cavity, κ is a derived coefficient slightly dependent on cavitator drag coefficient and cavitation number, and $\Delta P(s,t)$ is the pressure difference between the exterior and interior of the cavity. $\Delta P(s,t)$ is given by

$$\Delta P(s,t) = P_{hs}(s) + P_{ac}(s,t) - P_c \tag{6}$$

where P_{hs} is the hydrostatic pressure, P_{ac} is the acoustic pressure and P_c is the internal cavity pressure. Franc and Michel (2004) [34] suggest that κ is constant for elongated cavities and can be approximated by the asymptotic results

$$\kappa \approx \frac{4\pi}{ln(1/\sigma)} \tag{7}$$

Vasin [99] deduces from energy considerations that

$$\kappa = \frac{4\pi C_D}{a^2} \tag{8}$$

where a is a constant slightly dependent on cavitation number and spans the range $1.5 \leq a \leq 2$.

Assuming that κ is constant with time, the integration of equation (5) can be written as

$$S(s,t) = S_0 + \dot{S}_0 t - \kappa \int_0^t \int_0^u \frac{\Delta P(s,v)}{\rho} dv du \tag{9}$$

S_0 is the area of the cavity cross section at $t = 0$ which is equal to the cavitator area, so $S_0 = \pi r_c^2$. $\dot{S}_0$ is the initial rate of change of the cavity cross-section area, and u and v are dummy variables of integration. Again from energy considerations, Vasin [99] derives and expression for $\dot{S}_0$

$$\dot{S}_0 = \frac{2\pi C_D r_c v}{a} \tag{10}$$

where the speed v is the cavitator speed when the cavity section is formed and everything else is as previously defined.

2.1.1.3 Some Other Supercavity Prediction Models

There are several other similar models in the literature that, although not used in this work, are mentioned here for completeness.

The technical report of May (1975) [65] presents a complete compilation of data and theory on supercavitating projectiles up to its publication date. The report compares equations of other authors with experimental data and derives equations which appear to best fit the data. Given here (in a different notation to be consistent with earlier definitions in this dissertation) are the equations May presents for the maximum diameter and length of a supercavity formed by a disk cavitator:

$$\left(\frac{r_c}{d}\right)^2 = 1.35 C_D \sigma^{-0.93} \tag{11}$$

$$\frac{h}{d} = \sigma^{-1.15} \tag{12}$$

The cavity outline is also discussed by May who notes that several authors have altered the perfect ellipse slightly using

$$\frac{x}{h}^2 + \frac{R}{d}^n = 1 \tag{13}$$

with exponent $n \neq 2$. R and x are the radius of the supercavity and the distance along the axis of the supercavity. However, in this work, following Garabedian and May, the perfect ellipse with $n = 2$ will be used. May compares plots from several variations and deems them indistinguishable from one another.

Vlasenko (2003) [102] derives an empirical formula for calculating cavity shape that approximates his experimental data.

$$\bar{R}^2(\bar{x}) = 3.659 + 0.847(\bar{x} - 2) - 0.236\sigma(\bar{x} - 2)^2, \bar{x} \geq 2 \tag{14}$$

where $\bar{R}$ and $\bar{x}$ are the radius of the supercavity and the distance along the axis of the supercavity both normalized by the cavitator radius. The shape is compared

to Logvinovich's model. The maximum radius and cavity length are compared to Garabedian's model along with the original data. For the range of cavitation numbers investigated ($0.01 < \sigma < 0.06$) good agreement is shown up to the cavity closure point. This is expected because none of the models take account for any closure mechanism. More importantly, however, it indicates that the closure mechanism does not significantly effect the forward cavity geometry which is an assumption made in this work.

Schaffar, Rey and Boeglen (2005) [85] compare a model by Levinson (1946), that Garabedian also used for comparison, and one by Serebryakov (1997) to their experiment data. It is concluded that both models give very good agreement with the data close to the cavitator.

2.1.2 Numerical Modeling for Cavitation and Supercavitation

Numerical models used for the prediction of cavitating and supercavitating flow is an area under rapid development and advancement. There are generally three modern methods used for numerical modeling of supercavitating flows which are prevalent in research efforts in the United States: boundary element methods (BEM), slender-body theory (SBT), and computational fluid dynamics (CFD). BEM and SBT are potential flow techniques. For high Reynolds number flows, viscous effects become increasingly confined to a thin boundary layer near the body surface, or in this case the shear layer forming the cavity boundary. This implies the assumption of irrotational flow which, in turn, implies the existence of a velocity potential ($v = grad(\phi)$) and thus allows the use of potential flow techniques for solving the problem. Indeed, Logvinovich's model described in section 2.1.1.2 is derived assuming the existence of a velocity potential. Under these conditions, the velocity field can be determined based

solely on kinematic considerations and knowledge of conditions at the domain boundaries [52].

2.1.2.1 Boundry Element Methods

The boundary conditions on the domain vary with complexity of the analysis. Common conditions of consideration are the following:

- Kinematic condition that the flow must be tangential to the body and cavity surfaces.
- Pressure on the cavity water interface must be equal to the cavity pressure.
- Cavity termination condition. Common conditions are the Riabouchinsky wall or a re-entrant jet model [55].

Kirschner, Fine, Uhlman and Kring (2001) provide notes on various studies using BEM [52]. They discuss problems involving (1) steady, subsonic flow around an axisymmetric disk; (2) unsteady, subsonic flow around general cavitator shapes [56]; and (3) steady flow around cavitating control fins for application to supercavitating vehicle flight control. Results are compared to May (1975) and are in very close agreement on cavity shape and drag for axisymmetric cavities [88]. Kring, Fine, Uhlman and Kirschner (2001) discuss the use of BEM for a three dimensional unsteady potential flow problem and show preliminary results [56].

2.1.2.2 Slender Body Theory

In slender body theory the aspect ratio of the cavity is assumed large and the problem is solved by determining a distribution of sources and sinks on the cavity axis. Vasin (2001) presents some results for subsonic flow [98].

2.1.2.3 Computational Fluid Dynamics (CFD)

There is extensive literature on multiphase and cavitation mass transfer CFD models. Numerical simulation providing an accurate prediction of supercavitating flow is a particularly difficult situation to model. The flow field contains distinct boundaries between the phases which represent large localized gradients in fluid properties, compressibility effects can be significant due to the high speeds involved, and cavitation is an inherently unsteady process.

Owis and Nayfeh provide a line of research at Virginia Tech on the development of a code which is tailored toward calculation of cavitating flow over projectiles. Their work involves free and propelled projectiles, natural and ventilated cavities, partial and supercavitating flow. Compressible and incompressible models are compared with work of other researchers and experimental data. Great effort is made to generate a very general code for all situations with the vision of more complex dynamics and control applications in the future. Owis and Nayfeh (2001) [71] present an unsteady, incompressible, axisymmetric CFD approach. A mixture model is used with the governing equations being the continuity equation, the momentum equation for the mixture and the volume fraction equation. Owis and Nayfeh (2002) [72] add inclusion of compressibility effects. It is noted that for high speed flows, compressibility becomes significant in the liquid phase as well as in the vapor phase and this may even be the case when the flow speed is small compared to the speed of sound in water. At cavitation numbers of 0.4 and 0.3 (corresponding to velocity of 20 m/s and 25 m/s for compressible flow) it is shown that the compressible and the incompressible results are in close agreement as would be expected due to low density variations at low speeds. At a cavitation number of 0.05 results are very close for both models with the compressible model being slightly better but this could be due to other differences in the model and cannot be solely attributed to the inclusion of compressibility.

Owis and Nayfeh (2004) [73] present more results from the unsteady incompressible model including ventilated flows and projectiles with an angle of attack relative to the direction of motion.

Kirschner et al. (2001) [53] present applications and adapt a code named UNCLE-M at ARL/PSU for use modeling the physics associated with high speed maneuvers, control, body-cavity and fin-cavity interactions, viscous effects, compressibility effects, ventilation, bubbly mixtures, and high speed projectile motion.

Code OTi-HULL (available from General Dynamics, formerly Orlando Technology Inc.) is applied by researchers in the study of supercaviting projectiles fired through and air/water interface at transonic and supersonic velocities (in water) [85, 86, 87]. The code is not written specifically for supercavitating bodies and is valid only for these very high velocities and for penetration of an interface. It is stated that a projectile velocity of 870 m/s is practically the lowest limit of its validity. Schaffar and Pfeifer (2001) [86] compare the results with a two phase model (Cocchi Ph.D thesis). Differences in results are attributed to the fact that phase change is not taken into account in the HULL model (cavity is entrained air from the penetration). The OTi-HULL code (Euler module) solves the Euler equations without heat conduction, viscosity and phase change.

The cavitation model implemented in $FLUENT^{\text{TM}}$ 6.2.16 is based on the "full cavitation model" developed by Singhal, Athavale, Li and Jiang (2002) [90]. However, unlike their approach, assuming single-phase, variable fluid density flows, the cavitation model in $FLUENT^{\text{TM}}$ is under the framework of multi-phase flows, and it has the capability to account for the effects of the slip velocities between phases. It accounts for phase change, bubble dynamics (formation and collapse), turbulent pressure fluctuations, and non-condensable gases. Salvador and Frankel (2004) [82] present comparison of results using the FLUENT cavitation model in Version 6.1

(same model as version 6.2) to experiment and find accurate predictions for the flow situations studied.

2.1.3 Projectile Dynamics

Forces on cavitating bodies became a focus for numerous researchers when cavitating hydrofoils and propellers became a topic of interest in the 1950's [96]. Work on supercavitating projectiles and torpedos was not seen in the public literature until the 1970's. The dynamics of a supercavitating projectile is an area still under extensive investigation, with the control and design of supercavitating torpedoes and vehicles being the main focus and motivation.

The forces acting on a free, naturally supercavitating projectile are considered. Conventional flight stability of a projectile that has no spin requires that the center of pressure be aft of the center of gravity. A body experiencing supercavitation does not adhere to the conventional stability rule since the hydrodynamic forces are largely concentrated on the cavitator. Rather, it achieves global stability from the interaction of the body surface with the cavity wall, a process known as tail-slap. In this case the forces on the body are the lift and drag forces on the cavitator disk, lift and drag due to interactions of the tail of the body with the cavity/water interface, and weight. Weight is important for horizontal trajectories, however, it has little effect on vertical trajectories other then altering the acceleration in the direction of flight, which is most often negligible.

Cavitator forces are often based on empirical lift and drag data published as far back as 1954. Interactions of the body tail with the cavity wall are presented in the literature with various degrees of complexity and with models that are still being revised and modified today. Most of the dynamics simulation models found in the

literature have been developed over the last ten to fifteen years and incorporate the hydrodynamic forces on the body and control surfaces as well as propulsion forces and coupled interactions between the body dynamics and the shape of the supercavity.

Some general conditions that are assumed are give here before specific forces are discussed. These conditions are all relevant to the case of supercavitating flight studied in this thesis.

1. The projectile has sufficient speed for the supercavity to cover the entire body.
2. The cavity is long enough so that the re-entrant jet does not impinge on the tail of the body.
3. The projectile is traveling slow enough so that the aerodynamic forces on the body due to the gas inside the cavity can be neglected.

A very comprehensive report is given by May (1975) [65] on numerous aspects of the dynamics of supercavitating bodies. His report addresses the forces acting on 'cavity running' missiles and trajectories of missiles while 'cavity running'.

The following review will cover some of the relevant experimental data and theoretical models. First, the forces on a supercavitating projectile will be discussed followed by the resulting implications on projectile trajectory. Then some of the dynamics models presented in the literature will be noted.

2.1.3.1 Forces on a Disk Shaped Cavitator

The forces on the cavitator are paramount to dynamics prediction because this is the only constant point of contact between the projectile and the water throughout the flight, and furthermore, the only point of contact for a large portion of the flight.

There are several shapes of cavitator presented in the literature; three prevalent types are disks, cones and ogives. Only disk shaped cavitators are considered in this work because it is a disk cavitator that is used in the experimental investigation. The following is a widely used approach for accounting for forces on a disk cavitator that is based on the experimental work of Kiceniuk published in 1954 [50].

The hydrodynamic coefficients of drag (C_D) and lift (C_F) are defined as follows:

$$C_D = \frac{F_D}{(1/2)\rho v^2(\pi r_c^2)}$$

$$C_L = \frac{F_L}{(1/2)\rho v^2(\pi r_c^2)}$$

where F_D and F_L are the drag force and lift force on the cavitator respectively.

The drag coefficient is a function of the cavitation number (equation (1)) and can be found for a disk at zero angle of attack from the equation

$$C_D = C_{D0}(1 + \sigma) \tag{15}$$

where C_{D0} is the cavitator drag coefficient at $\sigma = 0$. Garabedian [35] arrives at a value of $C_{D0} = 0.827$ for a circular disk in the case of an infinite cavity. He states that this number compares favorably with experimental data and quotes a spread of estimates from 0.79 (obtained by Reichardt in a free jet tunnel) to 0.83 (obtained in a high speed tunnel at the California Institute of Technology). Experimental values are estimated by extrapolating data since $\sigma = 0$ is not realizable for a real flow situation. Garabedian found that on substituting C_{D0} into the asymptotic expression for C_D

neglecting $O(\sigma)$ terms (resulting in equation (15)) the resulting curve was very close to experimental results in the range near $\sigma = 0.125$ where most experimental data was available. May [65] concludes that the best estimate for C_{D0} is $C_{D0} = 0.815$ after considering the work of many authors' theoretical and experimental work, including that of such influential researchers in the field as Garabedian and Reichardt.

For non-zero angles of attack (α), the resultant force on the cavitator is resolved into lift and drag components. The drag force (F_D) is defined as being parallel to the velocity of the cavitator and the lift force (F_L) is perpendicular to the drag force. Figure 3 depicts these forces in a schematic of the disk cavitator. In the figure, α is the angle of attack.

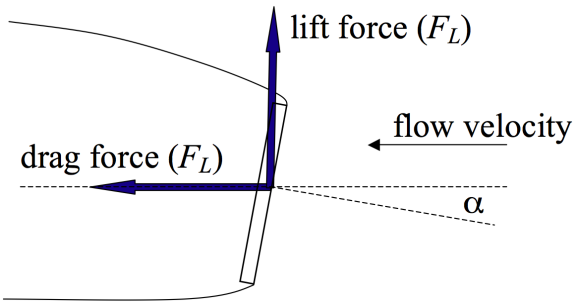

Figure 3: Schematic of lift and drag forces on a disk cavitator. F_L = lift force, F_D = drag force, α = angle of attack.

Kiceniuk (1954) [50] provides experimental data on lift and drag coefficients as a function of cavitation number and of angle of attack for disk cavitators (original plots are shown in appendix C, figures 75 and 76). Up to $\alpha = 30°$, C_D for a disk decreases as approximatley $cos^2(\alpha)$,

$$C_D = C_{D0}(1 + \sigma)cos^2(\alpha) \tag{16}$$

May states that for small angles of attack the lift force for a disk is nearly equal to $sin(\alpha)$ times the drag force at $\alpha = 0$. Kiceniuk's data implies that a more accurate representation of the experimental data up to $\alpha = 30°$ is,

$$C_L = C_{D0}(1 + \sigma)sin(\alpha)cos(\alpha) \tag{17}$$

Other authors also use this relation [1, 4, 20, 54, 57]. It is implied by equations (16) and (17) that the pressure force on the disk cavitator always acts parallel to the axis of the disk. This is obviously not entirely true, but the results implies that the friction force tangential to the disk surface is negligible compared to the normal pressure force. Kiceniuk's data [50] also presents values of moment coefficient as a function of angle of attack. For the disk cavitator, this is based on the moment about a line parallel and coincident with the upstream face of the disk and through the center of the circular upstream face. His data shows that the moment coefficient is approximately zero for the disk cavitator. This implies that the resultant force, in addition to acting parallel to the disk axis, acts at the center of the face.

2.1.3.2 Forces on the Projectile Tail

In contrast with the cavitator force models, the tail force impact model is one that is still being revised and refined in the literature. There is no generally accepted method for calculating the forces during tail impact with the cavity wall, rather and assortment of different approaches, none of which have been verified definitively by comparison with experimental data.

The simplest model is perhaps that used by Choi, Ruzzene and Bauchau (2004) [20]. They model the tail impacts as short duration impacts between the body and an elastic surface. The penetration depth is measured perpendicular to the axis of

the cavity section at the tail location. The direction of the applied force is also along this line and its magnitude is assumed proportional to the penetration depth. In their work the spring is assumed linear and the spring constant is determined from experimental observations. It is reported that this method is able to reproduce interactions observed experimentally [65]. One could however, model a nonlinear spring by letting the spring parameter vary with penetration depth.

In a paper investigating supercavitating projectile dynamics and focusing on the nature and frequency of the tail impacts, Rand, Pratap, Ramani, Cipolla and Kirschner (1997) [4] present a model based on momentum considerations. A control volume is established around a portion of fluid that is deflected by the tail of the cylindrical body during impact and the momentum equation is used to predict the resultant forces that the fluid imposes on the body. Assumptions regarding the size of the control volume are not clearly stated and a quantitative validity of the model is not given. As with Choi's model the coefficient of restitution is one implying a perfectly elastic collision.

A more complex model is presented in Kulkarni and Pratap (2000) [57] where the tail forces are considered in more detail. The model is, however, questionable on some aspects. The tail impact force is split into two components, each with a separate model, one termed the impact model and the other a drag model, although the impact model does have a component parallel to the primary direction of flight in the direction of drag. The impact model is based on the assumption that, during impact, fluid motion occurs primarily in the direction normal to the projectile axis, then formulated using a virtual mass approach. The drag model presents an elementary approach to finding the forces on a cylinder planing on a flat free surface, however, forces in both the axial and normal directions are calculated using the drag coefficient on a disk cavitator which is quite a crude assumption without the backup of experimental data.

The final model given here is one presented in Kirschner (2002) [54], Ahn (2007) [1], and Ruzzene (2008) [81]. The model is an extension of Wagner planing theory developed by Logvinovich [63], and in the case of Ahn and Ruzzene, further developed by Hassan (cited as a private communication but detailed in their publications) to include the effects of skin friction on the submerged tail.

This model was chosen for use in developing a dynamics model in a later section. It has been used extensively in the literature by credible authors and was suitable for this application. It is a simple analytical model which could be easily incorporated into the numerical model.

For a cylindrical body planing on a cylindrical free surface the pressure force normal to the axis of the cylindrical hull, F_{pn} is given by

$$F_{pn} = \pi \rho R_t^2 v^2 \sin(\alpha_p) \cos(\alpha_p) \frac{r_t + h_p}{r_t + 2h_p} \left(1 - \left(\frac{\Delta}{h_p + \Delta} \right)^2 \right) \tag{18}$$

where r_t is the hull radius (assumed to be constant over the planing region), R_t is the cavity radius (averaged along the planing region), α_p the angle of attack between the body axis and the cavity axis, and h_p is the immersion depth at the transom measured normal to the cavity centerline. $\Delta = (R_t - r_t)$ is the difference between the cavity and hull radii respectively. F_{pn} is in the direction tending to reduce the angle of attack, pushing the tail back into the cavity.

The moment of the pressure forces about the transom is given by

$$M_{pp} = \pi \rho R_t^2 v^2 \cos^2(\alpha_p) \left(\frac{r_t + h_p}{r_t + 2h_p} \right) \left(\frac{h_p^2}{h_p \Delta} \right) \tag{19}$$

M_{pp} is in the direction tending to increase the angle of attack.

More detail and further development of a cylinder planing in a cavity is presented by Vasin and Paryshev (2001) [100] and in Paryshev (2006) [75].

2.1.3.3 Projectile Trajectory

The projectile trajectory is obviously largely dependent on the specific body design, most importantly the cavitator and tail shape, along with the mass properties and slenderness (ratio of body length to diameter). The proximity of the cavity wall to the tail is also important.

May [65] provides a comprehensive discussion on supercavitating projectile trajectory. Only a small subset of the cases May considers that are relevant to this thesis are discussed here. Figure 4 shows several flight scenarios for a simple cylinder in vertically downward flight. Although this is a simple specific case, the concepts are universal and provide valuable insight into the behavior of other designs and other situations. Cases A through D in the figure is discussed in the following.

Case A shows the situation where the projectile only contacts the cavity at the nose. This can occur for a short time until the projectile falls onto the cavity wall. The aerodynamic forces on the after-body of the projectile inside the cavity are assumed to be negligible for the speeds of interest in this work. Therefore, any aft stabilizing surfaces on the projectile with the purpose of moving the center of pressure toward the tail (it is assumed there are no control surfaces such as fins protruding through the cavity wall into the water) do not perform their function and it is inevitable that the projectile will fall against the cavity wall, even in vertical flight. When this happens the resulting motion will likely follow either case B, C or D.

Generally, moments about the center of gravity as a result of forces on the nose will cause an overturning moment tending to increase the angle of attack and propel the

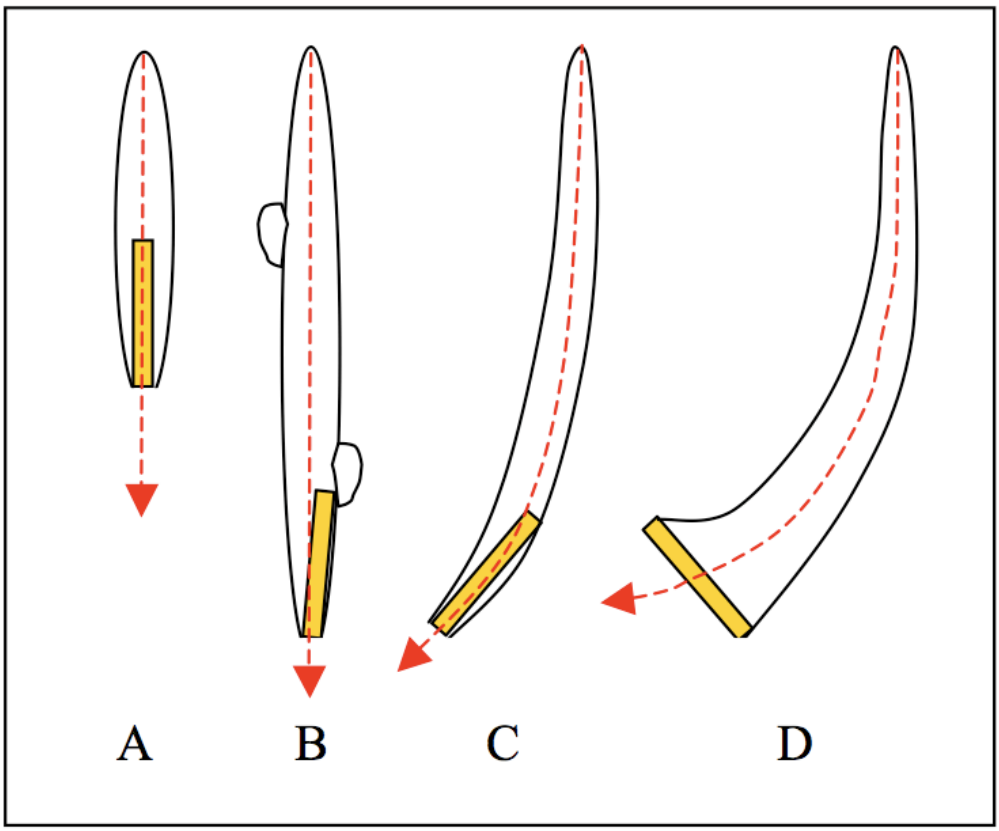

Figure 4: Projectile trajectory schematics for various modes of flight: A. Ideal flight with only nose contact, B. Oscillating trajectory. Markings on the outline are blisters or bubbles formed during tail impact, C. Circular arc trajectory, D. Broadsiding

tail into the cavity wall. When the tail of the body impacts the cavity/water interface, however, the resulting forces tend to counteract those moments due to forces at the nose and work to decrease the angle of attack.

In *case B* the moments produced by forces at the tail overwhelm the nose moments tending to reverse the angular velocity and reduce the angle of attack. This scenario is usually the case when the angle of attack at impact is small, the projectile is long, and the cavitator is blunt (e.g. disk or truncated cone or ogive). The tail then swings back through the axis and impacts the cavity on the other side. The result is a globally straight flight trajectory with local sinuous motion. This is the desired case

of the dynamics in this study because a straight flight is sought in the control case with no imposed acoustic pressure.

Various experimenters, including ourselves, have observed the oscillatory nature of the body impacting with the cavity wall. Experiments in this work have also verified the notion that this oscillatory motion causes a sinuous but globally straight trajectory. The frequency and rate of change of frequency of the impacts depends on the projectile design and initial conditions of the body motion.

There are circumstances when this oscillatory behavior does not occur. *Case C* shows a projectile following a circular arc trajectory which can happen when the forces due to the tail impact with the cavity wall are not sufficient to reverse the direction of the angular velocity to the extent that the tail will swing back through the axis of the trajectory. The moments due to force at the nose and the force of weight are trying to increase the angle of attack while the force at the tail is trying to reduce it. The competition of these forces along with energy loss during impacts will cause damped vibration (usually underdamped) of the projectile against one side of the cavity. When the transient oscillation dies out and the forces balance, the tail will remain against one side of the cavity wall. The lift force produced at the nose and the tail in this mode of flight are both in the same direction causing the projectile to proceed in a curved path. For a slender cavity and a projectile with a disk cavitator (disk cavitator produces little moments as previously discussed) the radius of curvature can be very large. Very massive projectiles in non-vertical flight or projectiles with cone or ogive cavitators are more prone to this mode of flight.

This motion is undesirable for the projectile design in this study but has significance as a mode of flight to induce with the countermeasure in order to divert the projectile. It also has application in design when a curved path is desired, for example, the attack on a surface ship. If a missile is launched from the air into the water either from a

ship or from an aircraft, it initially travels deeper away from the surface. If the net vertical force due to the weight, the lift at the nose, and the lift at the tail is upward then the missile will travel in a curved trajectory back toward the surface.

Case D shows the scenario of an unstable projectile broadsiding. This will occur when the forces on the tail at impact are insufficient to stop the increasing angle of attack. A long slender body that experiences this will continue in sideways motion. A shorter body will tend to tumble.

When the cavitation number is reduced the cavity eventually collapses, or closes in on the tail of the projectile. This happens due to decreased speed or increased external pressure. If the projectile has rear stabilizing surfaces then the flight will continue in a straight trajectory but with a large increase in drag. If there are no stabilizing surfaces then the body will likely become unstable and tumble or broadside.

2.1.3.4 Projectile Dynamics Simulations

Modeling the dynamics of a supecravitating projectile is a complicated problem. There were several simplifying assumptions stated at the beginning of this section, however, one must still consider the forces at the cavitator and during tail-slap, as discussed in detail above, along with the fact that cavity-body interactions present a coupling issue because the cavity shape directly affects the dynamics and the dynamics directly effect the cavity shape.

A very simple but instructive model is presented by Rand et al (1997) [4]. They simulate dynamics based only on simple models of the forces at the cavitator and tail and do not consider any coupling issues; it is assumed that the cavity retains its shape and orientation during motion. Assumptions are also made that the cavitator moves in a straight line, the projectile rotates about its nose, does not spin, and there are

no moments produced about the center of mass by the cavitator. This means that all rotational motion is a consequence of the initial conditions as the projectile leaves the firing mechanism. Additionally, the impacts have a coefficient of restitution of one implying perfectly elastic collisions. Focus is on predicting the frequency and duration of the impacts and explaining some of the intuitive aspects of the dynamics as well as giving some equations for quantitative prediction. The resulting oscillatory motion discussed earlier is simulated and basic physical processes accounted for but the over simplification leaves the quantitative predictions questionable. In this work the initial conditions are unknown, but this simple model indicates that it is the initial conditions that must be controlled in order to achieve the desired flight. Recorded flight dynamics can give an estimate of initial conditions and impact durations calculations can be used to predict drag force impulses.

This model is developed further in Kulkarni and Pratap (2000) [57]. The cavitator is now confined to a plane instead of a straight line and the tail-slap forces are considered in more detail. Equations of motion are derived and motion simulated for two projectile configurations. The two projectiles have the same mass and outside diameter but one is hollow and so had its mass distributed over a larger length. The additional complexity introduces the result that both the frequency and angular velocity of the rotation about the tip increase in initial stages of flight, then angular velocity reduces thereafter, while frequency remains constant. Influence of the mass distribution on flight dynamics is an interesting consideration for projectile design. The conclusion drawn is that the increased moment of inertia and the decreased angle of attack upon impact cause the initial rate of increase of angular velocity and the magnitude of the maximum angular velocity to be reduced and in turn reduce the frequency of impacts and the forces at the tail during tail-slap.

Literature addressing further developments on the theory of supecavitating projectiles

has generally been for much more complex vehicles. The vehicles themselves include complexities that are not relevant to the focus of this work, however, the concepts and model developments can be valuable for the study of more simple vehicle configurations. Recent simulations are included in the works of Ahn [1] and Kirschner et al [54]. Developments include: hydrodynamic fin models, propulsion and ventilated cavity models incorporating gas losses from the cavity and cavity boundary oscillations, relative motion between the main body and cavitator, changes in cavity shape due to variations in cavitator orientation, and memory effects which are the result of cavity evolution being independent future events.

2.1.4 Experimentation

This section outlines some of the relevant experiments that were found in English language publications. These experiments are studied to gain insight and design ideas for experimental apparatus that allows for the study of small scale supercavitating projectile in the laboratory environment and design of devices that measure and record information about projectile dynamics and supercavity geometry. These are two goals of the current work as has been outlined in section 1.5. Attention is directed toward low-cost design although more elaborate experiments are also studied as they too may provide valuable contributions.

Experimental work in the United States on supercavitating bodies has been carried out mainly at the Naval Undersea Warfare Center (NUWC) in Newport, Rhode Island and at Pennsylvania State University's Applied Research Laboratory (ARL). The numerous research and development efforts have produced such items as the Adaptable High-Speed Undersea Munitions (ASHUM) and projectiles for the Rapid Airborne Mine Clearance System (RAMICS). An overview of the facilities and experiments is described in detail by Kirschner et al (2001) [53]. Additionally, Hrubes (2001) [46]

gives a detailed description of an experiment carried out at NUWC with very high-speed projectiles (up to and exceeding the speed of sound in water, approximately 1500 m/s). This experiment is elaborate, costly to reproduce, and requires major construction and fabrication efforts. For example, they use a 49.4 x 6.1 x (5.5-7.0) m (Length x Width x Depth) water tank, a 30 mm gun, and large quantities of expensive recording and measurement equipment including ten cameras. While this experiment has been very successful and may be required for such high speed observations it is certainly possible to avoid a lot of this cost by implementing a lower speed, scaled down setup.

Vlasenko (2003) [102] presents results from experiments conducted at the National Academy of Sciences of Ukraine. His experimental setup is also very elaborate and requires large-scale expensive facilities. Two tests are reported in this work. One involves 40 to 60 mm diameter self propelled vehicles at 120 to 140 m/s and the other involves 10 to 17 mm diameter free flying projectiles close to the speed of sound in water in a 40 x 2 x 2 m (Length x Width x Depth) test tank. Savchenko (2001) [84] also presents results and experimental activity there.

On a much smaller scale Schaffer, Rey and Boeglen (2002 and 2005) [87, 85] investigate a free, naturally supercavitating projectile in an experiment conducted at the French-German Research Institute, ISL, in Saint-Louis, France. This experiment involves firing projectiles horizontally in water on a similar scale to the present work. Projectiles are fired from a 20 mm gun with sabot into a 1 x 0.5 x 0.5 m (Length x Width x Height) tank of water and viewed through windows with a high-speed digital camera. The large gun is needed to reach the desired speeds of 600 to 1036 m/s (in fact higher transonic speeds are being sought). Speed is measured at two points using laser barriers. The results are presented with some degree of ambiguity. The experimental results are compared to theory of Levinson and Serebryakov with close

agreement, and to the CFD code OTi-HULL with poorer agreement.

Mostafa, Nayfeh, Valchos, and Telionis (2001) [68] at Virginia Tech have also conducted experiments firing projectiles in water. A digital particle image velocimetry system that has been developed by the same authors is used to measure the velocity field utilizing a Copper-Vapor laser and a high speed digital camera.

There are also several experimental configurations that utilize a water tunnel. Some examples of such experiments are discussed in Wu and Cahine (2007) [106] at Dynaflow Inc, in Maryland and Wosnik, Schauer and Arndt (2003) [105] at St. Anthony Falls Laboratory, University of Minesota.

Fowler, Sheehan and Silver (2005) [33] present an idea and a setup that attempts to provide long duration supercavities on cavitator disks on the order of one centimeter diameter without the expense and commitment of water tunnel equipment. It involves a rotating arm with a cavitator attached to the end submerged in a tank of water. No quantitative results are presented in the paper.

2.2 Focused Acoustics in Water

In this thesis it has been established as a necessary goal that an underwater acoustic array must be designed and tested that is capable of focusing high intensity acoustic energy at a desired location to interfere with a supercavity surrounding a moving body in water. To this end, the following will outline some of the background useful in designing and understanding the sound field. Additionally, discussion on the effects that the high intensity sound has on the medium is presented to establish an understanding of the fluid in which the supercavitating projectile will travel in. Firstly, section 2.2.1 highlights some of the relevant literature on acoustic focusing.

Section 2.2.2 then discusses acoustic cavitation which is the dominant nonlinear effect in focusing sound at the frequency and range involved in this work. Section 2.2.3 discusses effects of the acoustic cavitation on the properties of the water. Lastly section 2.2.4 presents some background in an adaptive focusing technique that, although not used in this work is studied in order to guide future work in developing a practical application of the current countermeasure concept.

2.2.1 Focused Signals

Acoustic focusing is a subject area addressed primarily in the field of medicine where focused sound energy can be particularly useful in noninvasive treatments [40]. Ultrasound applications are also very appealing in medicine because they do not utilize harmful radiation. Some applications are the following. High intensity focused ultrasound (HIFU) [17, 19] is used to destroy tissue and cells and achieves this by creating high localized temperatures or cavitation which can mechanically destroy tissues. Lithotripsy is a commonly used procedure that utilizes shock waves to destroy kidney stones [5, 21, 22, 23, 32, 40]. Therapeutic hyperthermia treatment, acoustic microscopes [36] and enhanced drug delivery are other applications.

Medical applications generally require very precise prediction and measurement of the entire field since harm can be caused to surrounding tissue if high intensity sound is present outside the desired region. Traveling shock waves can also cause undesired harm. In the present application the size and magnitude of the focal region of the sound are important but detail of the surrounding field is not.

There are several methods to produce a focused signal, some of which are described by Cathignol and Chapelon (1993) [17, 19] for the medical application of lithotripsy. Focusing can be achieved by an array of transducers that send signals such that each

is in phase resulting in constructive interference at the desired focal region. This can be done by either locating all the sources the same distance from the array center and driving them in phase or locating them on any other geometry and altering the phase of the drive signal to each source. Alternatively, a high intensity spreading wave can be produced by an individual source and the wave can be reflected from a concave surface back to a focus. Another method is to use some kind of acoustic lens to refract the waves much like an optical lens.

In the current investigation, considering the scale and resources available, a conventional phased array consisting of a number of transducers will be used to create the desired field. To simplify the problem, the transducers will be located so that they can all be driven in phase. This is sufficient in the laboratory environment since the target's location, the medium's properties, and the surrounding environment are known. The problem of focusing sound in the ocean environment at a target with unknown location and velocity has been considered by Dr. P. H. Rogers and D. Trivett at Georgia Tech for research proposals but without publication. The intended principle to be utilized is time reversed acoustics. This is necessary since, in this case, the exact location of the target is unknown and the surroundings through which the signal will travel are unknown and variable. The method of time reversed acoustics is discussed further in section 2.2.4.

2.2.2 Acoustic Cavitation in Water

Acoustic cavitation is the term used to describe the situation where an acoustic pressure field in a liquid medium causes the liquid to cavitate. It is of interest in this study as well as the previously discussed phenomenon, hydrodynamic cavitation, because the acoustic pressures used in the cavity disruption experiments can be of sufficient amplitude to cause the water medium to cavitate (up to around 500 kPa

of acoustic pressure at around 12 kHz and 1 m depth in water at 20°C that has not been degassed). It is important that we know the state of the medium in which the projectile is traveling and, therefore, we must know the effects of the imposed acoustic field and the threshold pressure levels that will cause alterations to the medium. This is explored experimentally in this work in chapter 4, section 4.4.6.

Reviews of cavitation in water, mentioned previously, that discuss acoustic cavitation, are given in references [18] and [42] by Herbert et al 2006. A longer report on acoustic cavitation, which reviews the physics and basic theoretical and experimental data, is given by Neppiras in reference [70], 1980. Bayer [9] also discusses theoretical and experimental work.

The field of acoustic cavitation is a very complex one involving time dependent pressure and velocity fields in a two-fluid medium, and the physical motion of the bubble walls. Many of the physical processes are not agreed upon in the literature or are highly dependent upon the conditions of the liquid medium and impurities present. However, for the purposes of this work, conclusions that are relevant to, and aid in the explanation of observed experimental outcomes, will be highlighted.

Light can also be shed on the acoustic interactions with the supercavity that are the ultimate interest in this work because one aspect of acoustic cavitation is the interaction of the acoustic field with the bubbles that are produced. However, the situation is incredibly complex and will not be tackled analytically. The supercavity bubble is obviously not spherically symmetric, is continually growing by hydrodynamic means, is not spatially uniform on the interior, and is not small relative to the wavelength.

Acoustic cavitation can occur in two forms, in a similar manner to hydrodynamic cavitation. One is gaseous cavitation in which the acoustic field causes growth and collapse of bubbles filled with gas that is already present in the liquid, either in the

form of existing bubbles or in solution; these bubbles can grow by means of rectified diffusion or bubble coalescence. The other form is vaporous cavitation in which the water vaporizes creating the cavity and condenses as the cavity collapses. It is also possible, and indeed likely, that a combination of these two cases will occur producing bubbles containing a mixture of gas and vapor. There are also two distinct phases of acoustic cavitation, one is *stable cavitation*, where the pressure fluctuations cause the cavitation bubbles to oscillate, usually in a nonlinear manner, and the other is *transient cavitation*, where the bubble grows and collapses violently. Stable cavitation occurs at lower pressure amplitudes than transient cavitaton.

2.2.2.1 Experimental Findings and Cavitation Theory

Articles in the literature present a large range of threshold levels for the inception of acoustic cavitation and individual authors note large variances in their results. Herbert et al [42] cites values in various works ranging from 100 kPa for distilled water saturated with air to 21 MPa for degassed water. Akulichev and Il'ichev, 2005 [2], present a paper on the acoustic cavitation thresholds of sea water in different regions of the world's oceans. They report threshold acoustic amplitudes ranging from 180 kPa to 560 kPa at 10 m depth and at 10 kHz. For comparison to this work, in which the depth is around 1 m, the difference in hydrostatic pressure between 1 m and 10 m depth is around 88 kPa.

The large variation is due to a number of factors. Firstly, the threshold is largely dependent on the condition/purity of the medium. The condition of the medium refers to the level of dissolved gasses in the liquid and whether there are existing bubbles or solid particles in the liquid. Secondly, the detection methods and criteria vary, and lastly the pressure amplitude required for cavitation inception is dependent on the frequency of excitation.

The experimental findings agree favorably with the theory presented by Neppiras [70] on cavitation thresholds. Calculated stable and transient cavitation thresholds for air-saturated water at 10 kHz and 10 m depth are calculated using equations (20) and (21):

$$P_T^2 = \frac{3}{2}\left[\frac{AP_{hs}^2}{A+R_0}\right]\left[(1-R_0^2B)^2 + R_0^2B\delta\right] \tag{20}$$

$$P_T > P_{hs} + \frac{4}{3}\left(\frac{2\mu^3}{3R_0^3(P_{hs}+2\mu/R_0)}\right)^{1/2} \tag{21}$$

where P_T is the cavitation threshold pressure, $A = \mu/P_{hs}$ and $B = \omega^2\rho/3\gamma P_{hs}$ (γ = specific heat ratio; μ = surface tension; ω = angular acoustic frequency; R_0 = equilibrium bubble radius), and δ is the damping factor for a resonant bubble. Plots produced by these equations are shown in figure 5. Akulichev states that, depending on conditions, gas bubbles in the upper ocean layer may vary in size from 10^{-5} to 10^{-1} cm radius. From figure 5 this corresponds to transient thresholds between 199 kPa and 726 kPa.

A theory of rectified diffusion, and the acoustic pressure amplitude threshold required to cause bubble growth, is presented by Eller and Flynn in 1965 [30] and is followed up by Eller in 1969 [29]. The later work compares the theory to experimental data. A more recent theoretical study is given by Louisnard in 2003 [64]. These papers all deal with low frequency (around 20 - 30 kHz) and acoustic pressures up to 500 kPa which are relevant to this work.

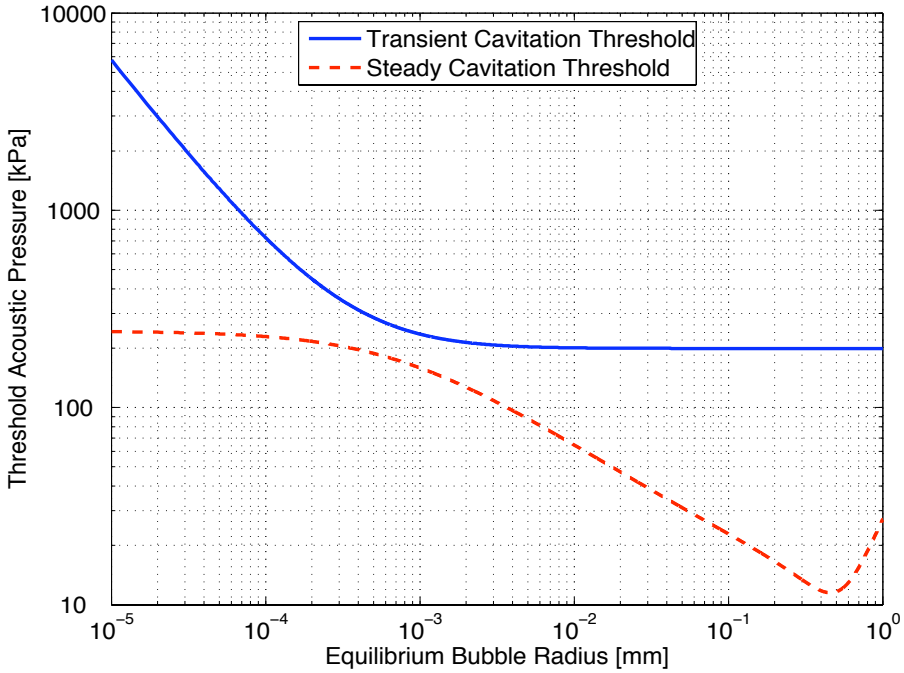

Figure 5: Stable and transient cavitation thresholds for air-saturated water at 10 kHz and 10 m depth calculated using equations (20) and (21) [70].

2.2.2.2 Detection of Acoustic Cavitation

The onset of cavitation as acoustic pressure is slowly increased cannot be detected very easily by eye, even with the aid of high speed video photography. It is only clearly visible in more severe instances. A common way to detect the presence of cavitation is by detecting the sound produced by the bubble activity. There is some conflict about which acoustic signature corresponds to the onset of cavitation, largely because there is an inconsistent definition of cavitation inception. Other methods of observation that are not considered here include the observation of of various effects of cavitation such as sonoluminescence, erosion, emulsification and sonochemical reactions [101].

References [69], [70] and [43] provide discussion and experimental evidence of the spectral change in acoustic pressure due to cavitation bubbles as the driving signal is increased in amplitude. It is shown that, as the driving pressure is increased,

various features arise in the spectrum: harmonics of the drive frequency, subharmonic components and sometimes their harmonics, and white noise.

Neppiras [69] conducted measurements in water, not specially prepared, but free from large bubbles and not over saturated with dissolved air, and at frequencies in the same order of magnitude as this work (frequencies as low as 18 kHz). He concluded the following:

> "In unprepared liquids containing no large bubbles, the thresholds for subharmonics and transient cavitation coincide."

It should be noted, however, as mentioned there and in more detail in a later article by the same author [69], subharmonics, and also higher order harmonics, can be produced at acoustic pressures below the transient threshold level due to nonlinear bubble oscillations but that there is a sharp rise at the transient threshold. It is also possible, if environmental conditions do not allow the relevant sized bubbles to exist, that transient cavitation may be observed without any subharmonic. Nepparis [69] predicts that, for the subharmonic ($f_0/2$) to be an indicator of the onset of transient cavitation there must be no large bubbles present in the liquid. This will be the case for water that has been left to settle for some time.

Vaughan (1968) [101] agrees with Neppiras' work and presents a compelling argument that strong subharmonic excitation only occurs when the liquid cavitates. However, he does suggest that a measure of cavitation threshold should be the first peak of subharmonic response and not just the detection of the subharmonic. There is a peak because the level of the subharmonic increases and then decreases as the driving pressure is increased. The decrease is thought to be due to scattering of the signal by other bubbles.

Increase in the level of white noise is also an indicator of transient cavitation and is due to the collapse of cavitation bubbles. As drive level is increased the level of noise tends to be fairly low and constant until the onset of cavitation, whereafter it exhibits a gradual increase with further drive level increase [70].

2.2.3 Properties of Bubbly Water

Acoustic cavitation creates bubbles in the water that contain vapor or an air-vapor mixture. The presence of these bubbles changes the overall density and compressibility of the medium. As a consequence of these changes, the sound speed in the medium is effected, often drastically. The density of the fluid is reduced because the gas phase has a much lower density than the liquid water. The compressibility of the fluid is increased; for a given applied pressure there is a greater change in the volume because the bubbles containing gas are more easily compressed than water.

The fraction of any given fluid volume that contains gas is quantified by the gas fraction (ν). Generally, for a population of bubbles that have a mean radius of R_0 and a number density of n_b (number of bubbles per cubic meter), the gas fraction is given by

$$\nu = \frac{4}{3}\pi R_0^3 n_b \tag{22}$$

A simple model for studying a bubbly liquid is to treat the two-phase medium as an equivalent single phase fluid with bulk properties. The density and compressibility of the equivalent fluid can be found by adding the values of the components of the mixture by the gas fraction as follows [95, 104]:

$$\rho_{eq} = \nu\rho_g + (1-\nu)\rho_l \tag{23}$$

$$K_{eq} = \nu K_g + (1-\nu)K_l \tag{24}$$

where ρ_{eq}, ρ_g, and ρ_l are the equivalent density and the density of the gas and liquid respectively. K_{eq}, K_g, and K_l are the equivalent compressibility and the compressibility of the gas and liquid respectively. No account is taken here for the dynamics of individual bubbles and consequently any radiation from the pulsating bubbles. This can be particularly erroneous when the disturbance frequency is close to the bubble resonance or when the wavelength of the disturbance is comparable to the bubble dimensions and scattering plays an important role. It is also a bad assumption for high gas fractions.

A sound speed can be calculated for the mixture using (23) and (24) with the relation

$$c = \sqrt{\frac{1}{K_{eq}\rho_{eq}}} \tag{25}$$

An alternative equation for calculating the mixture sound speed assuming a homogeneous fluid and isothermal behavior of the gas is given by Wijngaarden [104] and gives very similar results to (25)

$$c = \sqrt{\frac{P}{\rho_l \nu(1-\nu)}} \tag{26}$$

where P is the pressure in the mixture. Wijngaarden gave justification for the use of (26) addressing the assumptions of isothermal behavior, no relative motion between gas and liquid phases, and disregarding viscosity. Additionally, he noted comparison

to experimental measurements which agreed with (26) for excitation frequencies well below the bubble resonance frequencies.

Leighton (1994) [61] and Caflisch (1985) [15, 16] present more detailed and complex analysis of sound wave propagation in bubbly liquids. The equivalent sound speed (c_{eq}) is the phase speed of infinitesimal disturbances and is given by the equation [15]

$$\frac{1}{c_{eq}^2} = \frac{1}{c_l^2} + \frac{3\nu}{R_0^2(\omega_0^2 - \omega^2)} \tag{27}$$

where ω is the disturbance frequency, ω_0 is the resonance frequency of the bubbles (assumed to be all the same size), and c_l is the liquid sound speed. This relation does not include dissipation and so is unbounded at the resonance frequency. The bubble resonance frequency can be found by the Minnaert resonance frequency (ω_M):

$$\omega_M = \frac{1}{R_0}\sqrt{\frac{3\gamma p_0}{\rho_l}} \tag{28}$$

When ω is much less than the resonance frequency and if the term c_l^{-2} can be neglected in equation (27) then we get back to a case where the sound speed is predicted by equations (23) and (24) where the second term on the right hand side of (23) is dominant and the first term on the right hand side of (24) is dominant. This occurs when the gas fraction is low, but not too low - on the order of a percent.

The dynamics of the bubbles when subject to an increase in external pressure depends on the content of the bubble. Particularly, the ratio of air to water-vapor in the gas phase. As a bubble is compressed, the water vapor behaves differently from the air. Air tends to 'cushion' the collapse as the dissolution process does not occur rapidly enough for the air to dissolve into the water. The vapor tends to condense more rapidly than the air dissolves resulting in a more violent collapse. Leighton [61] shows

that condensation can not, however, occur rapidly enough to maintain conditions of constant temperature and vapor pressure within the bubble.

2.2.4 Time Reversal Acoustics

Time reversal acoustics has been investigated for several purposes by a number of researchers. There are numerous references: Jackson and Dowling (1991) [47], Fink (1995,1997) [31, 32], Root and Rogers (2002) [80] which provide an excellent introduction and overview of the subject and mention several practical applications.

The ocean environment can be difficult or time consuming to characterize, making it difficult to predict the propagation of sound accurately. Time reversal techniques require no *a priori* knowledge of the propagation environment and permit acoustic focusing and beam forming in inhomogeneous and/or high scattering environments. The concept involves exploiting the time reversal invariance of the linear lossless wave equation or including loss, reciprocity. In practice, time-reversal mirrors are realized by constructing an array of collocated source and receiver elements in an array (SRA). The SRA receives a signal from the source, the signal is then time reversed and transmitted back out, re-tracing its path and thus focusing on the original source. Large focal distances are attainable in the ocean because, in a waveguide geometry, an SRA has images which increase its effective aperture.

As pointed out by Root and Rogers, perfect time reversal is indeed not possible for a couple of reasons. The array used to receive then emit the time reversed signal is not generally a closed surface in the sense required by the Helmholtz equation. Also, true time reversal would require that the source which created the outgoing signal also be time reversed and become a sink. The sink prevents the incoming wave from passing through the origin and interfering with its self to produce a focal region whose size is

consistent with what would be expected from diffraction theory. However, researchers have shown that a practical form of time reversal is useful for many applications.

Some investigation into the literature relevant to the proposed application has been done although it will not be used in the present work as discussed earlier. In particular there have been relevant experiments conducted off the west coast of Italy by Hodgkiss, Kuperman and Song [58, 91, 44, 92] from the Scripps Institution of Oceanography, University of California, San Diego which demonstrate the use of a phase conjugated (equivalent of time reversal but in the frequency domain) array in shallow waters of the ocean (123 m to 145 m depth). Originally the technique was demonstrated over a 6 km range then subsequently on a 30 km range. Their experiments transmit a signal from a point source, receive and retransmit from the SRA, then look for the focused signal back at the source location with a second receiving array. The result of these experiments was that the time reversal mirror can produce significant focusing out to long ranges in a shallow water environment.

In the present case where there is no source but instead a moving target a more sophisticated procedure is required to focus sound on the target. The idea is to emit a signal from the source/receive array to ensonify the target then look at the reflected/scattered signal and use this with the time reversal methods to focus additional high intensity sound on the scatterer. The concept of an iterative time reversal mirror is applied to waveguide propagation in the ocean by Song et al. (1999) [92]. Later work, again by the same authors and Lingevitch at NRL, looked at focusing with a time reversal operator in the case of stochastic reverberation returns from a rough sediment interface in an ocean wave guide [62].

Work at Georgia Tech has been done investigating the properties of an underwater acoustic volumetric array using time reversal focusing with the idea in mind that the array might be situated in the free-flooded spaces on a submarine [80]. Thus it is evident that research work is being done which will facilitate the use of this technology in the proposed application.

CHAPTER III

SIMULATIONS

This chapter presents and discusses some application of the theory mentioned in chapter 2. Predictions of cavity dimensions are made using Garabedian's model in section 3.1. These were used for projectile design and first estimates of effects of an external pressure change on the supercavity. Section 3.2 presents a six degree of freedom dynamics simulation of the supercavitating projectile. Lastly, section 3.3 examines the use of Logvinovich's model for predicting the effects of an external acoustic pressure on the supercavity.

3.1 Modeling the Supercavity Shape Around the Projectile

Analytical models for shape prediction of a supercavity were presented in section 2.1.1 of chapter 2.

Garabedian's model (see section 2.1.1.1) was used for predicting the overall shape of a supercavity produced by a disk cavitator to aid in projectile design. This model was sufficient for examining the supercavity shape in the vicinity of the projectile for long cavities because the closure region was not important. Equations (2) and (4) were used to calculate the major and minor radii of an assumed elliptical shape, along with equation (15) for the drag coefficient and (1) for the cavitation number.

Comparisons were made with other shape prediction models presented in section 2.1.1 (for example, Logvinovich [99] and May [65]) and showed close agreement. Predictions of maximum cavity diameter and cavity length are compared to the experiments and discussed in section 4.3.4 (measurement from experiments is discussed in section 4.2.1.3).

Figure 6 shows plots of the supercavity shape around the projectile body. The different line colors represent the cavity profile at various projectile speeds shown on the legend in the figure. Figure 7 shows the cavity radius at the projectile tail (2.2" aft of the cavitator, see projectile drawing in figure 71, appendix B) as a function of projectile speed. The projectile was designed to operate at speeds of greater than 80 m/s. Average speeds at the mid point in the trajectory where the acoustic signal was focused ranged from 133 m/s to 147 m/s for the different experiment cases. As can be seen in figure 7, the theory predicts that for such projectile speeds, the proximity of the cavity boundary at the projectile tail does not exhibit much variation. Some authors have concluded that for a supercavity (the cavity is large compared to the body dimensions) the initial cavity profile is independent of cavitation number [99, 102].

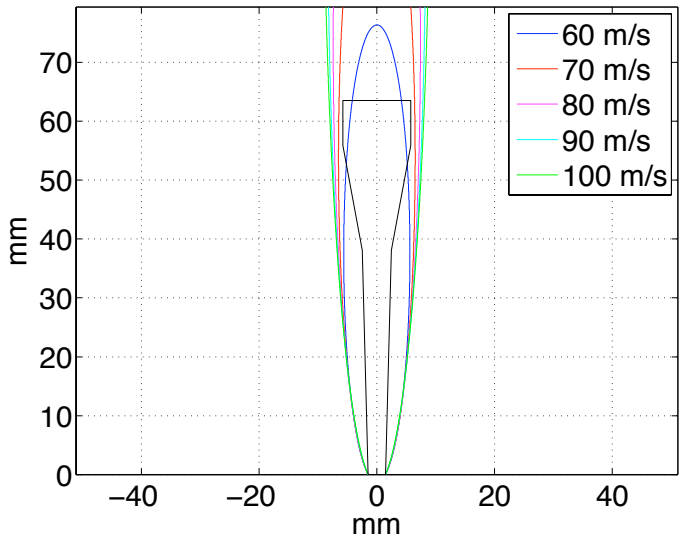

Figure 6: Cavity shape predictions using Garabedian's model for a range of projectile speeds. The hydrostatic pressure is that in a standard atmosphere and at 0.75 m depth of water. In the figure, higher speeds correspond to larger cavity diameters.

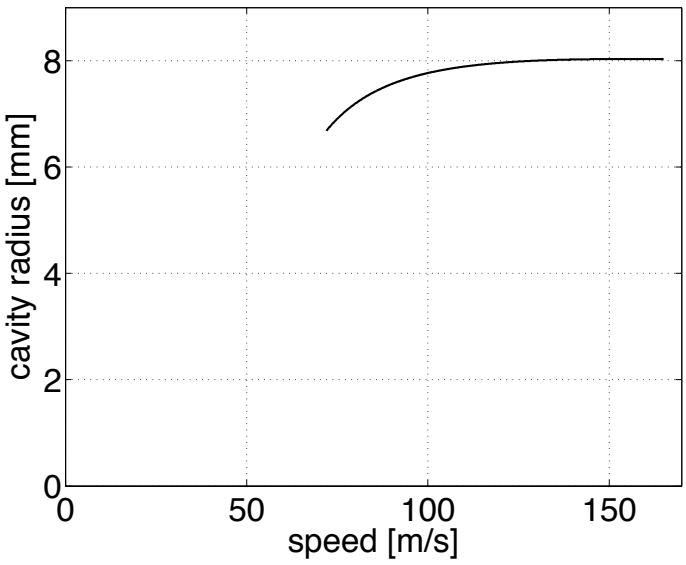

Figure 7: Predictions of cavity radius at the projectile tail (2.2" aft of the cavitator, see projectile drawing in figure 71, appendix B) using Garabedian's model for a range of projectile speeds. The hydrostatic pressure is that in a standard atmosphere and at 0.75 m depth of water.

Garabedian's model was also used to estimate the change in cavity shape due to a variation in the external hydrostatic pressure to obtain a first estimate of the pressures required to significantly alter the shape of the supercavity. Figure 8 shows cavity shape predictions for several increased hydrostatic pressures. The lowest level shown is the pressure due to a standard atmosphere and 0.75 m of head pressure in water ($\sim$109 kPa). This is the depth that the projectile was subject to the acoustic signal in the experiments. For the left plot which corresponds to a projectile speed of 133 m/s, increases are in increments of one atmosphere ($\sim$101 kPa). For the right plot which corresponds to a projectile speed of 266 m/s, increases are in increments of four atmospheres ($\sim$404 kPa).

At a projectile speed of 133 m/s, approximately three to four atmospheres of additional positive sustained pressure would be required to close the cavity in on the projectile (figure 8 left) at the 0.75 m depth. The relationship between cavity diameter and the projectile speed is nonlinear. For a doubling of the projectile speed, to 266 m/s, it takes around sixteen atmospheres of positive pressure to achieve the same effect (figure 8 right). The nonlinearity is primarily due to the fact that cavitation number is inversely proportional to the speed squared and only directly proportional to the reference pressure. This implies that it may be difficult to alter the cavity geometry with applied pressures at high projectile speeds.

The plots in figure 8 also predict the cavity shape at different water depths since they are showing changes in hydrostatic pressure. For every 10.3 m of submersion depth the hydrostatic pressure increases by one atmosphere.

It is noted that with reduced pressure (and thus cavitation number) both the length and maximum diameter of the cavity increase as does the overall aspect ratio (ie. the cavity elongates).

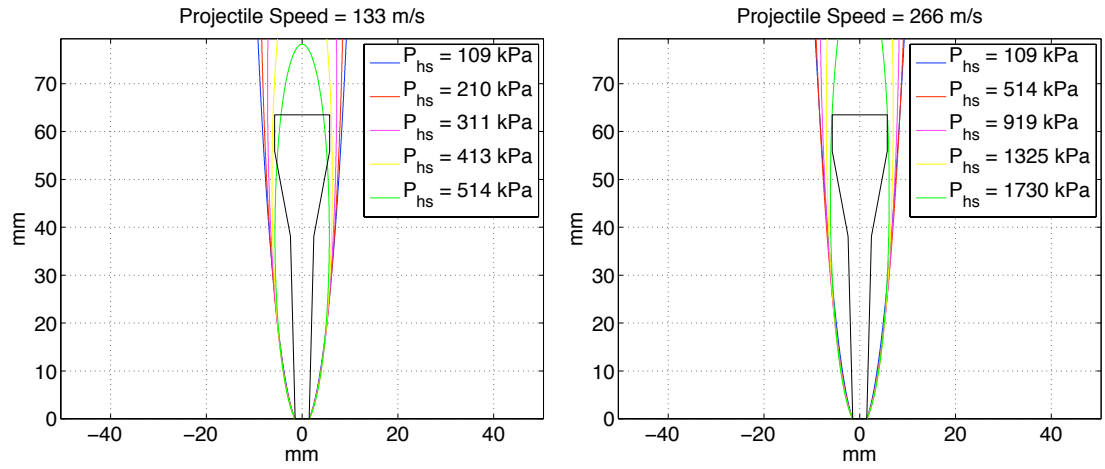

Figure 8: Cavity shape predictions using Garabedian's model for a range of hydrostatic pressures at a projectile speeds of 133 m/s (left) and 266 m/s (right). In the figure, higher pressures correspond to smaller cavity diameters.

Figure 9 shows plots of the cavity shape at 133 m/s for various angles of attack (this speed was chosen because it was the average measured speed at the array focal region in the experiments). Again, Garabedian's model was used to calculate the supercavity shape. These plots were considered in projectile design and when examining tail-slap dynamics.

3.2 Supercavitating Body Dynamics Simulation

A simulation of the projectile dynamics was written in $MATLAB^{\text{TM}}$. The model considered a free body with six degrees of freedom that had the dimensions of the projectile used in the experiments (see appendix B for a technical drawing). The shape of the supercavity and the forces on the projectile body were the aspects of the system modeled. The cavity/projectile system is coupled since the cavity depends on projectile dynamics and the forces on the body depend on the shape and orientation of the cavity.

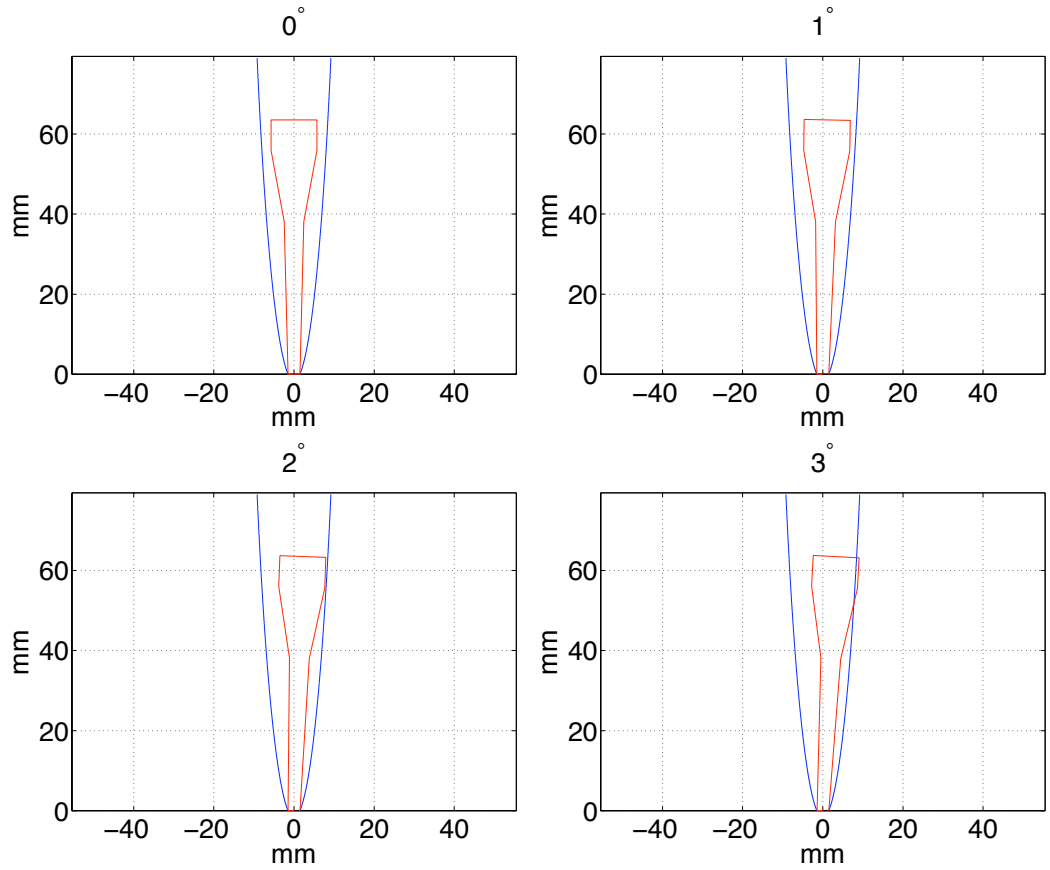

Figure 9: Proximity of the supercavity boundary with the projectile body at different angles of attack

The model that was used to predict cavity shape was Logvinovich's model (see section 2.1.1.2). This model predicts the evolution of supercavity cross sections based on the cavitator motion and orientation upon cavity inception, and on the pressure difference between the interior and exterior of the cavity during expansion and contraction. This model has been used extensively in the literature and was suitable for this application. It is a simple analytical model which could be easily incorporated into the dynamics simulation. In using this model, cavity sections were assumed axisymmetric; however, the centerline of the cavity could take a curved shape that followed the path of the cavitator.

Forces on the projectile body were assumed to be due only to hydrodynamic forces at locations where the projectile was in contact with the water (that is, at the cavitator and at the tail during incidences of tail-slap), and gravity acting at the center of gravity. Forces on a disk shaped cavitator are discussed in detail in section 2.1.3.1. Equations (16) and (17) were used to find drag and lift coefficients which act in directions shown in figure 3. Planing forces during tail-slap are discussed in section 2.1.3.2. The pressure force normal to the inclined longitudinal axis of the cylindrical hull and the moment of the pressure forces about the transom are given by equations (18) and (19) [54, 1]. These planing forces were the dominant forces, however, additional corrections were made for the friction force during planing following Ahn (2007) [1].

The approach taken in the simulation was to predict the forces on the projectile body and then calculate the motion over a small time step assuming that the forces were constant. The motion was calculated using an ordinary differential equation solver in MATLAB and with twelve state variables corresponding to position and speed in three cartesian coordinate directions and in three rotation directions. Forces were then calculated based on the new conditions and the process was repeated. At each time step the entire evolution of a cavity cross section that was produced at

that moment was calculated using Logvinovich's model based on cavitator speed, orientation, and the ambient pressure. Recording the evolution of cavity sections was crucial because planing forces at the tail are dependent on sections of the cavity formed at a previous time step and have undergone some subsequent growth. Details involved in the process of calculating forces can be found in reference [1] including defined reference frames and the vector calculus involved.

Equations (29) shows the state variables x_1 *through* x_{12}.

$$\begin{aligned} x_1 &= (r_{OC})_x & x_7 &= \phi \\ x_2 &= v_x & x_8 &= \omega_x \\ x_3 &= (r_{OC})_y & x_9 &= \theta \\ x_4 &= v_y & x_{10} &= \omega_y \\ x_5 &= (r_{OC})_z & x_{11} &= \psi \\ x_6 &= v_z & x_{12} &= \omega_z \end{aligned} \tag{29}$$

where $\bar{r}_{OC}$ is a vector from point O which is the origin of XYZ (an inertial reference frame in fixed space $\mathcal{I}$ with associated unit vectors $\bar{I}, \bar{J}$ and $\bar{K}$) to the center of mass of the body at point C

$$\bar{r}_{OC} = (r_{OC})_x \bar{I} + (r_{OC})_y \bar{J} + (r_{OC})_z \bar{K} \tag{30}$$

and $\bar{v}$ is the time derivative of (30)

$$\bar{v} = v_x \bar{I} + v_y \bar{J} + v_z \bar{K} \tag{31}$$

The rotation scheme used for setting up the equations of motion for this simulation was the following:

1. Rotation θ about the Y - axis resulting in a coordinate system $x_1y_1z_1$.
2. Rotation ψ about the z_1 - axis resulting in a coordinate system $x_2y_2z_2$.
3. Rotation ϕ about the x_2 - axis giving the orientation of the body β with body fixed reference frame xyz.

An expression for the angular velocity of the body in the inertial reference ($\vec{\omega}_{\beta/\mathcal{I}}$) frame was written based on this scheme

$$\vec{\omega}_{\beta/\mathcal{I}} = \omega_x\bar{I} + \omega_y\bar{J} + \omega_z\bar{K} \tag{32}$$

with

$$\begin{aligned}
\omega_x &= \dot{\psi}sin(\theta) + \dot{\phi}cos(\psi)cos(\theta) \\
\omega_y &= \dot{\theta} + \dot{\phi}sin(\psi) \\
\omega_z &= \dot{\psi}cos(\theta) - \dot{\phi}cos(\psi)sin(\theta)
\end{aligned}$$

The first derivatives of the state variables are given in equations (33) and complete system of differential equations.

$$
\begin{aligned}
\dot{x}_1 &= x_2 & \dot{x}_7 &= \frac{x_8 + x_{11}}{sin(x_9)cos(x_{10}) + cos(x_9)cos(x_{10})} - \frac{x_{11}}{cos(x_{10})sin(x_9)} \\
\dot{x}_2 &= \Sigma F_x/m & \dot{x}_8 &= \Sigma M_{Cx}/I^C_{xx} \\
\dot{x}_3 &= x_4 & \dot{x}_9 &= x_7 - \frac{sin(x_{10})(x_8 + x_{11})}{sin(x_9)cos(x_{10}) + cos(x_9)cos(x_{10})} + \frac{x_{11}sin(x_{10})}{cos(x_{10})sin(x_9)} \\
\dot{x}_4 &= \Sigma F_y/m & \dot{x}_{10} &= \Sigma M_{Cy}/I^C_{yy} + \frac{I^C_{zz} - I^C_{xx}}{I^C_{yy}} x_8 x_{11} \\
\dot{x}_5 &= x_6 & \dot{x}_{11} &= \frac{x_8 + x_{11}}{sin(x_9) + cos(x_9)} \\
\dot{x}_6 &= \Sigma F_z/m & \dot{x}_{12} &= \Sigma M_{Cz}/I^C_{zz} + \frac{I^C_{xx} - I^C_{yy}}{I^C_{zz}} x_{11} x_7
\end{aligned}
\tag{33}
$$

I^C_{xx}, I^C_{yy}, and I^C_{zz} are moments of inertia of the mass of β about x, y, and z axes through point C. F_x, F_y, and F_z are x, y, and z components of the resultant force on the body β. M_{Cx}, M_{Cy}, and M_{Cz} are x, y, and z components of the moment about point C.

Figure 10 shows a frame from a typical simulated flight. Conditions of flight and viewing angle shown in the figure are similar to those in a flight captured by the high-speed camera shown in figure 23 in chapter 4.

The simulation was found to agree with experimental observations, thus validating the model and allowing its use in predicting flight dynamics. Calculated speeds are compared to experiment results in figure 27 of chapter 4 and agree favorably. Additionally, the projectile dynamics, including duration and frequency of tail-slaps, agreed with those discussed in section 4.3.1 and in the literature [57].

Prescribed initial conditions during simulation dictate the frequency and severity of the tail-slaps. Because the initial conditions could not be measured in the experiments, reasonable values were chosen for the simulation to produce dynamics similar to the experiment observations. The required initial conditions could reasonably be

expected in the experiment, therefore the subsequent dynamics are deemed to be consistent with the experiments.

Consideration of the notion that initial conditions are so important to the flight dynamics, especially in the case of a vertical trajectory where the weight of the projectile provides little moment about the point of rotation, lead to stringent attention to minimizing them during the apparatus design (section 4.1). Attention was focused on the firing mechanism structure and operation, the mechanism barrel, and the projectile dimensions to minimize the projectile angle of attack upon leaving the firing mechanism. In addition to the forces predicted by the model, if the projectile left the muzzle with an initial angle of attack, the gas pressure would cause asymmetric loading resulting in forcing moments which would increase the angular velocity.

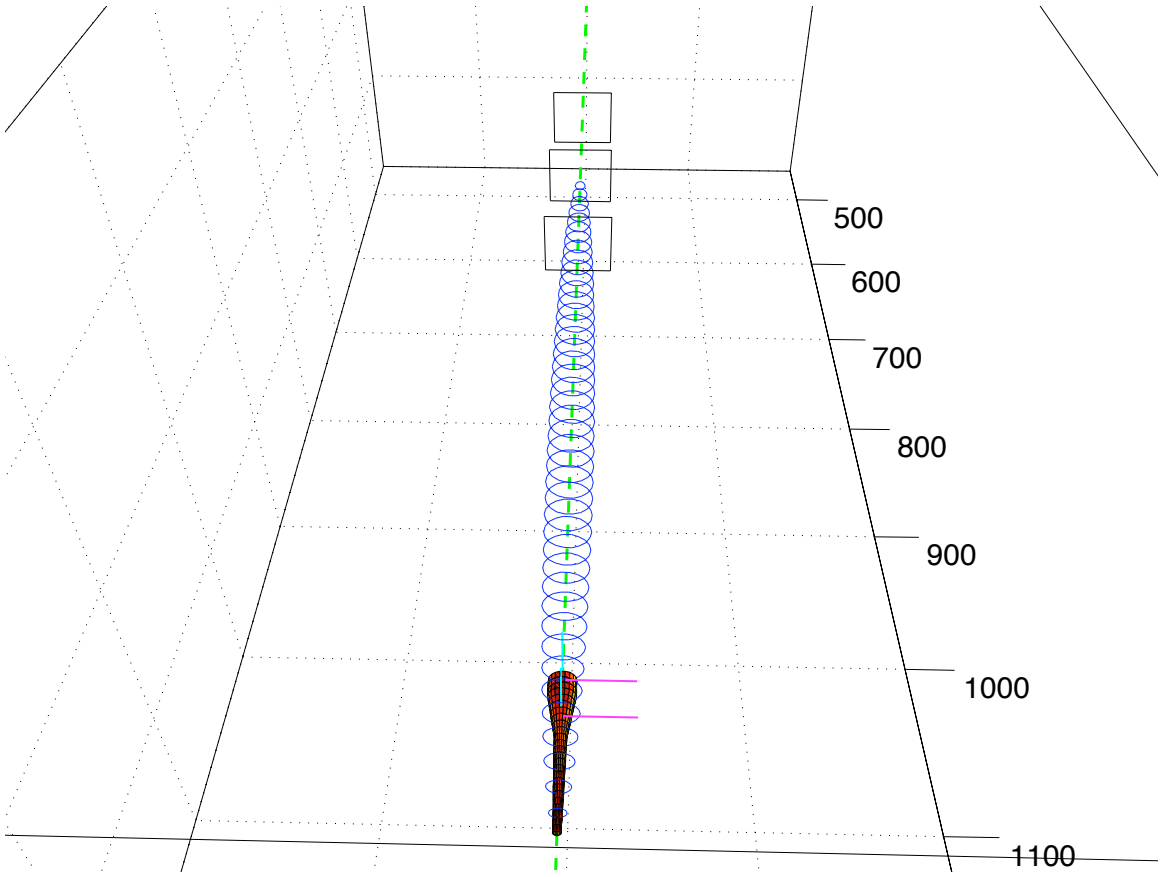

Figure 10: Screen shot from the dynamics simulation showing the overall cavity shape but with a reduced cross-section density. The scale shown on the right is water depth in millimeters. This image shows the situation in a similar view to that captured by the high-speed camera during some of the experiments. Figure 23 in chapter 4 shows photographs from the experiment.

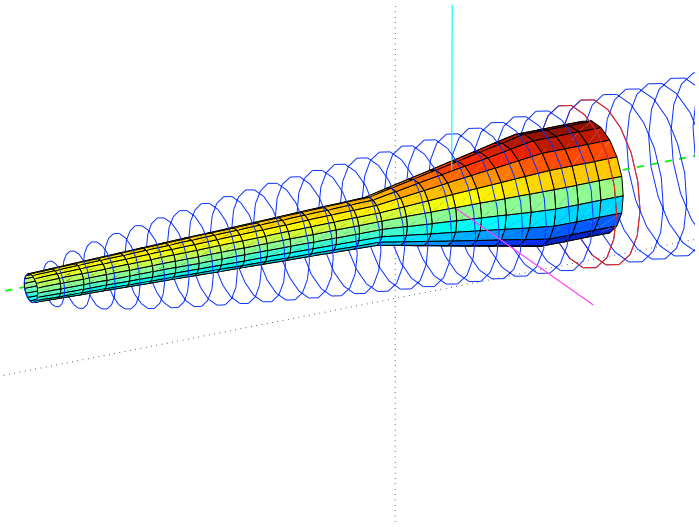

Figure 11: Screen shot showing a close up of the projectile and cavity model in the dynamics simulation. The line coming out of the projectile body at the cone shaped tail are axes of a coordinate system at the body's center of mass. The two red rings on the supercavity highlight sections that were located at the transom and used in the planing model.

3.3 Effects of Imposed Pressures on A Supercavity

In this section, Logvinovich's theory of independent cavity section expansion is examined as a means of predicting the effects of an external acoustic pressure signal on the development of a supercavity.

3.3.1 Relevant Work in the Literature

Vasin (2001) [99] used Logvinovich's model to investigate two cases in which the pressure was varying either inside or outside the cavity. Firstly, the cavity shape was determined for the case of a fixed cavitator disk in a moving vertical flow. The external pressure varied with time as the cavity section was swept to locations of increased hydrostatic pressure. Secondly, the cavity shape due to a sinusoidally varying internal cavity pressure was investigated. Vasin described the perturbation of the cavity wall due to the varying internal pressure using Logvinovich's model. Although no details

were given, Vasin noted that the general trend of increasing perturbations toward the downstream end of the cavity was confirmed by experiments. That is, the change in cavity radius due to the internal sinusoidally varying pressure is found to increase with time.

Paryshev (2006) [75] has developed a theory of cavity stability and oscillations. The system of equations for cavity dynamics was derived from Logvinovich's theory of cavity section expansion along with an expression for the gas volume within the cavity, gas mass balance inside the cavity, and Newton's second law to describe cavitator motion. These equations formed a closed problem and were used to formulate a linear theory of cavity stability and oscillation. Additionally a nonlinear numerical solution was obtained which accounts for periodic detachment of gas bubbles. Forced oscillations were examined but the excitation was modeled by periodic variation of the cavity volume. This would be achieved in practice through a cavity ventilation system which allows gas to be injected and withdrawn from the cavity. The solution was not applicable to this investigation.

Work at the Fluid Mechanics Institute of the Ukrainian Academy of Sciences by Savchenko (1996) [83] and Semenenko (2001) [89] showed a theoretical and experimental result for pressure pulse effects on cavity geometry. A computer code (PCAV) based on Logvinovitchs theory was used to predict the cavity reaction to a pressure impulse. The theory was compared to experimental photographs where a compressed air catapult was used to impose a pressure impulse on a ventilated cavity. Detailed investigation of work at the institute was difficult since the majority of papers are only available in Russian.

3.3.2 Investigation of an Externally Imposed Acoustic Signal

The investigation of the effects of external acoustic pressure on cavity section growth was similar to that done by Vasin (2001) [99], discussed in section 3.3.1.

The case considered here mirrored the experimental set up. The cavitator was moving through a stagnant fluid in which the external pressure was varying due to a generated sound field; the external pressure was assumed to be sinusoidal. Obviously, the signal at the array center in the experiments was not simply a gated sinusoid as is discussed in sections 4.4.4.2 and 5.3.1.1. However, looking at the effects of a gated sinusoid does provide a reasonable approximation and allows for an analytical solution to the governing equation. A numerical solution was also done to verify the analytical solution and to allow for the examination of cases where no analytical solution is possible.

A cavity cross section area that was formed at $t = 0$ is described by the equation (see section 2.1.1.2)

$$S(s,t) = S_0 + \dot{S}_0 t - \kappa \int_0^t \int_0^u \frac{\Delta P(s,v)}{\rho} dv du \qquad \text{(equation (9) repeated)}$$

When a cavity section is formed it has an initial area equal to the area of the cavitator disk, S_0, and an initial area growth rate denoted by $(ds/dt)_{t=0} = \dot{S}_0$. Values for κ and $\dot{S}_0$ are given by equations (8) and (10) respectively in section 2.1.1.2. For the case considered here the pressure difference ΔP is given by

$$\Delta P = P_{hs} - P_c + A sin(\omega t + \theta) \qquad (34)$$

The sinusoidally varying pressure on the exterior of the cavity and has a phase angle θ to allow for initiation of the cavity section at any time during the period of the sinusoidally varying acoustic pressure. The constant A is the acoustic pressure amplitude. The acoustic pressure was included in equation (9) in ΔP in the same manner as would be done if the pressure inside the cavity were varying. The difference between this and the case considered by Vasin was that the varying pressure was in the surrounding fluid and therefore changed the instantaneous pressure that was present in the fluid at cavity section inception. Based on the observation in chapter 5 that the corrugations on the cavity/water interface were due to conditions at inception, this was an important difference.

The solution of equation (9) with ΔP given by equation (34) and the additional substitution of $\Delta P_0 = P_{hs} - P_c$ is:

$$S(t) = S_0 + \dot{S}_0 t - \frac{\kappa \Delta P_0}{2\rho} t^2 + \frac{A\kappa}{\rho\omega^2}\left(sin(\omega t + \theta) - \omega t cos(\theta) - sin(\theta) \right) \tag{35}$$

The first three terms on the right hand side of equation (35) describe the area evolution of a cavity not subject to any pressure variation after formation.

This solution was used, along with a numerical solution to equation (9), to produce the top right plot in figure 12. The case shown is for a 12 kHz signal with an acoustic pressure amplitude of $A = 300$ kPa. All other conditions were taken from the experimental work: a projectile speed $v = 130$ m/s, a disk cavitator with a radius $r_c = 1.46$ mm, and a water depth of 0.75 m. The plot shows the cavity radius as a function of position along the axis of the supercavity measured from the cavitator. The evolution in time of individual sections formed at different instants were computed using the solution (35) and then radii of each section were plotted for a given time. The position was found assuming a constant cavitator speed.

Computations for the upper plots of figure 12 did not take into account that the high negative pressures could not be sustained by the water medium due to cavitation. This effect was included into the simulation by setting absolute pressures below the water vapor pressure equal the vapor pressure ($P_v = 2337$ Pa). The resulting signal is shown in the lower right plot. The lower left plot then shows the effect on the cavity radius. Although the clipped negative peaks result in a reduction in the amplitude of the troughs of the corrugations, the overall higher average pressure causes the cavity to grow to a smaller radius. This effect has been observed in the experiments of chapter 5.

When compared to the experimental observations in chapter 5 it was found that this model was able to predict the trends but it was not able to predict the correct amplitude of the effect. The corrugations had the same frequency and were found to only go inward with respect to an undisturbed cavity. Table 6 and figure 57 in chapter 5 show an inner and outer radius of the corrugations of 5.9 mm and 7.6 mm respectively for similar conditions. This is a difference of 1.7 mm compared to the theory which shows a difference in radius of ~ 0.5 mm at the same location.

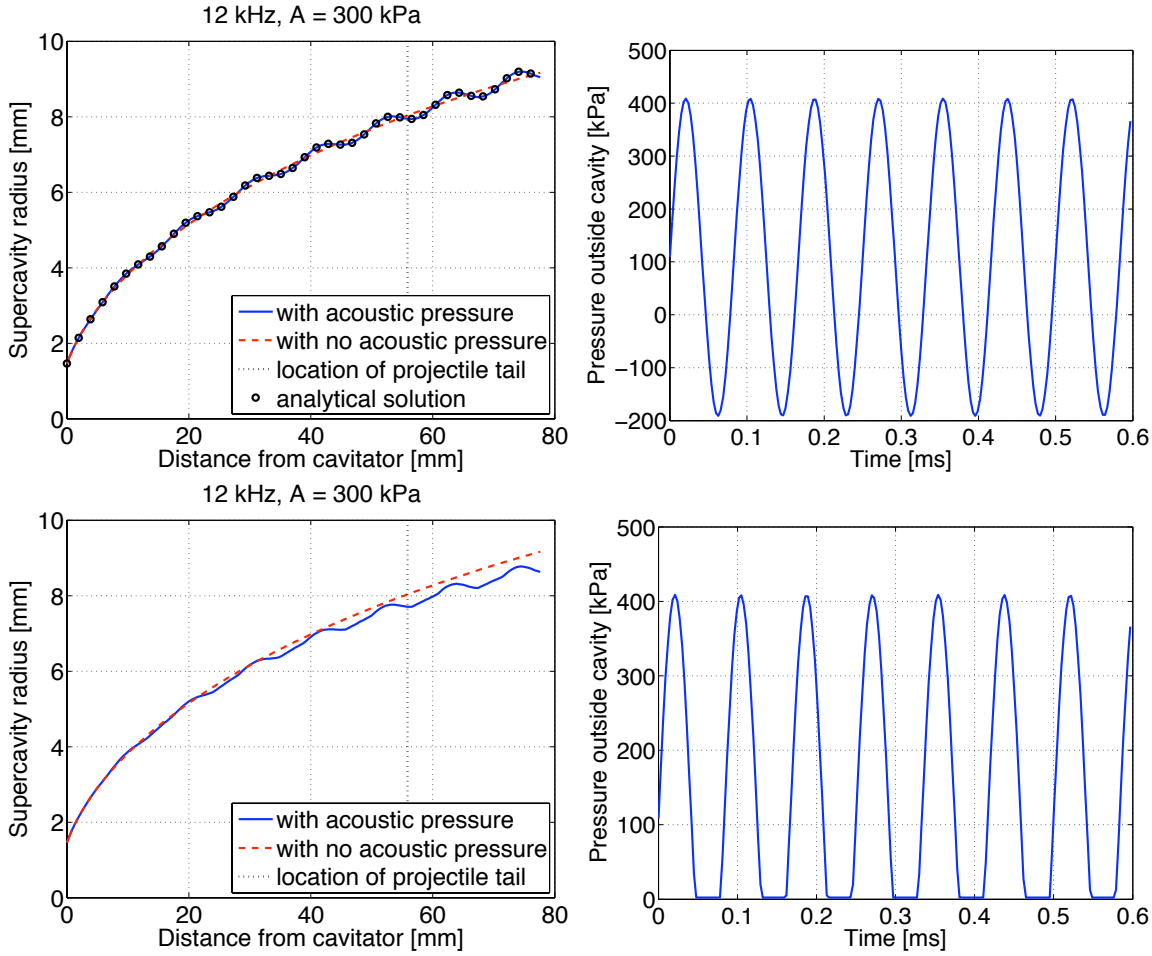

Figure 12: Plot showing effect of acoustic pressure signal on cavity shape predicted by Logvinovich's model. The left plots show the predicted supercavity radius as a function of location along the cavity compared to a case with no acoustic signal. The right plots shows the signal used in the calculation. The upper plots show a case where the medium can sustain negative pressures. The lower plots show a case where effects of cavitation are modeled at the water vapor pressure.

CHAPTER IV

EXPERIMENT DESIGN AND TESTING

This chapter presents the design of several important, unique components of the experimental apparatus and testing of the equipment as a whole. As mentioned previously, the goal of the experimental work was to determine the effects of a high pressure sound field on the dynamics of a naturally supercavitating projectile. Section 4.1 details the general approach and the design of the equipment that allowed for the study of supercavitating projectiles. Section 4.2 then details the experimental measurements that were made which consisted of projectile speed measurement, target impact location and supercavity dimensions. Section 4.3 presents the results from testing the apparatus and measurement techniques. The results from a set of experiments with no applied soundfield are shown that verify the successful operation of the apparatus and serve to provide an initial sample of control data. Finally, section 4.4 presents the design of the transducer array that was used to produce a high-intensity focused sound field at the mid-point of the projectile trajectory. The pressure field has been characterized in both a free field environment and in the confinement of the experiment apparatus.

4.1 Apparatus Design

4.1.1 General Approach

Options for experiment configuration include the use of a stationary projectile in a moving liquid flow or the launch of a moving projectile in a stationary body of liquid, the latter being the approach taken in this work. Both methods have their advantages and disadvantages. The moving fluid configuration has the advantages of long observation time and ease of administering ventilated cavities. Additional advantages are ease of measuring cavity shape, cavity composition and forces on the supercavitating body. Disadvantages of the moving fluid design include high equipment, fabrication, operating and lab space costs as well as a more limited flow speed. Alternatively, the moving projectile configuration has a relatively low cost and ease in achieving high speeds as well as direct observation of the free running body. The disadvantage of the moving projectile configuration, however, is that the observation time is extremely short.

Study of supercavitating bodies has largely been conducted in water tunnels or using other elaborate, expensive facilities. This work presents the design and testing of a low-cost small-scale experimental approach to producing a free-flying, naturally supercavitating projectile. The projectile is fired vertically downward along a trajectory of approximately 1.1 m from a firing mechanism that is itself submerged.

Figure 13 shows photographs of the apparatus. The left image is a view from the outside of the test tank showing the tank itself, a high-speed digital cameral positioned at one of the viewing windows, and the support structure that holds the firing mechanism. The image on the right is a view looking down into the test tank at a time when it was not filled with water. At the very top is the firing mechanism. Also seen are some speed measurement devices that the projectile travels through

along the trajectory, lighting for the high speed camera, and the cylindrical array of acoustic transducers positioned around the inside of the tank.

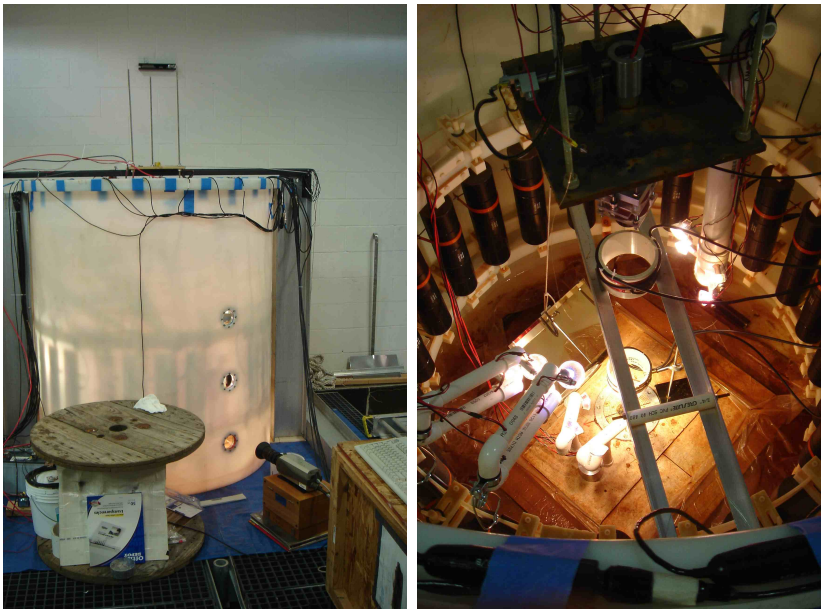

Figure 13: Photograph of experiment: left) external view of experiment tank, right) internal view looking down into the tank

4.1.2 Water Tank

The water tank had an inside diameter of 1.35 m (53") and a height of 1.6 m (62''). It was filled with a volume of water of 1.9 m^3 (500 U.S. gallons). Shots were fired vertically downward towards a steel backstop with a thickness of 13 mm (0.5"). Viewing windows were installed in the tank wall and were made of acrylic with a thickness of 25 mm (1.0"). These allowed imaging while keeping the camera on the exterior which reduced the risk of equipment damage due to water or violent motion.

4.1.3 Firing Mechanism

The firing mechanism was mounted on an independent structure, not connected to the water tank, that had sufficient mass and strength to withstand the large impulsive

forces generated during a projectile launch. The projectiles were accelerated using gunpowder as the propellant in a colt 45 brass cartridge with a standard large pistol primer.

Several measures were taken to reduce the angle of attack and angular velocity of the projectile upon exit from the mechanism muzzle. This was important because the dynamics of a projectile with the design used in the experiments that is experiencing supercavitation, in particular, oscillation in planes containing the flight trajectory are primarily due to the these initial conditions. The reason for this is that forcing moments when the projectile body is not in contact with the cavity wall are small. These moments are due to forces on the cavitator (see the following section on the cavitator design and section 2.1.3.1) and projectile weight.

The values of these initial conditions were minimized by careful consideration in design of the firing mechanism and loading procedures during operation. The firing mechanism itself was designed with no moving parts in order to minimize motion upon firing which improved the aim and repeatability of the experiment. The primer was ignited by the heat produced when an electric current passed through it. The positive terminal of a 12 volt marine battery was connected to an electrode that touched only the primer. The negative side was connected via the mechanism breech to the cartridge. A solenoid switch completed the circuit when the firing button was depressed which effectively short-circuited the battery for an instant. The large resulting current passed through the primer, generating sufficient heat for ignition. The barrel had a smooth bore and was 152 mm (6") in length. A high tolerance, tight fit between the projectile tail and the barrel inside diameter was an additional design feature conducive to repeatability and accuracy. In this experiment the projectile-tail and barrel-inside diameters were specified at 0.4525" and 0.4530" respectively. Great care was also taken during the loading process to get the projectile and barrel axes

collinear when loaded.

The working product was compact and inexpensive. A schematic of the design produced using solid modeling software is shown in Figure 14. Key design features are highlighted in the figure and explained in the following list:

1. A steel support structure held the mechanism in place at the top of the firing range.
2. A titanium dowel pin kept the breech (3) in place upon firing.
3. The breech housed the mechanism's working components, held the barrel (7), and was connected to the negative terminal of the power supply.
4. The conducting pin was connected to the positive terminal of the power supply and touched the primer.
5. An insulator electrically separated the conducting pin (4) and the breech (3).
6. The cartridge held the projectile and necessary chemicals. It also served to complete the electrical circuit connecting the conducting pin (4) and breech (3).
7. The barrel guided the projectile and maintained the pressurized region behind the projectile as it accelerated.

4.1.4 Projectiles

Photographs of the projectile used in all of the experiments in this work are shown in figure 15. The left image shows a side view of the projectile. The middle image shows the flat disk cavitator on the tip of several projectiles standing in a loading tray. The right most image shows a close-up of the transom of the projectile. The

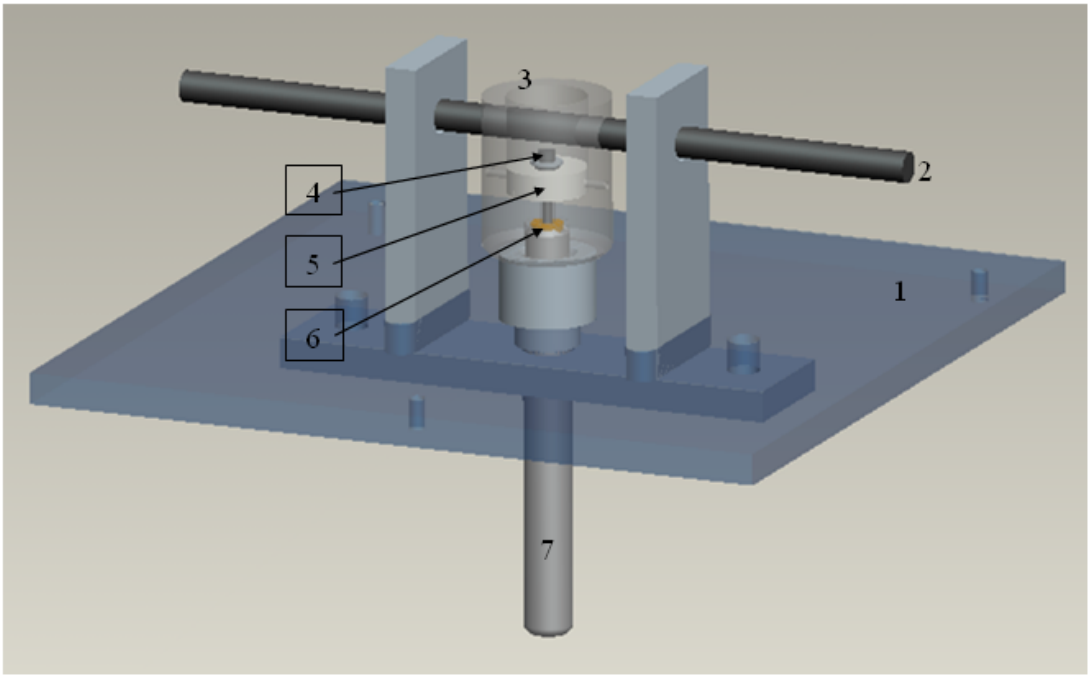

1.	Steel Support Structure
2.	Titanium Dowel Pin
3.	Breech
4.	Conducting Pin
5.	Insulator
6.	Cartridge
7.	45 Caliber Barrel

Figure 14: Schematic of experiment firing mechanism

dark circle is a magnet imbedded in the solid brass body that was needed for the speed measurement method (discussed in section 4.2.2). A technical drawing can be found in appendix B, figure 71 (This drawing excludes the magnet.).

Figure 15: Projectile photographs: left) side view, middle) disk cavitators, right) projectile tail showing imbedded magnet. Projectile dimensions are: length = 2.5", tip diameter = 0.115", tail diameter = 0.4525".

Primary projectile design parameters were cavitator shape and size, body aspect ratio, and material (mass density and machinability). In this work the projectile was designed to fly in a globally stable supercavitating regime. Initial conditions of angle of attack or angular speed and the local instability due to the center of pressure being forward of the center of gravity cause the projectile tail to fall against the inside of the cavity wall. This is known as tail-slap. The impact forces during tail-slap correct the overturning motion if designed correctly causing an oscillatory motion of the projectile inside the supercavity (see figure 4 in section 2.1.3.3 and accompanying discussion). Projectile dimensions for flight stability in the supercavitating regime were designed using an axisymmetric, steady supercavity geometry theory developed by Garabedian [35, 34].

Spin stabilized versus fin or control surface stabilized flight dynamics was a consideration in design. In fully wetted motion, spin stabilized dynamics are not practical

because of the high density of water which would produce very large hydrodynamic forces. Spin during supercavitation can improve the flight dynamics while the projectile is only in contact with the water but can have detrimental effects on the dynamics when the tail hits the cavity wall. Upon impact the rotation can cause the projectile to revolve around on the inside of the cavity. The resulting helical motion has been reported to increase the scatter of target impacts [65].

The design in this work had the following key features:

Flat nose, disk cavitator: In order to take full advantage of the reductions in drag available it was desired that the supercavity form at the nose of the projectile so that it enveloped the entire body. To achieve this the projectile was designed with a flat face nose normal to the axis of the body with a sharp edge to control the flow separation/cavity formation point; this produced a disk shaped cavitator (see figures 15 and 71). It was important that the cavitator had an appropriate radius for the body geometry and speeds of interest. Garabedian's model for cavity shape prediction was used to determine the correct cavitator diameter (see section 3.1 and figure 6 in chapter 3). The appropriate size formed a cavity/water interface in relatively close proximity to the body in the operating speed range so that tail-slap occurred at small angles of attack. Additionally, the cavitator had as small an area as possible so as to minimize the pressure drag and retain sufficient velocity to maintain the supercavity over the experimental test range. There are alternative designs to the disk cavitator that could have been used to achieve these results such as the cone and ogive cavitators; however, the disk cavitator has the advantage of stability over these alternatives. This stability advantage is due to the fact that the resultant pressure force on a disk cavitator is directed along the disk axis (see section 2.1.3.1). One negative aspect of a disk cavitator, however, is that it produces large drag forces

compared to the alternative designs [50]. However, the short test range in our experiment negated this disadvantage.

A cone shaped tail: The cone functioned to move the center of pressure toward the rear of the body during flight in a non-supercavitating regime at low flight speeds or in the muzzle gasses upon exit from the firing mechanism barrel. Although the projectile was designed to operate primarily in the supercavitating regime this feature was deemed necessary after instability problems with a previous design (see appendix B for projectile designs). Fluid flow modeling was done using $FLUENT^{\text{TM}}$. The cone achieved this effect without the complexity and cost of machining fins. Fins would have provided the same effect with less drag, however, at the projectile speed and range in our experiment fins were not necessary. Also, during supercavitating flight at low mach numbers the hydrodynamic drag on the projectile body inside the cavity is negligible. In fact, a finned projectile was made prior to the final design discussed here and worked with equal success but was too expensive to produce in the large quantities needed (see appendix B for projectile designs). An additional feature of the cone shaped tail was that it provided a surface at the projectile tail ideal for 'surfing' on the inside of the cavity as it was uniform around the circumference. The finned projectile just mentioned had to have a shroud around the fins to allow for this.

The mass is distributed over a large length: Distributing the projectile mass over a large length increased the moment of inertia and reduced the angle of impact between the projectile tail and the cavity boundary during tail-slap. The long moment arm of the force at the tail during impact also resulted in a large moment which was conducive to the desired oscillatory flight regime mentioned at the beginning of this section. Studies by Kulkarni and Pratap (2000) [57] show that this design feature also reduces the initial rate of increase of angular velocity and the magnitude of the

maximum angular velocity reached by the projectile inside the cavity. This leads to a reduction in the frequency of impacts, a reduction in the magnitude of the forces at the tail during impact and, consequently, a reduction in the deviation from a straight line path. The projectile aspect ratio could not be too large however. The cavity needed to be substantially longer than the body in the desired speed range so that the re-entrant jet at the cavity closure did not affect the stability of the body. Knapp et al. (1970) [55] referenced work by Self and Ripken (1955) [88] stating that cavities of moderate length exhibit re-entrant flow, filling, and break-off that can be fairly rhythmic. As cavity length grows the filling becomes partial and break-off more irregular. Although the trailing end of a long cavity (vertical or horizontal) may remain unsteady, the front portion becomes essentially steady.

The projectile is made of brass: Brass was easy to machine which reduced the fabrication cost. It also had a density that put the projectile in the desired mass range so that it could be accelerated to the operating velocity with a reasonable propellant load in the colt 45 cartridge. Aluminum projectiles were also tested, but the low inertia and mass caused an increased frequency of tail impacts and reduced the initial linear momentum causing large reduction in speed over the test range. This indicates that there would be an optimal material density for the projectile to achieve the best accuracy while still allowing for operation at the design speed, however, further investigation was not necessary for this work.

For experiment consistency it was important to have tight tolerances on the projectile geometry. Specifically, the tail diameter was machined precisely because the fit of the projectile in the barrel directly affected the projectile accuracy and the muzzle speed. Also the cavitator diameter had to be be consistent because the cavitator diameter affected the projectile drag and the size of the supercavity produced. Table 1 presents the design value and mean and standard deviation statistics of the measured values

for various parameters. Each statistic is based on 248 measured values.

Table 1: Statistics of manufactured projectile mass and dimensions

Property	Design Value	Mean Value	Standard Deviation
mass (grams)	18.8	18.6	0.083
length (inches)	2.500	2.503	0.0021
cavitator diameter (inches)	0.115	0.115	0.0004
tail diameter (inches)	0.4525	0.4525	0.0025

4.2 Experimental Measurements

Section 4.2.1 deals with imaging using the high-speed digital camera. Following a presentation of the experimental technique and camera specifications, measurement of projectile speed and and cavity shape using the resulting images is discussed. Section 4.2.2 then explores projectile speed measurement using electromagnetic induction. Finally, section 4.2.3 presents the technique that was used for measuring the projectile impact location at the end of the trajectory.

4.2.1 Photography: Imaging and Measurement

4.2.1.1 Photography: Imaging

A high-speed digital camera was used to obtain images of the projectile and cavity during flight. Viewing windows were located at three points along the trajectory: one at the muzzle of the firing mechanism, one half way along the flight path and the other at the point of impact with the backstop. Imaging at the muzzle location allowed for interrogation of the muzzle exit projectile dynamics, propellant gas dispersion and calibration of the muzzle speed measurement device. Imaging at the mid-flight point provided side view frames that were used for cavity shape and projectile speed

measurements that will be discussed shortly (figure 24 in section 4.3 shows sample images). Only a small portion of the supercavity could be seen in any one frame in this configuration because the length of flight path that could be captured was only about 15 cm (6"). A schematic of this set up is shown in figure 16. The minimum focusing distance between lens and object (limited by the lens) was 1.1 m. The lowest viewing window, positioned at the impact location, was used for looking at the projectile impacting with its target. Alternatively, a mirror was placed on the base of the tank and positioned so that when looking through this window the entire flight path could be seen. Figure 17 shows a schematic of the two camera positions and their respective views. This configuration enabled the experimenter to see overall cavity shape and general projectile dynamics. Most importantly the full trajectory view provided verification that the desired flight regime had been attained. Specifics of the flight regime were also determined. These were the frequency of the tail-slap instances and the extent of cavity wall penetration during tail-slap. An example image from this setup is shown in figure 23 in section 4.3.

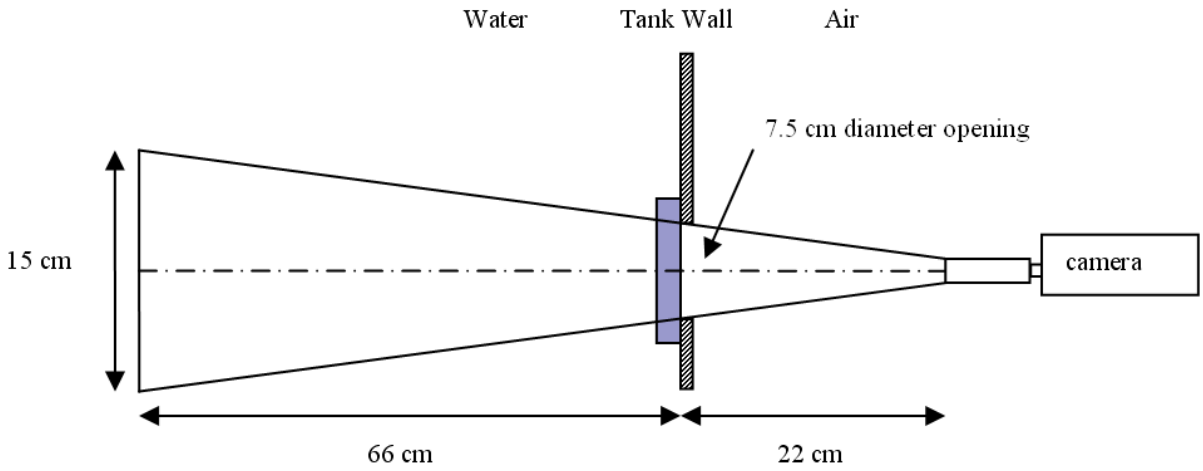

Figure 16: Schematic of direct view camera setup at minimum object to lens separation (Not to Scale)

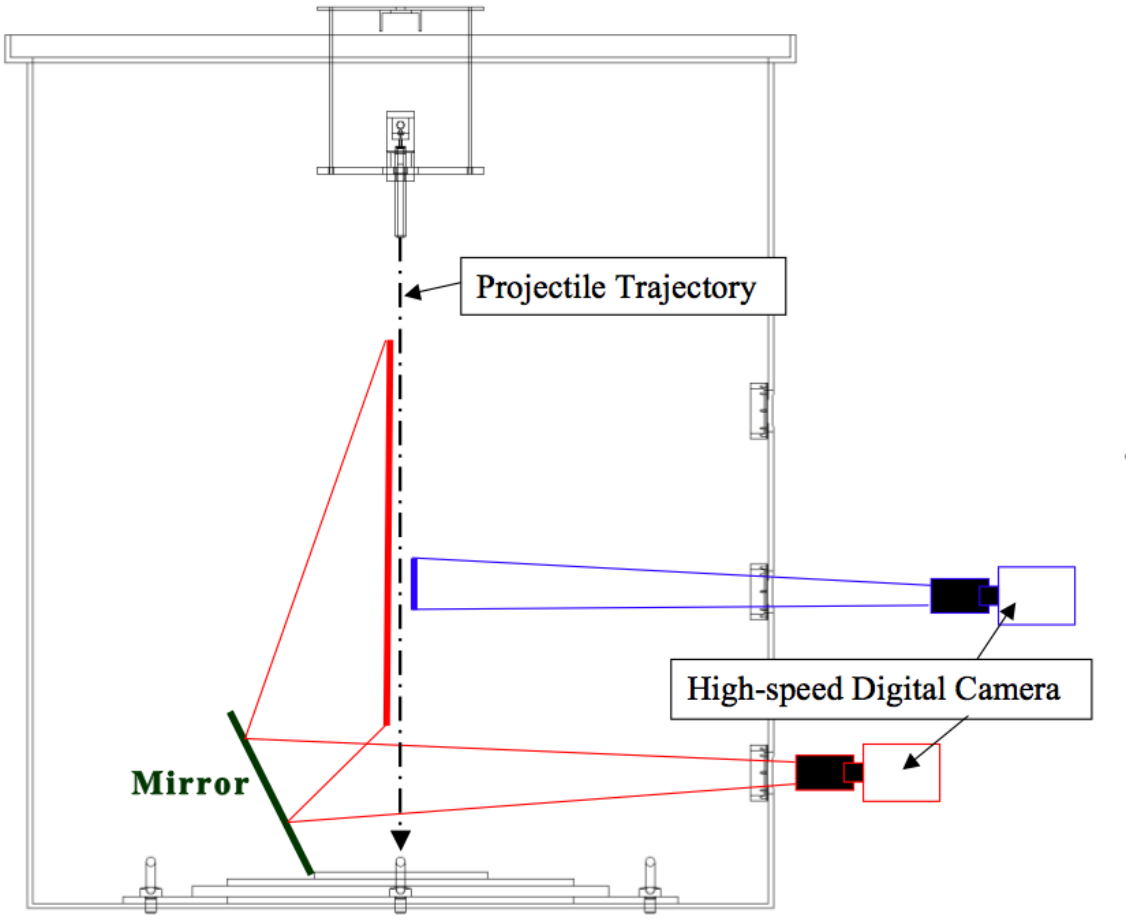

Figure 17: Schematic showing camera viewing positions

Initially the camera used was a Phantom v4.1 made by Vision Research Inc. with a Canon V6x16-1.9 Macro lens. For the final two experiment sets the camera was changed to a Photron FASTCAM 1024 PCI 1k. The change was due to malfunction of the original camera. The Phantom camera provided a high frame rate, ideal for visualizing the cavity evolution process and for measuring projectile speed, but its low sensitivity and resolution at the desired frame rate resulted in a relatively poor image quality. The Photron camera was not capable of reaching the desired frame rate to capture multiple images of the projectile in the viewing window, but its increased sensitivity and improved resolution resulted in higher quality images.

To measure projectile speed from the recorded images there needed to be at least two frames capturing the projectile nose. The nose was the only point that could always be identified and located visually. As previously mentioned, the maximum trajectory section that could be viewed was 15 cm if the projectile was flying straight down the middle of the circular window. At 130 m/s this corresponds to a frame rate of 2600 fps. The Phantom camera was used at a resolution of 256 by 256 pixels at 3731 fps. 256 pixels over 150 mm implies that each pixel represented 0.59 mm in length and width. The maximum frame rate available from the Photron 1024 PCI 1k was 1000 fps. The resolution at this frame rate could be set at a maximum of 1024 by 1024 pixels. 1024 pixels over 150 mm implies that each pixel represented 0.15 mm.

The Phantom and Photron cameras were capable of exposure times of as low as 10 μs and 1.5 μs respectively, independent of frame rate. Exposures used were typically between 10 and 80 μs. At these two times, and at a flight speed of 130 m/s the travel distance during exposure was 1.3 mm and 10.4 mm respectively. High levels of light were needed because of these fast shutter speeds. The fast shutter speed was required to attain images with sufficient resolution and clarity to determine flight dynamics information. The light was provided by twelve 75 watt, 12 volt, DC halogen spot lamps that could be submerged in the water without any modification. The connections to the bulb terminals were sealed using a silicone gel to prevent corrosion. An effective and readily available power source for these lamps was an automobile battery charger set to start mode. This configuration provided sufficient current at 12V.

The camera was triggered electronically to record the event by the firing mechanism trigger.

4.2.1.2 Photography: Speed Measurement

Speed was calculated by measuring the number of pixels traveled between any two frames. To relate pixels traveled to units of distance an image of a reference distance was taken maintaining the same camera settings as were used while imaging the projectile. To avoid lighting issues and legibility of ruler markings a measurement stick with two LEDs separated by a known distance was made and used successfully in this work. Accurate displacement measurement was facilitated using a $MATLAB^{\text{TM}}$ image processing program written by the author. This measurement method had the limitation of only being able to measure speed at one location in the flight path when viewing the cavity in profile because only one camera was available.

4.2.1.3 Photography: Cavity Shape Measurement

Supercavity maximum diameter and length were measured for comparison to theoretical predictions. Additionally, for inferences about the projectile dynamics and for quantifying the effect that the imposed sound had on the supercavity, the cavity diameter at the location of the projectile tail was measured.

Maximum diameter was found simply from the number of pixels measured across the cavity at the largest section. The software provided with the Phantom camera had such measurement capabilities built into it and so was used for this purpose. Obviously, a reference length was needed to determine the physical length associated with one pixel and was provided by images taken of the measurement stick just mentioned in section 4.2.1.2.

Supercavity length, however, was more difficult to measure. It is a quantity that inherently varies with time because cavity closure is an unsteady process. To estimate length, the number of frames were counted between passage of the projectile cavitator

and the cavity closure. This time along with the measured projectile speed were used to calculate an estimated supercavity length. If the location of the cavitator in the first image and the cavity closure point in the second image were not in the same location on the first and last images respectively then the time between events was not exactly equal to the number of frames times the frame rate. In this case adjustments were made for the difference in locations.

The cavity diameter at the projectile tail required a little more sophisticated and involved method. As this measurement was to be used for quantifying acoustic effects and in discussion of projectile dynamics it was important to develop an accurate technique for measurement. A $MATLAB^{TM}$ program with a graphical user interface (GUI) was written for this purpose.

The radius at the tail was found by fitting an ellipse to the cavity shape in the images from the digital camera. Garabedian's model [35] was used to estimate the parameters of the ellipse based on the measured projectile speed. The ellipse could then be translated, rotated, and the major and minor axes could be adjusted to find a best fit. Increments of movement could be adjusted to any number (or fraction) of pixels for displacement or degrees for rotation. Once a satisfactory shape was fitted, the program found the width of the ellipse at the desired distance along the cavity centerline aft of the projectile tip. Figure 18 shows an example of an ellipse fitted to a cavity image.

This method was used because the tail could not be seen through the cavity on most shots. Also, the lighting was not always the same making it difficult to measure an accurate width at one specific location.

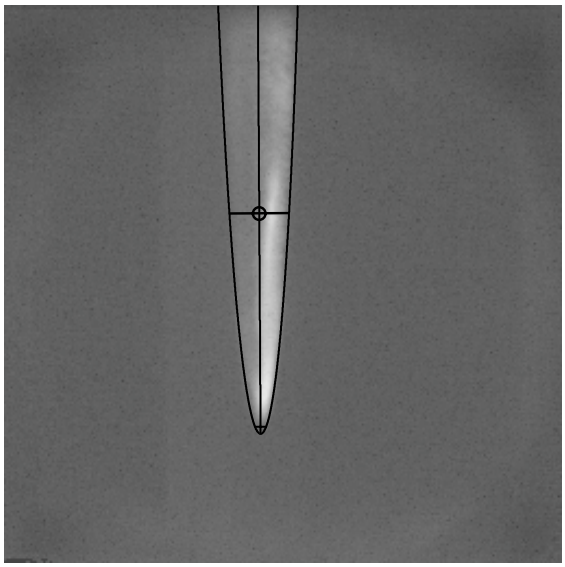

Figure 18: Example plots of an ellipse fitted to a supercavity

4.2.2 Projectile Speed Measurement Using Electromagnetic Induction

The projectile speed was also measured at three other points in the trajectory using an alternative method to that just described. The three points consisted of one at the muzzle to measure exit speed and two others at locations that were adjustable.

The technique used to measure speed utilized electromagnetic induction. A small neodymium iron boron magnet was imbedded in the transom of the projectile (see figure 15 in section 4.1.4). The magnet had a diameter of 0.1875" and a thickness of 0.0625" [28]. Each of the three measurement devices contained two wire coils that were a known distance apart. As the magnet passed through the wire coils there was a changing magnetic flux that produced an electric field inducing an *emf*. The induced *emf* is related to the rate of change of magnetic flux by Faraday's law of electromagnetic induction,

$$\epsilon = -N\frac{d\Phi_B}{dt} \tag{36}$$

where ϵ is the emf in volts, N is the number of turns of wire, and Φ_B is the magnetic flux though one coil.

The *emf* measured as the magnet passed through the coils was measured and used to deduce projectile speed. The expected signal can be reasoned considering Lenz's law. If the north pole of the magnet is facing downward then as the magnet approaches the coil the field points down and is increasing so the induced current would be in the counterclockwise direction looking down on the coil. After the magnet passes the coil the magnetic field points downward and is decreasing so the induced current is in the opposite direction. Therefore we expect to see a signal looking somewhat like the first derivative of a Gaussian.

Figure 19 shows photographs of the device at the firing mechanism muzzle. The top image shows a side view of the device attached to the firing mechanism barrel. The bottom image shows a view looking down onto one of the wire coils. The wire had red insulation. The coils on this set were precisely laid out flat in a single layer by hand with 150 turns each then covered with epoxy for protection. The red disks seen in the figure at the bottom of the device are the coils laid on clear plastic plates. The aluminum block seen above the coils was used to improve structural integrity of the device and divert the expanding muzzle gasses. The rest of the device allowed for attachment to the firing mechanism barrel. The flat construction of the coils made the separation distance easy to measure accurately with calipers and improved the shape of the recorded signal. This design was feasible close to the muzzle because the diameter could be small and the speed was highest there.

Figure 20 shows one of the other two devices (both were identical). It is shown positioned after the array at the end of the flight path, just before impact with the backstop. This coil set, and the third one that is not shown in this figure, had to have a much larger number of turns for two reasons: 1) they had to be a larger diameter

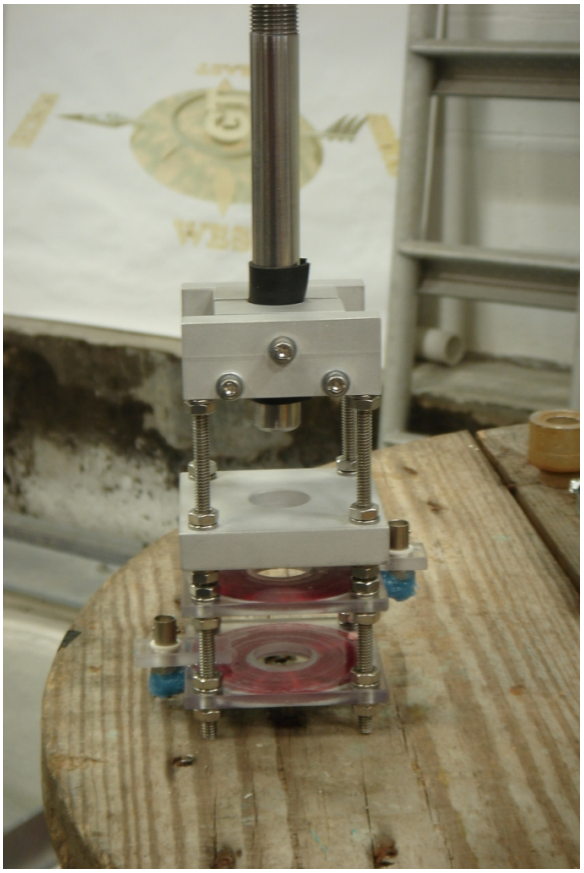

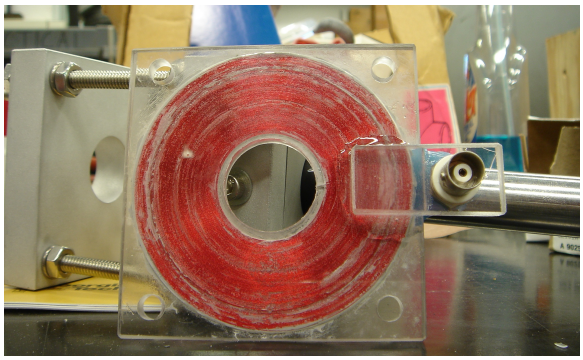

Figure 19: Photographs of muzzle speed measurement device. The top image shows a side view. The device is shown attached to the firing mechanism barrel. The bottom image shows a view looking down onto one of the wire coils. The wire had red insulation.

because variation in the projectile location was greater near the end of the trajectory, especially when the acoustic signal was being used to decrease the projectile accuracy, and 2) the projectile was traveling slower at later points of the trajectory. The number of turns used was six-hundred. Grooves were cut in short sections of PVC pipe, then wire was wound into the grooves feeding the wire as the cylinder was turned on a lathe. Finally, epoxy was poured into the groove on top of the wire to protect and seal the windings.

Figure 20: Photograph of induction coil device. Image shows the coil positioned after the array right before impact with the backstop.

An example of a typical measurement is shown in figure 21. This figure shows the voltage reading as a function of time for each of the six independent coils of wire as the projectile passed. There are several possible ways of extracting speed from this data. The most effective and accurate method found in this work was to cross-correlate the signals from each reading in a coil pair to find the time delay. The speed

was then calculated using the known distance between the coils. Filtering techniques were incorporated into the algorithm to reduce high frequency noise and unwanted signal picked up from the transducer drive signal.

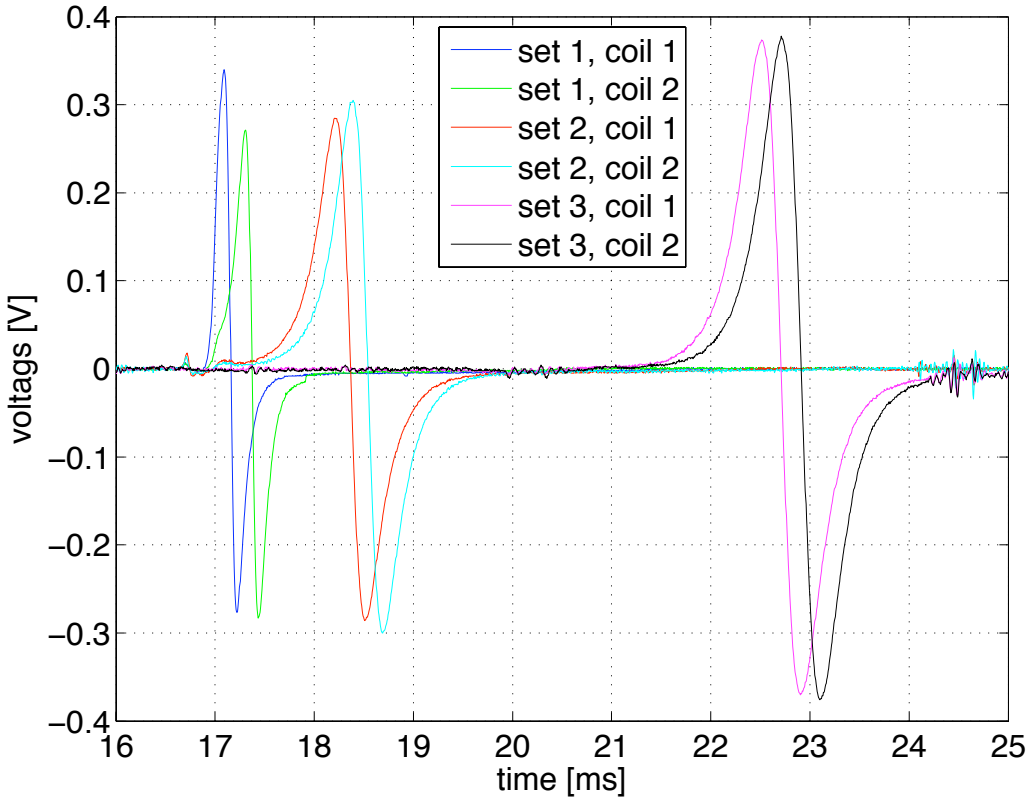

Figure 21: Example of a typical reading from the speed measurement coils

Initially, the method used was to find the time delay between the zero crossings after correcting for any DC signal. This was precise in the absence of any noise, such as the sample shown in figure 21, and gave readings in close agreement to those measured using cross correlation and from the high-speed camera images. In the presence of noise, however, particularly when the array was turned on, cross-correlation proved to be the best way and allowed the same technique to be used for all measurements. The zero-crossings method was used throughout as a form of verification to improve confidence in the results. A method based on measuring the signal amplitude was also experimented but proved to be less reliable.

For shots where the acoustic array was turned on there was a large amplitude unwanted signal as a result of pick up by the coils of the drive signal sent to the sources. In these cases, when the pickup overlaps the signal, a noise cancellation method was used to reduce the amplitude of the drive signal frequency components before filtering. The noise cancellation involved subtracting a sample of the pickup from a subsequent pulse that occurred one half second later. This second pulse occurred after the projectile had passed and therefore did not contain the signal information.

Accuracy of the speed measurement was based upon the accuracy with which the distance between the windings was measured and the quantization error in the crosscorellation. An estimate of the standard deviation of the error for a single measurement was calculated at $\pm$ 1.7 m/s at 133 m/s and $\pm$ 2.1 m/s at 147 m/s [8, 45].

4.2.3 Measurement of Impact Location

Impact location was recorded to give a measure of aim accuracy. Measurement was made by placing a target on the backstop and measuring where the projectile hit. The target pattern is shown in figure 22. Plastic projector transparencies proved to work very well as a material for the target. They were readily available and obviously easy to print targets on. Additionally, the sharp tip of the disk cavitator on the projectile nose cut a circle out on impact, which could be easily identified even if the subsequent motion damaged the target further, giving a reliable and accurate measure. This plastic target was mounted to an aluminum ring that was aligned on steel dowel pins that were attached to backstop. This ensured accurate placement of the target minimizing measurement error.

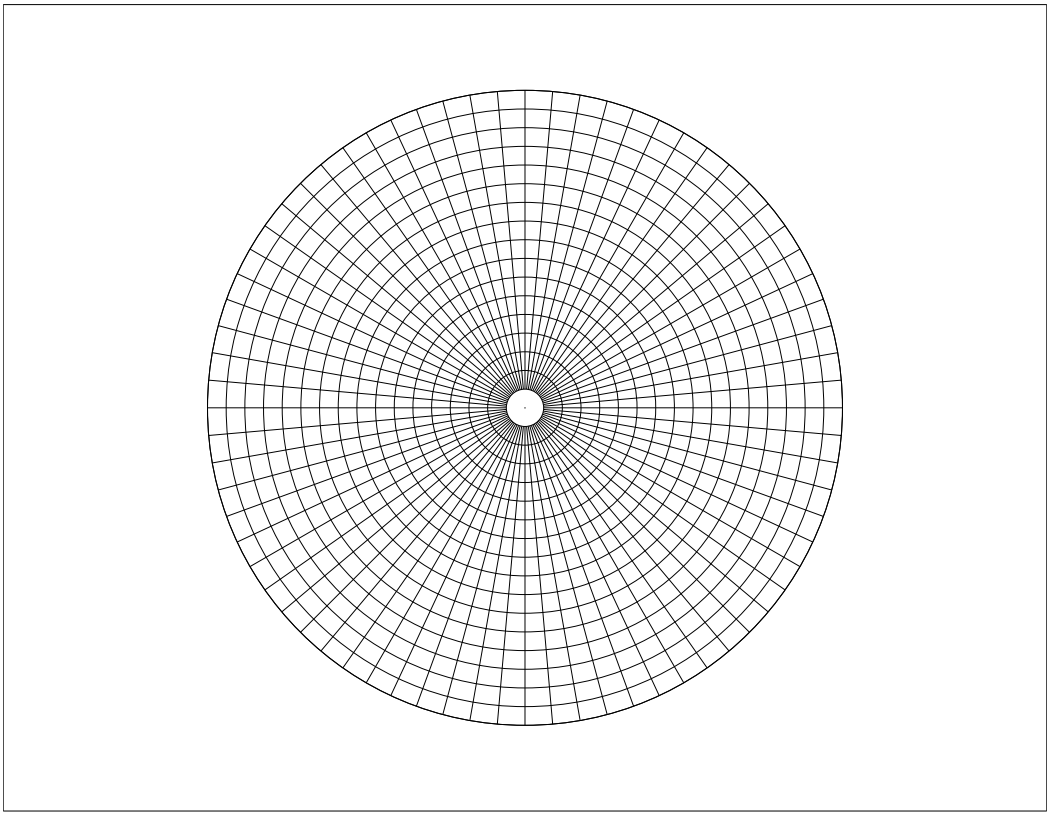

Figure 22: Target pattern that was used for measuring target impact location. Rings had radius increments of 5 mm and radial lines are spaced 5° apart.

4.3 Apparatus Testing and Control Experiment Data

This section presents testing and control experiments that utilized the apparatus and measurement techniques that have been discussed in sections 4.1 and 4.2. It is noted also that there was extensive testing and design iterations that were carried out before the results given here. However, those results are not presented because they only served to facilitate in getting the apparatus to function satisfactorily so that the data collection experiments could be done.

For initial testing, twenty projectiles were fired with the acoustic array turned off. The resulting data was used to confirm successful operation and produce a sample of control data. Any data set with the array off constitutes a sample from the control population. The control experiments determined apparatus performance with no imposed pressure field. Additional control experiments were done throughout the duration of the experimentation, distributed amongst the array-on experiments. This was done to increase the control sample size and to ensure that the performance of the apparatus was not changing with use. Compiled results from the control experiments are included in this section and are crucial for statistical inferences and hypothesis testing in chapter 5.

Section 4.3.1 discusses general qualitative flight characteristic observations that helped to verify attainment of the desired flight regime. Section 4.3.2 presents the impact location results for the control experiment samples along with the statistical measures used in analysis. Section 4.3.3 presents the speed data with a comparison to results of the simulation described in section 3.2. In section 4.3.4 cavity geometry was measured for the control experiments and compared to theoretical predictions. Lastly section 4.3.5 presents a summary of the results for the control experiments.

4.3.1 General Flight Characteristics

Full flight imaging with the high-speed digital camera was used for the first twenty shots in order to get an overall picture of the flight dynamics. Subsequent control shots were viewed from the side in the middle of the flight trajectory. Figures 23 and 24 present sample images showing the cavity produced by a projectile during a typical shot for the two different viewing configurations.

Figure 23 shows three images spanning nine frames at 2500 fps and so covering a time of 3.2 ms. The projectile is seen coming down and toward the viewer as is depicted in the schematic of figure 17. The only thing seen in the image is the supercavity that was formed by the cavitator at the projectile tip. The projectile was inside the cavity and so can not be seen. The blister seen on the cavity wall in the middle and right images was formed where the projectile tail hit the cavity wall during an instance of tail-slap. The far right image shows the closure region of the cavity.

On examination of the frequency and timing of the tail-slaps it was seen that there were shots exhibiting from zero to three instances of tail-slap during flight. Shots that exhibited more frequent tail-slap generally had deeper, more severe tail penetration. This makes sense because a higher projectile angular velocity requires more impulse during instances of tail-slap in order to reverse the direction of rotation and the greater angular velocity results in more frequent occurrences of tail-slap. The actual depth of penetration could not be measured with the data recorded.

Figure 24 shows side view image samples, one from each camera used. In the left image a blister is again seen on the cavity wall due to an instance of tail-slap. The tail of the projectile was rotating out of the page. To give an idea of scale, the vertical length of these images corresponds to five inches.

The dynamics seen in these images, and in many others not presented here, verifed that the desired flight regime had been achieved.

4.3.2 Projectile Trajectory Data

The projectile trajectory data consists of impact locations on the target at the end of the projectile trajectory as discussed in section 4.2.3.

In assessing the accuracy of a weapon system, it is common to use the measure of circular error probable (CEP) [94, 78]. CEP is a statistical measure defined as the radius of a mean centered circle within which fifty percent of the shots are expected to hit. Statistical inferences about the significance of results in later sections are based on error distributions in the x and y directions of a cartesian coordinate system. This has is done because common statistical methods and measures are based on normally distributed data, and without evidence to the contrary one might reasonably assume that the errors in any direction of shots from the firing mechanism were random and normally distributed.

The target was oriented with x and y axes corresponding to axes of the experiment apparatus. These directions were the most likely to have different error distributions due to physical asymmetries of the apparatus and so this choice of x and y helps to highlight possible asymmetries in the impact location distribution. If there are found to be no asymmetries in the distribution then the choice of axes orientation is irrelevant.

The impact locations of the control shots are plotted in figure 25. Frequency distributions in the x and y directions are shown for this data in figure 26. There were a total of 87 control shots. In figure 25 the mean of the individual samples has been normalized to the origin of the target. In figure 26 a theoretical normal distribution with

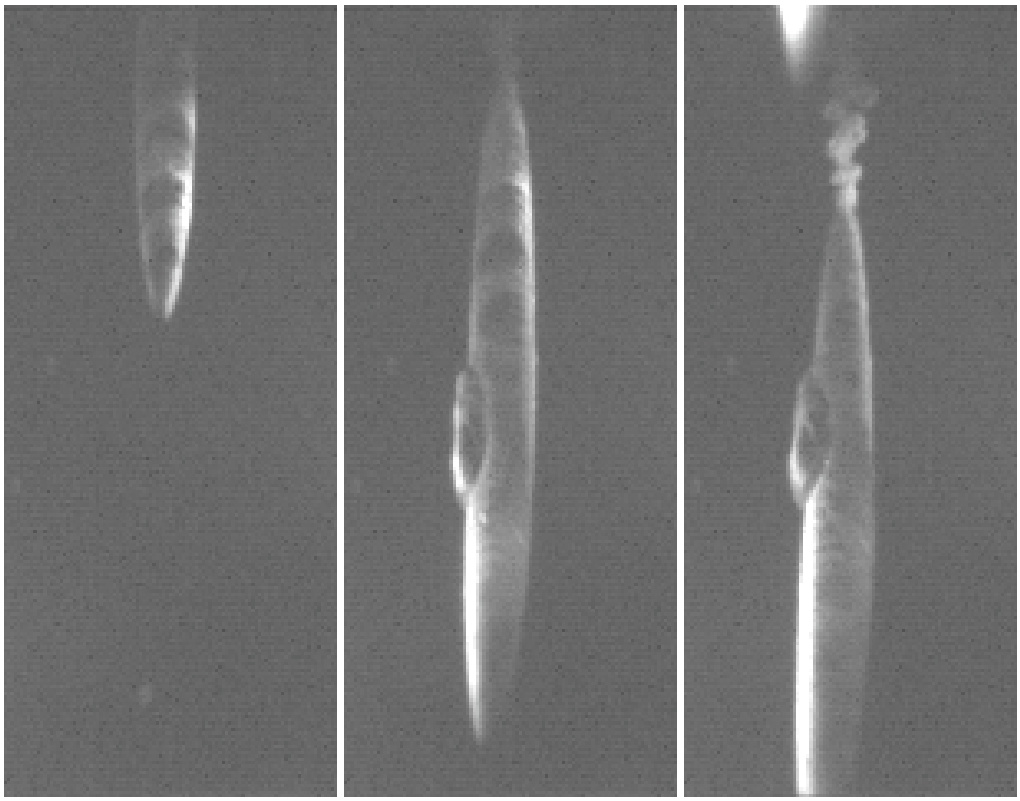

Figure 23: Images from high speed digital photography of a supercavitating projectile using the Phantom v4.1 camera. The projectile is viewed through the bottom tank window using a mirror to see a large portion of the trajectory (see figure 17). The figure shows three images spanning nine frames which span 3.2 ms, time increases from left to right. The blister seen in the cavity wall about half way down the middle and right images is due to the projectile tail hitting off the cavity wall in an instance of tail-slap.

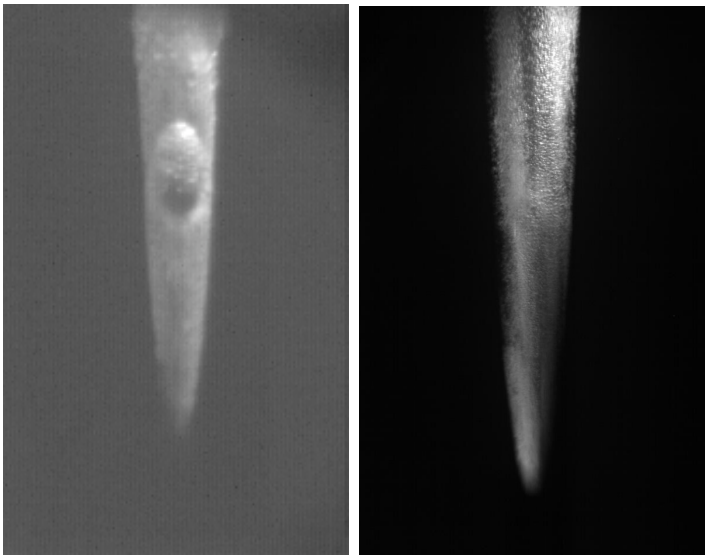

Figure 24: Image from high-speed digital photography of a supercavitating projectile. Left) image frame using the Phantom v4.1 camera, right) image frame using the Photron 1024 PCI 1k camera. The vertical length of these images corresponds to five inches.

the sample standard deviation has been plotted as a solid line over the histogram. Standard deviations for the sample were found to be $s_x = 6.35$ and $s_y = 6.51$ with 95% confidence intervals on the population mean of 1.40 and 1.36 respectively. The confidence interval (CI) is an interval estimate constructed using the point estimate of the sample mean $\bar{Y}$, the standard error of the mean $(s/\sqrt{n})$ for the observations, and properties of the normal distribution [27]:

$$CI = \bar{Y} \pm t_{\alpha/2}\frac{s}{\sqrt{n}} \tag{37}$$

where α is the desired confidence (chosen at 95%), t is the t - value for the distribution that can be found in tables in most statistics texts (for example Duncan (1983) [27]), and n is the number of data points. The confidence interval on the mean location uses a t distribution because the standard deviation of the population is not known. The t distribution takes account for the fact that the sample standard deviation (s)

is used to estimate the population standard deviation (σ). From the data plotted it does not appear that the distribution is elliptical.

The common method for calculating CEP assumes a circular normal distribution which implies that

$$\sigma_x^2 = \sigma_y^2 = \sigma^2$$

In this case the radial error ($R = (x^2 + y^2)^{\frac{1}{2}}$) has a Rayleigh distribution with the cumulative distribution function

$$P(r) = 1 - exp(-\frac{r^2}{2\sigma^2}) \tag{38}$$

Equation (38) then gives the probability of projectile impact within a radius r. The CEP in this case can be found by setting P equal to 0.5 in equation (38) and solving for r. This leads to the common equation for CEP:

$$CEP = 1.1774\sigma \tag{39}$$

The use of this relation requires a common value for σ. If σ_x and σ_y are not equal then one can use an estimator for elliptical normal errors. Taub and Thomas [94] compare five different estimators for CEP using sample variances. In this work the arithmetic mean of σ_x and σ_y is used in equation (39), which is in fact one of the estimators in reference [94]. Taub and Thomas show that this is a reasonably good estimate for the CEP when the ratio $\sigma_{min}/\sigma_{max}$ of an elliptical normal distribution is greater than about 0.2. For our data the ratio was 0.98. For the control data the CEP was calculated to be 7.56 mm.

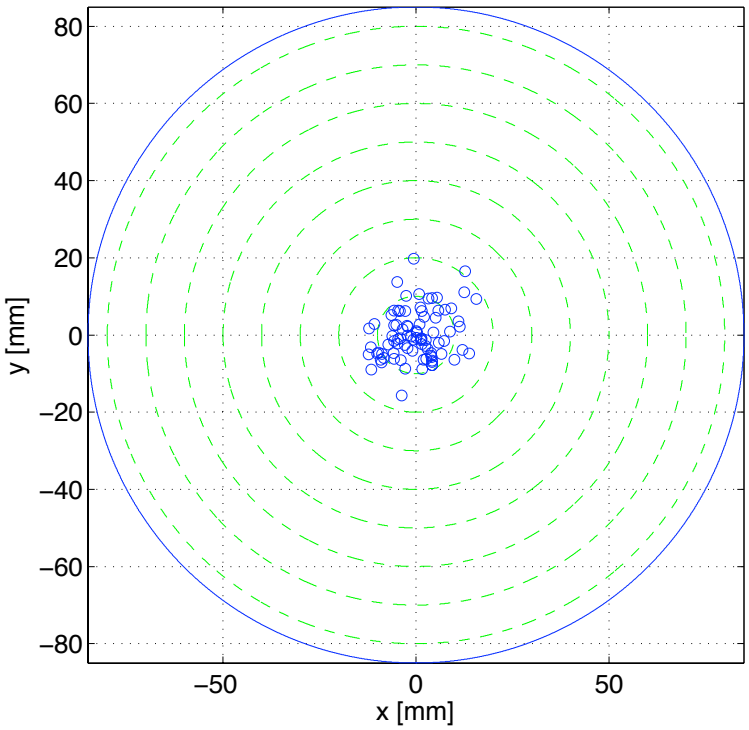

Figure 25: Target impact locations for the control experiments (total of 87 shots). Data from individual experiment cases are normalized to the mean of each sample.

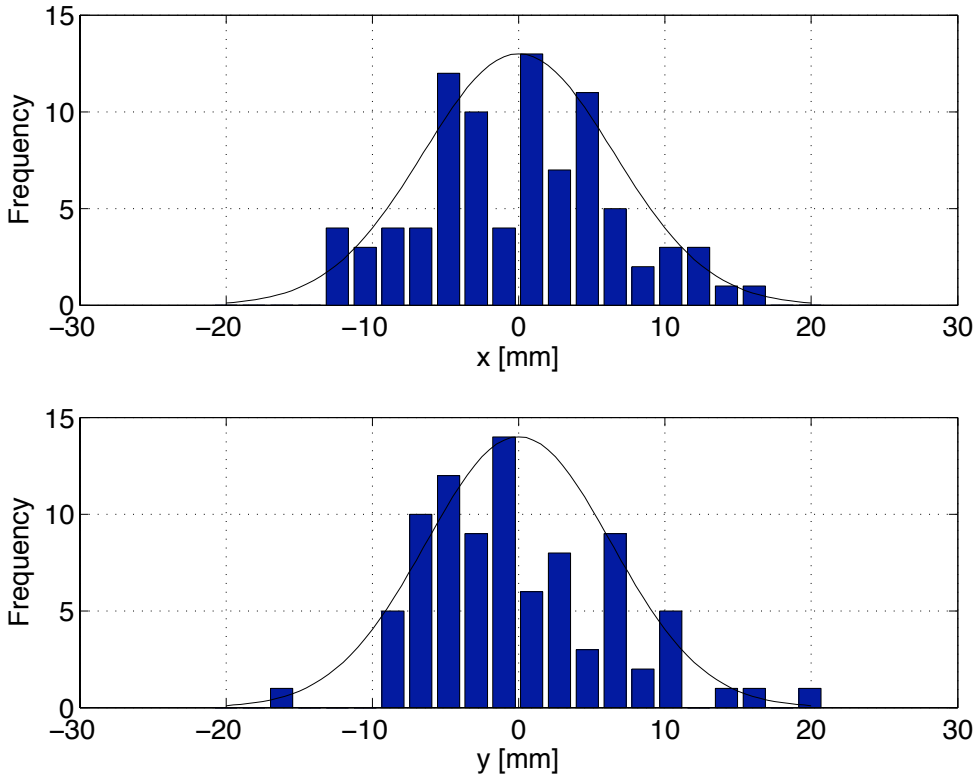

Figure 26: Frequency distributions of the control experiments in x and y directions (total of 87 shots).

4.3.3 Projectile Speed Data

Projectile speed as a function of time is presented in the graph in figure 27 for the initial sample of twenty control shots. The speed plotted was the vertical component of the tail velocity because this was the speed measured as described in section 4.2.2. The solid circles represent measured data and have been connected with solid straight lines. The different colors and legend labels represent different muzzle speed ranges. The speed measured at the camera location was not plotted in this figure because the time that the projectile was at the camera location relative to the times of the coil measurements was unknown. The dashed lines plotted are predicted curves and have been plotted for muzzle speed ranging from 100 m/s to 170 m/s in increments of 10 m/s.

The measured data was compared to theoretical predictions. The main drag force was due to the cavitator disk, however, small dips were present in the predicted speed-time curve due to incidences of tail-slap. Although the effect of the relatively light and short duration tail impacts was small, it served to bring the theoretical curves into line with the experimental data. A previous simpler model including only cavitator forces under-predicted the drag force. In examining the full trajectory imaging of these shots it was found that there was a variation in the number and the severity of the tail-slap incidences. Observations ranged from zero to three visible impacts. The majority of the flights showed one light impact in the middle and another right before impact with the backstop; therefore, the simulation curves that were plotted in figure 27 represent this case. This situation was achieved in the simulation at a moderate initial velocity with an initial projectile angle of attack and angular velocity of 1° and 9 rad/s respectivley. Unfortunatley, the initial conditions of the projectile orientation and angular velocity were not measured in the experiments. No simple measurement technique has been thought of by the author at this time. The conclusion can be

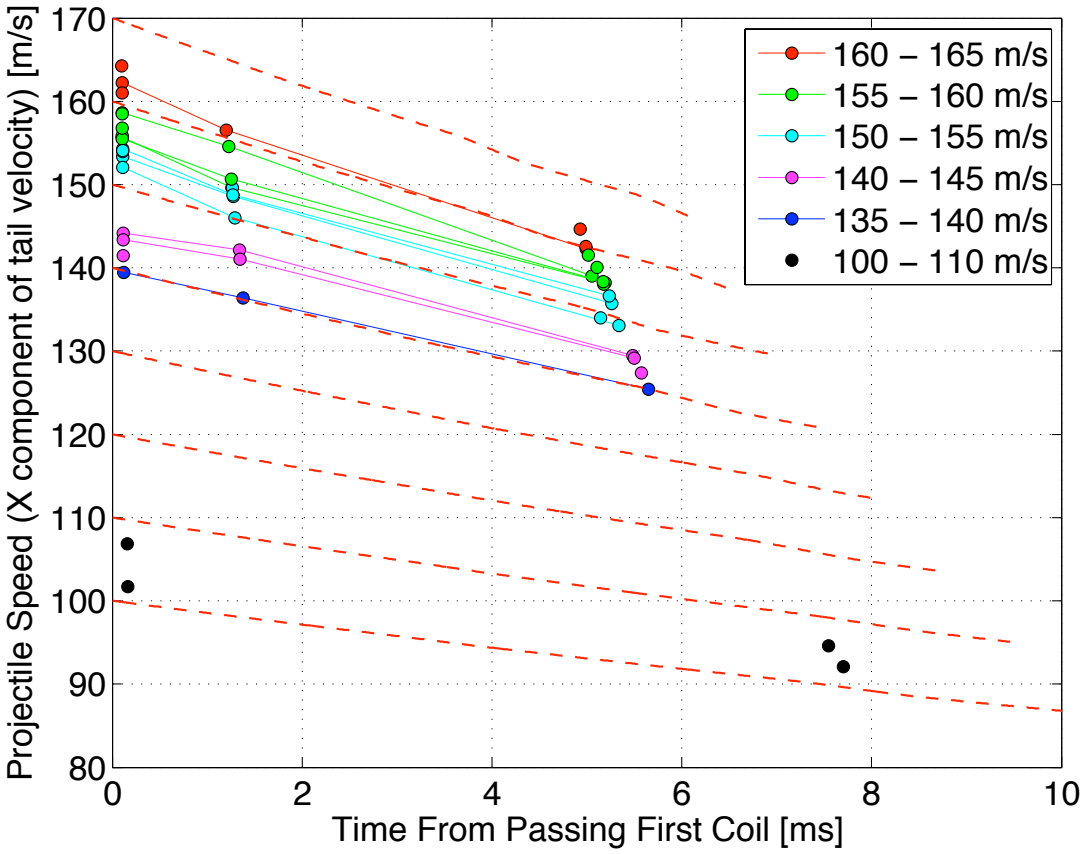

Figure 27: Projectile speed at various muzzle velocities; comparison between experimental and simulated curves. The different colors and legend labels represent different muzzle speed ranges. The dashed lines are curves predicted by the dynamics simulation (see section 3.2)

drawn from these results that the projectile was indeed supercavitating and that the theoretical model captures the most significant aspects of the physical situation in a qualitative and quantitative manner. For details on the simulation see section 3.2 in chapter 3.

For these shots there was no correlation between projectile speed and impact location.

Now looking at the entire sample of control shots we can look at the overall performance. Figure 28 shows the same plot of speed versus time but for all of the control shots. An average muzzle speed for all of the control shots was found to be 148.5 m/s with a standard deviation of 14 m/s based on 74 measurements. There were several shots where there was no measurement taken due to noise or failure of the measurement device so there were only 74 measurements compared to the 87 target impact location points.

Drag coefficient was calculated based on speeds measured at the second and third coil sets because it was not clear at the muzzle location as to whether the projectile was experiencing supercavitation or not due to expanding muzzle gasses in this region. Unfortunately, the coil set before the array did not yield a measurement on many of the shots due to noise.

Additionally, the muzzle speed measurement was found to be inconsistent between the various experiments at the muzzle location. This can be seen in figure 28 by the variations in slope of the line drawn between the first and second data points on each curve. The inconsistency was due to the fact that the coils could be moved in the vertical direction relative to each other as a consequence of the device design. The retaining nuts came loose on one experiment set, and due to coil damage the device was disassembled and reassembled during another experiment set. It was found that setting the distance between coils by measuring with calipers was not

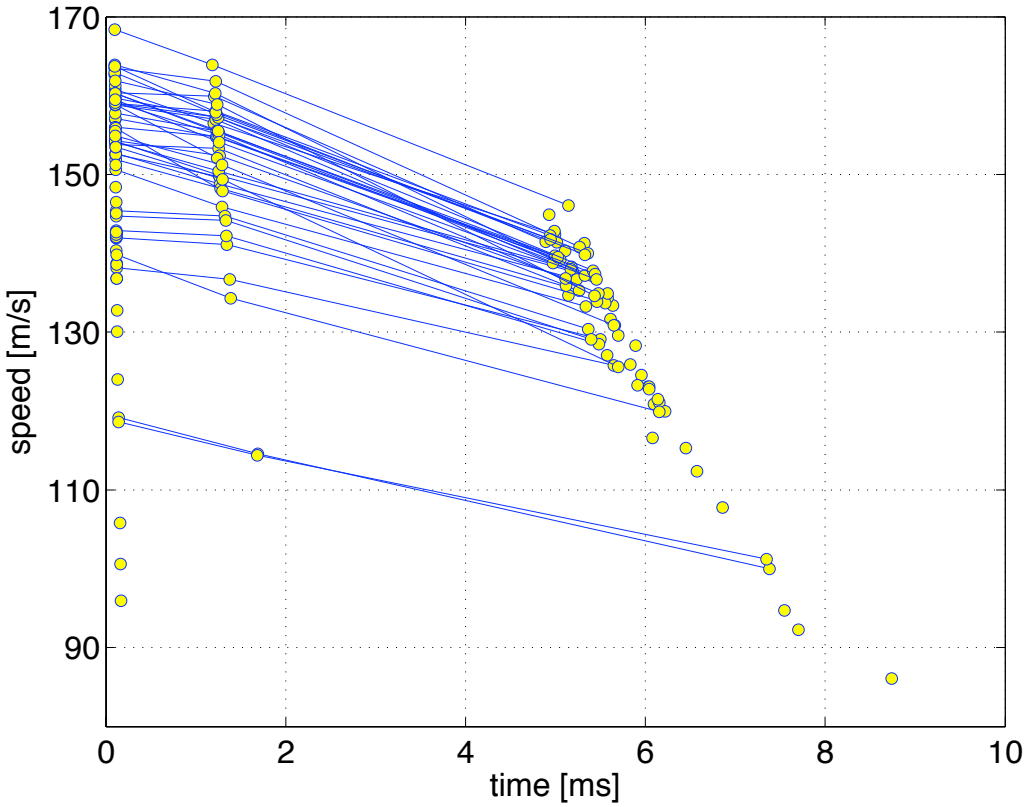

Figure 28: Plot showing measured speed versus time for all of the control experiments

sufficient to maintain an acceptable level of consistency. The coils on the other sets had a fixed distance between individual coils (measurement device design is discussed in section 4.2.2).

To calculate the drag coefficient it was assumed that a drag force and weight were the only forces acting on the body and that the drag force was constant over the time interval used to find acceleration. This was a reasonable assumption given the relatively constant slope seen on the speed time graph in figures 27 and 28. Then the drag coefficient was found from the simple equation of motion,

$$mg - C_D(\pi r_c^2)\frac{1}{2}\rho_w v^2 = ma_p \tag{40}$$

where m is the projectile mass, a_p is the projectile acceleration, The mean drag coefficient calculated for the control shot data was $C_D = 1.10$ and was calculated from only 37 measurements. The standard deviation was 0.175. A theoretical prediction for the drag on a cavitator disk gave a drag coefficient of $C_D = 0.836$ (The commonly used relation for the drag coefficient of a disk cavitator for zero angle of attack is given by equation (15), $C_D = C_{D0}(1 + \sigma)$, and is discussed in section 2.1.3.1). It is expected that the actual drag coefficient would be greater than that predicted for a disk cavitator because there are drag forces on the projectile body. The occurrence of tail-slap is probably the main contributor.

4.3.4 Cavity Geometry

Side view imaging was used for all experiments following the initial sample of twenty control shots. This section discusses results from measurements of the cavity geometry in the control experiments. Measurements made were of cavity length and maximum diameter (as discussed in section 4.2.1.3). The measurements were then compared to theoretical predictions for a supercavitating disk cavitator. From an apparatus testing perspective this further verified the attainment of supercavitation. Additionally, the comparison gave first hand validation of the theory used in the dynamics model.

Figure 29 presents plots of cavity dimension against projectile speed. The upper plot shows the maximum cavity diameter and the lower plot shows cavity length. In both plots the solid green line represents a theoretical prediction using Garabedian's model [35] (see section 2.1.1.1), the blue circle markers represent measured values of the cavity dimension, and the red dashed line represents a best fit second order polynomial to the measured data.

For both maximum diameter and length it is seen in the figure that the measured

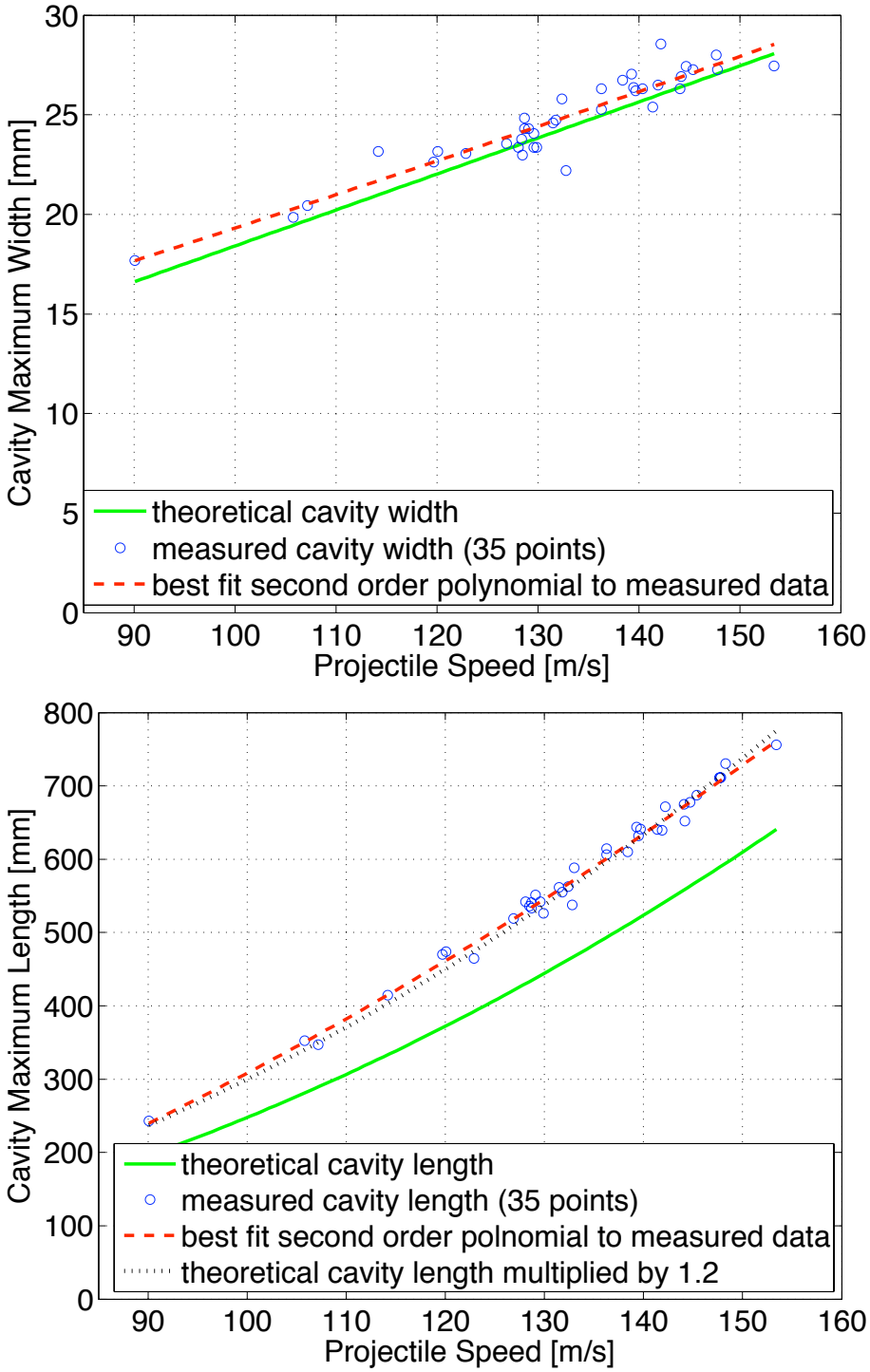

Figure 29: Plots of cavity dimension against projectile speed: top) maximum cavity diameter, bottom) maximum cavity length

Table 2: Polynomial coefficients for best fit lines and theoretical curves in figure 29. Coefficients a, b, and c correspond to terms of the generic quadratic polynomial in equation (41)

		a	b	c
Maximum Cavity Width	best fit	0.0001	0.142	3.92
	theoretical	0	0.178	0.488
Cavity Length	best fit	0.0251	2.14	-156
	theoretical	0.0341	-1.28	34.7

values are greater than the theoretical values. The measurements of maximum diameter show a very close match with theory. Cavity length, however, clearly does not match as well.

To quantify the fit of the data, two measures have been used. Firstly, the random error of the data was quantified by the standard error of the estimate for the best fit line. These values were 0.85 mm for the cavity width and 12 mm for the cavity length. Secondly, the coefficients of the best fit polynomial were compared to coefficients of a similar polynomial fitted to the theoretical curve. The coefficients are presented in table 2. Values of a, b and c correspond to coefficients of the generic polynomial shown in equation (41).

$$y(x) = ax^2 + bx + c \tag{41}$$

The maximum cavity width is seen to be almost a straight line. The data is mainly offset from the theory, evident by the increase in the c value. The cavity length coefficients are less informative but it is clear from the plots that the main difference is an offset and the black dotted line indicates that the observed data is approximately 20% greater than the theoretical prediction.

4.3.5 Summary of Control Shot Statistics

Table 3 presents a summary of the control sample statistics that were found in sections 4.3.4, 4.3.3 and 4.3.2. These statistics are used in chapter 5 for inferences about the impact of the imposition of the acoustic signal on the dynamics of the supercavitating projectile.

Table 3: Summary of control sample statistics

Statistic	**Result**
Impact Location (section 4.3.2)	
Circular error probable	7.56 mm
x direction standard deviation	6.35 (95% confidence interval of 1.40)
y direction standard deviation	6.51 (95% confidence interval of 1.36)
Projectile Speed and Drag (section 4.3.3)	
Average drag coefficient	1.10 (from 37 samples)
Average muzzle speed	149 m/s (from 74 samples)
Standard deviation of muzzle speed	14 m/s (from 74 samples)
Cavity Dimensions (section 4.3.4)	
Standard error of the estimate for cavity maximum width	1.0 mm
Standard error of the estimate for cavity length	108 mm

4.4 Acoustic Array Design and Sound Field Measurements

All of the sections in chapter 4 so far have been concerned with the design and testing of an experiment that enabled the investigation of a supercavitating projectile. Once this facility was available, the next step in achieving the goals of this thesis was to design and build an array of acoustic sources that was capable of imposing a high pressure sound field on the supercavitating projectile. This allowed investigation the effects of the sound which was the ultimate objective.

Section 4.4.1 discusses the general array design including characterization of the component source transducers and description of the driving electronics. The remaining sections present results from a series of tests that characterize the sound field in the array focus. Tests were done with increasing levels of complexity so as to build an understanding of the equipment, sound field, and the factors contributing to the more complex cases. Firstly, the case of a free environment and low pressure amplitude was examined and is presented in section 4.4.3. The array was then placed in the confinement of the test tank to determine effects of the more complex environment and low pressure tests were repeated (section 4.4.4). Finally, the driving voltage was increased in increments toward the maximum level available to determine the effects of the high pressure nonlinearities, especially acoustic cavitation (section 4.4.3).

Calibrations for the hydrophones used in this work were done and are presented in appendix D.

4.4.1 General Array Design

4.4.1.1 Geometric Configuration

Some relevant issues and approaches to acoustic focusing were discussed in the literature review, section 2.2. Considering the resources available and the geometry of the setup it was determined that a conventional phased array would be used to create the desired field. Figure 30 shows a schematic of the array design produced using the solid modeling software $Pro/ENGINEER^{TM}$. Twenty-four cylindrical transducers were positioned on a circle one meter in diameter. The restriction on the number of transducers was the number of available amplifiers and matching transformers. As can be seen in the figure, a larger number could have been used within the geometry constraint of the apparatus. The irregular spacing at one location on the circle was necessary to produce a gap that was aligned with the windows in the tank wall through which observations of the projectile could be made be made.

With the sources positioned to form an annulus around the interior of the water tank, focusing was achieved geometrically without the need to adjust the phase of individual sources. Additionally, the radius of the circle that the sources were positioned on could be adjusted to tune the system to take advantage of constructive interference from the wall reflections at a given frequency or for a given short duration pulse. The adjustment was done at the clamps that hold the transducers and allowed for sufficient travel to tune the array at the desired operating frequency.

The simplicity of this approach to focusing sound pressure on the supercavitating projectile was made possible by the idealized laboratory setting. There were several known factors in this setting that would be unknown in a practical application of the countermeasure in the ocean environment: the location of the target, time of arrival of the target, the properties of the medium, and the geometry of the surroundings.

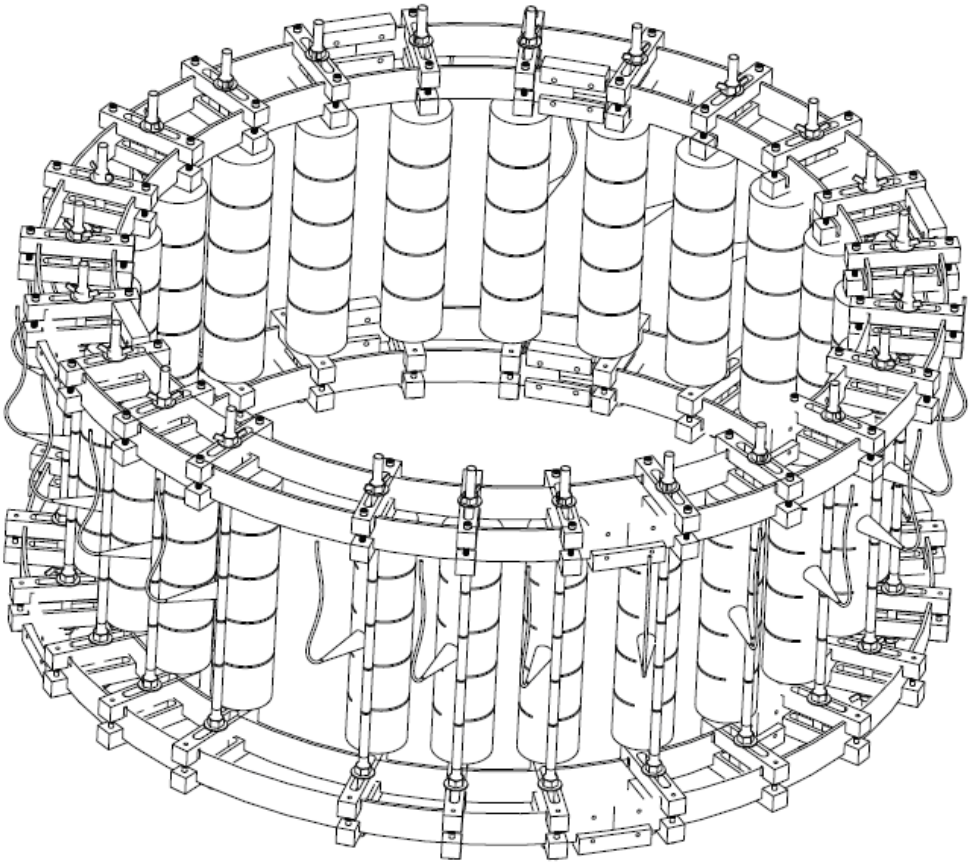

Figure 30: Schematic of the annular transducer array. The twenty-four cylindrical transducers shown are positioned on a circle approximately one meter in diameter (diameter is adjustable: $\pm$ 5 cm).

Our controlled situation simplifies the problem for testing the proof of concept that this thesis addresses, however, in a real world practical application a more elaborate target detection and adaptive focusing technique would be required. Section 2.2 in chapter 2 discusses a proposed method of addressing these issues.

4.4.1.2 Source Transducer Characterization

The frequency response of the available transducers was a key factor in determining the frequency range and pressure amplitude that could be used in the experiments. The frequency and Q-factor of the fundamental resonance determined the optimum frequency for maximum amplitude, and the bandwidth that could be used without large sacrifices in pressure amplitude.

The available source transducers were made by International Transducer Corporation (ITC) and have model number ITC 6135-1. This transducer consists of five cylindrical piezoelectric ceramic elements arranged axially and potted in a polyurethane compound. A photograph of one transducer is shown in figure 31. The transducer has an overall length of 356 mm (14"), and a diameter of 83 mm (3.25"). These are the dimensions of the external surfaces of the source.

A transmitting voltage response (TVR) curve has been obtained experimentally and is shown in figure 32. Appendix E contains calibration curves for one of the transducers provided by the manufacturer. In figure 32, the circles represent a calculation from pressure and voltage amplitudes measured in the time domain for a gated continuous wave signal at different frequencies. The measurements were obviously made once a steady state had been reached. The short lines represent a calculation from pressure and voltage amplitudes in the frequency domain. This curve agrees very closely with the curves provided by ITC. The low frequency region is seen to have a slope

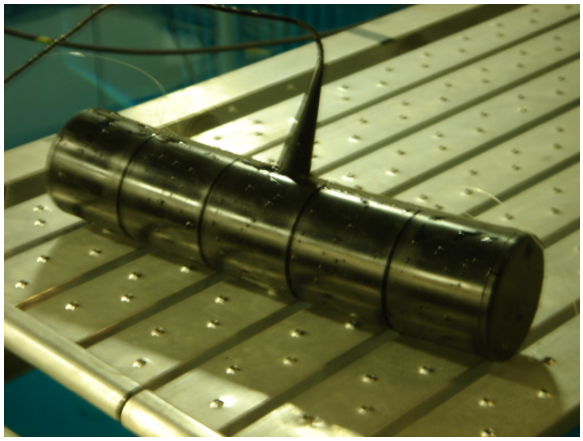

Figure 31: Photograph of an ITC 6135-1 source transducer. Overall dimensions: length = 356 mm (14"), diameter = 83 mm (3.25")

of approximately 12 dB per octave corresponding to frequency squared amplitude dependence (spring dominated effect and $ka << 1$, where k is the acoustic wave number and a is the individual transducer-element equivalent radius which is related to the transducer volume velocity). The slope then increases toward the fundamental resonance peak at approximately 13.5 kHz. Above resonance, as frequency increases, the transducer response becomes inertia dominated which, in theory since $ka > 1$, should result in an amplitude decrease as frequency increases; however, there can be many things going on above resonance. One likely explanation is that the positive slope shown could be due to another higher resonance. The transducers were operated between 7.5 kHz and 17.5 kHz in this work so the higher frequency region was not considered.

In the array configuration (see figure 30), the distance between the source and focal region was approximately 0.5 m. A 6 dB increase in acoustic pressure was used when extrapolating the TVR data from 1 m to 0.5 m based on experimental measurement. Experiments were done because at this distance spherical spreading can not be assumed because of the close proximity to the source. The Rayleigh length for this source can be found using the equation [76]

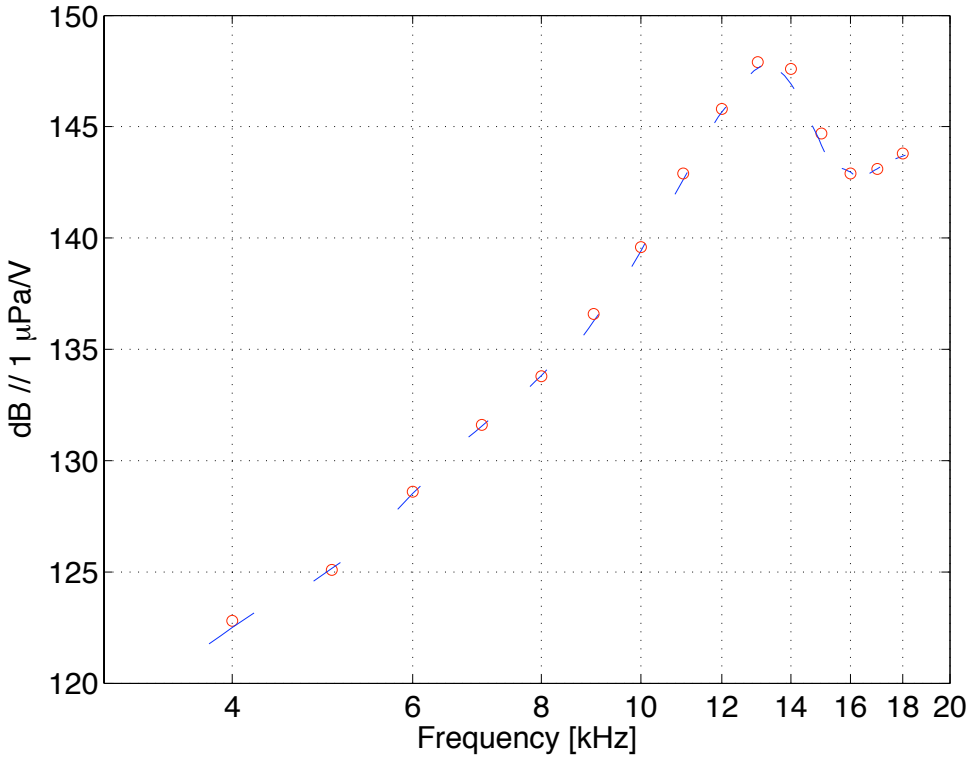

Figure 32: ITC 6135-1 source transducer transmitting voltage response curve at 1 m. The circles and short lines represent different data processing techniques that are discussed in the text.

$$Rayleigh\ Length = \frac{L^2}{\lambda} \tag{42}$$

where L is the total length of the source and λ is the wavelength of the acoustic signal. Using equation (42) with a source length of 0.28 m (11") the Rayleigh length at 4 kHz and 18 kHz are 0.21 m and 0.95 m respectively. Since this range covers values greater than 0.5 m, an experiment was done to measure the sound pressure level increase.

Also observed in figure 32 is a deviation from the 12 dB per decade slope around 6-8 kHz. An approximate point source model was used to investigate possible effects. Indication was that there may be effects due to $ka \approx 1$ around this frequency and also phase difference effects due to arrival of waves originating from the different transducer elements.

To complete the transmitting voltage response investigation the experiments were repeated with the transducer attached to the clamp that they are held by in the array. This was done to determine whether there were any structural resonances being excited in the frequency range of interest. These experiments concluded that there were indeed no noticeable changes in the response due to the presence of the clamp.

4.4.1.3 Power Supply

Twelve amplifiers and matching transformers were used to power the transducer array. Figure 33 shows a photograph of these in equipment racks. Each amplifier had two channels and so one channel was available for each each transducer. The amplifiers were Crown Com-Tech Series CT-810 audio amplifiers (documentation can be found at the manufacturers website, see reference [24]). Since these amplifiers were designed

Figure 33: Photograph showing amplifiers and matching transformers. Each equipment rack contains four of each device stacked on top of each other and alternated.

to drive loudspeakers which have a low impedance, matching transformers were used to improve impedance matching with the higher impedance ceramic transducers. The matching transformers were made by ONYX Power Inc. Appropriate tap settings were determined by experiment.

4.4.2 Triggering the Acoustic Signal

The timing of the signal trigger was crucial. The pressure wave needed to arrive at the array focus at exactly the right time so as to disrupt the cavity as it was being formed and when the projectile was in the focal region. The signal generator was triggered using the measured signal from the first induction coil of the muzzle speed measurement device (See section 4.2.2 and figure 21. In the figure the red curve, "muzzle speed - coil 1", was used as the trigger).

This method was found to be satisfactory with no need to account for variation in the projectile speed within a specific loading configuration. The simpler method of using the firing button trigger was not used because of the inconsistency of the time

between the switch closing and the ignition of the cartridge primer. It was found that the variation was too great to achieve the required accuracy.

4.4.3 Sound Field in a Free Field Environment with a Low Amplitude Sound Pressure

Initial testing of the acoustic source array was conducted in the large water tank test facility at Georgia Tech (12 m length, 6 m width, and 6 m depth (40' x 20' x 20')) and was intended to characterize the sound field and give performance measures of the array in the absence of boundaries. The current section outlines the various tests that were done to this end.

The purpose of the free field testing was to develop a knowledge of array performance in the simplest case so that the specific effects of wall reflections and acoustic cavitation could be identified in later testing. In order to ensure the condition of a free field environment, all data was taken within 2 ms of the beginning of the input signal. Travel time from any source to the nearest boundary (tank wall or free surface) and back in the large tank for the given geometry was approximately 3.5 ms. Maximum peak acoustic pressures at the focus were maintained at a low level ($\sim$16 kPa) so that there were no nonlinear effects due to cavitation.

Photographs of the setup are shown in Figure 34. The left image shows the array suspended above the water line. The right image shows the array located at the center of the test tank. In the center of the array a hydrophone is seen hanging from a three-axis positioner that was used to take measurements of the sound field.

The following sections briefly discuss the method and outcome of these experiments.

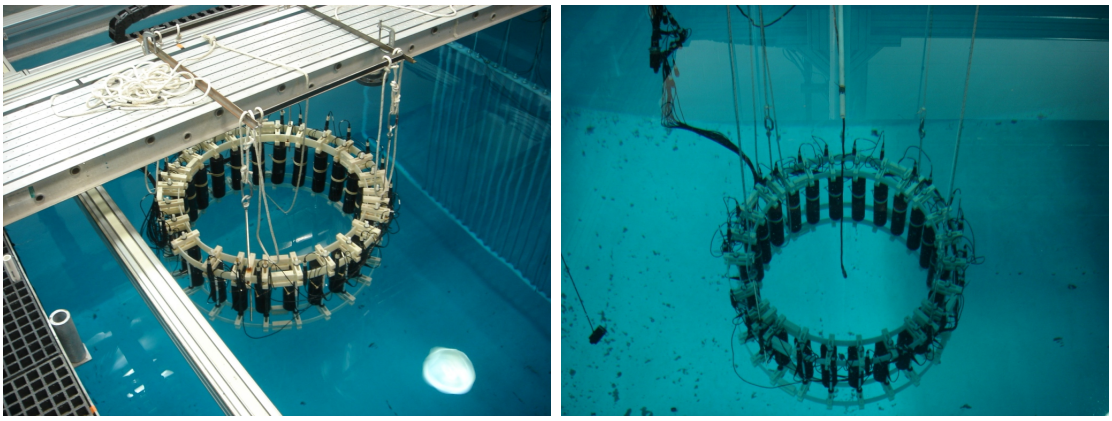

Figure 34: Photograph of acoustic array: top) suspended above test tank, bottom) in test tank with hydrophone shown at array focus

4.4.3.1 Geometric Array Symmetry

To check and quantify the degree of circularity of the array, the time of travel for a pulse from each source to the center of the array was measured. The results are presented in two plots shown in figures 35 and 36. Figure 35 shows the location of the transducers on a polar plot (radial axis is in millimeters: angles are in degrees). The green dot-dash line represents the average radius of 513 mm. Figure 36 shows the radial displacement of each source from this mean radius as a function of angle around the array. Positive displacement was measured radially outward from the mean radius. The two periods of a sine wave evident from the points and shown by the smooth curve in figure 36 indicates that the array was somewhat elliptical in shape. The red circle on the figures shown at approximately 205 degrees represents a transducer that was not operational during these tests. It is marked at being on the average radius in both plots.

The deviations had a maximum of approximately plus and minus 12 mm which is around a tenth of a wavelength near the transducer resonant frequency. For the purposes in this study it was not deemed necessary to adjust the radii of the individual

sources further to achieve any greater a degree of geometric symmetry.

4.4.3.2 Measure of Array Focus and Tuning

Another aspect of the array symmetry was the degree to which the pressures add at the focus. This measure determined the accuracy with which the array needed to be tuned and indicated any loading effects between the sources that may have affected the overall output. The variation in distance to the focus was shown in the previous section to be around a tenth of a wavelength in the worst case. Therefore, one would expect less than perfect addition but only a small impact on the peak pressure attained.

Sources in the array were first driven individually, and then all sources were driven together in parallel using one amplifier. A comparison plot is presented in figure 37 which shows the pressure at the array center divided by input voltage to the source in decibels as a function of frequency. The blue curve (solid line) shows the sum of the pressure to voltage ratio for all the sources driven individually, one at a time, and the red curve (dashed line) shows the measured result for all sources driven together.

It can be seen that, although there is some variation, the curves follow each other with a difference of no more than 1 dB at any point in frequency range shown; in particular, the curves are almost identical around the intended operating frequency of 12 kHz. This indicates that the circularity of the array was sufficient in the frequency range shown (It is noted that the maximum frequency investigated here was only 14 kHz which did not reach the maximum used in experiments. This was because the 17.5 kHz experiments had not been anticipated at the time of measurement.). With no loading effects (that is, the pressure signal from neighboring sources affecting the response of a transducer) one might expect the red dashed line to always be below

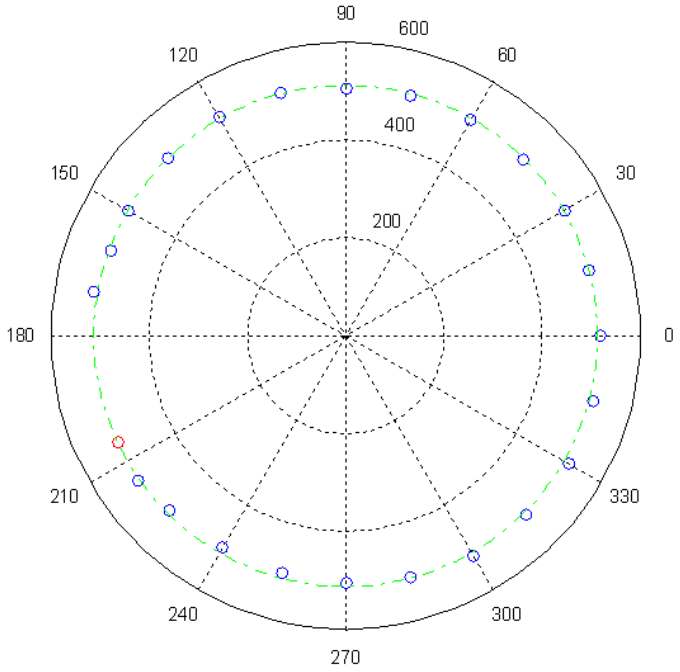

Figure 35: Plot showing measured array symmetry. Green (dot-dash) line represents the average radius of 513 mm. Radial axis is in millimeters. Angles are in degrees. The source at 205 degrees was not operational and so is taken to be on the average.

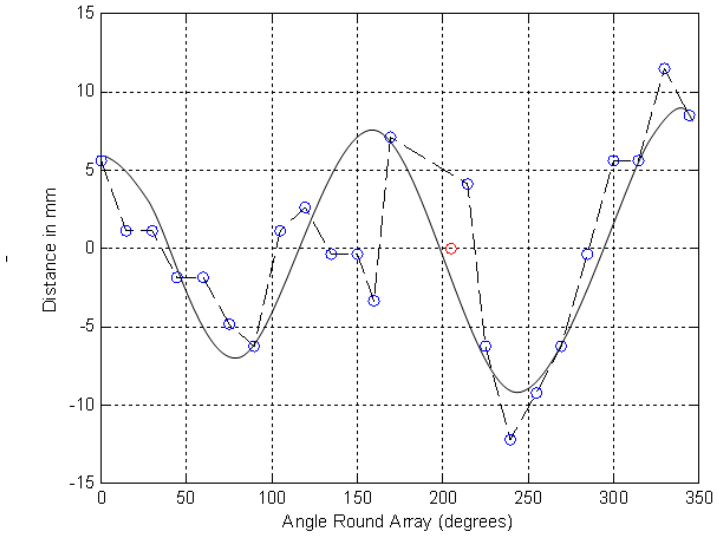

Figure 36: Plot showing the distance of each source in the transducer array from the average radius of 513 mm. Positive distance is measured radially outward from the average radius. The source at 205 degrees was not operational and so is taken to be on the average.

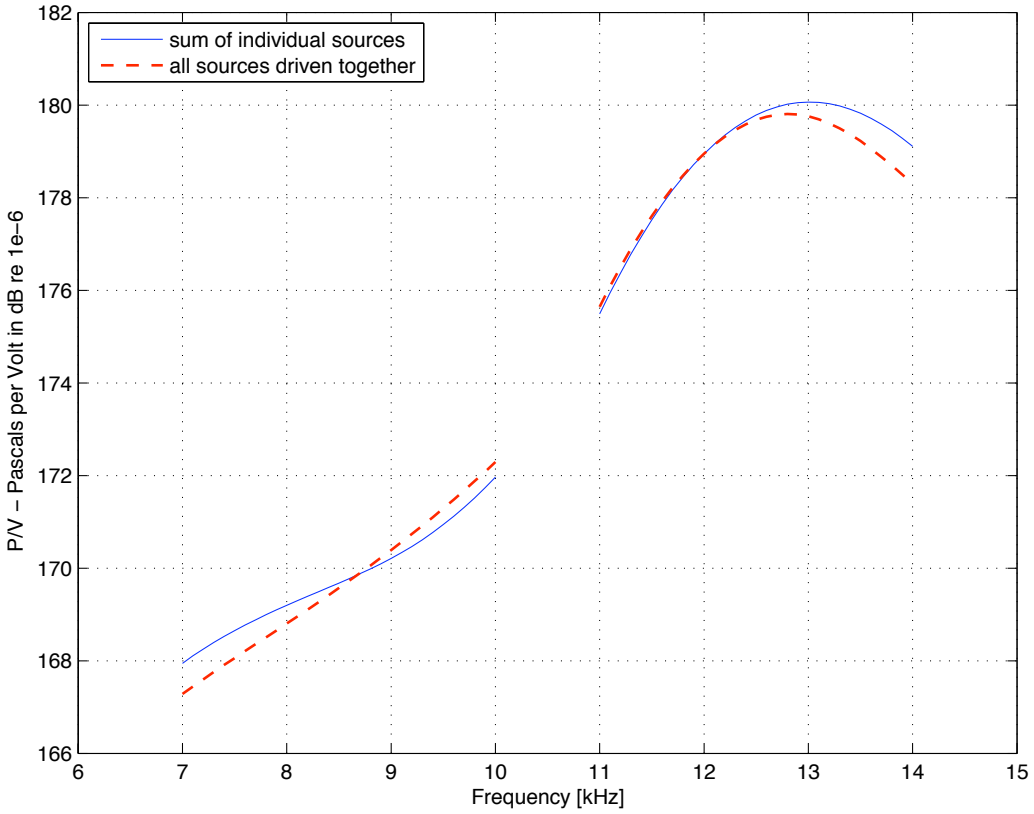

Figure 37: Plot showing a comparison between the array voltage response with all sources driven together and the sum of pressures from individual sources

the blue solid curve, however, this is not the case. There were potentially some loading/interaction effects. It is seen that between 8.7 kHz and 12.0 kHz the sum of the sources driven individually was below the value attained with all sources driven together.

4.4.3.3 Sound Field

The sound field produced near the center of the array in the focal region in both the horizontal plane and in the vertical direction along the flight path were of interest. The size of the focal region in the direction along the flight path was important because it determined the length of the section of flight path in which a high pressure could be imposed on the cavity. It also determined the accuracy needed in the timing of the signal generation so that the desired acoustic pressure would be present while the projectile was within the focal region. The size in the horizontal plane perpendicular to the flight trajectory was of interest because it determined the accuracy with which the projectile needed to be fired through the center of the array in order to ensure that a certain amplitude of pressure was present.

The reference frame that was be used to describe the pressure field in all of the measurements taken with the array in a free-field environment is shown in figure 38. The hydrophone was first moved along the z - axis and pressure readings were taken at 0.5 cm intervals and for a range of frequencies. Identical measurements were then taken along the x - axis. Finally, the hydrophone was moved through a grid of points in the x - z plane, this time only at a frequency of 12 kHz. The following describes the recorded sound field and presents measurements of the size of the focal region.

Measurements taken on the z - axis:

Figure 39 presents a compiled plot of the results of a scan on the z - axis from 4 kHz

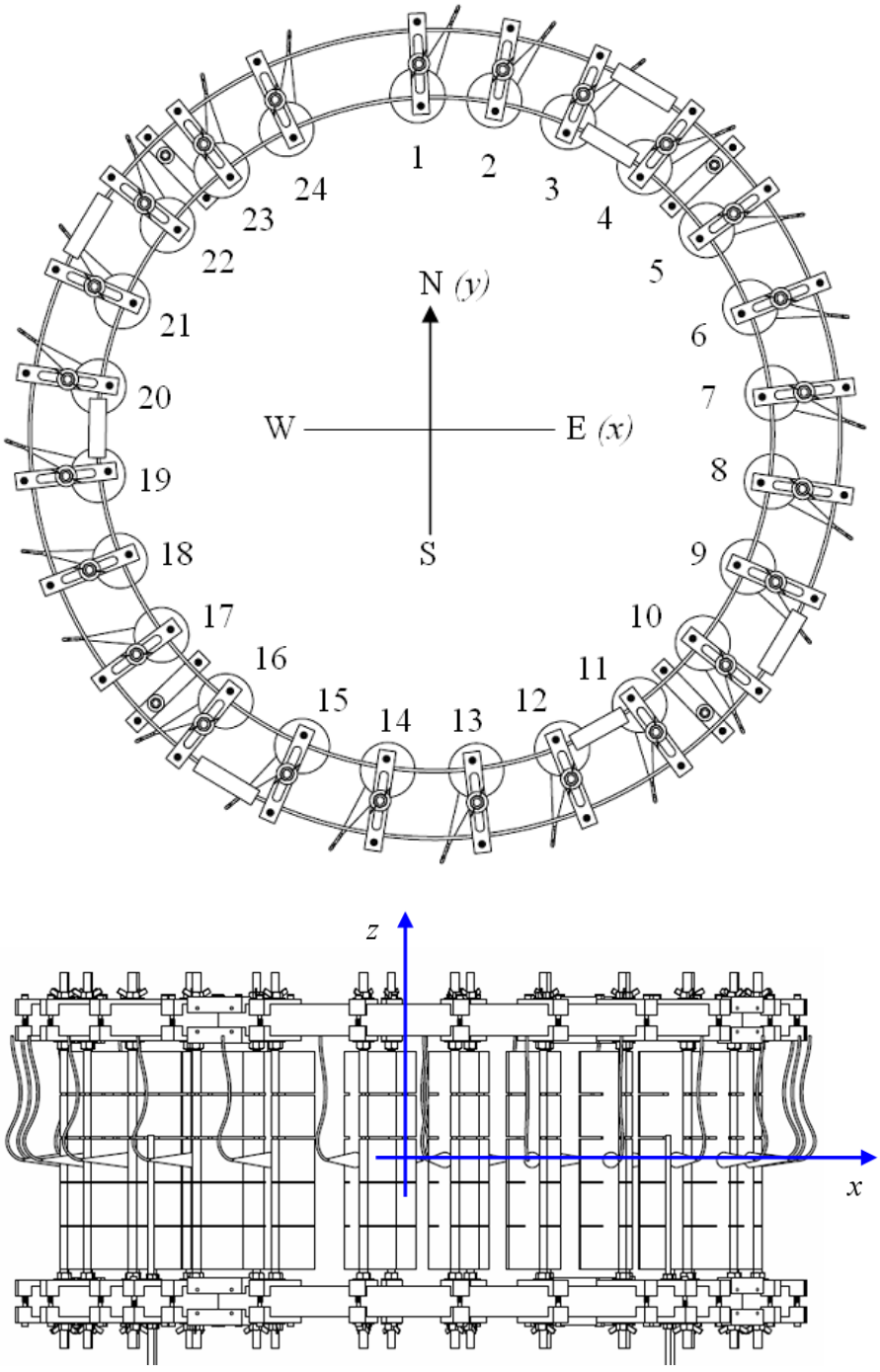

Figure 38: Schematic showing the reference frame and array geometry for free environment testing

to 18 kHz. The scan started at a location 45 cm above the array center, which was close to where the muzzle speed measurement device was during the supercavitation experiments, and ended 25 cm below the array center. The plot serves to show the amplitude variation in the direction of the flight path and the degree of symmetry about the x - y plane. Symmetry about the x - y plane was expected because the sources and the array were symmetrical about this axis and the measurements were taken in free-field conditions.

Measured at the points 3 dB down from the peak amplitude, the size of the focal region ranged from 25 cm at 7.5 kHz to 13 cm at 17.5 kHz. At 12 kHz the size was 17 cm. The maximum amplitudes at 7.5, 12, and 17.5 kHz were 167.8, 178.1, 175.7 dB ($\mu Pa/V$) respectively.

Measurements taken on the x - axis:

Figure 40 presents a compiled plot of the results of a scan on the x - axis from 6 kHz to 17 kHz at the vertical center ($z = 0$). The scan started at a location on the x - axis of $x = -25$ cm and ended at $x = 25$ cm. This plot serves to show the amplitude variation perpendicular to the direction of flight and the degree of symmetry about the y - z plane. Symmetry about the y - z plane was also expected because the array itself was almost symmetrical about this plane. There was a slight asymmetry due to the asymmetry of the source distribution that, as mentioned previously, was necessary to allow viewing of the focal region from the side.

In this direction, measured at the points 3 dB down from the peak amplitude, the size of the focus ranged from 7 cm at 7.5 kHz to 3 cm at 17.5 kHz. At 12 kHz the size was 5 cm.

Measurements taken on a grid in the x - z plane:

A scan in the x - z plane was done at 12 kHz to investigate the off-axis field. A

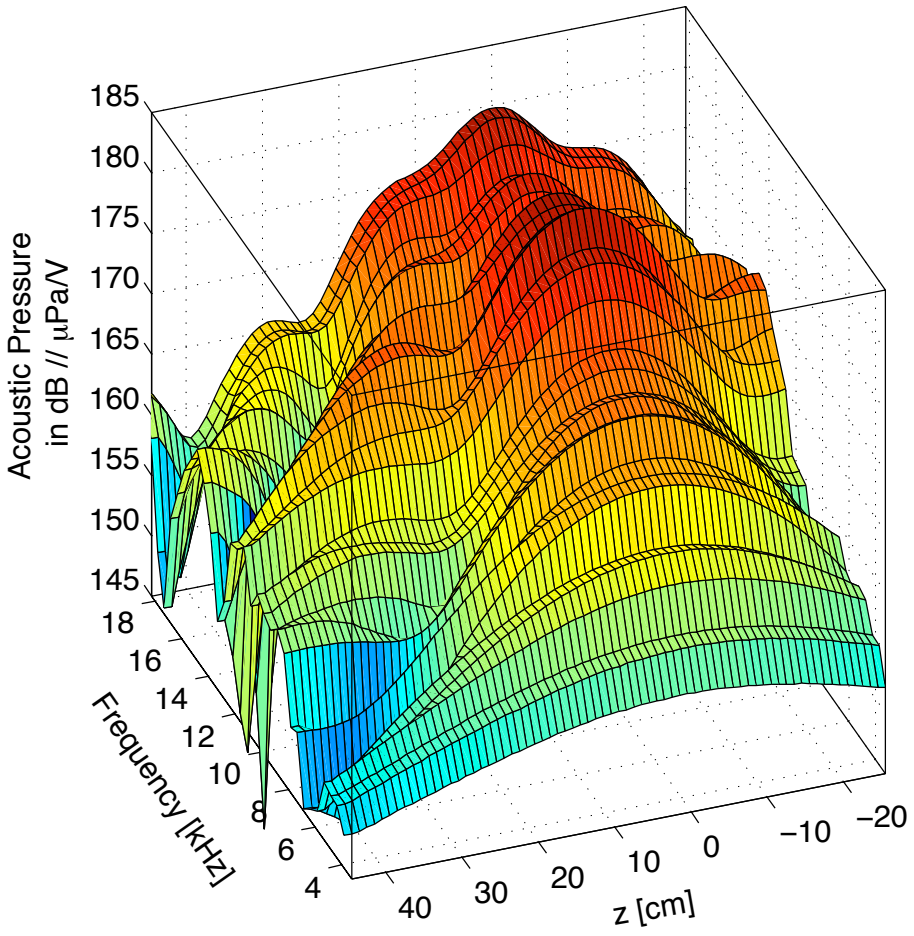

Figure 39: Plot of the acoustic pressure amplitude along the z-axis for the array in a free-field environment.

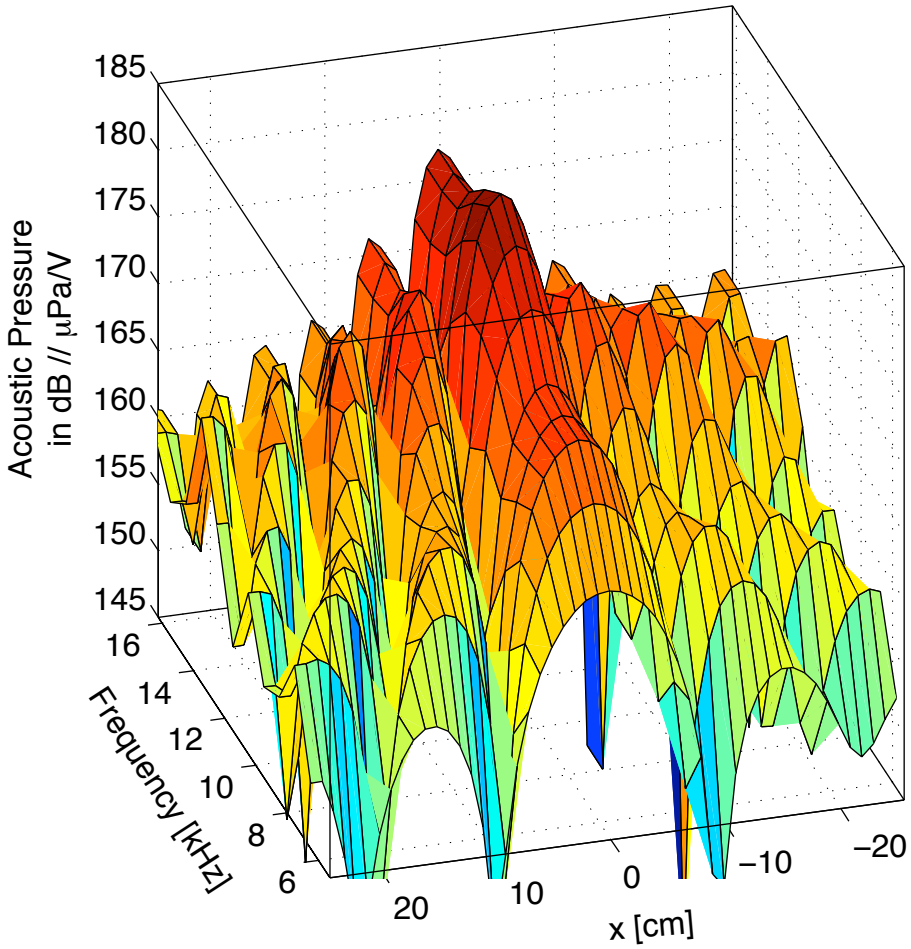

Figure 40: Plot of the acoustic pressure amplitude along the x-axis for the array in a free-field environment.

compiled plot of the results is shown in figure 41.

The plots presented show that the array behaved very much as one would expect. Pressures were largest at the geometric center of the array and the focus reduced in size with increasing frequency, both in a horizontal and the vertical directions. The radial distance from the peak to the first minimum was approximately a quarter wavelength (in fact slightly larger due to the slight asymmetry of the array discussed in a previous section). It was also evident that the presence of other sources in the array and the array structure its self did not significantly affect the pressure magnitudes at the array focus at the frequencies of interest. This was evidenced by the fact that the sum of the pressures from the individual source TVR curve in figure 32 gave an almost identical pressure amplitude as that measured for the array. At 12 kHz the individual source TVR reads 146 dB at 1 m. Transferring this to 0.513 m we add 5.8 dB and get 151.8 dB. Then there are 23 sources, so add another 27.2 dB and get 179 dB. For the array measurements at 12 kHz both the curves in figure 37 show 179 dB at 12 kHz and figures 39, 40 and 41 show 178 dB.

Table 4 in section 4.4.5 presents a summary of the numerical results found in this section that describe the important features of the sound field for this research work.

4.4.4 Sound Field in the Confined Environment with a Low Amplitude Sound Pressure

Measuring the sound field at low pressure levels in the small tank was done to determine the effects of the wall reflections. The goal was to describe and quantify the changes in the field from the free-field experiments (section 4.4.3.3). The most interesting question for the purpose of this work, that is, with the goal of achieving the maximum possible pressure amplitude at the array center, was how much of an increase in sound pressure level can be gained by taking advantage of constructive

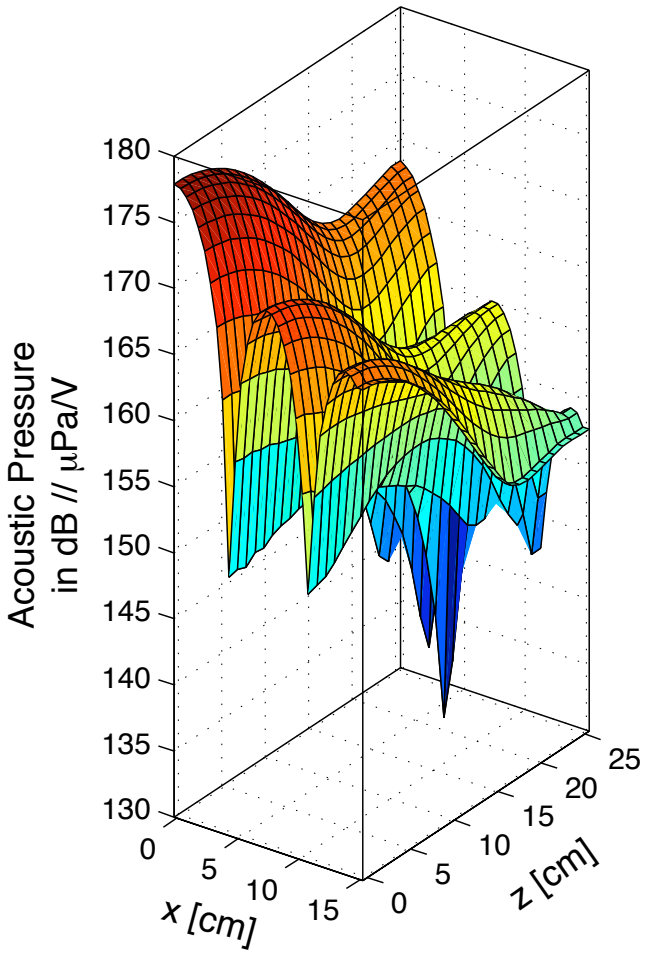

Figure 41: Plot of the acoustic pressure amplitude along the x and z-axes for the array in a free-field environment at 12 kHz.

interference of the direct and wall reflected signals?

4.4.4.1 Configuration

Building on section 4.4.3, the array was now placed inside the small test tank in which the projectiles were to be fired (see section 4.1.2 and figure 13 in section 4.1.1). Photographs of the array situated in the empty water tank are shown in figure 42. The left image shows a view looking down into the tank. The device in the foreground in the top left is one track of a two axis positioner system that was mounted above the tank and was used to sweep the hydrophone through the sound field. The image on the right shows a view looking through one of the tank windows at the array center with a hydrophone hanging from the positioner arm. A schematic of the of the array in the tank viewed from the top is shown in figure 43. This figure depicts the coordinate system that was used when describing measurements taken with the array in the confined environment. The two-axis positioner allowed for movement on the vertical axis ($z - axis$) and one horizontal axis (y - axis). Once installed, the positioner could not be reoriented to scan on a different horizontal axis.

The proximity of the array to the tank wall, the tank bottom and the free surface were measured and had the following values:

- Average distance to exterior tank wall from center of source: 15.4 cm (6.05")
- Distance from the center of the array to the tank bottom: 55 cm (21.7")
- Distance from the center of the array to the water surface: 65 cm (25.6")

These are shown on the diagram in figure 44 along with travel times for an acoustic pressure wave along the various paths from a source to the hydrophone.

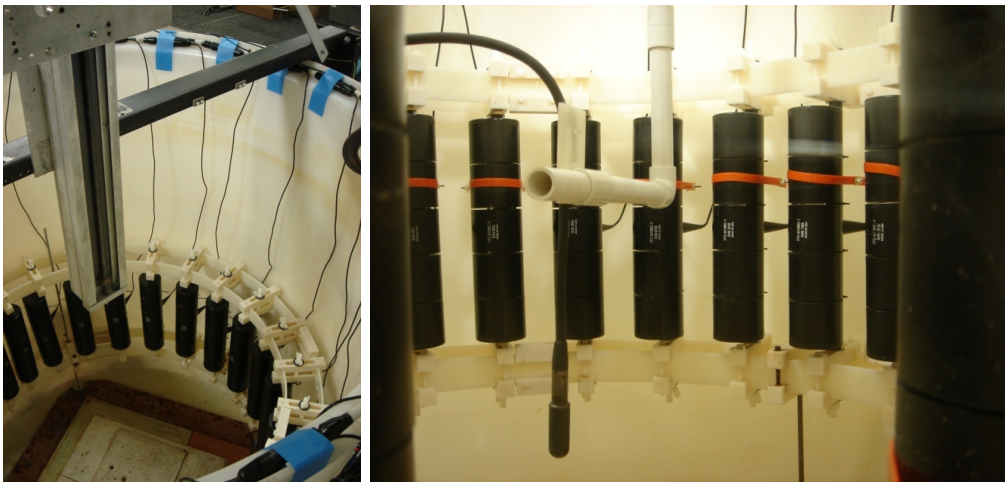

Figure 42: Photograph of the transducer configuration in the experiment tank. Left) view looking down into the tank, right) view looking through one of the tank windows at the array center.

4.4.4.2 Sound Field

As was done in the free-field environment experiments, measurements were taken at intervals along the z - axis (vertical direction through the array center) for a range of frequencies followed by measurements along the y - axis (horizontal direction) with the same frequency range. Finally, the hydrophone was moved through a grid of points in the y - z plane, again only at a frequency of 12 kHz.

Reflected signals from the tank wall interfered with the direct signal when the duration of the input pulse was long enough. In the frequency domain, the nature of the interference was dependent on frequency. Some frequency components interfered constructively and some destructively. For short duration pulses the nature of the interference depended on the delay time between pulses.

If it is assumed that the tank wall can be approximated as a pressure release surface then, for a continuous wave signal, constructive interference will occur when the radial distance between the sources and the tank wall is an odd number of quarter

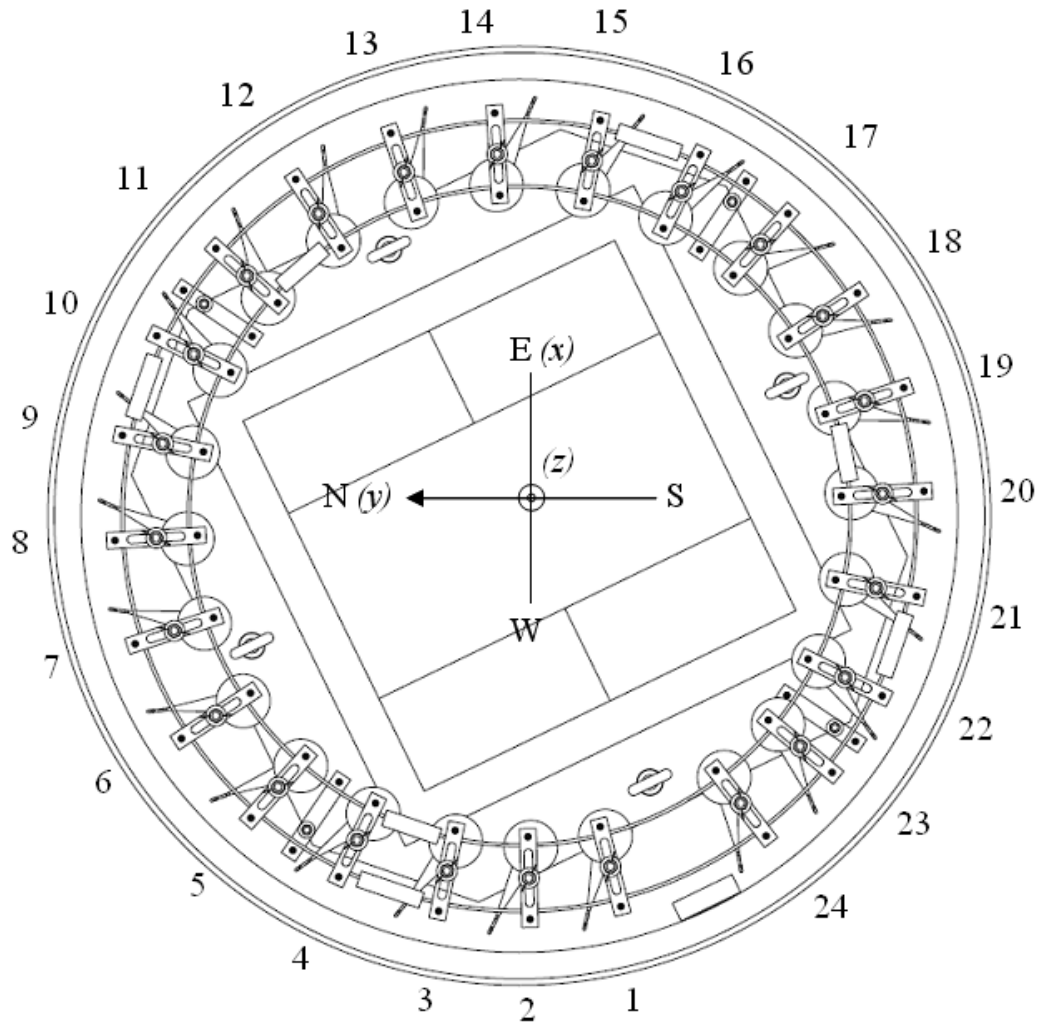

Figure 43: Top view schematic of the transducer configuration in the experiment tank. Also shown is the reference frame that is used to describe the sound field on all confined environment testing. The viewing window is seen between transducers labeled 1 and 24. The backstop is also shown on the tank bottom.

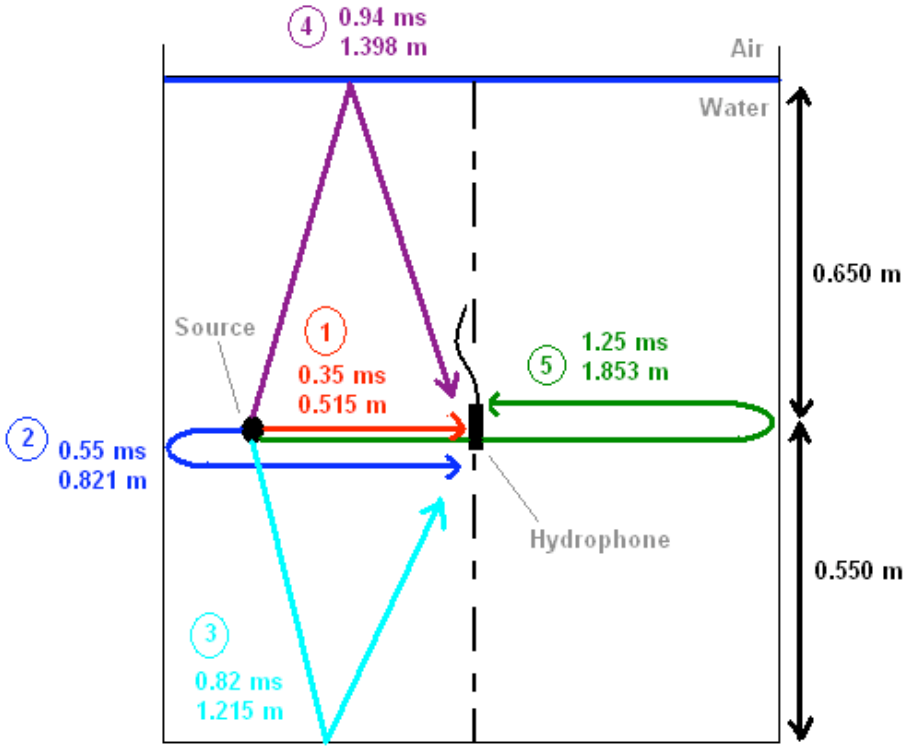

Figure 44: Diagram showing the location of the center of a source relative to the tank wall, bottom and water/air interface. Also shown are travel times for a pressure wave along the various paths from source to hydrophone labeled one through five.

wavelengths. With a distance of 15.4 cm between the source center and the tank wall, the optimum frequencies for constructive interference in the relevant frequency range were calculated to be 7.2 kHz, 12.0 kHz, and 16.9 kHz.

Figure 45 presents a compiled plot of the results of a scan on the z - axis from 3.5 kHz to 18.5 kHz. The scan started at a location 35 cm above the array center and ended 35 cm below. The constructive and destructive interference pattern is seen as a sinusoidal trend in the curve along the frequency axis. Constructive interference peaks are seen at 7.5 kHz, 12 kHz and 16.5 kHz with destructive interference troughs in between. These values are in agreement with those calculated based on measured dimensions that were mentioned earlier. Measured at the points 3 dB down from the peak amplitude, the size of the focal region ranged from 28.5 cm at 7.5 kHz to 11 cm at 17.5 kHz. At 12 kHz the size was 17.5 cm. The maximum amplitudes at 7.5 kHz, 12 kHz, and 17.5 kHz were 172.3 dB, 181.4 dB and 177.7 dB (dB // μPa/V) respectively. All of these values are summarized in table 4 along with those from the free-field environment experiments. Amplitude gains that were achieved at the 7.5 kHz, 12 kHz and 17.5 kHz were 4.5 dB, 3.3 dB and 2.0 dB respectively. Possible explanations for this trend of decreasing gain are: that the presence of the transducers is more apparent to the reflected signal from the tank wall at higher frequencies so that there is more scattering, and the fact that the reflecting surface is curved causes different parts of the reflected signal to interfere.

The record length of the sound pressure analyzed was 0.6 ms for producing the plots in figure 45. It is important to understand the major contributing factors to the field during that time because there are scattered signals of significant amplitude present due to the close proximity of reflecting surfaces. The roundtrip distance from the source to the wall and back was 0.308 m on average which corresponds to a 0.208 ms travel time (see figure 44). The pulse used in these experiments was 0.4 ms

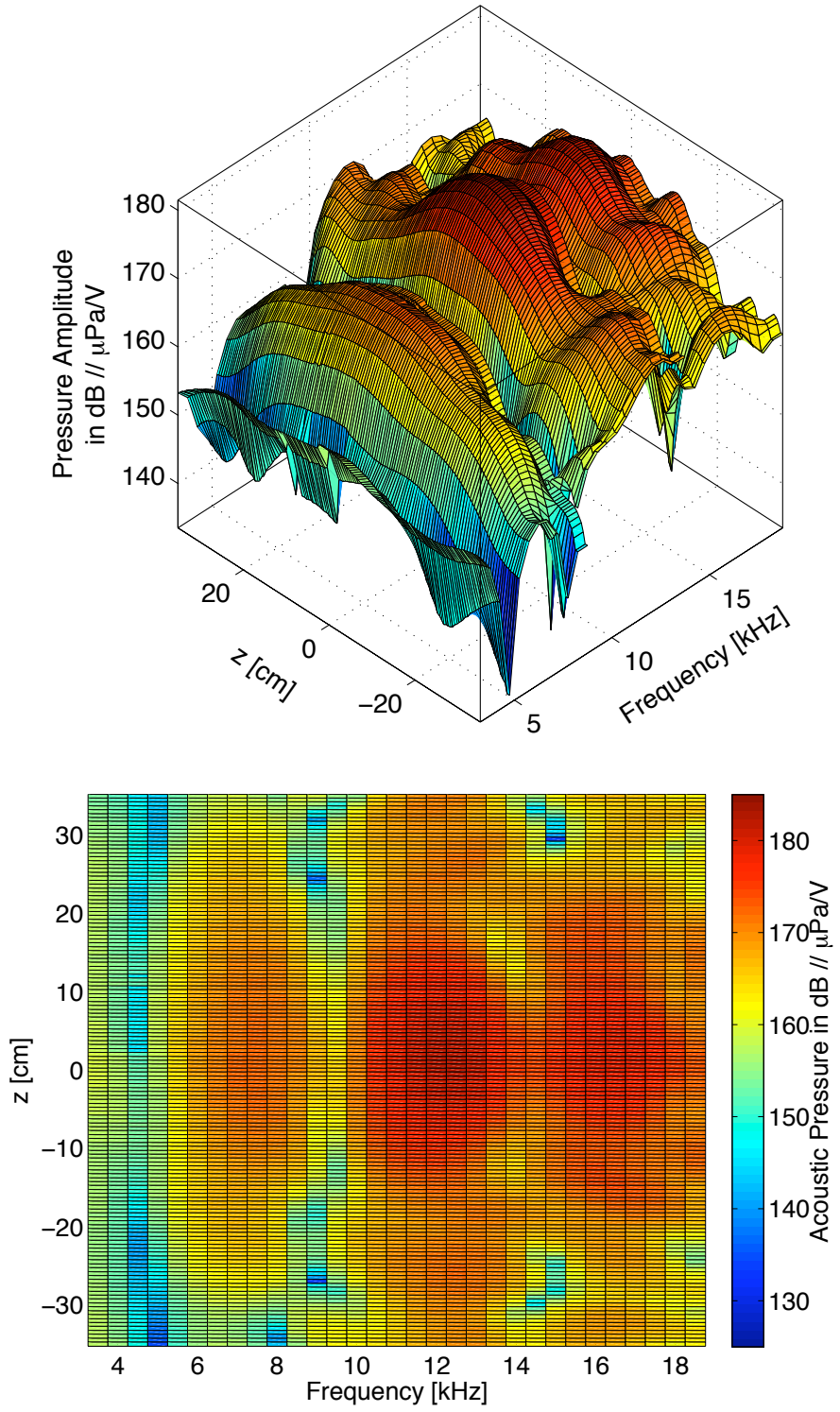

Figure 45: Plot of the acoustic pressure amplitude along the z-axis for the array in the confinement of the water tank. The record length is 0.6 ms.

in duration. Therefore, analyzing a recorded signal of 0.6 ms duration after the arrival of the beginning of the direct signal at the hydrophone captured the entire direct and reflected signals. Reflections from the tank bottom began to arrive 0.13 ms before the end of the 0.6 ms recording but reflections from the free surface and from the opposite side of the tank did not arrive within the recording. The amplitude of the bottom reflections was much smaller than those from the tank walls, however, because the sources did not emit as high an amplitude off-axis and the surface was flat, not concave like the tank wall and therefore had no focusing effect.

To illustrate the interference peaks and the difference in amplitude between the confined environment and the free-field environment cases, a plot was produced that shows the peak amplitude measurements for each case for a range of frequencies at the location $z = 0$. The plot is shown in figure 46.

The trends already discussed are clearly seen in this figure. Gains were made of up to around 5 dB at low frequency. As the frequency increased, the gain in amplitude that could be achieved using wall reflections reduced. The wavelength of a 7 kHz signal in water is 21.2 cm and at 17 kHz is 8.7 cm. So for the higher frequencies in the range of interest the wavelength was becoming similar to the dimensions of the sources and so there was more scattering of the reflected signal from them.

In order to clarify further the effect of the wall reflections, some time domain plots were investigated. An experment was done with longer duration gated sine wave input signals. The duration was chosen to be the longest possible that could be sustained without including reflections from the opposite side of the array in the measured response. Pulses were used with frequencies ranging from 6 kHz to 18 kHz in 1 kHz intervals. Two recorded signals are shown in figures 47 and 48 for 12 kHz (constructive interference) and 14 kHz (destructive interference) respectively. In these plots, the cyan shaded patch highlights the direct signal. The vertical red dashed

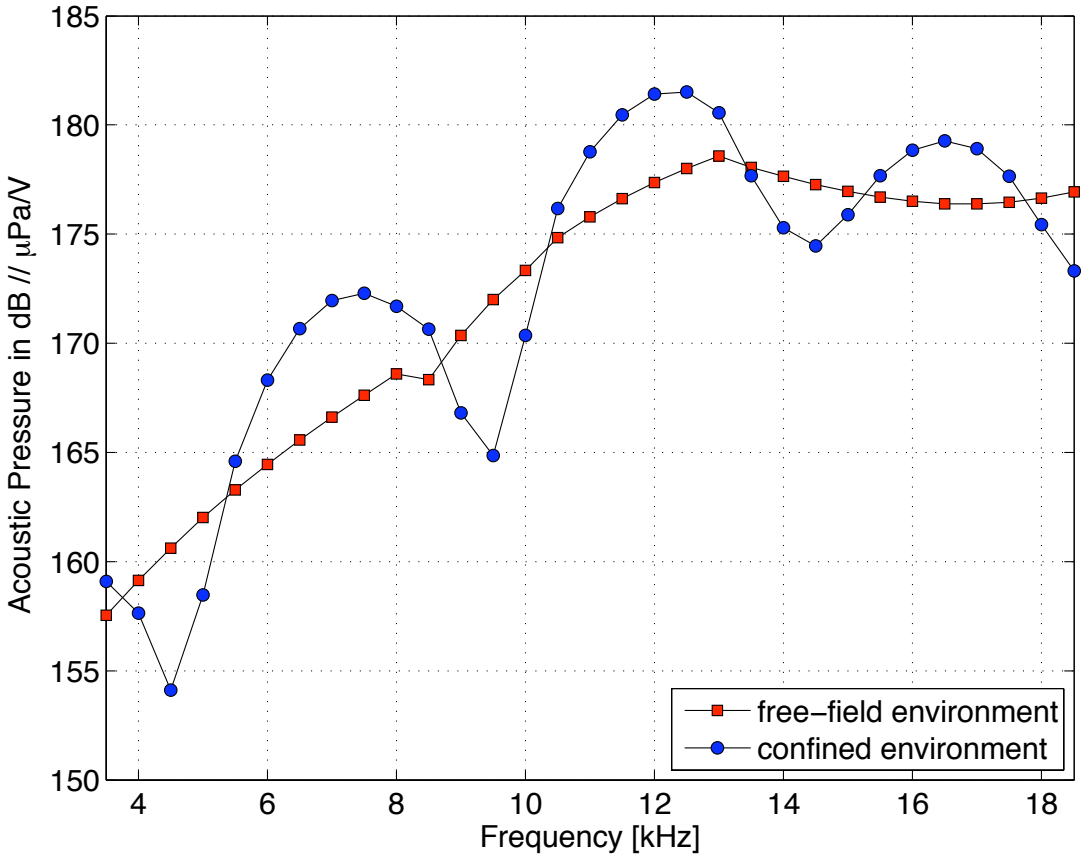

Figure 46: Maximum sound pressure amplitude comparison plot between free and confined environment cases. Peak amplitude at the location $z = 0$ versus frequency.

lines in the lower plot of each figure indicate the beginning and the end of the wall reflection based on the measured distance and the speed of sound in water (1481 m/s at 20° C [11]). The changes in the signal amplitude at these highlighted points is clear. In figure 47 the increasing amplitude when the reflected signal arrives and the reduction in amplitude when the direct signal ends are evident.

For the case of constructive interference (figure 47), the measured signal grew, firstly due to the transient period as the source amplitude built up close to resonance, then because of interference of the reflected signal from the tank wall with the direct signal that was still being produced by the source. The amplitude then dropped as the direct signal ended and then continued to decrease when the reflected signal ended and the ringing of the source died out. The result was that the signal amplitude was changing with time. Therefore, during the experiments when the projectiles were fired through the sound field, they were subject to a signal that had changing amplitude over time. This may have had consequences on the ultimate alteration in shape of the supercavity because cavity sections produced at different times were subject to different pressure amplitudes.

4.4.5 Summary of Sound Field Results for Linear Acoustic Amplitudes

The results of sections 4.4.3 and 4.4.4 are summarized in table 4. This summary highlights the important findings. The frequencies reported are those that were be used for the experiments in chapter 5.

It has been shown that the array was successfully tuned to take advantage of the wall reflections at the desired operating frequency of 12 kHz and that a gain of slightly over 3 dB was possible at that frequency. The next higher and lower frequencies that also take advantage of the wall reflections have been identified and confirmed to be

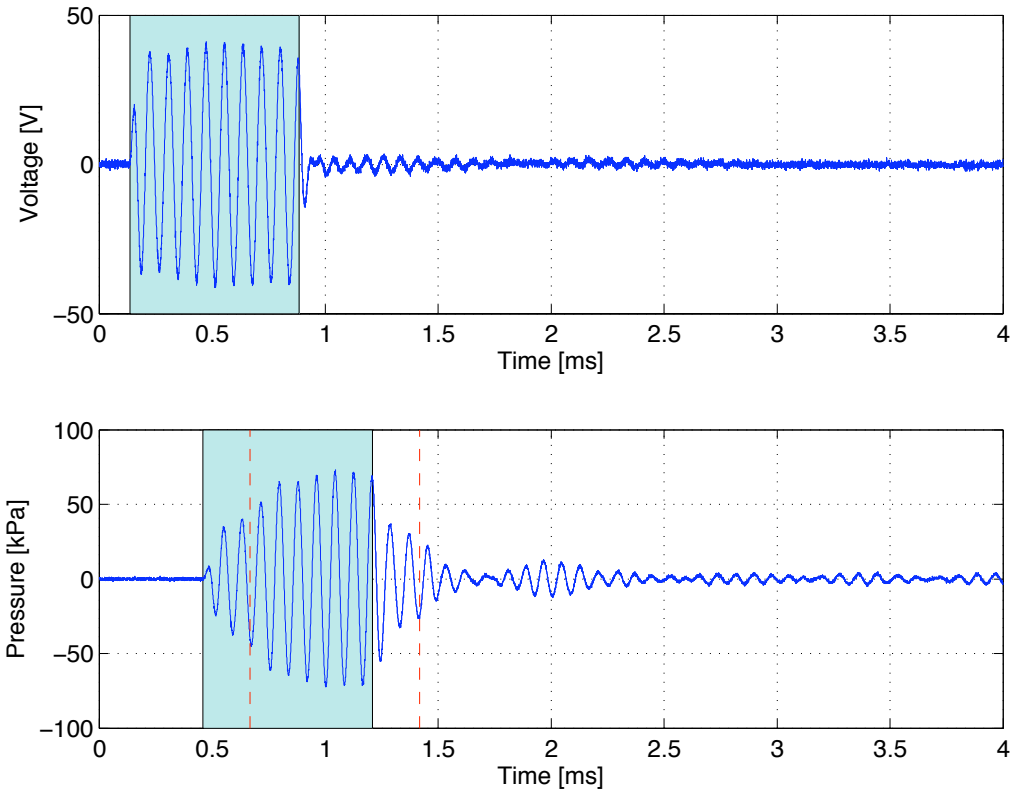

Figure 47: Plot showing recorded signals at the array center in the confined environment showing the effects of constructive and destructive interference between the direct and reflected signals at 12 kHz. Top plot shows a sample of the voltage out of one power amplifier. Bottom plot shows the recorded pressure at the array focus.

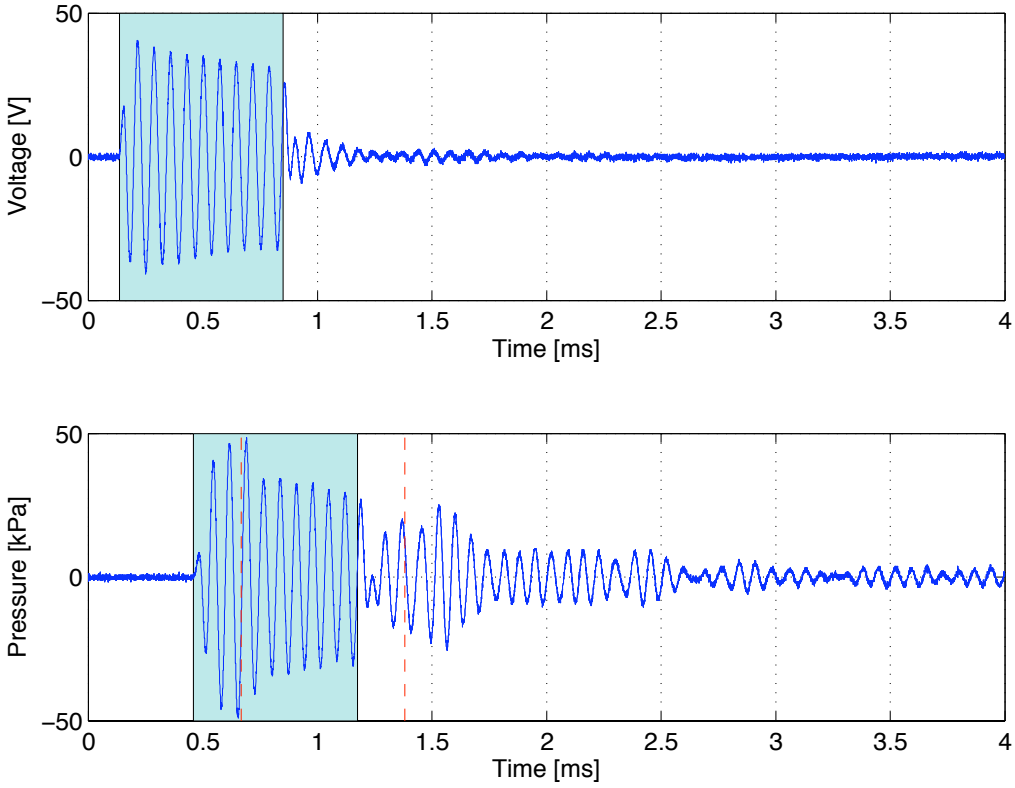

Figure 48: Plot showing recorded signals at the array center in the confined environment showing the effects of constructive and destructive interference between the direct and reflected signals at 14 kHz. Top plot shows a sample of the voltage out of one power amplifier. Bottom plot shows the recorded pressure at the array focus.

at the values expected when the wall was treated as a pressure release surface.

The size of the focal region has also been quantified.

Table 4: Summary of the array focal region in a free-field environment. The size of the focal region is the distance where where P/V is greater than the maximum amplitude minus 3dB

	Frequency		
	7.5 kHz	12 kHz	17.5 kHz
Free-field environment			
Maximum amplitude (P/V ref. 1 μPa/V)	167.8 dB	178.1 dB	175.7 dB
Size of focal region in z - direction	25 cm	17 cm	13 cm
Size of focal region in x - direction	7 cm	5 cm	3 cm
Confined environment			
Maximum amplitude (P/V ref. 1 μPa/V)	172.3 dB	181.4 dB	177.7 dB
Size of focal region in z - direction	28.5 cm	17.5 cm	11.0 cm
Size of focal region in x - direction	8.5 cm	4.5 cm	3.5 cm
Comparison			
Amplitude Gain	4.5 dB	3.3 dB	2.0 dB

4.4.6 Sound Field in the Confined Environment with a High Amplitude Sound Pressure

Building on, and using results from section 4.4.4, high amplitude acoustic signals are investigated in this section. Based on a linear extrapolation with the TVR data and the measured voltage level on the output of the power amplifiers we expected to be able to attain acoustic pressure levels of between five and six atmospheres. At pressure levels of this magnitude acoustic cavitation was almost inevitable in water that has not been degassed or specially prepared. The goal of the work in this section was to determine what effect the acoustic cavitation had on the pressure signal at the array focus. Also, we wanted to determine the threshold pressure amplitude for acoustic cavitation to be observed.

The pulse used in this investigation was a 0.7 ms duration gated sine wave. The reason

was that with this pulse shape we were able to achieve the maximum amplitude sound pressure available by passing the initial transient and taking advantage of the wall reflections. The frequency chosen to produce high amplitude pressure was 12 kHz. The reasons for this were stated previously and are summarized here. The set up was designed for this operating frequency because the source transducer resonance was around 13 kHz, as seen in figure 37, and so at 12 kHz the output was high. Consequently, the array was installed such that wall reflections were in phase with the direct signal at 12 kHz, and the matching transformers were set to maximize the output around this frequency. Figure 47 in section 4.4.4 shows a measurement of the pressure at the array center using this pulse.

The input was ranged from a low level to maximum amplitude with a 60 dB dynamic range. Maximum input was determined by the output distortion light on the amplifier. This light indicated when a channel's output waveform differed from its input by 0.05% or more [24]. The gradual increase in amplitude facilitated the detection and classification of nonlinear effects. It was expected that, with the predicted pressure levels, cavitation would occur during the negative pressure peaks. Cavitation should be detectable by observing an abrupt change in the wave-form over a small change in pressure amplitude, whereas other nonlinear effects should appear more gradually as the pressure amplitude is increased. This change can be detected by spectral changes in the measured signal as discussed in section 2.2.2.

Figure 49 shows the pressure reading at the center of the array to give an idea of what the signal looked like and the actual pressure amplitudes that were being produced. The input levels displayed (shown in the figure legend) were chosen to show sufficient information without over populating the plot window. The levels are shown in attenuation steps of 2 dB from the maximum, with 5 dB introduced to give more resolution in the transient cavitation transition region, and 25 dB shown as the low

level, linear standard.

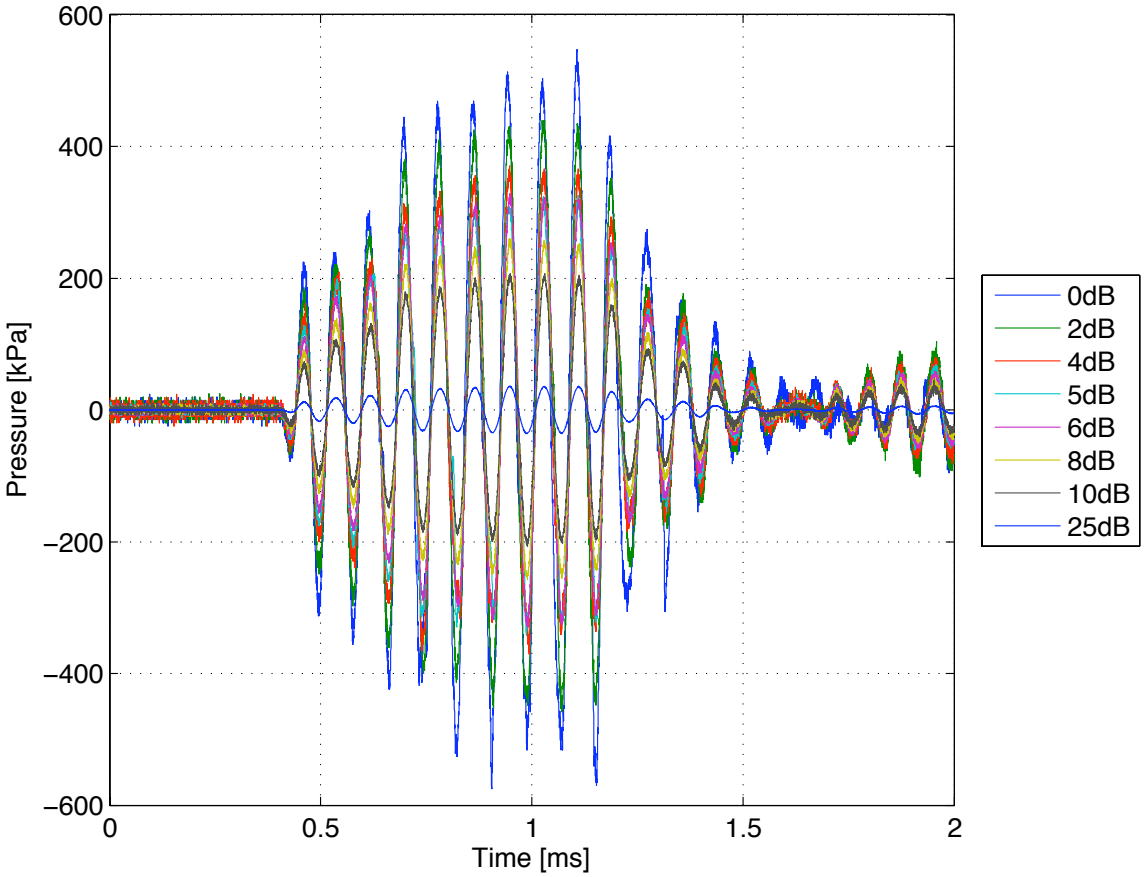

Figure 49: Plot showing the pressure signal at the array center in confined environment testing. 25 dB dynamic range with 0 dB being the maximum possible level without amplifier distortion.

It was informative to look at the signals with a normalized amplitude. By doing so, if everything in the system were behaving in a linear manner, then all the plots should be on top of one another. Nonlinear effects could then be detected by changes in shape or level of the recorded pressure signal. It was possible for nonlinearities to occur anywhere in the system, namely in the power amplifier or in the acoustic medium, therefore, the signal going into and out of the amplifier were also recorded. It was determined that nonlinearities in the water medium were highly dominant.

Figure 50 shows the beginning of a pressure record at the array center, with the

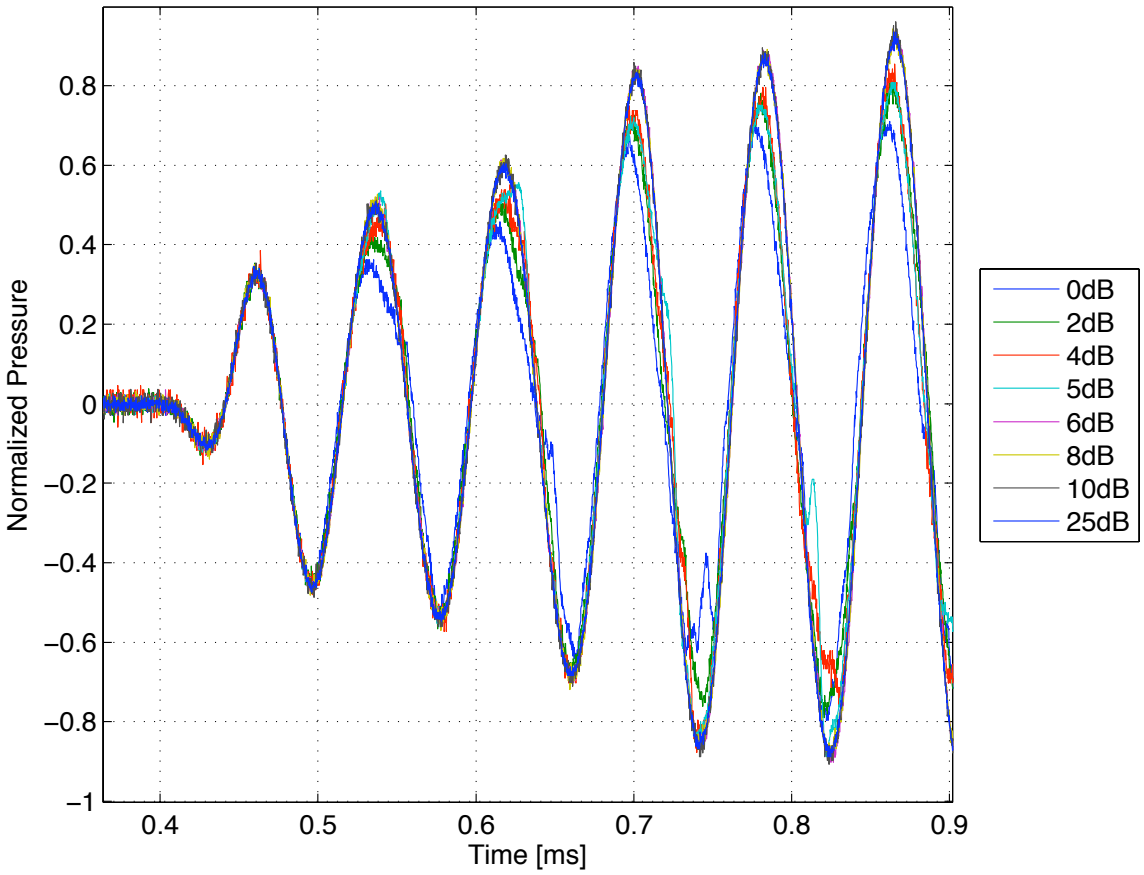

Figure 50: Plot showing the pressure, normalized to a maximum amplitude of one, at the array center in confined environment testing. 25 dB dynamic range with 0 dB being the maximum possible level without amplifier distortion.

vertical axis scaled so that the peak absolute value of the pressure was normalized to one. It can be seen here that for 6, 8, 10 and 25 dB attenuation, the traces do indeed lay very closely on top of one another. However, at 5 dB attenuation and lower, the signals no longer behave in this way when the acoustic pressure amplitude is increased. The negative peaks are seen to be very uneven which is believed to be due to cavitation. It is also noted that when there was a train of identical pulses in half second intervals those negative peaks were noticeably different on subsequent pulses. This implies that there was some lasting effect on the medium between one pulse and the next or that the phenomenon occurred very differently each time; cavitation would also explain this behavior. Cavitation effects are transient phenomenon and the spacing in time of the transients are varied. In particular, for nonlinear pulsating of bubbles, transients can be widely spaced especially close to the threshold of cavitation and at low frequencies [69]. The transients of true *transient cavitation* are very short in duration, occurring within one acoustic period. The explanation of lasting effects in the amplifier, which can be a result of driving beyond the operating limits, was eliminated by measuring the output on each amplifier in turn as the phenomenon was being observed on the pressure trace.

Detection of acoustic cavitation was discussed in the literature review, section 2.2.2; a more detailed discussion can be found in reference [70]. The dynamics and non-linearities of acoustic cavitation are known to produce harmonic components in the pressure spectrum (harmonics of the drive frequency) as well as subharmonics and broad band noise [43]. The threshold is largely dependent on the condition/purity of the medium, that is, whether there are existing bubbles or solid particles in liquid, and the level of dissolved gasses. The medium in this experiment was tap water that was filtered with an aerating filter and left to settle to allow larger bubbles to rise to the surface before measurements were taken. A higher concentration of nuclei permits cavitation at a lower amplitude acoustic signal.

Looking back at figure 49 it is seen that the pressure amplitude at which the negative peaks are beginning to be affected is around -350 kPa.

Figure 51 shows the amplitude of the frequency components in the signal plotted in figure 49.

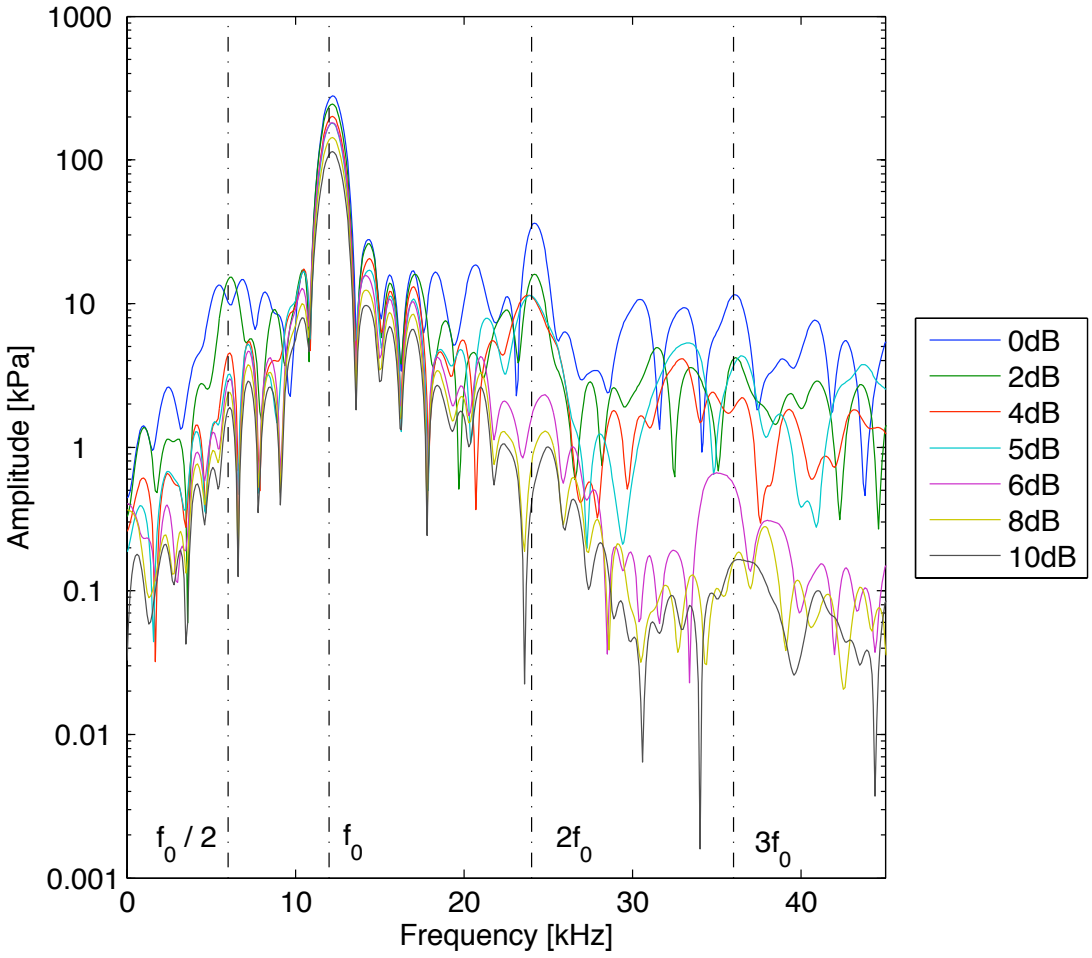

Figure 51: Plot showing the frequency content of recorded high pressure signals in confined environment testing

It can be seen in this figure that there was a change in the frequency content as the drive level was increased. Looking at the figure it is seen that at around 5 dB attenuation the high frequency noise increases and harmonics are evident.

In order to investigate the spectrum change, the amplitue of several harmonics and that of the fundamental frequency component were plotted versus attenuation from maximum drive level. These plots are shown in figure 52. The upper graph presents the amplitude of the fundamental frequency (f_0). The lower graph presents the amplitude of the subharmonic, $f_0/2$, and the first and second harmonics, $2f_0$ and $3f_0$ normalized by the fundamental (f_0). These harmonics are also identified in figure 51 with vertical dashed lines.

This plot shows that at around 5 to 6 dB attenuation there is an abrupt change in the level of the harmonics plotted. This is another indication that the cavitation threshold at 12 kHz in these experiments is at 5 to 6 dB attenuation corresponding to around 350 kPa of negative acoustic pressure.

After cavitation effects were investigated using the hydrophone measurements and the experiment was reconfigured for launching the projectiles, the high-speed camera and lighting were set up and images were taken of the array focus with the sound field on. Figure 53 presents three consecutive frames at intervals of 1 ms showing the acoustic cavitation produced by a 3 ms duration pulse of the maximum amplitude 12 kHz pressure signal in the absence of a supercavity (see figure 85 in appendix H for the pressure recording). These images were taken from a side view of the array focus and measure approximately four by four inches.

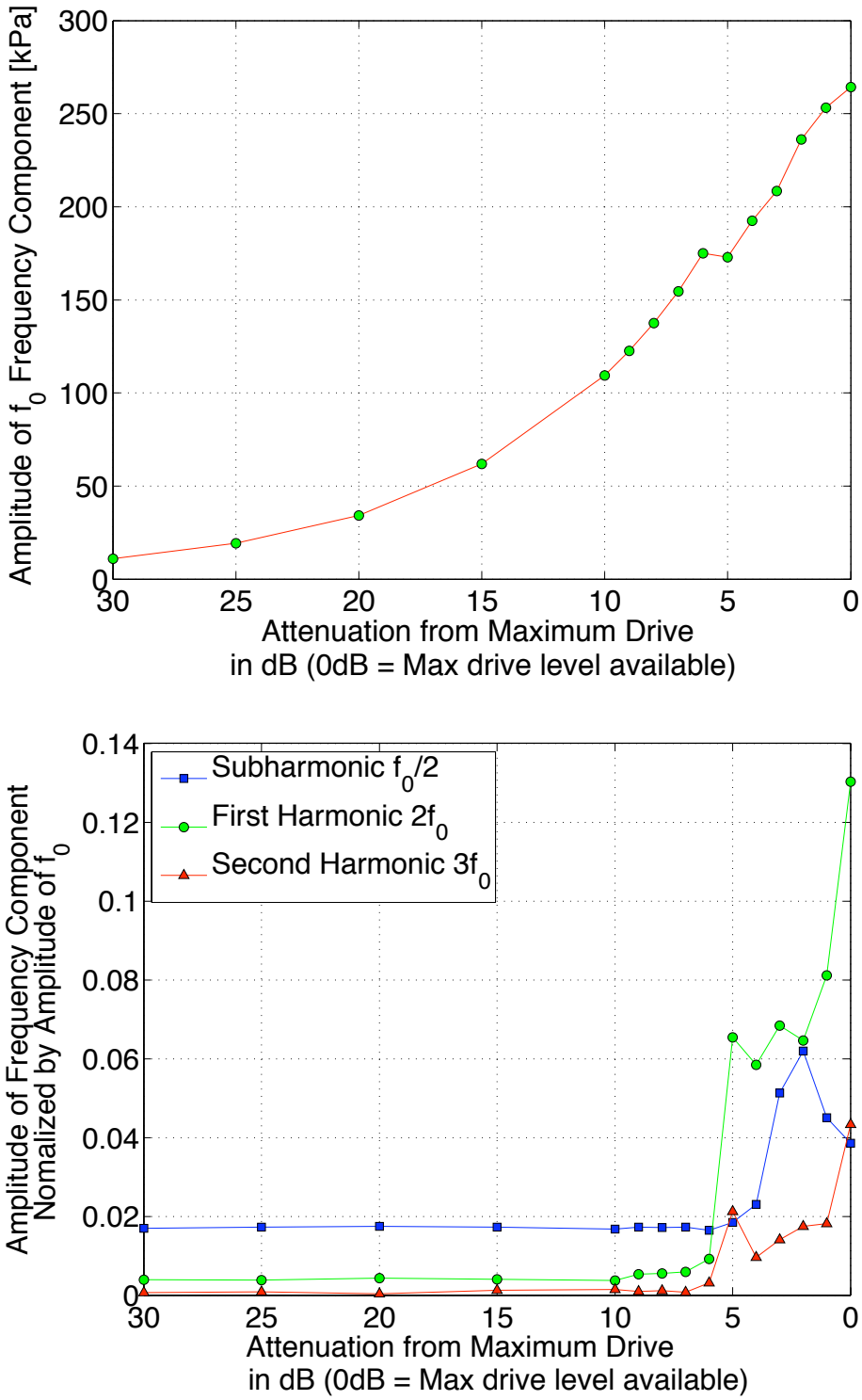

Figure 52: Plots showing the amplitudes of frequency components at the drive frequency, first harmonic, second harmonic, and half-order suharmonic. $f_0 = 12\ kHz$

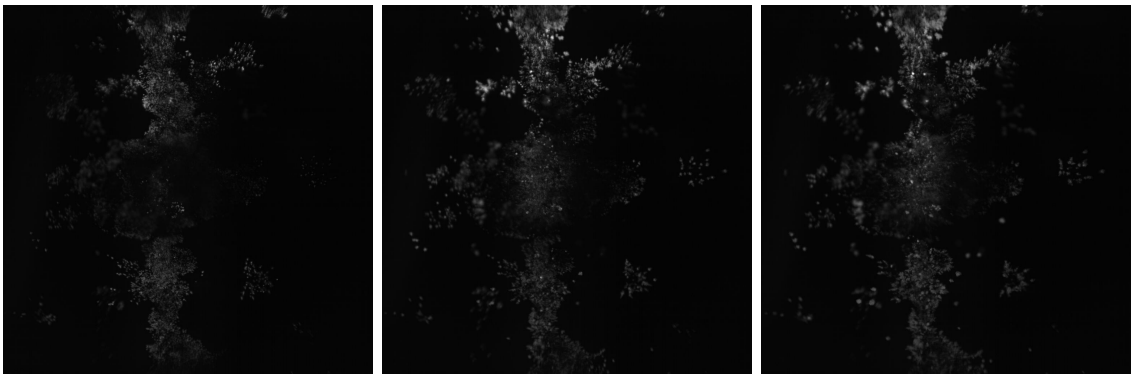

Figure 53: Three consecutive frames at intervals of 1 ms showing the acoustic cavitation produced by the high amplitude 12 kHz pressure signal in figure 85. Images are square with sides approximately four inches in length

CHAPTER V

EXPERIMENTS AND RESULTS

This chapter presents results from experiments carried out with the supercavitating projectile subject to an acoustic pressure signal. The experiments were designed to address the research questions set out in section 1.5. Additionally, they were intended to provide information that was pertinent to future investigations into the development of an acoustic countermeasure to supercavitating torpedoes. Firstly, section 5.1 gives and overview of the experiments conducted, followed by section 5.2 that discusses methods of statistical inference used to analyze the results. Sections 5.3.1 and 5.3.2 then give details of each experiment set and present the results for each case. Lastly, section 5.4 summarizes the results and presents a discussion on the significance as it pertains to understanding the interaction of an acoustic signal with a supercavity and using this technique as a countermeasure.

5.1 General Overview of Experiment Cases

The experiments that constituted the focus of this work were intended to provide information on the effect of an acoustic pressure signal on a supercavity and on the dynamics of a supercavitating projectile. The goal was to choose the limited number of experiment cases available to provide the most meaningful results to advance the state of knowledge in this area and provide a useful benchmark for further study. Outcomes that achieve this would provide not only evidence that a reasonable or attainable level of acoustic pressure can have desired effects (that is, an effect on the shape of a supercavity; on the dynamics of a projectile; and on the accuracy of a projectile), but would also show results that indicate what level of pressure is required and what frequency range is desirable.

A full range of frequency-variation and amplitude-variation experiments would provide a fully populated matrix displaying trends in experimental observations. Pinpointing optimum configurations, however, is beyond the scope of this work. The experiments here were only designed to give indications to guide future work on optimization. A few sparse points in the matrix were picked using the range of frequency and amplitude available with our apparatus and with the number of cases that could reasonably be tested in this study.

Each experiment case used a set of either twenty-four or thirty projectiles. Two thirds of the shots in any experiment case were subject to the acoustic pressure and the remaining third were used as a control. As mentioned in section 4.3, distributing additional control shots amongst the shots that were subject to the pressure field served to monitor the consistency of the apparatus with use over time and to add numbers to the overall control sample.

The first experiment case involved imposing the maximum amplitude of acoustic

pressure available and then lowering the amplitude from the signal generator to investigate the relative effects with a range of pressure amplitudes. Three different amplitudes were used. Then, when it was found that a pressure level lower than the maximum available level did have a statistically significant effect, the frequency was varied maintaining that same amplitude in order to investigate the relative effects of higher and lower frequency signals. This was done at two different amplitudes. All of these experiments were done with an axially symmetric pressure field, that is, axially symmetric about the expected flight path of the projectile. The details of the experiments are discussed in sections 5.3.1 and 5.3.2.

It was expected that a positive result from these experiments, where the projectile was subject to a symmetric pressure field, would be an increase in the *spread* of the impact locations (therefore, decreasing the projectile accuracy) and/or an increase in the *drag* on the projectile. It was not expected that a symmetric field would divert the projectile in any biased direction, that is, move the centroid of the impact location points relative to the control sample. It is thought that a bias in the impact location centroid could possibly be achieved by imposing an asymmetric pressure field on the supervcavity.

It is instructive at this point to give a general idea of the time scales and length scales for the supercavity, the passing of the projectile body, and the sound wave. The average time taken the for a supercavity cross-section to grow and collapse to cavity closure was measured from the control experiments of section 4.3.4 and was found to be 4.3 ms. The average time taken for the projectile to travel its own length at the array focus was 0.48 ms. The period of a 12 kHz sine wave is 0.083 ms. Therefore, the cavity was subject to many cycles of the acoustic signal as it grew and collapsed. On average the cavity was subject to around 6 cycles while the projectile traveled its own length. The signal pulses used were only 3 ms in duration and began

slightly before the projectile arrived at the array focal region. The wavelength of a 12 kHz signal in water is 123 mm. The diameter of the supercavity at the projectile tail was around 15 mm and it subsequently grew to a maximum diameter of around 25 mm at the mid section before collapsing.

5.2 Notes on Statistical Measures and Inferences

This section discusses methods of statistical inference that were used in interpreting the results throughout this chapter.

5.2.1 Target Impact Location Analysis

5.2.1.1 Inferences Based on Coordinate Direction Standard Deviation

The impact location statistic that was used to test the null hypothesis was the standard deviation of the impact points in the x and y coordinate directions (discussed in section 4.3.2). When statistics from experiments performed with the sound signal on were compared to the control sample then an increase in standard deviation indicated a decrease in projectile accuracy. The associated p-value was the probability that a standard deviation at least as high as that of the experiment sample could have in fact come from the control population purely by chance. The null hypothesis for this test was that the imposed acoustic pressure had no effect on the accuracy of the projectile. If this p-value was less than or equal to 0.05 then the addition of the acoustic pressure was deemed to have had a significant effect.

The control population statistics were estimated from the sample of 87 control experiments, the results of which were shown in chapter 4, section 4.3.2. The estimated control population statistics were then used to estimate a distribution of standard deviations. From this the probability that a standard deviation for a sample could

be equal to or above a given value and have come from the control population was found.

5.2.1.2 Inferences Based on Circular Error Probable

In section 5.4, statistical inferences are made using the circular error probable (CEP). CEP is discussed in section 4.3.2. Equation (39) shows that the CEP is directly proportional to the standard deviation. Therefore, statistical inferences are done in a manner similar to that discussed for the standard deviation in the previous section. The significance value calculated is the probability that the CEP could be equal to or greater than the observed value and have come from the control population purely by chance.

5.2.2 Projectile Speed Analysis

During analysis of projectile speed, the drag coefficient was compared for the experiment cases with the sound on and the sound off. Statistical inference involved determining if there was significant change in the mean drag coefficient.

Calculation of t values was done using equation (43) and measured the distance between the experiments sample mean and the control mean in units of the standard error [27]. This method is generally referred to as a one-sample hypothesis tests. In using this method of comparison between two frequency distributions it is assumed that the standard deviation of each sample is the same.

$$t = \frac{\bar{Y} - \mu}{s/\sqrt{n}} \tag{43}$$

where $\bar{Y}$ is the observed sample mean, μ is the control sample mean, s is the control

sample standard deviation (assumed equal to the observed sample standard deviation), and n is the number of measurements in the sample.

5.3 Experiment Description and Results Presentation

5.3.1 Experiment Description and Results: Varying Signal Amplitude

This section describes details of the set of experiment cases that was used to investigate relative effects of ranging the amplitude of the imposed acoustic pressure on the supercavity and on the dynamics of the supercavitating projectile. Results led to the design of the frequency variation experiment sets in 5.3.2.

5.3.1.1 Experiment Description

The first test case imposed the maximum amplitude pressure signal available upon the supercavity to determine if the supposed worst case scenario would produce measurable effects. For generation of maximum pressure the frequency of the signal was set at 12 kHz and the pulse had a duration long enough to take advantage of constructive interference from the tank wall. The frequency was constrained to be in the vicinity of 12 kHz due to the transmitting voltage response of the individual sources (see figure 32 in section 4.4.1.2). The array geometry and matching transformers were then tuned to maximize the pressure amplitude at this frequency. Details of the confined environment sound field are given in sections 4.4.4 and 4.4.6. To subject the projectile to the maximum amplitude generated it was fired down the center of the array focus.

Two subsequent experiment cases were then done with the same input signal shape but at 6 dB and 12 dB amplitude attenuation. Amplitude reduction was achieved using an appropriate attenuator on the output of the signal generator. To maintain

the same conditions for comparison, the projectile was again fired down the center of the array focus.

From this point on, the cases - maximum amplitude, 6 dB attenuation and 12 dB attenuation - will be referred to as high, medium, and low pressure amplitudes respectively. The specific numerical amplitude was not used as a general description because the actual amplitude varied from pulse to pulse at the high and medium levels due to acoustic cavitation. Ranges in the peaks pressures observed are shown in table 5. Additionally, the positive and negative peaks had different absolute values, again due to acoustic cavitation. Sound pressure measurements are discussed in detail in section 5.3.1.2.

Approximate typical pressure amplitudes for the signals measured in the absence of the supercavity are shown in table 5 for each experiment case. The nonlinear relation between attenuation and pressure amplitude was due to the acoustic cavitation in the medium.

Table 5: Approximate typical amplitudes for the attenuation levels discussed in the text. For plots of typical pressure measurements for each case see appendix H

Attenuation of input voltage amplitude	Approximate peak negative pressure	Approximate peak positive pressure
0 dB (high)	-150 kPa	500 - 700 kPa
6 dB (medium)	-150 kPa	400 - 600 kPa
12 dB (low)	-200 kPa	200 kPa

The input signal shape used in all cases is shown in figure 54. The figure shows a measurement from the signal generator output.

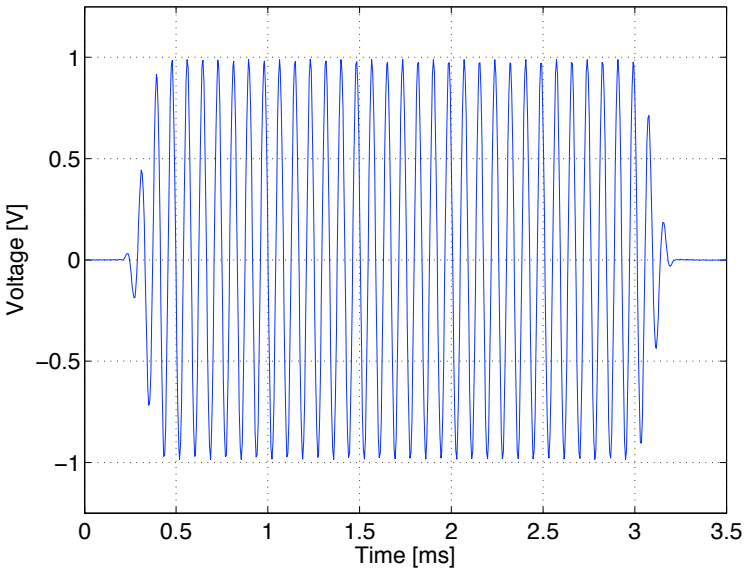

Figure 54: Plot showing an output trace from the signal generator for the 12 kHz, 3 ms duration pulse (36 cycles).

5.3.1.2 Sound Pressure Recordings

Figures 85, 86, and 87 in appendix H show pressure signals at the high, medium and low pressure amplitudes respectively for the 12 kHz signal. In each figure are three plots. The top figure shows the case where a hydrophone was located at the focus of the array in the absence of a supercavity. The middle and bottom figures show signals measured in the case where a model cavity was placed in the array focus and the hydrophone was located at two positions next to the model cavity. The measurements in the absence of any cavity represent an example of the signal that was present in the water before the arrival of the projectile (In the experiments the signal began before the arrival of the projectile.). The measurements with the model cavity were done to help understand the effects that the presence of the cavity in the array focus had on the sound field.

Acoustic Signal in the Absence of the Model Cavity:

At the high and medium signal levels, the pressure amplitude was clearly sufficient to cause acoustic cavitation in the water in the absence of the supercavity. The relevant plots, therefore, show an example of the pressure signal but do not represent the actual signal for each shot. It can not be said definitively what the pressure amplitude was at the array focus or exactly what the signal looked like for any individual shot, only what a typical pressure signal looked like. Variation was observed in the signal trace for repeated measurements when acoustic cavitation was occurring. When acoustic cavitation occurred it was observed that the negative peak was clipped at approximately -150 kPa of acoustic pressure and that the shape of the signal was severely distorted (see the upper plot in figures 85 and 86). Also, the positive peaks were erratic showing both higher and lower peaks than would be expected by linear extrapolation from the low level experiments. It is additionally noted that the signal present in the high and medium amplitude cases were very similar to one another.

At the low signal level, the negative cycle of the acoustic signal caused absolute pressures below the vapor pressure of the water; however, the recorded signal did not indicate acoustic cavitation. It was observed that cavitation generally did not occur with the 12 kHz signal at this pressure amplitude. There were, however, occasions when cavitation was evident which could have been due to differences in conditions between measurement times. The most likely condition causing this difference is the amount of gas dissolved in the water which varied with time after the tank was filled with water from the mains supply. The water slowly degassed after being released from the supply where it was under pressure. The upper plot in figure 87 is considered to be a good representation of the signal for most shots in the experiment performed at that amplitude. Cavitation bubbles were not seen in the movies taken of those shots although small unobservable cavitation bubbles may have been present.

Acoustic Signal in the Vicinity of the Model Cavity:

The model supercavity was made in the shape of the real cavity and constructed from closed-cell styrofoam. This was thought to be a reasonable approximation to the actual situation because it provided a boundary of the correct shape and size with a characteristic impedance much lower than that of water. The main difference between the model case and the real situation was that the model cavity boundary was static compared to the real case where the cavity was formed and expanded. In the time when the acoustic signal was present in the real cavity experiments there was initially no cavity, then inception and growth of the cavity. This difference may have had important consequences for the outcome of the experiments.

Pressure measurements were taken at various distances from the model cavity. The location of the hydrophone was varied only in a radial direction because the field was approximately axisymmetric. There were three hydrophone locations: all were 2.3" (59 mm) aft of the cavity tip (where the tail of the projectile would have been inside the cavity) and the radial distances from the cavity boundary were 4.6 mm and 11.6 mm and 20.6 mm. Pressure signals at the first two of these locations are shown in figures 85, 86, and 87 in appendix H for the high, medium, and low pressure amplitudes with the 12 kHz signal.

For the low-level linear cases looked at, the pressure amplitude in the vicinity of the cavity wall was approximately three times less that that at the center of the array in the absence of a cavity. The measurements indicate that the pressure levels in the low amplitude case when the cavity was present were certainly not high enough to cause cavitation in the water around the model cavity. For the medium amplitude case, cavitation was evident close to the model cavity but the pressure levels were in the transition region near the cavitation threshold. For the high level case, pressures

measured in the vicinity of the model cavity were sufficient to cause acoustic cavitation.

The pressure amplitude in the absence of the supercavity was much greater than that close to the cavity when the model was present. Because in the real experiments the acoustic signal was present before the projectile arrived, there may be cavitation bubbles formed then that remain in the water around the newly formed supercavity. These would not be present for the same conditions in the model cavity experiments. These existing cavitation bubbles would increase the level of cavitation in the water surrounding the supercavity for the real experiments compared to the model cavity experiments. Pressure levels that would not normally cause cavitation in the water may excite the existing cavitation bubbles. The cavitation threshold may also be reduced due to the previous bubble activity.

5.3.1.3 Imaging

Figure 55 shows images from the high speed digital camera for typical shots from each experiment case for flights where no tail-slap was observed at the viewing location. A full series of images showing the entire life of the supercavity is shown in appendix G for the high amplitude case. Figure 56 shows three consecutive images from a shot in which there was an observed tail-slap while the acoustic signal was present. In these images, the tail hit the cavity wall coming out of the page.

The images clearly display a physical effect that the acoustic signal had on the supercavity; the corrugations on the cavity/water interface.

The small bubbles seen surrounding the cavity in figure 55 (especially in the high pressure amplitude image and to a lesser extent in the medium pressure amplitude image) and in figure 56 are due to acoustic cavitation in the water. As was discussed

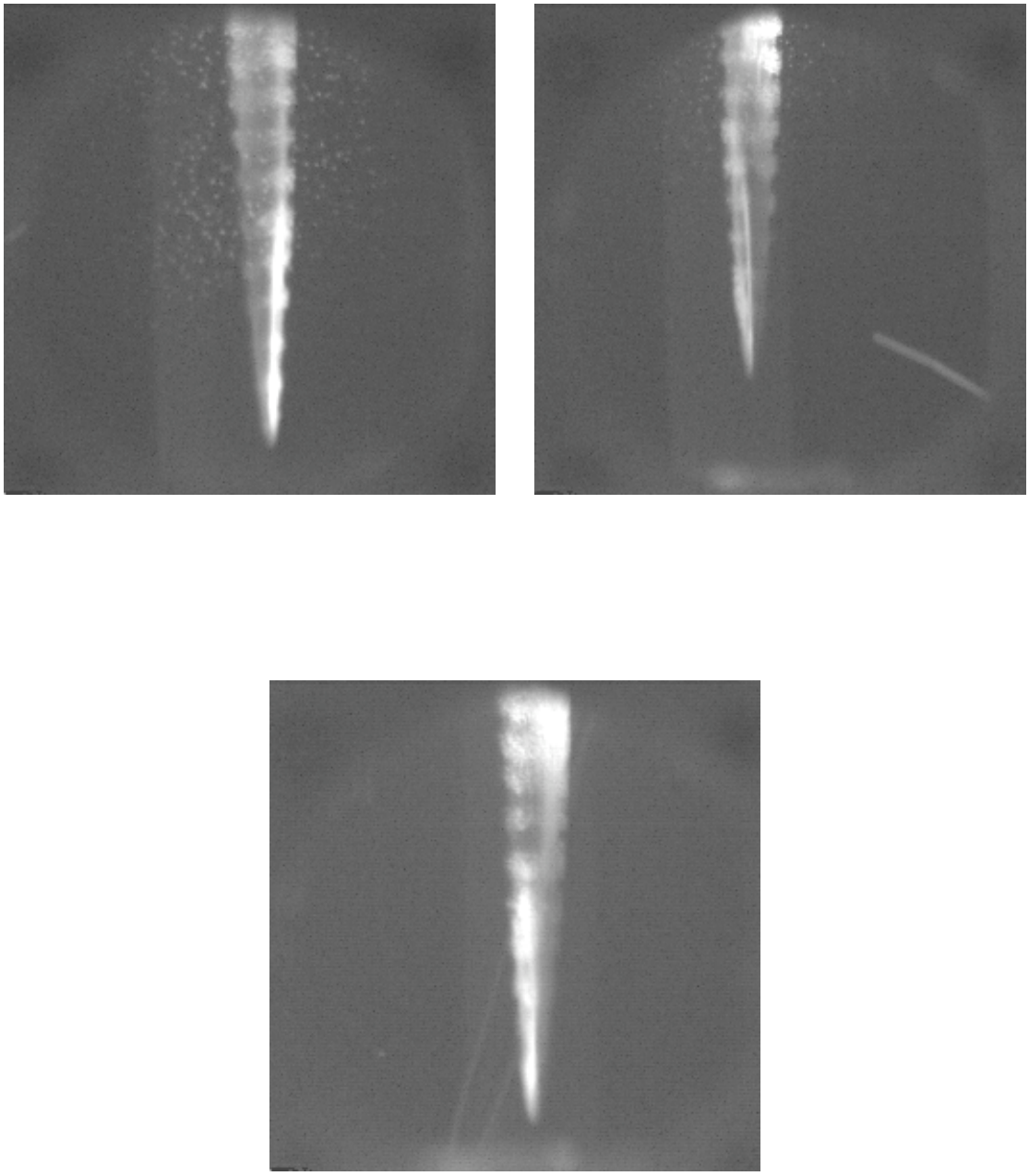

Figure 55: Sample images of the effect of a 12 kHz acoustic pressure on a cavity surrounding a supercavitating projectile. Three images show different pressure amplitudes: top left) 12 kHz, high amplitude, top right) 12 kHz, medium amplitude, bottom) 12 kHz, low amplitude.

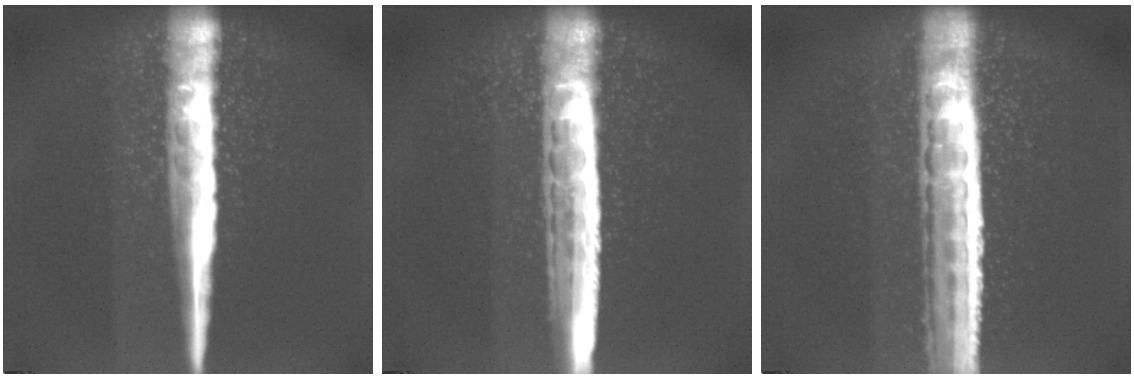

Figure 56: Sample images of the effect of a 12 kHz acoustic pressure on a cavity surrounding a supercavitating projectile during an instance of tail-slap. Left to right are successive images in time with an image interval of 0.27 ms

in section 5.3.1.2, these could be due to bubbles that were formed before the arrival of the projectile or in some cases could be new cavities formed by the acoustic pressure signal around the cavity.

5.3.1.4 Cavity Dimensions

The first observation is that the peaks or troughs of the corrugations on the cavity wall are spaced at a distance apart along the cavity length corresponding to the period of the acoustic signal multiplied by the speed of the projectile. This indicates that the effect was a consequence of the acoustic pressure at the cavitator location at the instant any cavity section was formed. This makes sense because every section of the supercavity was subject to almost the same acoustic pressure after inception and so the change along the cavity length at any snapshot in time must be due to conditions at inception.

In addition to this effect it is expected that the acoustic pressure imposed on the cavity sections after inception would effect the growth of the supercavity; however, this is not immediately obvious from the recorded movies. Theoretical considerations

based on Logvinovich's principle of independent cavity section expansion predict that the amplitude of this effect should be much smaller than that due to variations in the pressure during inception (see section 3.3). This also makes sense, because for a large bubble such as the supercavity, a 12 kHz excitation frequency is much greater than the bubble resonance frequency and so we might expect small amplitudes of oscillation. The oscillation referred to here is the oscillation of the section after inception due to the acoustic signal present during growth and collapse. The large effect observed in figures 55 and 56 is due to the pressure at inception which was discussed in the previous paragraph.

Experimental observations tend to agree with the theory. Images were captured at short exposure times to investigate because the typical camera exposure times were around 0.08 ms which happens to be about the same as the period of a 12 kHz signal; therefore, disturbances of the cavity wall at 12 kHz would not be seen. An exposure time of approximately 0.01 ms was attainable and was sufficiently short. With a time interval between frames of 0.27 ms (3731 frames per second as discussed in section 4.2.1.1) which is three and a quarter periods at 12 kHz, one would expect to see changes in the cavity dimensions from frame to frame. There was no change observed of a measurable size.

Now looking at the amplitude of the corrugations, the plots on the left side of figure 57 show the measured supercavity radius at the location of the tail of the projectile when the projectile was within the array focus. The plots on the right side of figure 57 show theoretical predictions of cavity shape for the same conditions (see section 3.3). Statistical values of the experimental measurements are presented in table 6 and are plotted in figure 58 along with theoretical predictions of the inner and outer radius of the corrugated cavity. The precise location of the cavity radius measurement was at the foremost part of the tail maximum diameter. This point is 56 mm (2.2") aft of

the projectile tip (see appendix B for a projectile drawing) and was chosen because it is the part of the projectile body that would touch the cavity wall first as the cavity diameter reduces. This location is highlighted in the theoretical plots in figure 57 by the vertical dotted line.

Table 6: Average values of the measurements of cavity radius at the projectile tail that are presented in figure 57. The average speed shown was calculated using only the shots where a cavity dimension measurement was made.

Acoustic signal (freq., Amplitude)	Inner radius (mm)		Outer radius (mm)		Average speed (m/s)	n
	Measured mean	Model (@ avg. speed)	Measured mean	Model (@ avg. speed)		
12 kHz, high	6.1 ±0.3 (s=0.3)	7.3	7.7 ±0.3 (s=0.2)	7.7	134 ±2 (s=10)	23
12 kHz, medium	5.9 ±0.3 (s=0.2)	7.4	7.6 ±0.3 (s=0.3)	7.8	133 ±2 (s=9)	30
12 kHz, low	6.3 ±0.3 (s=0.3)	7.9	7.5 ±0.3 (s=0.3)	8.1	135 ±2 (s=8)	13
CONTROL	-	-	7.6 ±0.3 (s=0.4)	8.0	135 ±2 (s=13)	43

The radius at the tail was found from the camera images using the method described in section 4.2.1.3. Basically it involved fitting an ellipse to the cavity shape and using the known geometry of the projectile to locate the tail based on the observed cavitator location. In figure 57, points labeled as experiment "outer" and "inner" refer to the radius of the ellipse fitted to the peaks and troughs of the ripples on the cavity wall respectively. These will denoted by r_o and r_i respectively. Figure 59 illustrates the measurement technique showing examples of the fitted ellipse for a supercavity disrupted by the acoustic pressure. The left image depicts the "outer" measurement and the right image depicts the "inner" measurement. Theoretical predictions of r_i and r_o were found similarly by using Logvinovich's model to model the cavity shape (section 3.3) and then fitting a curve to the corrugation troughs and peaks.

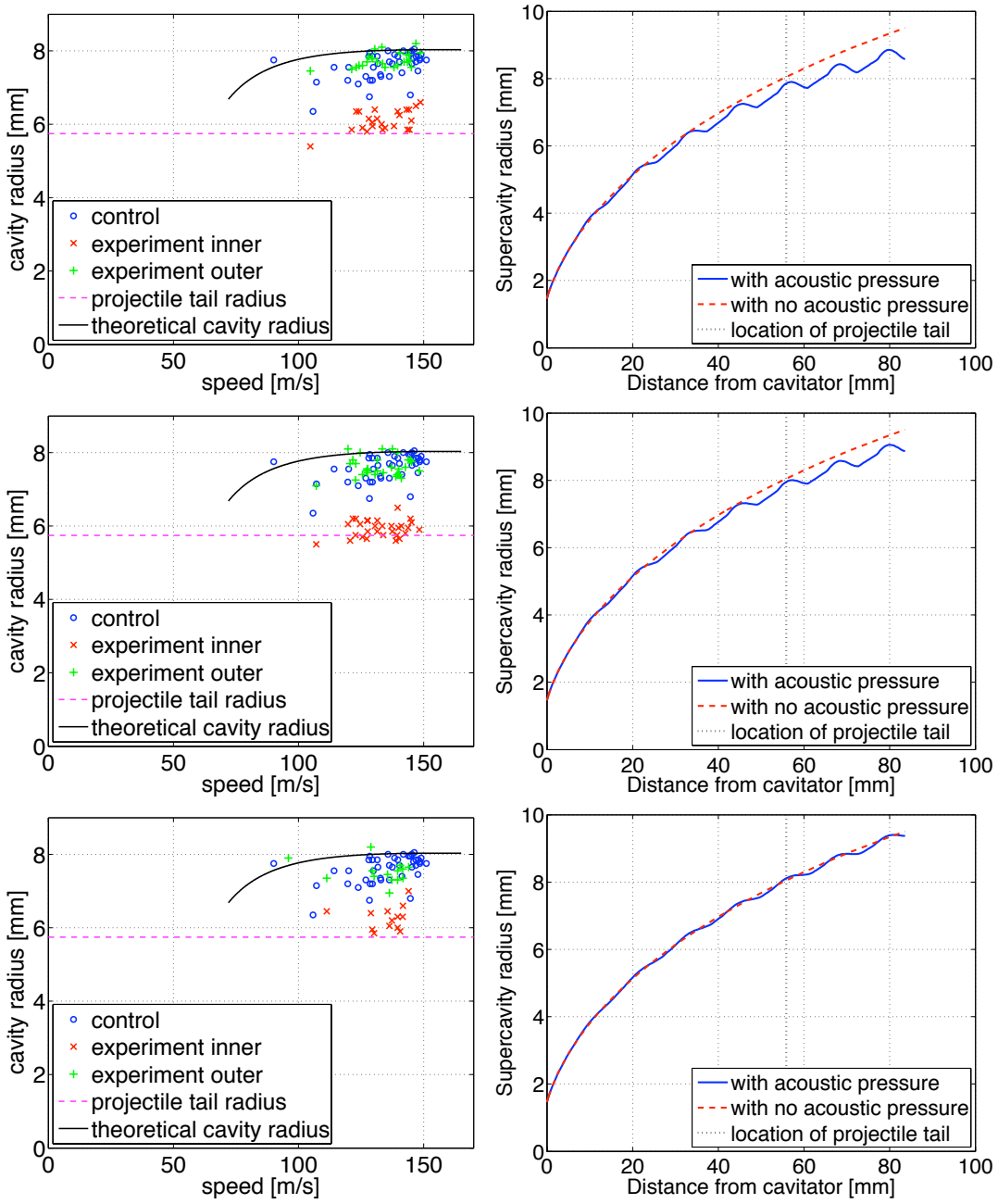

Figure 57: Plots showing the supercavity radius at the projectile tail when subject to the 12 kHz signal at high, medium, and low amplitudes; top) 12 kHz, high amplitude, middle) 12 kHz, medium amplitude, bottom) 12 kHz, low amplitude.

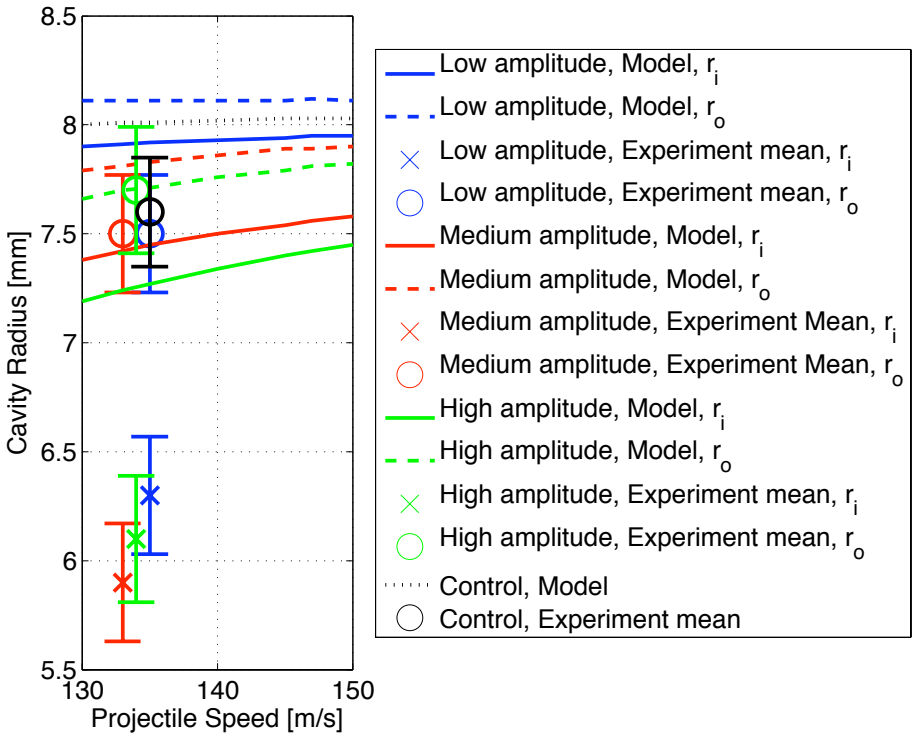

Figure 58: Plot showing the sensitivity of cavity radius to projectile speed for the 12 kHz experiment cases.

It should be noted that as a consequence of the measurement technique it was possible to have an inner radius smaller than the projectile tail because the measurement was made along all of the observed length and not just at the tail. On those cases the inner ripples would be touching the projectile tail even if the projectile was centered in the supercavity.

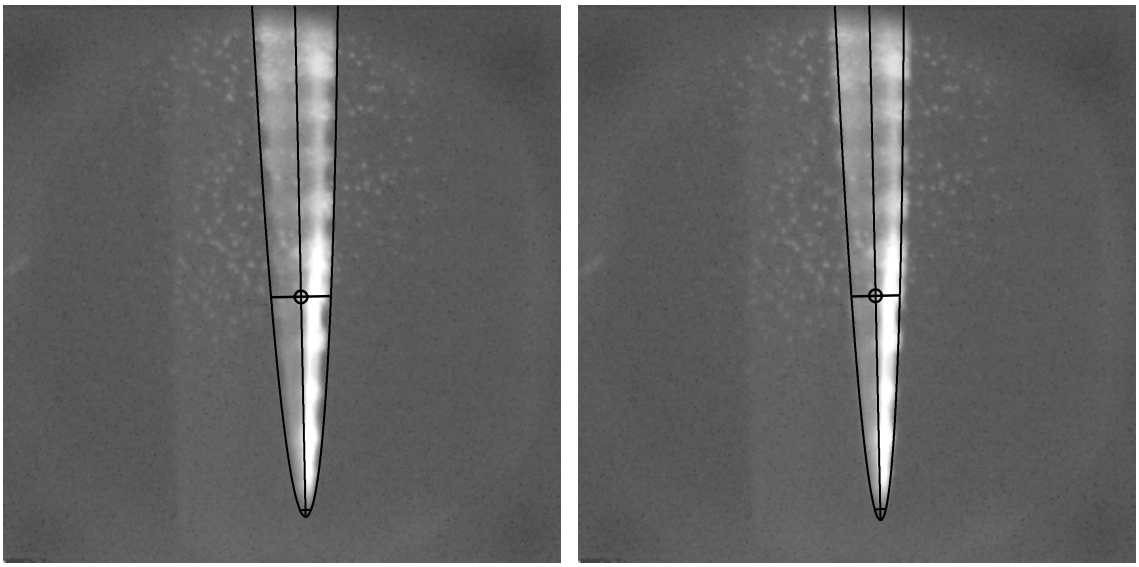

Figure 59: Example plots of an ellipse fitted to a supercavity subject to an acoustic signal: left) fitted to peaks of ripples, right) fitted to troughs of ripples

The average projectile speed for the different experiment cases varies. The curves in figure 58 show a predicted sensitivity of the cavity radius to projectile speed. The relationship is somewhat complicated because not only does the growth rate of the cavity vary with speed, but the relative effect of the acoustic pressure also varies. Over the range of average speeds the radius only varies by approximately 0.05 mm in the worst case. Considering that the uncertainty in the experimental measurement was ± 0.3 mm it was considered reasonable to compare the measured radii for trends in the cavity radius with signal amplitude.

It is noted that, although the model seems to predict the observed trends regarding

the effects of the acoustic signal, it does not predict the observed amplitude. Predicted amplitudes were approximately a third to a quarter of those observed in the experiments. Figures 57 and 58 clearly show this discrepancy.

Interestingly, as can be seen from the left plots in figure 57, the width of the ellipse fitted to the outer edge of the corrugations on the cavity wall on shots with an imposed acoustic pressure signal were scattered amongst the control points. The control shots were only subject to constant ambient pressure. However, the ellipse fitted to the troughs of the corrugations was always narrower than a cavity produced under constant ambient pressure. One might expect that the positive and negative cycles of the acoustic signal would have opposite effects and so the profile of the control shot supercavity would lie somewhere in-between the peaks and troughs of the corrugated supercavity; however, this was not observed to be the case.

A possible explanation for this was presented in section 3.3. It was suggested that the occurrence of acoustic cavitation, which causes a clipping of the negative pressure peaks, resulted in a mean positive pressure on the growing cavity. This arrested the overall growth causing the average cavity radius to be reduced. The corrugations are both outward and inward, in fact mainly outward, but onto a smaller radius cavity making it appear as if the corrugations are only inward. This behavior is seen in the right side plots in figure 57. The low amplitude case tends to disagree with this explanation as acoustic cavitation was very light or non existent at those pressure levels.

The alteration to the shape of the supercavity can be separated into two different effects. One is that the average cavity radius is reduced due to a net positive acoustic pressure. The net positive pressure is due to acoustic cavitation causing clipping of the negative peaks. The other is that the varying acoustic pressure at cavity inception changes the initial cavity section expansion rate for sections formed at different times

which results in corrugations on the cavity/water interface.

It is interesting to note that the troughs of the corrugations are probably due to the low pressure cycle of the acoustic signal and the peaks due to the high pressure cycle, which is contrary to what one might initially expect. Consider the energy method derivation of Logvinovich's principle. Energy is transferred to a cavity section of length Δs as kinetic energy from the work done by the cavitator in traveling the distance Δs. The work done by the cavitator when the positive peak of the acoustic signal is present would be greater than when in ambient conditions for the same distance traveled. Therefore, the initial expansion rate of the cavity section would be greater and since the pressure thereafter is similar for all sections, the ones with a faster initial growth rate would have a greater diameter at a given instant in time. The opposite would be true for the cavity sections that were created during the presence of the negative cycle of the acoustic pressure.

An additional and important point is that within experimental uncertainty it appears as though the different signal amplitudes do not cause significantly different effects on the observed corrugation amplitude.

5.3.1.5 Target Impact Location

Table 7 shows statistical results for the target impact location data. Information presented includes the standard deviation of the impact points in the x and y coordinate directions, the CEP, the number of shots in each data set, and the statistical significance of the result. The value of the statistical significance is the p-value discussed in section 5.2.2. Actual impact location plots are shown in the middle column of plots in figure 92, appendix I.

It is clear from the statistical significance numbers shown in the far right column

of table 7 that the high and medium acoustic pressure amplitude signals did have a significant effect on the projectile accuracy and that the low amplitude signal did not. Although the low pressure amplitude case did show increased values of standard deviation and CEP, the increase was not deemed to be statistically significant. This is a key result of this work and the cause of the decreased accuracy will be investigated in detail in section 5.4.

There was no significant bias exhibited in the location of the centroid of the data for the shots subject to the acoustic signal compared to the control shots. The data only showed an increase in the spread of the target impact locations.

Table 7: Measures of projectile accuracy for the experiment cases with ranging pressure amplitude at a signal frequency of 12 kHz

Acoustic signal (freq., amplitude)	Standard deviation (x, y)	CEP (mm)	Number of data points	Statistical significance p-value (%)
12 kHz, high	(10.5, 9.36)	11.7	20	(0.011, 0.42)
12 kHz, medium	(9.58, 9.66)	11.3	32	(0.001, 0.013)
12 kHz, low	(7.81, 7.70)	9.13	14	(10, 15)
CONTROL	(6.35, 6.51)	7.56	87	

5.3.1.6 Projectile Speed

Plots of measured projectile speed versus time are shown in figure 60 for the three different amplitude cases. A projectile drag coefficient was calculated from these speed measurements and presented in table 8 along with relevant statistics. Each curve plotted in figure 60 should contain three measured points, one from each induction coil pair along the trajectory. The speed at the camera location was not plotted because the time when the projectile was viewed relative to the projectile passing the induction coils was not known. The missing data and the small number of measurements included in calculating the average drag coefficient warrants some explanation and

related caution in interpreting the numbers. The muzzle speed was not used in calculating the drag coefficient, the reason was discussed in section 4.3.3. It was also explained in section 4.3.3 why there is very limited data from the coil set before the array. In addition to those considerations it is noted that when the transducers were being driven, the cross talk or pickup due to the drive signal was often present at the same time as the signal from the induced emf due to the passing projectile. Extracting the data posed problems in attaining an accurate speed measurement.

Table 8: Drag coefficients calculated from measured speeds for the varying amplitude experiments at 12 kHz. C_D is the drag coefficient, n is the number of measurements, s is the sample standard deviation. The t value calculated is the difference between the sample mean and the control mean in units of the standard error.

Acoustic signal (freq., amplitude)	Mean C_D	n	s	t value	$t_{\alpha=0.05}$
12 kHz, high	1.14	17	0.085	0.916	±2.11
12 kHz, medium	0.95	5	0.142	-1.97	±2.78
12 kHz, low	-	-	-	-	-
CONTROL	1.10	37	0.175		

The t values shown in table 8 represent one-sample hypothesis tests measuring the distance between the sample mean and the control mean in units of the standard error (see section 5.2.2).

The t value is less than $t_{\alpha=0.05}$ in both cases. Therefore, evidence does not conclude that the observed mean is significantly different from the control case which implies that there is no significant change in the drag coefficient between the control shots and those subject to an acoustic pressure signal.

It is expected that an imposed pressure signal should increase the drag force on a supercavitating projectile. The following paragraphs present some discussion.

Probably the most significant way that the drag force could be effected would be if the

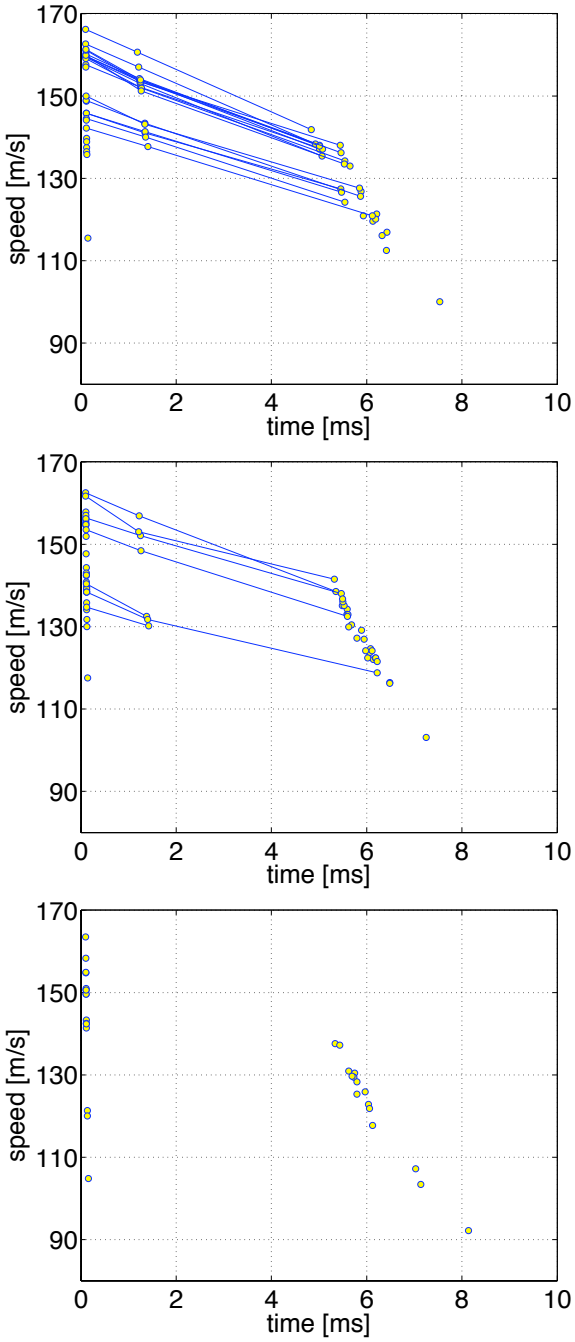

Figure 60: Plots showing measured speed versus time with the 12 kHz signal at different amplitudes; top) 12 kHz, high amplitude, middle) 12 kHz, medium amplitude, bottom) 12 kHz, low amplitude. Data points are represented by markers and were only joined with lines if adjacent points were available.

cavity were closed in on the projectile body from all angles. It has been shown that this was not the case by the quantitative measurements of the supercavity radius at the tail location that were shown in figure 57 and table 6. It can be seen in figure 57 that, for most shots, the cavity radius measured at the tail location was greater than the tail radius for the high pressure amplitude case.

Another source of increased drag could be that the tail-slap incidences were made more severe and so the tail penetrated into the water further and increased the work done by drag on the tail during tail-slap. This situation could be true as will be discussed later, however, theoretical considerations of the planing forces on the tail indicate that the tail-slap incidences themselves do not contribute greatly to the overall drag because of their short duration. Although the duration of the tail-slap may be increased, it was not increased by much, as is evidenced qualitatively by the recorded movies.

A third source of increased drag could be the generation of shock waves at the cavitator if the acoustic cavitation in the water caused the projectile flight to be supersonic in the bubbly water. The effects of acoustic cavitation on the properties of water was discussed in section 2.2.3 of chapter 2. A consequence of the presence of bubbles in water is that the sound speed (c), given by the relation $c^2 = B/\rho$, where B is the bulk modulus, can be significantly altered even for small gas fractions. Qualitatively, the medium has the high density of the liquid and the low bulk modulus of the gas resulting in a low sound speed. In fact, in the low excitation frequency approximation, gas fractions as low as one to two tenths of a percent can result in a sound speed lower than that in the gas alone [15]. Gas fractions as low as one percent cause the observed projectile speed to be around the sound speed in the bubbly medium. The situation at the projectile tip regarding shock waves could be very complicated. The number and size of acoustically generated cavitation bubbles present is changing as

the acoustic pressure fluctuates between positive and negative cycles, therefore, the sound speed in the bubbly water would constantly be changing.

5.3.2 Experiment Description and Results: Varying Signal Frequency

This section describes details of the experiment set that was used to investigate relative effects of acoustic frequency of on the supercavity and on the projectile dynamics. The general layout follows that of section 5.3.1 where the acoustic pressure amplitude variation experiments were discussed.

5.3.2.1 Experiment Description

The acoustic pressure amplitudes used for the frequency variation experiments were chosen to equal the levels in the amplitude variation experiments so that the previous 12 kHz cases could be used in completing the frequency variation experiment sets. Table 9 summarizes the experiment cases that were done. The circles represent the amplitude variation experiments that were discussed in section 5.3.1 and the asterisks represent the additional experiments discussed in this section at higher and lower frequencies. Experiments at alternate frequencies could not be done for the high amplitude case because that amplitude could not be maintained when driving the transducers away from resonance.

Table 9: Summary of the experiment cases done. The circles show the cases that make up the amplitude variation set described in section 5.3.1. The asterisks show the additional cases that make up the frequency variation experiment sets.

	7.5 kHz	12 kHz	17.5 kHz
high amplitude		•	
medium amplitude	*	•	*
low amplitude	*	•	*

The lower and higher frequencies were chosen to be 7.5 kHz and 17.5 kHz. These were the lowest and highest frequencies that could be used while maintaining the same pressure amplitude. They also happened to be frequencies that took advantage of the tank wall reflections by way of constructive interference (see figure 46 in section 4.4.4.2). As the frequency was lowered or raised by any more than these values, distructive interference started to reduce the attainable amplitude. This reduction was in addition to the reduction due to the frequency being further from the transducer resonance.

5.3.2.2 Sound Pressure Recordings

Example hydrophone recordings at 7.5 kHz are shown in figures 88 and 89 in appendix H. As before, in each figure there are three plots. The top plot shows the case where a hydrophone was located at the focus of the array in the absence of a supercavity. The middle and bottom plots show signals measured in the case where a model cavity was placed in the array focus and the hydrophone was located at two positions next to the model cavity. The model cavity experiment was discussed in section 5.3.1.1. Similarly, hydrophone recordings at 17.5 kHz are shown in figures 90 and 91 in appendix H.

The amplitude of the pressure signal itself could not be quantified accurately due to acoustic cavitation. Therefore, pressure amplitudes were matched at very low level amplitudes and the input signal was scaled up accordingly.

5.3.2.3 Imaging

Figures 61 and 62 show images from the high speed digital camera of disruptions to the shape of the supercavity for the 7.5 kHz and 17.5 kHz acoustic signals respectively.

In both figures the bottom image shows an instance of tail-slap occurring where the projectile tail is penetrating the cavity wall toward the viewer. The images shown in these figures are from the low amplitude experiment cases.

The corrugations on the supercavity wall are again clearly seen in these figures. The higher corrugation frequency for the 17.5 kHz case and the lower corrugation frequency for the 7.5 kHz case are evident.

5.3.2.4 Cavity Dimensions

The distance between corrugation peaks along the cavity length was measured and again found to be equal to the period of the acoustic signal multiplied by the speed of the projectile. This measurement verified that it was the acoustic signal that caused the corrugations and that it was not just by chance that the spacing previously had this relationship (see section 5.3.1.4 for the previous discussion).

The plots on the left side of figures 63 and 64 show the measured supercavity radius at the location of the tail of the projectile when the projectile was present at the array focus for the medium and low amplitude cases respectively. The plots on the right side of the figures show theoretical predictions of cavity shape for the same conditions (see section 3.3). Statistical values of the measurements are presented in tables 10 and 11 and are plotted in figures 65 and 66 along with theoretical predictions of the inner and outer radius of the corrugated cavity.

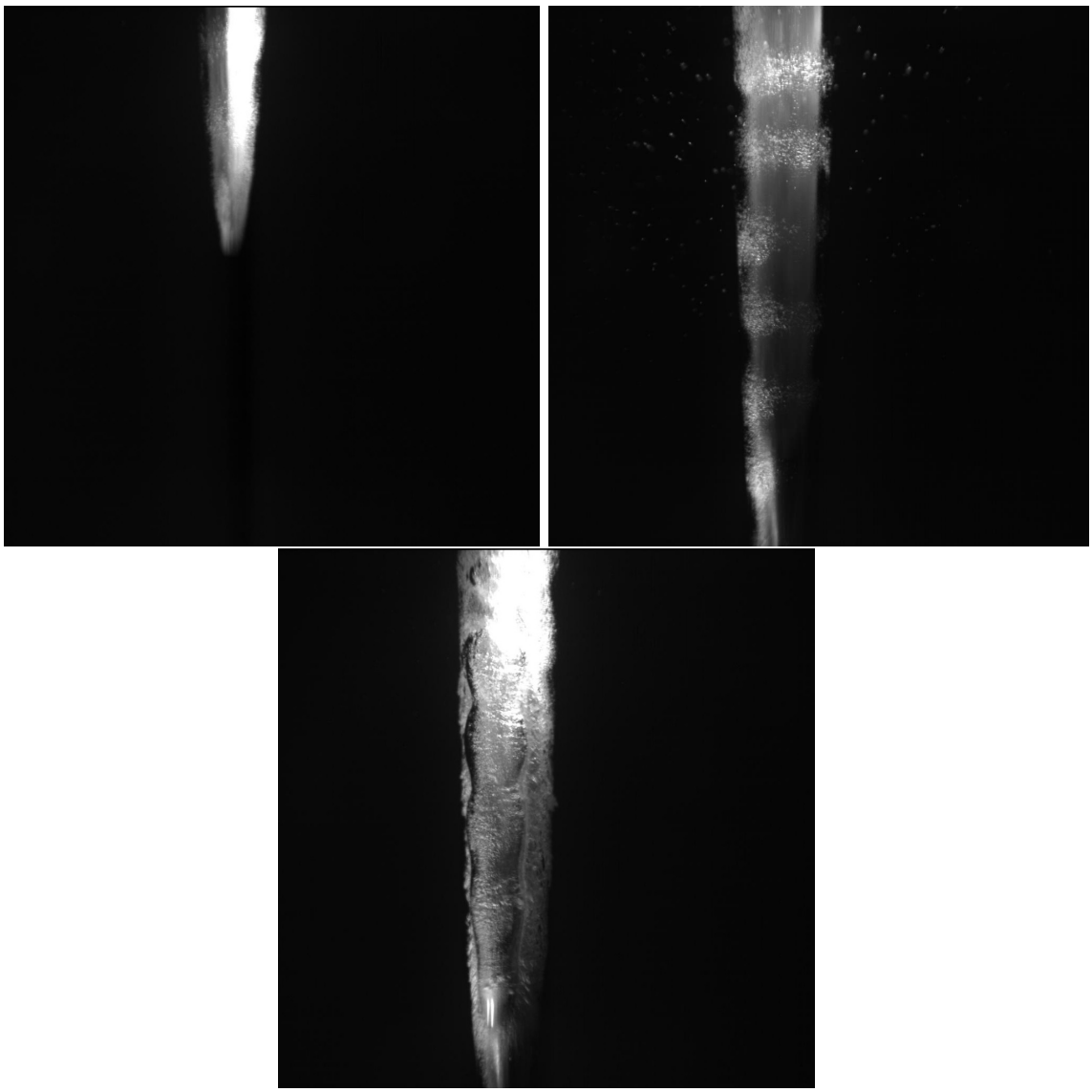

Figure 61: Images from the high speed digital camera showing disruptions to the shape of the supercavity for the 7.5 kHz acoustic signal. The bottom image shows the disruption to the cavity during an instance of tail-slap.

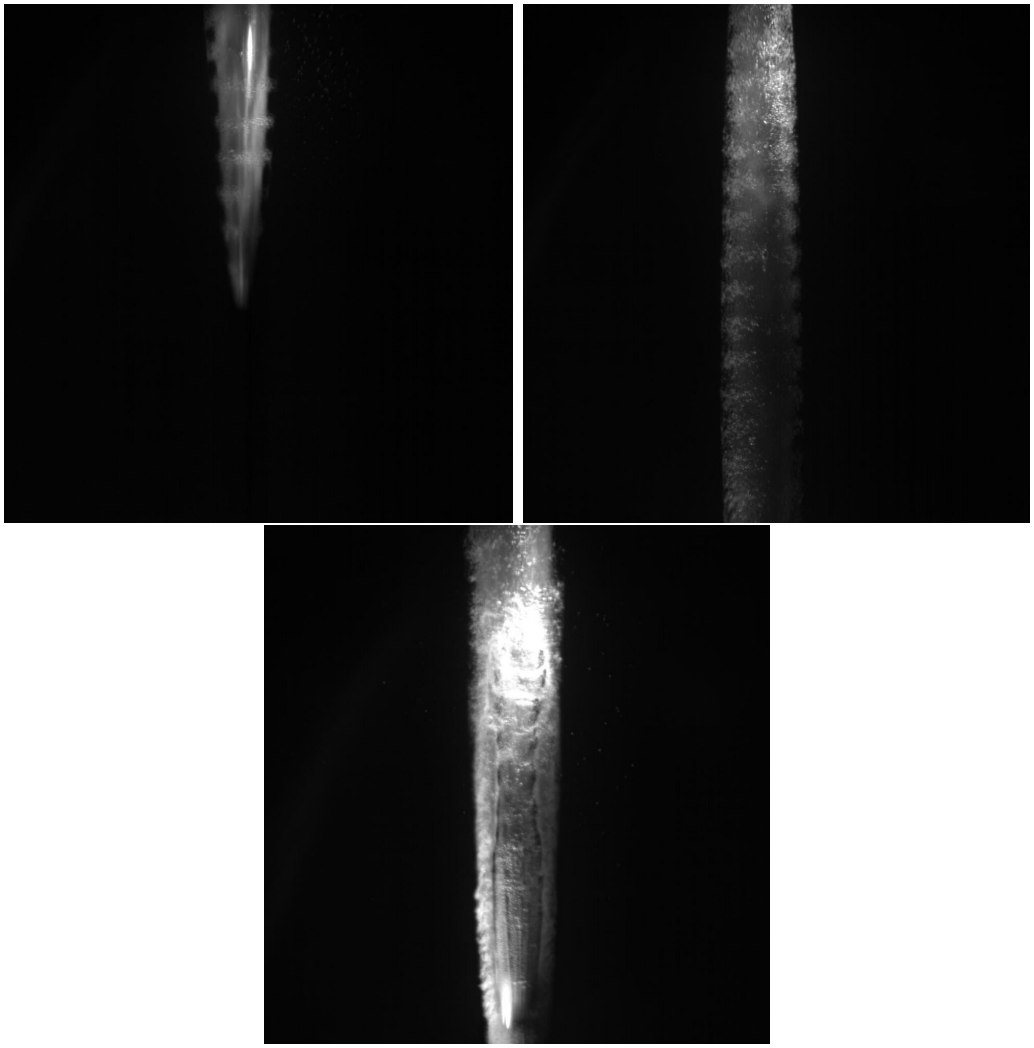

Figure 62: Images from the high speed digital camera showing disruptions to the shape of the supercavity for the 17.5 kHz acoustic signal. The bottom image shows the disruption to the cavity during an instance of tail-slap.

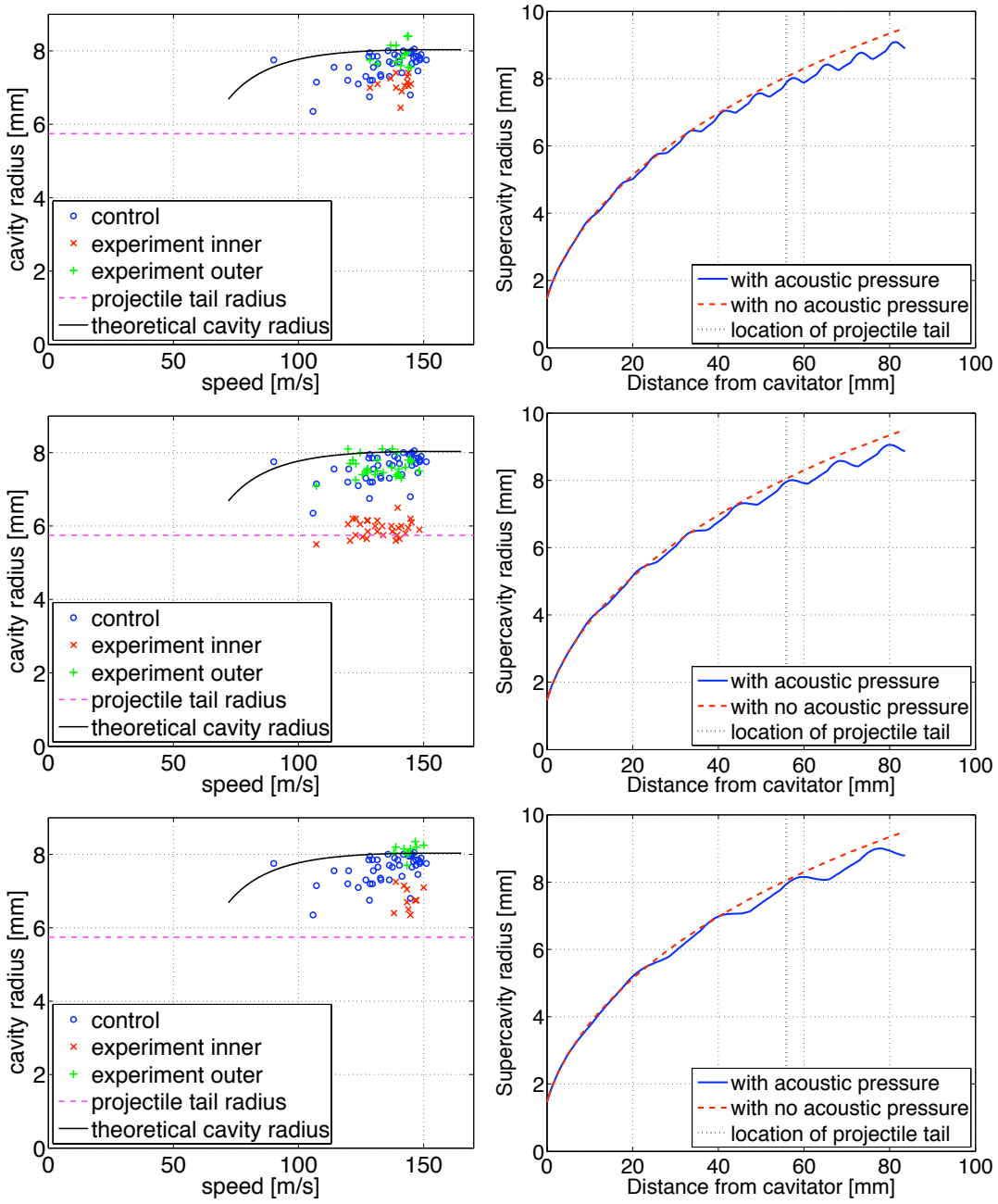

Figure 63: Plots showing the supercavity radius at the projectile tail - medium amplitude, ranging frequency. Top) 17.5 kHz, medium amplitude, middle) 12 kHz, medium amplitude, bottom) 7.5 kHz, medium amplitude.

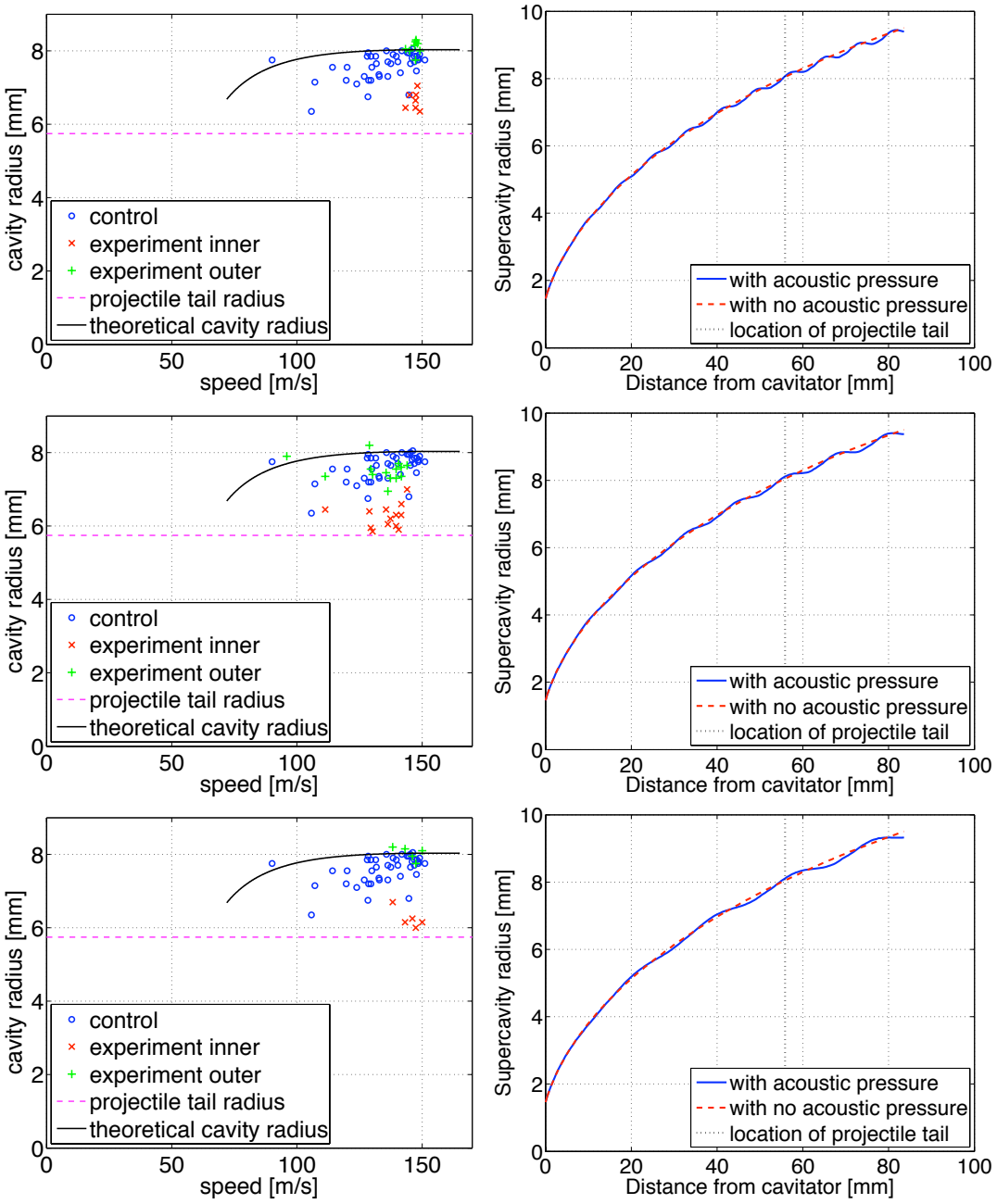

Figure 64: Plots showing the supercavity radius at the projectile tail - low amplitude, ranging frequency. Top) 17.5 kHz, low amplitude, middle) 12 kHz, low amplitude, bottom) 7.5 kHz, low amplitude

Table 10: Average values of the measurements of cavity radius at the projectile tail that are presented in figure 63. The average speed shown was calculated using only the shots where a cavity dimension measurement was made.

Acoustic signal (freq., Amplitude)	Inner radius (mm)		Outer radius (mm)		Average speed (m/s)	n
	Measured mean	Model (@ avg. speed)	Measured mean	Model (@ avg. speed)		
17.5 kHz, medium	7.1 ±0.3 (s=0.2)	7.5	7.9 ±0.3 (s=0.3)	7.8	140 ±2 (s=5)	13
12 kHz, medium	5.9 ±0.3 (s=0.2)	7.4	7.6 ±0.3 (s=0.3)	7.8	133 ±2 (s=9)	30
7.5 kHz, medium	6.8 ±0.3 (s=0.3)	7.5	8.1±0.3 (s=0.2)	7.9	144 ±2 (s=3)	10
CONTROL	-	-	7.6 ±0.3 (s=0.4)	8.0	135 ±2 (s=13)	43

Table 11: Average values of the measurements of cavity radius at the projectile tail that are presented in figure 64. The average speed shown was calculated using only the shots where a cavity dimension measurement was made.

Acoustic signal (freq., Amplitude)	Inner radius (mm)		Outer radius (mm)		Average speed (m/s)	n
	Measured mean	Model (@ avg. speed)	Measured mean	Model (@ avg. speed)		
17.5 kHz, low	6.7 ±0.1 (s=0.2)	8.0	8.1 ±0.1 (s=0.2)	8.1	147 ±2 (s=2)	7
12 kHz, low	6.3 ±0.3 (s=0.3)	7.9	7.5 ±0.3 (s=0.3)	8.1	135 ±2 (s=8)	13
7.5 kHz, low	6.3 ±0.1 (s=0.3)	7.9	8.0 ±0.1 (s=0.2)	8.1	145 ±2 (s=4)	5
CONTROL	-	-	7.6 ±0.3 (s=0.4)	8.0	135 ±2 (s=13)	43

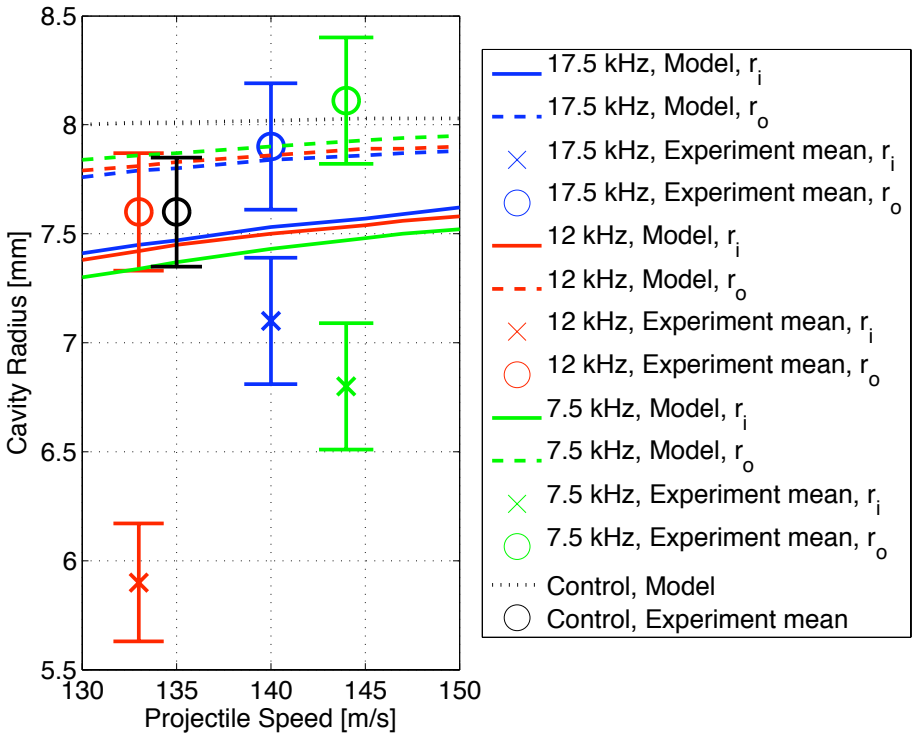

Figure 65: Plot showing the sensitivity of cavity radius to projectile speed for the medium amplitude experiment cases.

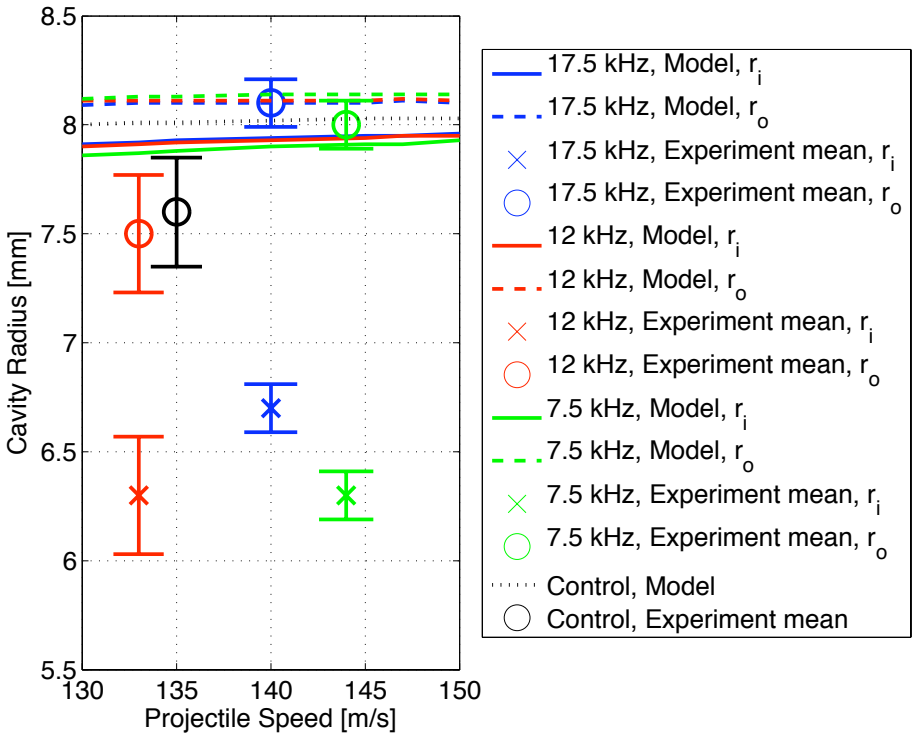

Figure 66: Plot showing the sensitivity of cavity radius to projectile speed for the low amplitude experiment cases.

Over the range of average speeds, the predicted radius only varies by approximately 0.15 mm for the medium amplitude cases and less than 0.05 mm for the low amplitude cases. Considering that the uncertainty in the experimental measurement was 0.3 mm for all of the medium amplitude experiments and 0.1 mm for the low amplitude experiments it was considered reasonable to compare the measured radii for trends in the cavity radius with signal frequency.

The results presented in these figures and tables provide no additional conclusions to those drawn in section 5.3.1.4. If anything, it looks as though the high frequency 17.5 kHz acoustic signal has the least effect. Curiously, the 12 kHz signal seems to have had the greatest effect. This could be due to a measurement error. There is no explanation known to the author at this time. The theoretical predictions indicate that one would expect the effect on the cavity radius to increase with decreasing frequency.

The limited data in the low amplitude cases at 7.5 kHz and 17.5 kHz is due to the fact that the Photron camera was used in those experiments. The fastest available frame rate on the Photron camera was 1000 fps which was not sufficient to be sure of capturing an image of the projectile tail location in every shot and so measurements could not be made for every shot.

5.3.2.5 Target Impact Location

Medium Amplitude Case:

Table 12 shows results of the standard deviation of the impact points in the x and y coordinate directions for the different frequency cases at the medium pressure amplitude level. Also shown in this table are the CEP, the number of shots in each data set, and the statistical significance of the result. The value of the statistical significance

is the p-value discussed in section 5.2.2. Actual impact location plots are shown in the middle row of plots in figure 92, appendix I.

Table 12: Measures of projectile accuracy for the experiment cases with medium level acoustic pressure amplitude and ranging signal frequency

Acoustic signal (freq., amplitude)	Standard deviation (x, y)	CEP (mm)	Number of data points	Statistical significance p-value (%)
17.5 kHz, medium	(8.72, 7.16)	9.39	21	(0.96,23)
12 kHz, medium	(9.58, 9.66)	11.3	32	(0.012,0.002)
7.5 kHz, medium	(9.02, 8.92)	10.6	23	(0.32,0.75)
CONTROL	(6.35, 6.51)	7.56	87	

The results from these experiments show a significant change in the standard deviation for the 7.5 kHz and 12 kHz cases indicated by the p-values being below 5%. The 17.5 kHz case, however, shows an ambiguous result and must be deemed insignificant due to the p-value of 23% in the *y-direction*. Indication is that lower frequency signals have a greater effect. These results will be discussed in greater detail in section 5.4.

Low Amplitude Case:

Table 13 shows results for the different frequency cases at the low pressure amplitude level. Actual impact location plots are shown in the bottom row of plots in figure 92, appendix I.

Table 13: Measures of projectile accuracy for the experiment cases with low level acoustic pressure amplitude and ranging signal frequency

Acoustic signal (freq., amplitude)	Standard deviation (x, y)	CEP (mm)	Number of data points	Statistical significance p-value (%)
17.5 kHz, low	(7.63, 6.84)	8.52	16	(12,35)
12 kHz, low	(7.81, 7.70)	9.13	14	(10, 15)
7.5 kHz, low	(9.12, 7.04)	9.51	15	(1.1,24)
CONTROL	(6.35, 6.51)	7.56	87	

The results from these experiments show an insignificant change in the standard

deviation for all three frequencies, indicated by the p-value being above 5%. The one exception is the low frequency case that shows a significant result in the *x-direction* standard deviation with a p-value of 1% but not in the *y-direction*. This is an ambiguous result; however, looking at the actual data points in the lower left plot in figure 92, appendix I, it looks as though the one anomaly shot located to the right side on the third dashed ring from the center is solely responsible for the significant result in the *x-direction*. Indeed, if this data point was taken out of the calculations the result for the 7.5 kHz experiment was also not statistically significant. The trend in the CEP indicates that when the acoustic frequency decreased, the projectile accuracy also decreased.

Looking at tables 12 and 13 it is seen that all values of standard deviation and CEP are greater than the control experiments. This indicates that the sound does have an effect in all cases, it is just deemed that the probability of the results having come from the control population purely by chance are too great in several instances to make the decrease in accuracy statistically significant.

5.3.2.6 Projectile Speed

Medium Amplitude Case:

Plots of measured projectile speed versus time are shown in figure 67 for the three different frequency cases at the medium amplitude level. A projectile drag coefficient was calculated from these speed measurements and is presented in table 14 along with relevant statistics. Analysis of the projectile speed and drag for the amplitude variation experiments was presented in section 5.3.1.6 where some discussion was given about the measurements used for calculation.

Muzzle speed measurement were not recorded for the 7.5 kHz and 17.5 kHz experiment

cases. These were the last experiments to be run and previous analysis had not included the results because of inaccuracy of the measurements and uncertainty of the development of the supercavity at that point. One of the coils was damaged and it was not deemed necessary to fabricate a new one.

Table 14: Drag coefficients calculated from measured speeds for the varying frequency experiments at medium amplitude. C_D is the drag coefficient, n is the number of measurements, s is the sample standard deviation. The t value calculated is the difference between the sample mean and the control mean in units of the standard error.

Acoustic signal (freq., amplitude)	Mean C_D	n	s	t value	$t_{\alpha=0.05}$
17.5 kHz, medium	1.19	17	0.144	2.07	±2.12
12 kHz, medium	0.95	5	0.142	-1.97	±2.78
7.5 kHz, medium	1.35	20	0.173	6.29	±2.09
CONTROL	1.10	37	0.175		

The 7.5 kHz case is the only one that shows a significant increase in the mean drag coefficient with a t value three times that of $t_{\alpha=0.05}$. Because the t value (see equation (43)) is greater than $t_{\alpha=0.05}$ there is less than a 5% chance that a sample of 20 measurements with a mean of 1.35 came from the control sample. For the other two cases the evidence does not conclude that the observed mean is significantly different from the control case. The 12 kHz case having only 5 data points has to be considered with caution.

Low Amplitude Case:

Similar analysis is presented for the low amplitude experiment cases with varying signal frequency. Plots of measured projectile speed versus time are shown in figure 68 for the three different frequency cases. A projectile drag coefficient was calculated from these speed measurements and is presented in table 15 along with relevant statistics.

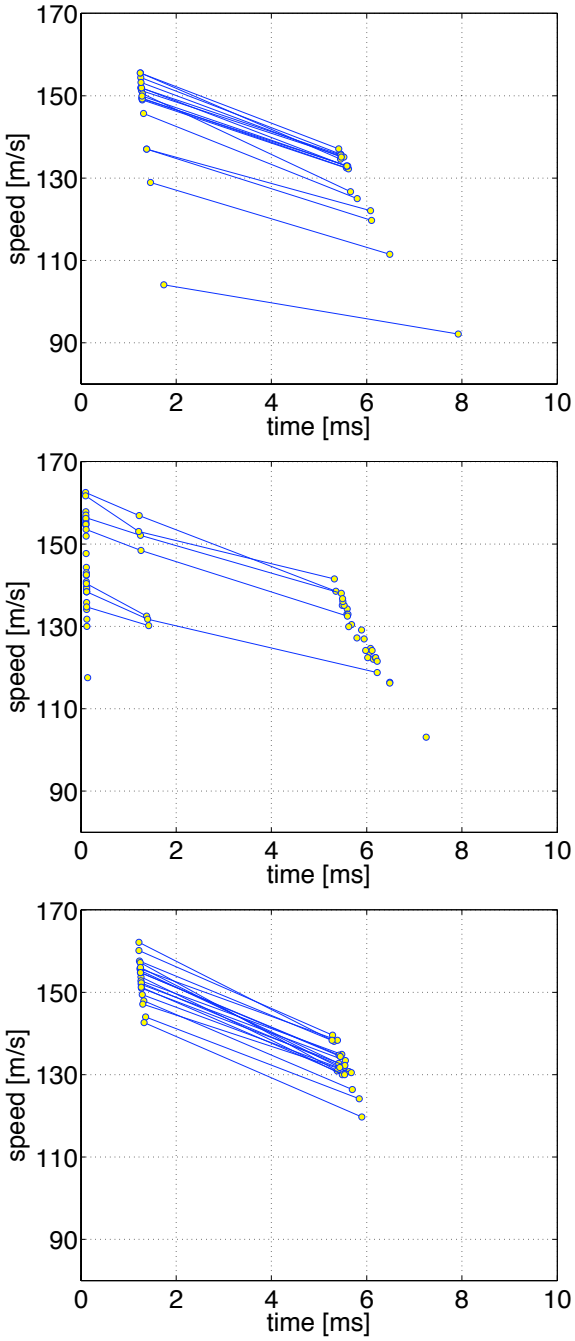

Figure 67: Plots showing measured speed versus time for the experiments cases with varying acoustic signal frequency and at medium level amplitude.; top) 17.5 kHz, medium amplitude, middle) 12 kHz, medium amplitude, bottom) 7.5 kHz, medium amplitude. Data points are represented by markers and were only joined with lines if adjacent points were available.

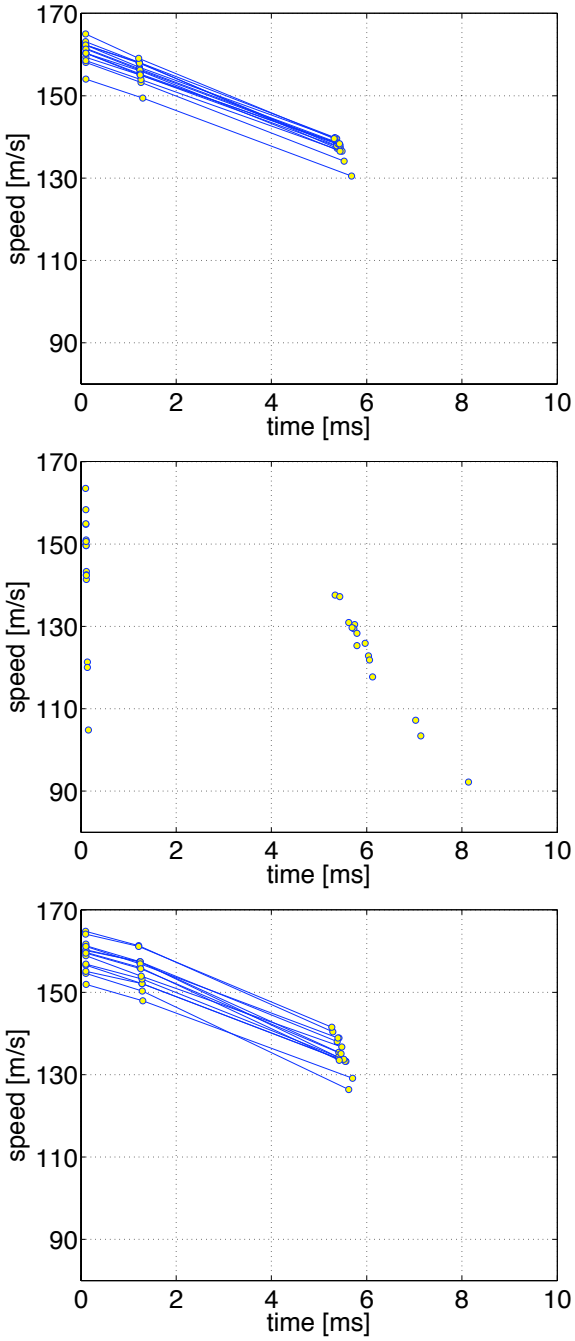

Figure 68: Plots showing measured speed versus time for the experiments cases with varying acoustic signal frequency and at low level amplitude.; top) 17.5 kHz, low amplitude, middle) 12 kHz, low amplitude, bottom) 7.5 kHz, low amplitude. Data points are represented by markers and were only joined with lines if adjacent points were available.

Table 15: Drag coefficients calculated from measured speeds for the varying frequency experiments at low amplitude. C_D is the drag coefficient, n is the number of measurements, s is the sample standard deviation. The t value calculated is the difference between the sample mean and the control mean in units of the standard error.

Acoustic signal (freq., amplitude)	Mean C_D	n	s	t value	$t_{\alpha=0.05}$
17.5 kHz, low	1.14	14	0.075	0.908	$\pm$2.16
12 kHz, low	-	-	-	-	-
7.5 kHz, low	1.28	14	0.137	3.75	$\pm$2.16
CONTROL	1.10	37	0.175		

The 7.5 kHz case is again the only one that shows a significant increase in the mean drag coefficient. For the other two cases the evidence does not conclude that the observed mean is significantly different from the control case.

Both experiments indicate that the lower frequency acoustic signal has more effect on the overall drag force on the projectile body. It is not immediately obvious from the observations why the low frequency signal had an effect on the drag when the other frequencies did not. Theoretical considerations using Logvinovich's model of independent cavity section expansion lead one to the conclusion that lower frequency signals should have a greater effect on the cavity geometry but from the observations and for the conditions in this work that did not appear to be the case. If this were true then the cavity may touch the projectile tail increasing the drag force.

The slightness of the drag increase shows that with the conditions in this work, increasing the drag would not be a viable countermeasure. However, if larger pressure amplitudes could be used and at lower frequencies and the imposed signal could follow the projectile along its trajectory then the increase in drag may have a significant effect.

5.4 Interpretation of the Experiment Results

5.4.1 Introduction

Section 5.3 presented various results from the experiments that were carried out along with some related discussion. The result most pertinent to the use of an acoustic signal as a countermeasure is the observed decrease in projectile accuracy. Significant reductions in accuracy were found for the high and medium acoustic pressure amplitude cases at the 12 kHz signal frequency (see table 7 in section 5.3.1.5) and the medium amplitude case at the 7.5 kHz signal frequency (see table 12 in section 5.3.2.5). Understanding this result becomes an important goal of this thesis. Table 16 summarizes the projectile accuracy result from the experiments.

Table 16: Summary of the projectile accuracy results. A check mark represents an experiment case where a significant reduction in accuracy was observed. A cross mark represents an experiment case where evidence did not conclude that there was a significant reduction in projectile accuracy.

	7.5 kHz	12 kHz	17.5 kHz
high amplitude	-	✓	-
medium amplitude	✓	✓	×
low amplitude	×	×	×

In this section we would like to address the questions set out at the beginning of the work. In particular, what form of cavity alteration might effect the accuracy of the projectile, and what is the desired frequency and amplitude of an acoustic signal used in a countermeasure? An explanation for the reduced accuracy deduced from the research results will provide answers to these questions and also help to guide future studies on related topics. Answers to these questions will be discussed in chapter 6.

5.4.2 Further Investigation of the Results

Further examination and investigation of the target impact location results revealed that the decreased accuracy was due to only a subset of the shots fired with the array on. This subset was comprised of only the shots that exhibited tail-slap in the array focal region.

For each experiment, shots were split into two subsets. One for which tail-slap was observed in the focal region and one for which it was observed not to occur. There were shots for which the occurrence could not be determined and so these were not included in the calculations; therefore, some statistics and shot counts are different from those presented in section 5.3.

The length of the array focal region along its axis ($z-axis$ in figure 43 of section 4.4.4) was measured and discussed in section 4.4.4. The length in the $z-direction$ was found to be 17.5 cm for an acoustic signal frequency of 12 kHz (the length of the focal region was defined as the length of the path along the array axis on which the amplitude of the acoustic pressure was within 3 dB of that at the center of the focus). The recorded images captured approximately 15 cm of the flight trajectory for all of the 12 kHz experiments and so most of the focal region was seen. It was therefore easy to determine from the images whether or not tail-slap occurred in the focal region.

At 7.5 kHz and 17.5 kHz the length of the focal region was found to be 28.5 cm and 11.0 cm respectively. Therefore, the occurrence of tail-slap could be determined with certainty for the 17.5 kHz case but not for the 7.5 kHz case. The focal region of the array extended approximately 6.75 cm above and below the recorded view. Because of this, it is possible that there were shots identified as exhibiting no tail-slap in the focal region that did in fact impact with the cavity wall in the focal region. This could account for the relatively high value of CEP for the "no impact" subset for this

experiment case.

The experiment sets that are presented here are the 12 kHz, varying amplitude set (table 17) and the medium amplitude, varying frequency set (table 18). The low amplitude, varying frequency set is not shown because the accuracy was not significantly effected in any case.

Table 17: Measurements of circular error probable (CEP) for shots identified to have or not have an incidence of tail-slap in the recorded view. Experiment cases with an acoustic signal frequency of 12 kHz and at high, medium, and low amplitude.

Acoustic signal (freq., amplitude)	CEP (mm)	p-value (%)	Number of Measurements
12 kHz, high	11.5	0.21	18 (all)
	13.4	0.55	10 (with impact 56%)
	8.67	14	8 (no impact 44%)
12 kHz, medium	11.3	0.01	32 (all)
	13.1	0.05	19 (with impact 59%)
	7.49	30	13 (no impact 41%)
12 kHz, low	9.13	14	14 (all)
	8.75	36	9 (with impact 64%)
	7.59	31	5 (no impact 36%)
CONTROL	7.62		72 (all)
	8.33		42 (with impact 58%)
	6.93		30 (no impact 42%)

The tables show measurements of the circular error probable (CEP) for experiment cases and for the control experiments where there was no imposed acoustic pressure wave. For each experiment case, values are shown for all of the shots (that is, all of the shots where it was able to be determined whether the projectile tail hit the supercavity wall or not in the viewing section) and for the subsets which did and did not have observed impacts. The third column shows values of statistical significance based on the CEP values. The significance value is the probability that the CEP could be equal to or greater than the observed value and have come from the control

Table 18: Measurements of circular error probable (CEP) for shots identified to have or not have an incidence of tail-slap in the recorded view. Experiment cases at the medium acoustic pressure amplitude and at signal frequencies of 7.5 kHz, 12 kHz, and 17.5 kHz.

Acoustic signal (freq., amplitude)	CEP (mm)	p-value (%)	Number of Measurements
17.5 kHz, medium	9.39	7.8	18 (all)
	9.89	18	10 (with impact 56%)
	7.88	25	8 (no impact 44%)
12 kHz, medium	11.3	0.01	32 (all)
	13.1	0.05	19 (with impact 59%)
	7.49	30	13 (no impact 41%)
7.5 kHz, medium	10.3	1.7	19 (all)
	11.1	7.7	9 (with impact 47%)
	8.40	15.3	10 (no impact 53%)
CONTROL	7.62		72 (all)
	8.33		42 (with impact 58%)
	6.93		30 (no impact 42%)

population purely by chance. The significance for the subsets of *with* and *without* tail-slap were calculated based on the corresponding control subsets. The fourth column in the table gives the number of measurements associated with each CEP calculation.

It is necessary to further discuss the method by which the CEP was calculated for tables 17 and 18. The CEP is the radius of a mean centered circle because it is calculated based on the standard deviation which itself is a measure of the spread of the data set from the mean. The CEP for each experiment set and each subset is therefore based on a different mean. This was relevant because it was an increase in the spread of the data that was being investigated. It has already been found that the sound had no effect on the location of the data centroid. Additionally, the tail-slap appears to have had no consistent effect on the mean. This was probably because the tail-slap occurred at a random angle due to the symmetrical nature of the setup. By nature of the method of calculation it is possible that the subsets both have a CEP

less that that of the whole set, as in the 12 kHz low amplitude case in table 17.

Calculations were also done for the same shot sets but based on an error from the centroid location of the control shots. The centroid of the control shots can be thought of as the point at which the firing mechanism is aimed at. This measure, therefore, includes any change in the impact location and not solely the spread. The results from this showed no significant change in the outcome for the experiment cases in tables 17 and 18.

Both tables highlight the assertion that the subsets exhibiting tail-slap in the focal region were the main contributor to the decreased accuracy. In table 17 the high and low amplitude cases, which show clear overall decreased accuracy, have p-values of 14% and 30% for the subsets that did not exhibit tail-slap. In table 18 a similar observation is made for the 7.5 kHz and 12 kHz cases. The 7.5 kHz case, however, is less convincing. The overall decrease in accuracy is represented by the p-value of 1.7%, but the subset with impact shows a 7.7% chance that the observations could have come from the estimated control population. It could be that there are not enough data points to establish significance. Thirteen data points with a CEP of 11.1 would have established statistical significance. Also, some of the no-impact cases could have in fact exhibited tail-slap in the focal region which would have altered the result. The reason for this error, as mentioned before, is that the entire focal region was not observed in the experiments.

The low amplitude, 12 kHz case and the medium amplitude, 17.5 kHz case clearly show insignificant differences from the control set for all subset values.

5.4.3 Hypotheses

In looking for an explanation as to why the shots that exhibit an instance of tail-slap when the acoustic signal was present are less accurate we will focus on mechanisms by which the forces on the projectile tail during tail-slap could be effected by the presence of the sound. Before proceeding to this, however, there are three questions that must be addressed in order to assure that tail-slap in the presence of sound is the pertinent phenomenon.

1. The first question is whether or not the shots exhibiting tail-slap are generally less accurate even in the absence of sound. The fact that the shots that exhibited tail-slap at this location were less accurate could be attributed to general projectile-dynamics and not the acoustic signal.

2. The second question is whether or not faster or slower shots were more likely to exhibit tail-slap within the array focus. If either were true then it could be said that the acoustic signal had more effect on the faster or slower projectiles somehow and the correlation between tail-slap at that location and accuracy may not be a direct correlation. Also, again, the control shots should be examined for a correlation between speed and accuracy because it may be that, in general, faster or slower shots were more or less accurate and that a bias in speeds for shot groups with or without observed tail-slap could explain the difference in accuracy.

3. The third question is whether or not these tail-slap instances were caused by some other mechanism acting at the cavitator that the presence of the sound wave was responsible for. In this case, the sound effects something else that caused the tail-slap and therefore the interaction at the tail would be of secondary importance in determining the cause of the reduced accuracy.

Addressing Question 1:

It is seen by examining the control shots that even in the absence of sound, shots that exhibited tail-slap at the location of the array focal region were generally less accurate. The first question is addressed in the way that the statistical significance values were calculated. Significance for the subsets of *with* and *without* tail-slap were calculated based on the corresponding control subsets. Therefore, *without impact* experiment case shots were compared to *without impact* control shots, and *with impact* experiment case shots were compared to *with impact* control shots. Thus, the lower accuracy of the control shots exhibiting tail-slap was accounted for and the experiment cases were still seen to have further significant decreases in accuracy.

The general trend of decreased accuracy for the *with impact* versus *without impact* control subsets can be explained considering the dynamics of a supercavitating body. On examination of the control experiments in which a view of the entire trajectory was recorded it was observed that most of the shots that did not exhibit tail-slap at the array focus either did so only once near the end of the trajectory or not at all. Very few shots had tail-slap occurring both before and after the focus. It was also observed that if there was an impact in the focal region then there was another after, near the trajectory end. Additionally, it was generally observed that more frequent impacts were more severe, that is, they penetrated deeper into the cavity wall and for a longer duration. Higher projectile angular velocity requires more impulse during instances of tail-slap in order to reverse the direction of rotation and the greater angular velocity results in more frequent occurrences of tail-slap. Shots with more frequent and more severe tail-slap impacts generally lead to more spread in the impact location because there is more motion in the horizontal plane due to greater impulse during tail-slap. The projectile has a winding trajectory because it is subject to transverse forces.

Addressing Question 2:

For investigation of the second question it was necessary to look for a correlation between projectile speed and observations of tail-slap at the array focus. The shots for each experiment case were separated into two groups, one containing shots above the median speed and one below (both including the median if there were an odd number of shots) and then the number of those that exhibited a tail-slap occurrence at the array focus was determined.

Referring to table 17, for the 12 kHz, high amplitude experiment case, it was seen that there were ten shots with an observed impact. It was found that six of these were in the slower half and four were in the faster half (split of 60/40). For the 12 kHz medium amplitude and 12 kHz low amplitude cases the splits were 53/47 and 44/65 respectively. This indicates that there is no correlation between projectile speed and an occurrence of tail-slap at the array focus location for these experiments.

Looking at the medium amplitude frequency variation experiments (table 18), the 17.5 kHz, 12 kHz, and 7.5 kHz cases has splits of 50/50, 53/47 and 44/56 (slow/fast) respectively. This again indicates that there is no correlation.

A similar investigation to that correlating tail-slap in the presence of an acoustic signal with accuracy was done in an attempt to correlate accuracy with projectile speed. This determines whether the sound had a greater effect on faster or slower shots regardless of tail-slap incidences. No correlation was found for these experiments.

Analysis of the control shot data showed that, generally, the slower shots were less accurate than the faster shots. This trend was not seen in all of the experiment cases with the sound signal present which is probably due to the fact that the sound was also effecting the dynamics.

Addressing Question 3:

Now the third question is addressed: Are the tail-slap instances in the array focal region during shots with the imposed sound field caused by some other mechanism for which the presence of the sound is responsible? To answer this question all that needed to be done was to determine whether the occurrence of a tail-slap occurring in this region was more likely when the sound was on than when it was off.

The fourth column of tables 17 and 18 contains the relevant statistic. The control data set shows a split of approximately 60% to 40% for "with-impact" versus "no-impact" observations. Looking at all of the non-control data it is seen that all of the experiment cases show a similar split, except for the 7.5 kHz, medium amplitude case which has approximately 50/50 split.

Therefore, it can be concluded that the assertion still holds. The observed tail-slap incidences occurred by chance and it was an interaction of the acoustic signal with the projectile during an instance of tail-slap that was responsible for the decrease in accuracy.

With these three questions addressed we can now look into the reason why the projectile dynamics were effected when the sound wave was present during an occurrence of tail-slap. The following sections present possible explanations and discuss their merits and pitfalls. The experimental data obtained was not sufficient by itself to prove or disprove any explanation. However, with the combination of the available data, relevant theory, and intuition, one can postulate probable explanations for the observed phenomenon and arrive at a likely hypothesis. It is indeed likely that there were several things acting together that resulted in the overall effect so the discussion is presented in a way so as to provoke thought as regards to each line of reasoning.

5.4.3.1 *The Hypothesis that Changes in Cavity Geometry Adversely Affect Projectile Accuracy*

Possibly the most obvious idea is that the effect the pressure signal had on the shape of the supercavity wall was responsible for the reduced accuracy observed. If there was an instance of tail-slap when the projectile was in the array focus then the tail of the projectile would interact with the corrugated gas/liquid interface instead of the usual smooth surface.

The corrugations on the cavity wall have no, or very little velocity along the projectile trajectory in an inertial reference frame (any fluid velocity is due to bulk motion of the fluid relative to an inertial reference frame). Cavity cross-sections expand and contract in a plane perpendicular to the trajectory just as undisrupted cavity sections would. The main difference due to the presence of the sound is the rate of expansion and the maximum diameter that the cavity section reaches. Therefore, the relative speed between the corrugations and the projectile tail is equal to the speed of the projectile. The projectile tail hitting these ripples in the interface would cause an applied force to the projectile tail. The frequency of the applied force would be equal to the frequency of the acoustic signal because the wavelength of the corrugations is equal to the speed of the cavitator times the period of the acoustic wave.

Examining the amplitude variation experiments at 12 kHz provides insight into this hypothesis. The low pressure-amplitude case did not conform to the hypothesis. The measured disturbances to the cavity shape due to the acoustic pressure-wave were comparable for all three of the pressure amplitudes used. This was shown in figure 57 and table 6. Therefore, if it was the shape of the cavity wall that was responsible for the decreased accuracy then the accuracy of the low-pressure experiment case should have been effected in a similar manner to the higher pressure cases. As this situation was not the observed, it can be concluded from the research that disruption to the

shape of the cavity/water interface alone cannot be responsible for the adverse effect on projectile accuracy. Indeed, a similar situation was observed for the alternate acoustic signal frequencies.

It was a possible concern that the forces at the tail as the projectile hit the corrugations could cause resonance behavior of the projectile body. The fundamental bending mode natural frequency of the projectile body was calculated. Two different boundary conditions were investigated because the actual conditions were unclear. Boundary conditions for the calculation were: 1) fixed at the cavitator - free at the tail; and 2) free at the cavitator - free at the tail. The resonance was calculated using the software $SolidWorks^{TM}$ and found to be approximately 150 Hz for the fixed-free case and 3200 Hz for the free-free case. Both are much less than any excitation frequency in the experiments. Therefore, excitation at resonance was not likely to have been responsible for any altered projectile dynamics. The finite element model calculation was confirmed using a theoretical calculation for the fundamental resonance of a beam for the two cases [77].

5.4.3.2 The Hypothesis that Acoustic Cavitation Alters the Medium and Thus Adversely Affects Projectile Accuracy

Another hypothesis is that acoustic cavitation in the water changes the properties of the fluid around the supercavity which effects the hydrodynamics during tail-slap. This alters the forces on the projectile and subsequently influences the projectile dynamics. An explanation consistent with this hypothesis would conform to the experiment results. The following paragraphs support this assertion.

To recall, for the 12 kHz, amplitude variation experiment set, the observation was that the projectile accuracy was similarly effected in the cases where the supercavitating body was subject to high and medium amplitude sound pressures but not

significantly effected in the low pressure amplitude case. This fits with the observation that there was severe acoustic cavitation present in the water for the high and medium acoustic pressure-amplitude cases and none, or only very light cavitation, for the low amplitude case. These cavitation observations were made in the absence of a cavity at the array focus. Experiments with a closed-cell styrofoam model of the supercavity (see section 5.3.1.2) showed that only the high amplitude case caused sufficient pressure amplitude in the water surrounding the model to cause obvious visible acoustic cavitation. It is possible, however, that the cavitation bubbles present before the arrival of the projectile were still present around the newly formed supercavity, and it is also possible that this already present cavitation caused the medium to be more susceptible to cavitation facilitating acoustic cavitation around the supercavity in the experiments. The images from the high speed digital camera clearly showed cavitation in the water surrounding the supercavity in the high and medium amplitude cases but not in the low amplitude case.

A similar situation to the 12 kHz experiments was observed for the 7.5 kHz experiments. A significant decrease in accuracy was observed for the medium amplitude experiment case but not for the low amplitude case. In the medium amplitude case there was severe acoustic cavitation in the water in the absence of a supercavity, and the pressure amplitudes were close to the cavitation threshold and light acoustic cavitation was observed when the styrofoam model was present. In the low amplitude case there was no cavitation, or only very light cavitation present in the water in the absence of the model and none in the presence of the model.

Finally, for the 17.5 kHz experiments, there was no significant decrease in projectile accuracy for any experiment case. Acoustic cavitation was less severe at this frequency than at the other two lower frequencies for a given pressure amplitude. Even in the absence of a supercavity at the array focus there was only light cavitation present in

the water at the medium pressure amplitude.

For acoustic signals of equal frequency one would expect acoustic cavitation to be more severe at higher amplitudes and this appears to be the case both from visual inspection of the images and from the sound pressure spectral analysis carried out in section 4.4.6. For acoustic signals of different frequency but with equal pressure amplitude, one would expect cavitation to be more severe at lower frequencies because the medium is subject to the reduced pressure for a longer period of time. This was also confirmed to be the case by experiments.

As mentioned previously, the effects that acoustic cavitation had on the medium could have influenced the dynamics of the supercavitating projectile. Some scenarios are discussed in the following.

Acoustic Cavitation Increases the Compressibility of the Medium Causing Changes in the Hydrodynamics:

The effects of acoustic cavitation on the properties of the medium were discussed in section 2.2.3 of chapter 2. Consider equations (23) and (24) which are repeated here:

$$\rho_{eq} = \nu\rho_g + (1-\nu)\rho_w \qquad \text{(equation (23) repeated)}$$

$$K_{eq} = \nu K_g + (1-\nu)K_w \qquad \text{(equation (24) repeated)}$$

The density of water (ρ_w) is three orders of magnitude greater than that of water vapor (ρ_g). Therefore, it is seen by equation (23) that if the gas fraction (ν) is low then the second term on the right hand side is dominant and the density change is small making the equivalent density close to that of water.

The compressibility of water (K_w) is four orders of magnitude smaller than that of

water vapor or air (K_g) [10]. Therefore, looking at equation (24) it is seen that even for small gas fractions the second term on the right hand side is not dominant and there can be large changes in the bulk compressibility. The overall compressibility increases due to the presence of the bubbles compared to that of the pure liquid.

The gas fraction in the water during acoustic cavitation in the experiments was hard to measure directly. An attempt was made to estimate the gas fraction of the fluid around the supercavity using images from the high-speed photography. The value measured was approximately 0.1%. Higher frequency sound signals appeared to produce a higher density of smaller bubbles but the measured gas fraction was about the same for each frequency. Gas fractions could actually have been significantly higher than this, however, due to a few factors. The bubbles were constantly changing in size and transient cavities would collapse during the high pressure cycle of the sound wave. The camera exposure time was less than one period of the sound wave so the instant captured may have represented a low estimate. Additionally, there were likely to be very small bubbles present that could not be observed in the images at all, and bubbles not seen due to the short depth of field in the images. It will be assumed for the following discussion that the gas fraction could have been as high as 1%.

If the gas inside the cavitation bubbles is assumed to be water vapor and the gas fraction is 0.1% then the compressibility of the mixture would be around $7.4e{-}9\ m^2/N$ which is 16.5 times greater than that of water. If the gas fraction were as high as 1% then the compressibility would be around $70e{-}9\ m^2/N$, or 155 times greater than that of water. The compressibility of water containing vapor bubbles may also be less than this because when subject to increased pressure the bubbles tend to collapse due to condensation [61] as opposed to resisting the collapse due to increasing pressure in the bubble as is assumed in calculating the compressibility. The acoustic cavitation bubbles likely contained some mixture of air and water vapor because the water in

the experiment was not degassed and the cavities may have been formed from very small cavitation nuclei such as air bubbles on tiny solid particulate in the water.

Whether or not a change in the bulk compressibility had a direct effect on the forces on the projectile is uncertain. It is usually the case in fluid flow problems that at low Mach number (below 0.3 and sometimes as high as 0.8 without significant errors [3]) the fluid can be considered incompressible, and at higher Mach numbers the compressibility manifests itself most significantly in the form of shock waves. The shock waves occur due to the finite speed at which pressure signals can propagate in the fluid. A rigid body interacting with a fluid does not normally cause a bulk compression of the fluid. Additionally, if the medium were compressed upon impact, the effective spring would be highly nonlinear and would become very stiff with a small compression. This is because the void fraction was low and the cavitation bubbles would condense when subject to the increased pressure due to their vapor content.

It is possible that the projectile tail was traveling at a high Mach number (based on the sound speed in the bubbly mixture) during tail-slap when the fluid surrounding the supercavity was acoustically cavitating. A large increase in the compressibility coupled with the negligible change in medium density is well known to have drastic effects on the sound speed in the bubbly mixture [15, 16, 61, 104]. The decrease in the sound speed would increase the flow Mach number. A plot generated using equation (26) for the sound speed as a function of void fraction is shown in figure 69.

The markers on the plot indicate the expected range of void fraction in the experiments (0.1% to 1%) and the upper and lower mean observed projectile speeds. The plot highlights the fact that it is feasible for the projectile tail to have been traveling supersonic relative to the local mixture sound speed during tail-slap. Mach numbers were likely in the range of 1.3 to 1.4 for $\nu = 0.01$.

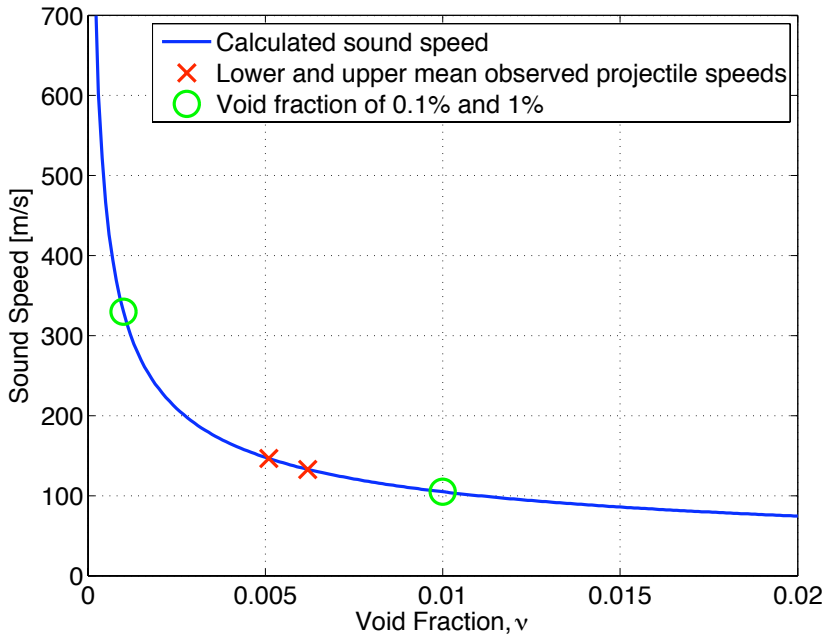

Figure 69: Speed of sound in a bubbly fluid. Mixture of air and water at 109 kPa.

The generation of shock waves could be responsible for the observed reduction in accuracy. Where the projectile tail protrudes through the cavity wall there would be a compression shock, the location and the angle of which would be determined by the Mach number and the body shape. At the transom of the projectile there would be an expansion shock or fan. This general situation is suggested in the literature for flow patterns over a supersonic projectile with a cone shaped nose with a cylindrical hull or flat base, although the details would be somewhat more complex [3, 9, 76, 103]. High-speed compressible flows involving bubbly liquids present additional complications compared to conventional compressible aerodynamics or hydrodynamics due to the presence of the bubbles that cause a frequency dependent sound speed and high attenuation [37, 38]. Figure 70 shows a schematic of the simplified situation. Grant *et al* (2006) [38] suggest that the drag on a body in a bubbly liquid at a given Mach number based on the mixture sound speed is similar to that on a body in a single phase liquid at the same Mach number based on the sound speed in that liquid.

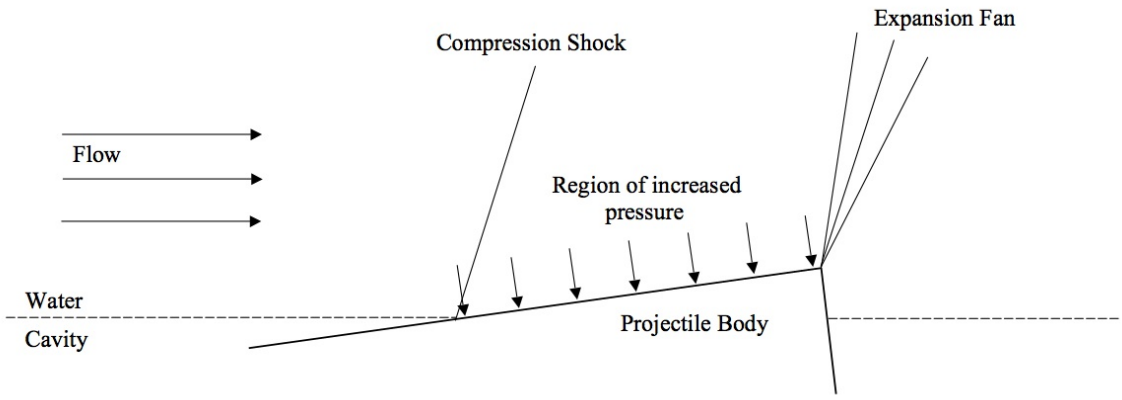

Figure 70: Schematic showing shock waves in the flow during tail-slap

The shock waves radiated from the body during tail-slap have an associated energy and momentum that they carry [26, 93, 103]. If one imagines a system that includes the projectile body and the disturbed fluid then it is apparent that the momentum of the body must be effected. The situation is asymmetric since the tail-slap occurs only once in the array focal region and, therefore, only on one side. The wave emanates at some angle and so there is a component of the momentum or intensity in a horizontal direction. A change in the linear momentum of the projectile body in a horizontal plane would effect the accuracy.

Acoustic Cavitation Increases the Susceptibility of the Medium to Hydrodynamics Cavitation:

Another consideration is that the acoustic cavitation in the water surrounding the supercavity increased the susceptibility of the medium to hydrodynamic cavitation and thus altered the hydrodynamics of the flow over the section of the tail that penetrated through the cavity wall. The tail of the projectile in the experiments had a cone shape which transitioned to a cylinder for the aft most 0.3" of the tail before the transom (see projectile drawing in appendix B). If the secondary cavity formed by the tail itself during tail-slap was formed on the shoulder between these

two sections or if it was formed at the transom, the planing forces on the tail would change significantly in magnitude, direction, and location of action.

If the additional acoustic cavitation in the water made the medium more susceptible to cavitation then the cavity may have formed at the shoulder instead of the transom for certain angles of attack. This would have resulted in the tail penetrating further into the cavity wall and for a longer period altering its dynamics.

On the other hand, it is likely that this region was highly susceptible to cavitation anyway, given that there were often small bubbles on the supercavity surface (it was rarely smooth enough to see through) and that gasses may have been entrained from the existing supercavity.

On examination of the images and movies from the high-speed digital camera it was seen that the location that the secondary cavity formed changes. There was not enough information available to determine whether this was purely a function of angle of attack, or speed, or whether it was effected by the presence of acoustic cavitation in the water.

CHAPTER VI

CONCLUSIONS

This chapter begins with a brief synopsis of the research in section 6.1, followed by discussion of the research questions in section 6.2. Research contributions to the field of acoustics and cavitation and the significance of those contributions are listed in section 6.3. Lastly, section 6.4 discusses directions for future work both by developments and expansions of the current research and directions for additional future studies.

6.1 Summary of the Work

During the course of the research an experiment was designed, built, and tested that facilitates the study of high level acoustic signals on the characteristics of the supercavity envelope around a free-flying projectile. A series of experiments were conducted using the apparatus to demonstrate the effect of a gated sinusoid at three different signal amplitudes and at three different frequencies. The purpose of the experiment was to investigate the potential use of the method as a countermeasure to supercavitating torpedoes. Relevant data was recorded and analyzed regarding the effects on the dynamics of the supercavitating body.

Theoretical models found in the open literature were used to simulate the dynamics of the supercavitating projectile and to investigate the effects of an external acoustic signal on the development of a supercavity. Experimental results helped to validate the models and, in turn, the models were used to help explain the experiment outcomes.

Positive results were found which show that the accuracy of a supercavitating projectile can indeed be adversely effected by the sound signal. Based on discussions in section 5.4 of chapter 5, hypotheses have been developed that address the pertinent question about what mechanism actually causes the reduction in projectile accuracy that has been observed in the experimental work.

Interestingly, although it was intended or hypothesized initially that it would be an expansion or contraction of the supercavitating envelope that would be the mechanism of disturbance, evidence suggests that in the research conducted, another mechanism looks more probable. In the opinion of the author, the most likely hypothesis that agrees with the recorded data is as follows: under certain circumstances, a high-level pressure wave causes acoustic cavitation in the medium surrounding the supercavity. This changes the properties of the medium so that when the projectile impacts with

the cavity wall as a mechanism of its stability, the hydrodynamics during impact are altered. Acoustic cavitation bubbles reduce the local sound speed in the medium increasing the Mach number of the flow causing compressible flow phenomenon. The shock waves formed carry energy from the system and alter the pressure distribution on the body altering the projectile dynamics.

This being said, it is not ruled out that alterations in the cavity geometry caused by an acoustic signal could be used to alter the dynamics of a supercavitating torpedo. It is possible that this effect contributes to the decreased accuracy observed with the drive signals used, and it is likely that lower frequency excitations could have more of an effect on cavity geometry which is discussed in section 6.4 on future work.

It was also found that the low frequency sound signal (7.5 kHz) caused an increase in the drag force on the projectile for both of the pressure levels used. Indication from the observations was that for the conditions in this work, increasing the drag would not be a viable countermeasure. However, if larger pressure amplitudes could be used and at lower frequencies and the imposed signal could follow the projectile along its trajectory then the increase in drag may have potential to be used in a countermeasure.

6.2 Discussion of the Research Questions

The research questions set out at the beginning of the work (section 1.5) drove the direction of the research and the outcomes have shed light on the answers and understanding of the questions themselves.

It was found that an acoustic signal does have an effect on the growth of a supercavity. The effect on the shape of the envelope as a result of the pressure signals that were used have been presented. The greatest effect, at the signal frequencies studied in

this work, were due to changes in conditions at inception of the cavity sections. A high pressure at inception caused the cavity section to grow faster initially and reach an ultimately larger diameter. A low pressure causes the opposite effect. The fact that the average acoustic pressure is zero meant that the overall shape was the same but with corrugations imposed on the surface. It was also found that at pressures great enough to acoustically cavitate the water, the net positive pressure resulted in arresting the overall growth of the supercavity.

As mentioned in section 6.1, it was found that the accuracy of a supercavitating projectile could be adversely effected with an attainable pressure level. However, the disruption to the cavity itself is not thought to be the cause of the effect, but instead, an alteration of the medium surrounding the supercavity. The dynamics were effected and caused a diversion on the projectile but global stability of the body was not overcome.

The research has shown that causing acoustic cavitation in the water surrounding the supercavity is desirable when using a high level sound signal to reduce the accuracy of the projectile. More severe cavitation caused by higher sound pressure levels at the focus is thought to be desirable because the void fraction would be increased, further increasing the Mach number and therefore the angle and strength of the compression shock.

Lower frequency sound signals are thought to be more desirable. A lower frequency signal will cause more severe acoustic cavitation at a given pressure amplitude and is believed to have a greater effect on the cavity geometry. Frequencies lower than those used in this work and at a greater amplitude have the potential to arrest cavity section growth so that the tail is wetted and the drag force is increased.

The question addressing instability of the projectile was not answered. It was not

determined how one would cause the projectile to become unstable so long as the supercavity is maintained.

6.3 Thesis Contributions

The following list summarizes the contributions of the research:

1. A low-cost experiment for study of supercavitating projectiles in the laboratory environment has been developed. The experiment design has intentionally been made low-cost and easily replicable for future applications.

2. Experimental investigation and results of the effects of an imposed acoustic pressure wave on a natural supercavity.

3. Experimental investigation and results of the effects of an imposed acoustic pressure wave on the dynamics of a free-flying supercavitating body.

4. Hypotheses have been developed about the mechanism by which an imposed sound field can decrease the accuracy of a supercavitating weapon. The hypothesis that seems most likely and agrees with the experiment results has been highlighted.

The contributions of the research are significant in a number of respects:

- The significance of this research to the field of acoustics and cavitation is that no other similar work has been done to date, both on the effects of external acoustic pressure waves on supercavity development and on the on the supercavitating body dynamics.

- This ground work makes it practicable to pursue research on other aspects of using the method as a countermeasure, such as design of an array and algorithm to adaptively focus sound on an incoming weapon.
- It also opens the door for future work on optimization of the effect and on possible enhancements.

6.4 Future Work

This research has addressed some of the questions regarding a proof of concept study on an acoustic countermeasure to supercavitating torpedoes. As such, there are many open-ended questions still to be answered both as regards the concept and the ultimate goal of a practical application. Section 6.4.1 discusses recommendations of developments to the current work and section 6.4.2 discusses suggested research directions for additional future studies.

The results of this research have concluded that it is indeed possible to have a detrimental effect on the accuracy of a supercavitating weapon using an acoustic signal; however, it has not been demonstrated that one can consistently and predictably alter the trajectory.

6.4.1 Developments of the Current Work

The most pressing research to follow this work would be aimed at obtaining evidence supporting or rejecting the proposed hypothesis. An experiment whereby bubbles in the water were produced by alternative means would provide useful evidence. If the accuracy of the projectile were still effected then it would confirm that it was the presence of the bubbles that was responsible and not some other consequence of the presence of the sound signal. Varying the void fraction of the bubbly mixture, and

therefore the medium sound speed, could identify if there were a significant effect as the projectile tail transitioned from sub- to super-sonic regimes.

The work carried out in this thesis, regarding the *acoustic* countermeasure, could be expanded in several ways. Some possibilities and recommendations are discussed in the following sections.

6.4.1.1 Conducting Experiment Cases with a More Comprehensive Range of Amplitudes

With the existing apparatus, experiment cases could be done with a with a larger range of acoustic pressure amplitudes. Decreasing the amplitude further could determine if there is a threshold pressure for the effect on the cavity shape. The range used in this work showed very little change in the alterations to the cavity shape.

With additional higher power amplification, the source transducers could be driven harder to attempt to increase the gas fraction in the water caused by acoustic cavitation to determine if there is significant advantage to attaining higher acoustic pressure amplitudes.

6.4.1.2 Conducting Experiment Cases with a More Comprehensive Range of Frequencies

With alternative acoustic transducers, the range of frequencies investigated could be greater. This would provide the opportunity for a few additional investigations discussed in the following paragraphs.

Work involving a wider range of frequencies could be targeted at determining if there are excitation frequencies that provoke instabilities in the supercavity wall. The bubble resonance frequency is likely to be much lower than any of the tested frequencies;

it is probably on the order of 100 Hz. It is also possible that there are additional instabilities in the cavity wall at higher frequencies than resonance that could be triggered using an asymmetric field.

Sustained high pressures during a low frequency signal could reduce the cavity diameter sufficiently for the cavity wall to close in on the projectile tail which would increase the drag force significantly. In the experiments in this work a frequency of around 1000 Hz would provide a positive pressure for the duration of the window of opportunity for affecting the cavity in the vicinity of the projectile. The window of opportunity is the time it takes for the projectile to travel its own length. This is because, viewed in an Eulerian reference frame, the situation can be seen as expanding and contracting cavity cross-sections through which the projectile passes, and once the tail has passed through a section, any future alterations can have no influence on the projectile body. For the 63.5 mm (2.5") long projectile traveling at 130 m/s the window duration is 0.488 ms which is approximately half of the period of a 1000 Hz wave.

It has also been suggested that subjecting the supercavity to a sustained low pressure could increase the diameter of the cavity significantly which could decouple the control surfaces of a torpedo with the cavity wall. Consideration of supercavitation theory and experimental results have shown that this is probably not a likely situation to be able to achieve. Very low cavitation numbers have little effect on the cavity shape in the vicinity of the projectile. Additionally, pressures lower than around two to three kilopascals cause acoustic cavitation in the water at the submersion depths in the experiment, which limits the amplitude of the low pressure that can be used.

A transducer that could produce a high-amplitude, low-frequency signal must have a high volume displacement. This is due to the low mechanical radiation impedance, which is a consequence of the wavelength being large relative to the source dimensions.

A source that relies on vibrating piezoceramic as the radiating surface, although it can have a low resonance frequency, cannot produce large volume displacements.

There are various methods of producing high-amplitude, low-frequency signals. In fact, this has been a focus of research in the School of Mechanical Engineering here at Georgia Tech [60]. Two possible alternative acoustic sources are the following:

Flextensional Transducer: A flextensional transducer achieves large volume displacements by taking advantage of leverage on a flexible shell [79]. The external shell is elliptical in shape and has a stack of piezoceramic elements inside along the major axis. Excitation of the ceramic stack causes strain in the major axis. The flexing of the shell provides the large volume displacement needed for high-amplitude low frequency waves.

Butler et al. at NUWC in Rhode Island have demonstrated a six element, directional, flextensional transducer array with each element having a TVR of 152 dB re: 1 μPa/V at 1 m at 885 Hz [14].

Air Gun: Air gun acoustic sources are most often used for seismic exploration, for example, searching for oil under the ocean floor. They are capable of producing high-amplitude, low-frequency impulsive signals. At the most basic level, an air gun transducer works by venting high-pressure air into the water, forming an air filled cavity, which expands and contracts violently producing and radiating sound [7]. Barger and Hamblen report typical pressure peaks of around 9 bars at 1m and a frequency of 120 Hz (period of approximately 8.3 ms). Discussion of air gun arrays is also presented.

6.4.1.3 Subjecting the Cavity to an Asymmetric Pressure Field

The effect on the accuracy of the supercavitating body in this work was limited to an increase in the spread of the impact locations, which was quantified by an increase in the standard deviation or of the circular error probable (chapter 5). A more desirable outcome for the use of the method as a countermeasure would be to affect the centroid of the impact locations and thus divert the weapon, possibly in a predictable manner. The symmetric pressure field that the projectile passed through in the experiments was not expected to produce a bias in the impact locations; however, it may be possible to achieve a bias with the use of an asymmetric field.

Subjecting the supercavity to a large pressure gradient may affect its growth in an asymmetric way and thereby produce a bias in the impact locations.

Producing a wave coming from only one side of the supercavity may cause acoustic cavitation to occur on only one side. If the hypothesis is true, that cavitation bubbles alter the hydrodynamics during tail-slap, then we would expect this effect on only one side which may result in a bias of the impact locations. If the acoustic signal could be present during a large portion of the trajectory by using an adaptive focusing technique then this would have a cumulative effect and may be able to divert the projectile significantly over a long trajectory.

6.4.1.4 Optimization and Enhancement of the Effect

Following the addition of the capability to investigate a larger range of frequencies, one would be in a position to investigate optimization of the effect, looking for the optimum center frequency, bandwidth, and waveform. It would also be interesting to determine whether the effect could be enhanced by way of seeding the water with particulate, or by mixing or dissolving some compound in the water.

6.4.2 Suggested Research Directions

It was highlighted in section 6.3 that one of the main significances of this research is that it constitutes ground work that makes it practicable to pursue research on other aspects of using the method as a countermeasure. Future research should be targeted at investigating these other aspects.

Additionally, future work should be done to scrutinize the hypotheses presented in section 5.4 of chapter 5 on the mechanism by which the presence of the acoustic signal effects the projectile dynamics.

6.4.2.1 Work Towards a Practical Application

Focusing Acoustic Signals on Real Moving Targets:

One major aspect of working towards a practical application is the development of an acoustic source array capable of focusing the required pressure amplitudes at desired locations in the ocean environment. In practice the array may be attached to the hull of a surface ship, be towed behind a ship or submarine, or consist of a battery of sources on a permanent structure protecting a harbor.

The research would involve the development of an algorithm capable of operating the array using an adaptive focusing technique. This would detect the presence of an incoming weapon and focus a sound wave on the target, correcting for target motion, and allowing for continual or periodic imposition of the sound wave on the incoming weapon. Research would include both theoretical/numerical modeling and experimental demonstration showing proof of concept, design requirements, and whether existing equipment owned by the navy could be utilized. Steering of a narrow directivity pattern would be required or use of time reversal techniques that, in shallow

water situations, could take advantage of reflections from the water surface or from the ocean floor in cases involving long ranges and/or fast bottoms. Additions to this investigation could include incorporation of multiple arrays to provide additional motion clues.

Larger Scale Testing:

Another necessary investigation required in developing a practical application is the extension of the work to a large scale. This research has concentrated on small projectiles (2.5" in length), short trajectories ($\sim$ 1.1 m), and a short fixed focal region in which the acoustic wave is present. After the development of a practical source array discussed previously, experiments could be done on a larger scale using large projectiles that would closer simulate a torpedo. On a large scale, the sound could be focused on a particular part of the projectile.

Issues Related to Submersion Depth:

The work in this thesis has all been conducted at in very shallow water (0.75 m) and therefore the ambient hydrostatic pressure was low. The results may be directly applicable to a torpedo approaching a surface ship or shore target, but the situation becomes quite different at greater depth. Submarine activity may be in the region of 700 ft (213 m) below the water surface. At this depth the hydrostatic pressure is approximately 22 atmospheres. Acoustically cavitating the water at this depth obviously requires very high signal amplitudes. Without the occurrence of acoustic cavitation one would be relying on disruption to the cavity shape to alter the projectile dynamics, or some other effect not observed in this work.

The pressure difference across the cavity/water interface plays a large part in the effect of a given pressure signal on the supercavity shape. The pressure difference depends on the nature of the supercavitation. Producing a natural cavity at 22

atmospheres of ambient pressure would require very high projectile speeds. It is likely that torpedoes will sustain a ventilated supercavity whereby gas is injected into the cavity which increases the internal pressure and reduces the cavitation number. The projectile speed is also an important factor. A very fast projectile sustaining a natural supercavity may be very hard to influence; however, a high acoustic pressure amplitude acting on a relatively slow projectile sustaining a ventilated cavity may have potential to alter the cavity geometry significantly.

Addressing More Advanced Weapon Technology:

For a practical application, one should also consider the effects on a supercavitating body that has active control surfaces. Based on research that can be found in the public literature it is evident that the latest supercavitating weapons will incorporate control surfaces both in the form of an actuated cavitator and fins that protrude into the water through the cavity/water interface.

Based on research in the current literature on free-flying projectiles it is not out of the question that supercavitating torpedoes could one day reach supersonic flight speeds underwater. In this event, there may still be the possibility of an acoustic countermeasure but it could not function in the proposed way. Detecting and locating the weapon would be impossible using sonar, as would adaptive focusing techniques. Future research should consider the likely hood of this development and the associated time scale.

6.4.2.2 Fluid Models and Experiments

Fluid models, in particular numerical CFD models, could be used to investigate the effects of acoustic signals on supercavities. It has been found that the only analytical model known to the author that is capable of including the effects of time dependent

pressure variations is not adequate to accurately predict the effects that have been observed experimentally. There are some CFD models that have been developed (for a discussion and citations see section 2.1.2.3 of chapter 2) and used to predict supercavitating flows and may be able to incorporate acoustic signals in the surrounding medium.

It would also be informative to conduct more controlled experiments in a high-speed water tunnel aimed at investigating the interactions of high level acoustic signals with the supercavity envelope. This would allow for the study of effects on ventilated supercavities, measurement of internal cavity pressures, and measurement of pressures in the water close to the cavity/water interface. It would also provide an environment that would make it easier to obtain more detailed photography of the phenomenon.

Numerical and experimental investigation could also be targeted at scrutinizing the hypotheses presented and discussed in section 5.4 of chapter 5. In particular, the hypothesis presented as the most likely explanation rests on the hydrodynamics of the projectile tail planing in a medium subject to acoustic cavitation which is a situation that is not fully understood. CFD analysis could be used to predict the hydrodynamics and the planing forces on the body and thus would provide further insight into the validity of the hypothesis.

Additionally, experiments could be done looking at the hydrodynamics of a rigid body planing on a water surface under which acoustic cavitation is present. This would serve to validate numerical models and help to confirm or reject the suggested hypotheses.

APPENDIX A

LOGVINOVICH'S MODEL FOR CAVITY SHAPE PREDICTION

This appendix presents the main ideas and equations of the theory without full derivation. Section A.1 shows the approach from energy considerations (for a full derivation from see Vasin 2001 [99]). Section A.2 shows the approach starting from the general differential fluid equations of continuity and momentum (for a full derivation from see Franc and Michel (2004) [34]).

A.1 Logvinovich: Energy Approach

This approach considers a moving cavitator in a stagnant fluid. A cavitator travels along a path in space with path variable s, where $s = 0$ is fixed in space. The work done by the cavitator in traveling distance Δs by the drag force on the cavitator F_D is simply $F_D \Delta s$. The drag coefficient for a disk cavitator is discussed in section 2.1.3 of this dissertation. This energy is transferred to kinetic energy of the fluid in the cavity section of length Δs. As the cavity section expands work is done by the pressure difference between the exterior and interior of the cavity which slows and reverses the section expansion.

Assuming no energy dissipation, this process can be represented by the following energy balance:

$$T(s,t) + U(s,t) = F_D(s,0)\Delta s \tag{44}$$

where T is kinetic energy and U is potential energy. A given cross section is considered which is formed at $t = 0$ when the cavitator is at a point along the path s. The equation that is sought is one that describes the evolution of this section in a plane perpendicular to the velocity of the cavitator at the instant of formation.

The kinetic energy of the liquid is given in Lamb [59] as

$$2T = -\rho \int \int \phi \frac{\partial \phi}{\partial n} dS \tag{45}$$

which for this problem can be written for a cavity section of length Δs as

$$T = -\frac{1}{2}\rho\phi 2\pi R\dot{R}\Delta s \tag{46}$$

where ϕ is the velocity potential on the cavity section boundary, R and $dR/dt \approx \partial\phi/\partial n$ are the radius and radial velocity of the cavity boundary, and ρ is the fluid mass density.

The potential energy for a cavity section of length Δs is given by

$$U = \Delta s \int_0^t \Delta P(s,t) 2\pi R\dot{R} dt \tag{47}$$

Note that in (46) and (47), $\dot{S} = 2\pi R\dot{R}$.

The equation of motion is found by setting the time derivative of equation (46) plus (47) equal to zero since there is no work done by nonconservative forces.

$$\frac{d}{dt}\big(T+U\big)=0 \tag{48}$$

This along with a dynamic boundary condition that is the general Bernoulli equation applied along the cavity boundary

$$\frac{\partial\phi}{\partial t}+\frac{v^2}{2}=\frac{\Delta P}{\rho} \tag{49}$$

are used to derive the equation of motion describing the cavity section cross section area S. Here v is the absolute velocity of the fluid particles on the cavity boundary and $\Delta P = P - P_c$. The assumption is made that in equation (49), $v^2/2$ can be neglected compared to $\Delta P/\rho$. This is because v is a small value for much of the time because $v \approx dR/dt$.

The sets the foundation of the principle. Vasin [99] presents the steps of the derivation to get from this point to the final result:

$$\ddot{S}(s,t)=-\frac{\kappa\Delta P(s,t)}{\rho} \tag{50}$$

The value of κ is discussed in the main body of the work, section 2.1.1.2.

A.2 Logvinovich: Newtonian Approach

This approach considers a moving flow over a fixed cavitator. The governing fluid equations are the continuity and momentum equations. From these, along with a kinematic boundary condition on velocity at the cavity/water interface, the equation describing the cavity section evolution (equation (50)) can be derived.

An expression for v_r can be found from the continuity equation which is then used in the momentum equation. It is first assumed that the velocity field has only radial (v_r) and axial (v_x) components and is axially symmetric which implies no change with theta. This assumption, along with the assumption that density is constant (fluid is assumed incompressible), the general continuity equation reduces to,

$$\frac{1}{r}\frac{\partial}{\partial r}(rv_r) + \frac{\partial}{\partial x}(v_x) = 0 \tag{51}$$

A further assumption is then made that the axial velocity component (v_x) is approximately equal to the flow velocity at infinity (v_∞), such that the second term in equation (51) is negligible. Then the general solution for v_r is

$$v_r \cong \frac{C(x)}{r} \tag{52}$$

The function $C(x)$ in equation (52) is found from the kinematic boundary condition on the cavity-water interface. The condition is that flow is tangential to the interface:

$$v_r(R, x, t) = \frac{\partial R}{\partial t} + v_\infty \frac{\partial R}{\partial x} \tag{53}$$

Where $R(x, t)$ is the cavity radius at location x. Finding $C(x)$ leads to an expression for radial velocity:

$$v_r = \frac{R}{r}\left(\frac{\partial R}{\partial t} + v_\infty \frac{\partial R}{\partial x}\right) \tag{54}$$

The Momentum equation in the radial coordinate direction for a Newtonian fluid with constant density is simplified with assumptions of an axis symmetric velocity

field, negligible body forces due to gravity, and an inviscid fluid:

$$\frac{\partial v_r}{\partial t} + v_r \frac{\partial v_r}{\partial r} + v_x \frac{\partial v_r}{\partial x} = -\frac{1}{\rho}\frac{\partial p}{\partial r} \tag{55}$$

The expression for v_r is substituted into the momentum equation and the following result is reached:

$$\left[\frac{\partial^2 S}{\partial t^2} + 2v_\infty \frac{\partial^2 S}{\partial x \partial t} + v_\infty^2 \frac{\partial^2 S}{\partial x^2}\right] = -\kappa \frac{p_\infty(t) - p_c(t)}{\rho} \tag{56}$$

where

$$\kappa \;=\; \frac{2\pi}{ln(\Psi/R)} \tag{57}$$

and $\Psi(x)$ is a function introduced in the derivation which corresponds to a fictitious surface far from the cavity. Franc and Michel [34] suggest that κ is constant for elongated cavities and can be approximated by asymptotic results by

$$\kappa \approx \frac{4\pi}{ln(1/\sigma)} \tag{58}$$

The result (56) is in an Eulerian frame of reference fixed to the body producing the cavity. We can, however, put the result in a Lagrangian frame of reference, that is, following a cavity cross section as it is convected down stream which will be equivalent to the result derived from energy considerations. If the cavity is convected at the axial flow velocity (v_∞) then essentially position in equation (56) is known as a function of time only. The time origin, t_0, corresponds to the instant when a given section originates at the cavitator, so

$$x = v_\infty(t - t_0) \tag{59}$$

and therefore,

$$S_{t_0}(t) = S(v_\infty(t - t_0), t) \tag{60}$$

So looking at S_{t_0} in equation (56), $\partial S_{t_0}/\partial x = 0$ and the result is

$$\frac{\partial^2 S_{t_0}}{\partial t^2} = -\kappa \, \frac{p_\infty(t) - p_c(t)}{\rho} \tag{61}$$

which is the same as (50).

APPENDIX B

PROJECTILE TECHNICAL DRAWINGS

B.1 Projectile Design Used in the Experiments

A technical drawing of the projectile design used for all of the experiments in this work is shown in figure 71 (designated as projectile SC4). The features of this design are discussed in detail in section 4.1.4 of chapter 4.

B.2 Projectile Designs Tested but not Used in This Work

There were three additional designs that were tested prior to the final design shown in B.1.

Figure 72 shows the first projectile tested (SC1). This design proved to be unstable and often experienced tumbling. The instability could have initiated in the early flight upon muzzle exit where the projectile may not have been supercavitating. Additionally, the moment provided during tail-slap may not have been sufficient to reverse the direction of the angular velocity of the projectile body due to its short length.

Figure 73 shows a design (SC2) that was developed to address the problems of SC1. The projectile mass was distributed over a longer length and fins were added for stability in a non-cavitating regime. A sabot was required to fire the projectile using the existing firing mechanism.

Figure 74 shows a design (SC3) that was developed to reduce the cost of machining

from SC2 because we were unsuccessful in capturing the projectiles undamaged for repeated use.

The final design (SC4) in section B.1 was a refinement of SC3 to simplify the complexity of the loading process that had come about due to the fined design. This was done to improve consistency of the loading process and to address problems caused by the sabot after muzzle exit.

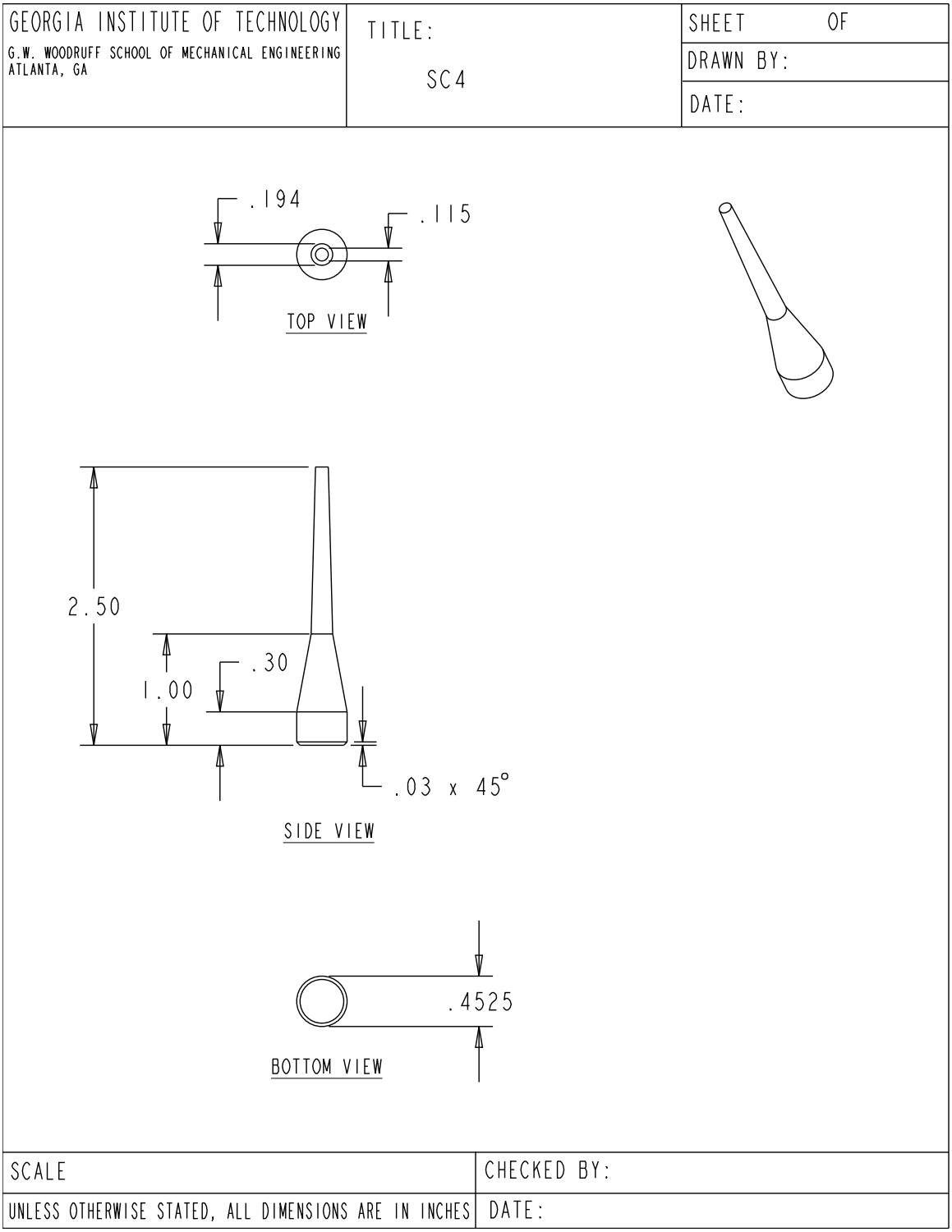

Figure 71: Technical drawing of projectile SC4

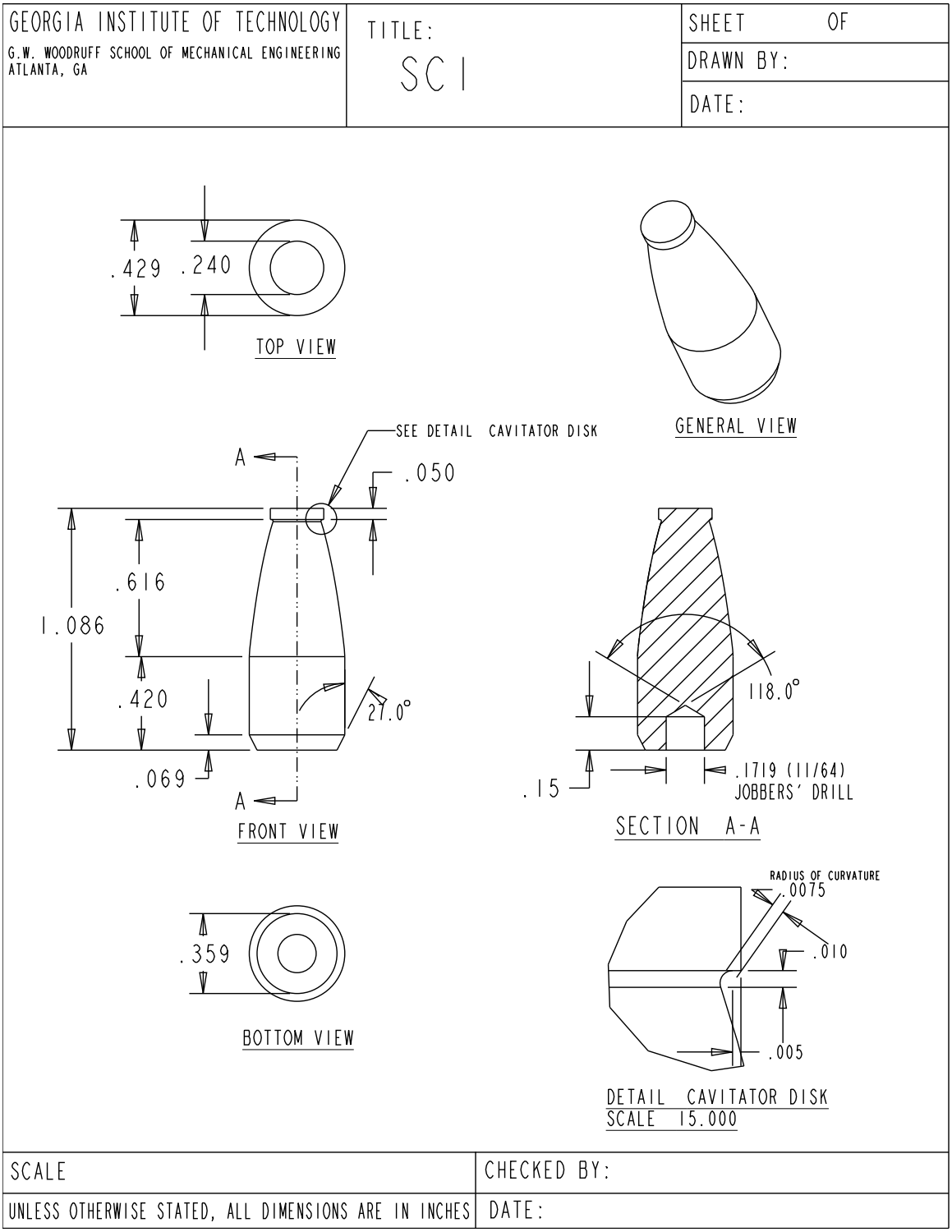

Figure 72: Technical drawing of projectile SC1

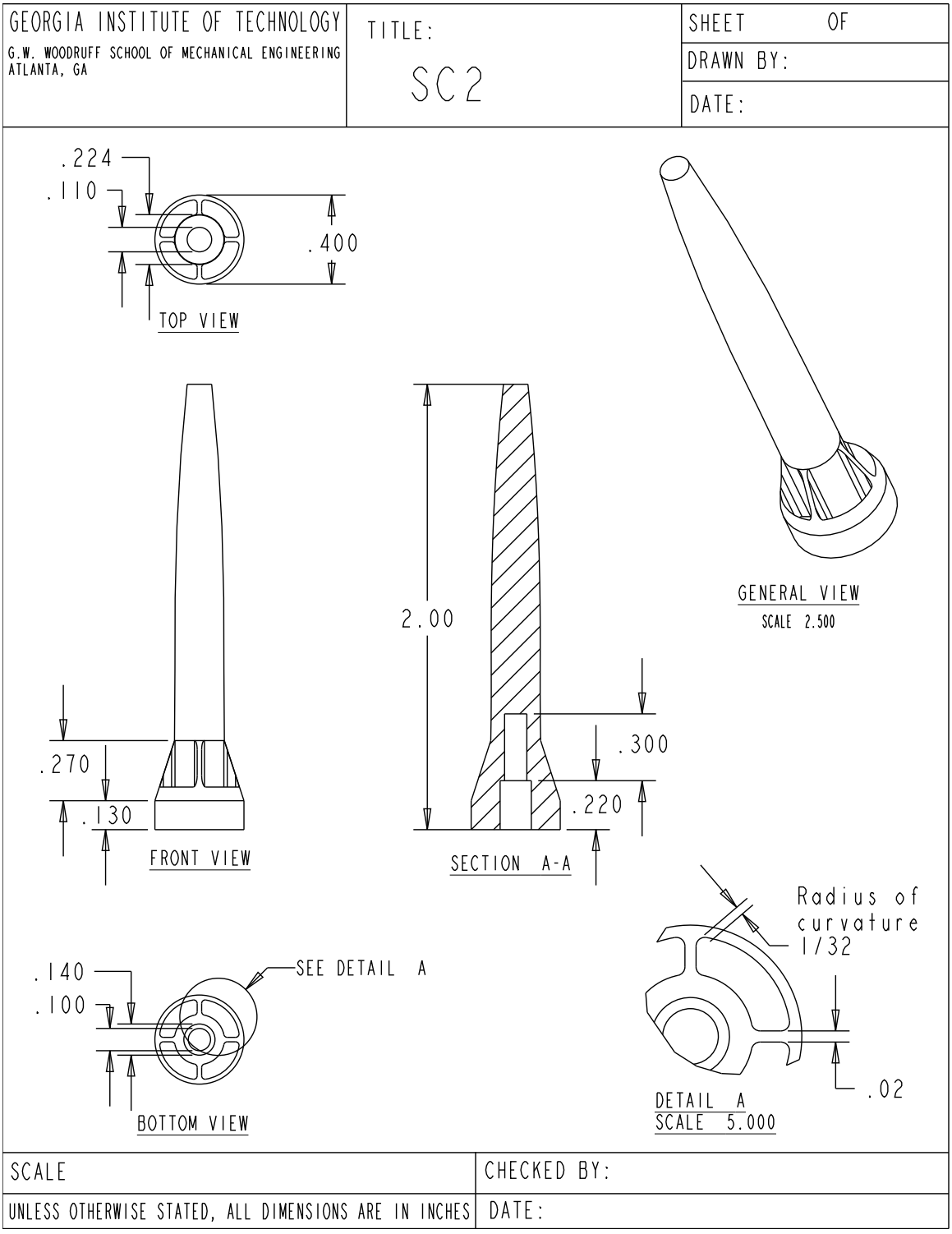

Figure 73: Technical drawing of projectile SC2

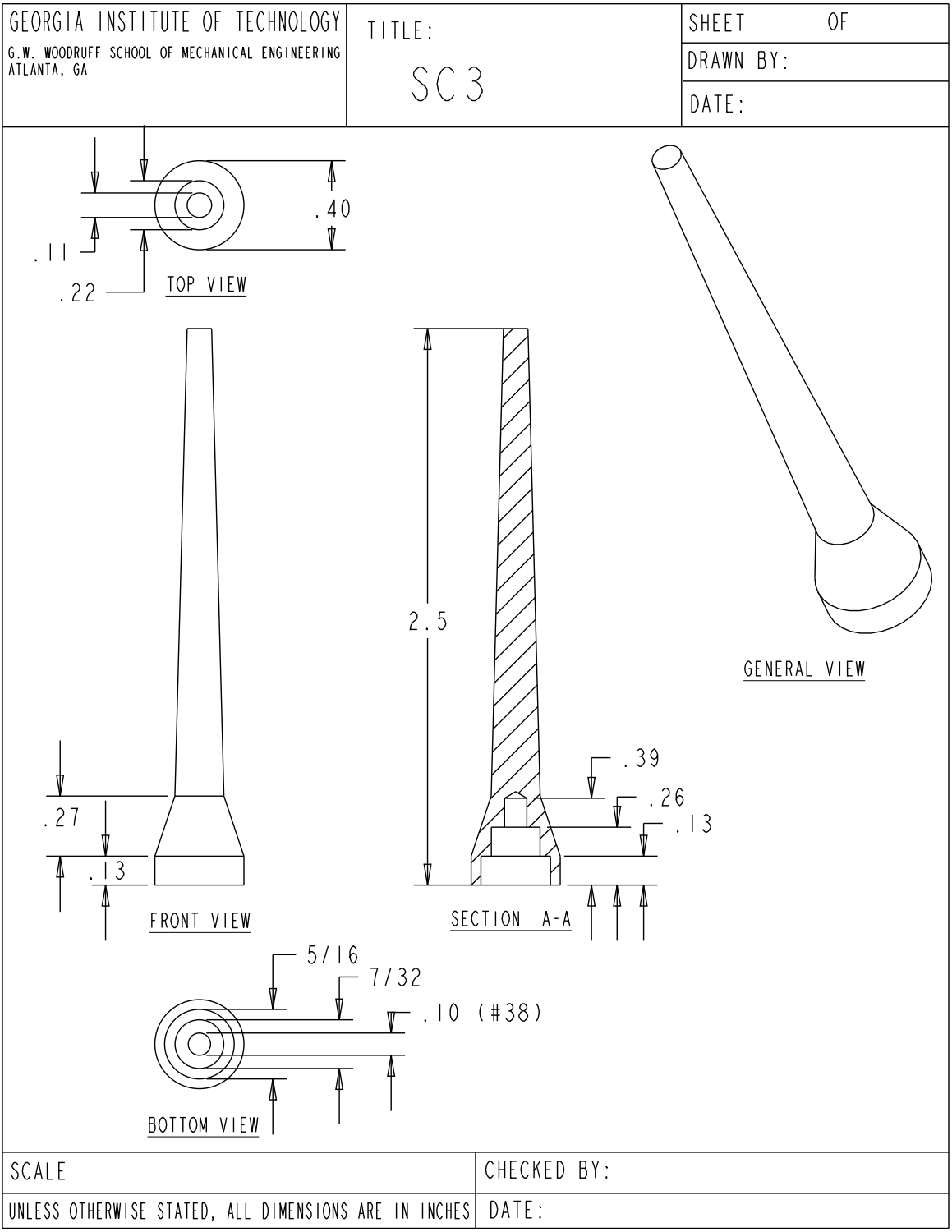

Figure 74: Technical drawing of projectile SC3

APPENDIX C

DRAG COEFFICIENT DATA FROM KICENIUK 1954 FOR DISK CAVITATORS

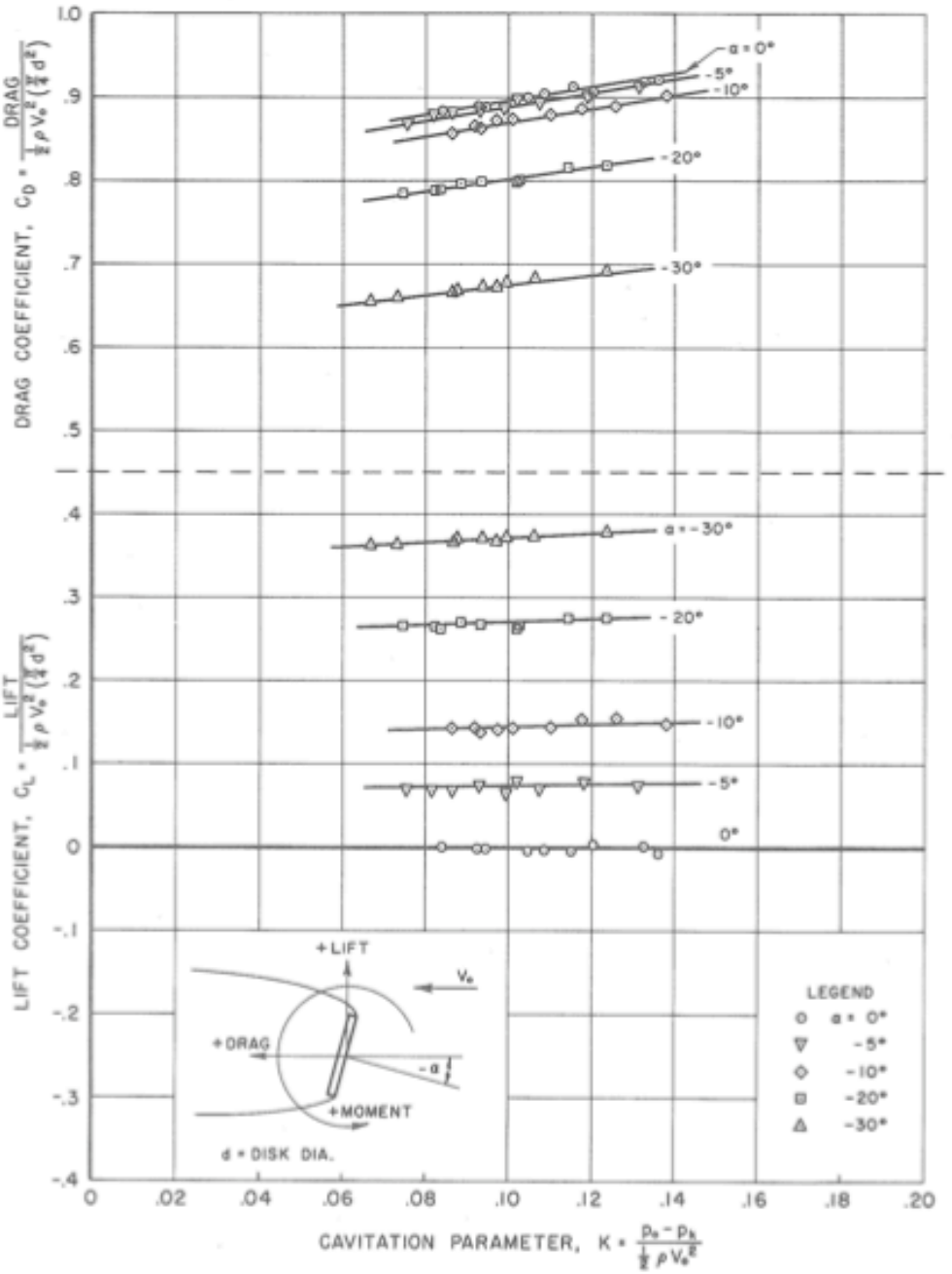

Fig. 3 - Lift and drag coefficients for a 1-in. diameter cavity-producing sharp-edged disc inclined to the flow at an angle α. Tunnel velocity 12.5 fps to 17.5 fps. Cavity bubbles are air-supported from an external supply.

Figure 75: Figure copied from Kiceniuk 1954 [50]

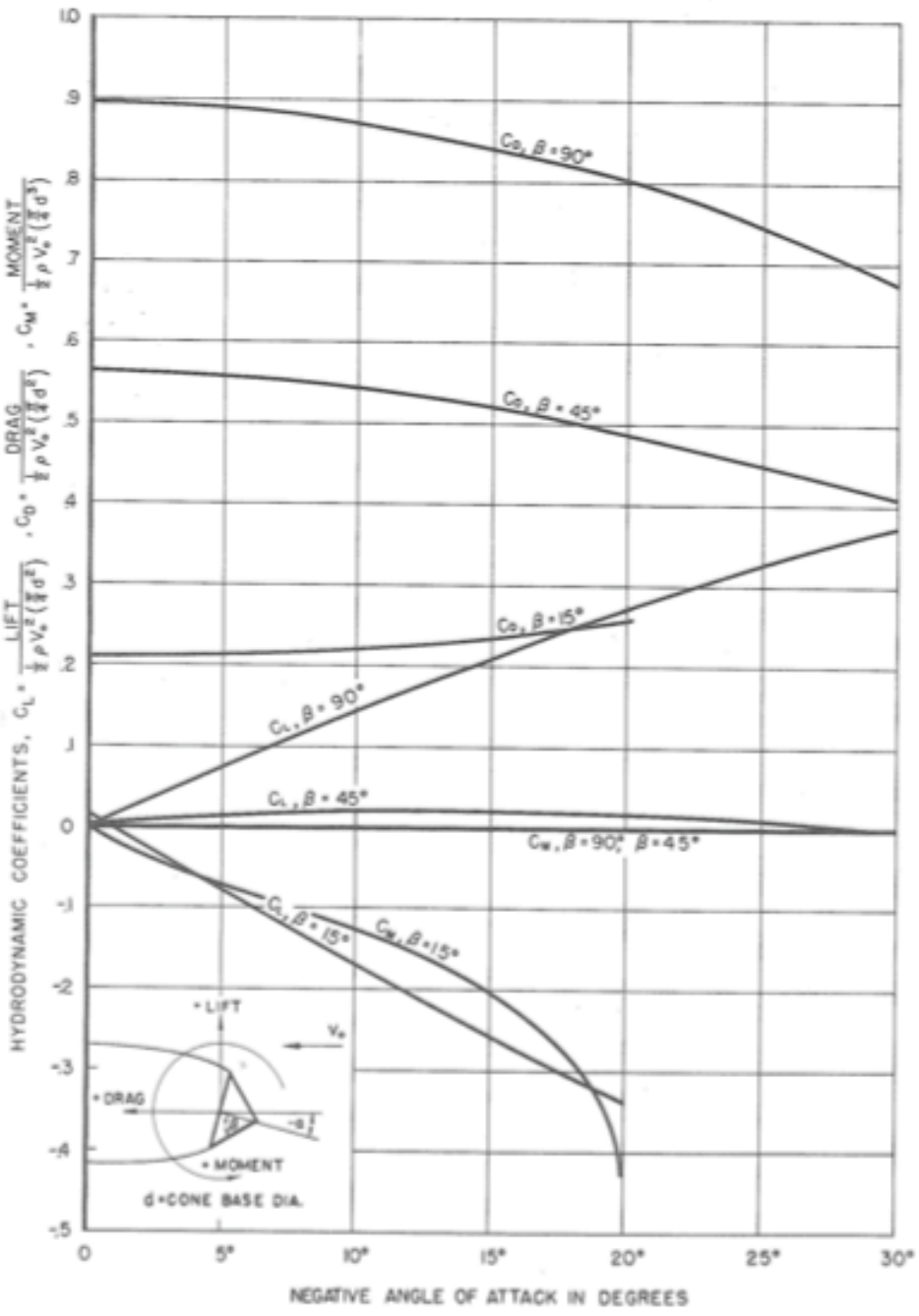

Fig. 6 - Cross plot of lift, drag and pitching moment coefficients against model angle of attack, α. Cavitation parameter,

$$K_c = \frac{P_o - P_k}{1/2\,\rho V_o^2} = 0.1$$ maintained by control of water velocity and air supply rate.

Figure 76: Figure copied from Kiceniuk 1954 [50]

APPENDIX D

HYDROPHONE CALIBRATIONS

The hydrophones used for array characterization were Brüel & Kjær (B&K) model 8100 (SN:1216465) and model 8103 (SN:2206083). In this appendix, section D.1 presents results of an absolute calibration of the B&K 8103 hydrophone using a reciprocity method and section D.2 presents a comparison calibration for the B&K 8100 hydrophone [12, 13]. Hydrophone polarization is discussed in section D.3. Calibration data provided by the manufacturer is shown in section D.4.

During calibrations, only the hydrophones integral cable was used. For other experiments, however, the hydrophone voltage sensitivity is adjusted for the effect of added extension cable. At the frequencies used in all parts of this work it is sufficient to use an approximate correction using the low frequency capacitance of the hydrophone and extension cable [41]:

$$M_C = \left(\frac{C_H}{C_H + C_{OC}} \right) M_O \tag{62}$$

where

M_C = overall system sensitivity

C_H = capacitance of hydrophone

C_{OC} = capacitance of extension cable

M_O = open circuit hydrophone sensitivity

The assumption made here is that both the hydrophone and the extension cable are purely capacitive. This is often valid for frequencies much less than the resonance

frequency of the hydrophone, which is always the case in this work. The resonance frequency of the B&K 8103 hydrophone used is around 120 kHz and that of the 8100 hydrophone is around 55 kHz.

D.1 Reciprocity Calibration for the Hydrophone: B&K 8103 (SN:2206083)

The reciprocity calibration was carried out following procedures given in the B&K literature [13] and by Bobber (1970) [12]. This particular technique is referred to in the literature as a *conventional reciprocity* or *three-transducer spherical-wave reciprocity*. The experiment involves a hydrophone H, a projector P and a reversible transducer T located at the vertices of an equilateral triangle submerged in a large water tank. Sides of the triangle must be of sufficient length to locate the transducers such that measurements can be taken assuming far field conditions. Conditions for the far field assumption are: 1) that the receiver be far enough from the projector to be in a region of spherical spreading, 2) the receiver be small in comparison to the separation distance so the imposing wave can be assumed to be a plane wave and 3) the separation distance is much larger than a wavelength. Two experiments are conducted and repeated with several different pulses:

1. Drive projector P with current I_P and measure the output voltage from H and T, (E_{PH} and E_{PT} respectively)

2. Drive transducer T with current I_T and measure the output voltage from H and P, (E_{TH} and E_{TP} respectively)

The following equation is used to calculate the hydrophone free field voltage sensitivity and is derived in the literature.

$$M_H = \left(\frac{E_{PH} E_{TH}}{E_{PT} I_T} J \right)^{1/2} \tag{63}$$

where

M_H = the receiving sensitivity of the hydrophone in V/Pa

J = the reciprocity parameter

The reciprocity parameter is given by:

$$J = \frac{2d}{\rho_w f} \tag{64}$$

where

d = the distance between the transducers in meters

ρ_w = the density of water $[kg/m^3]$

f = the frequency in Hz

In this work the hydrophone H is a B&K 8103, the reciprocal transducer T is a B&K 8100 and the projector P is a The frequency response produced by this method is shown in figure 77. The trend compares agreeably with the manufacturers calibration curve (see figure 81) that shows a voltage sensitivity of 24.8 μV/Pa (-212.1 dB) with a tolerance (excluding measurement uncertainty) of:

0.1 Hz to 20 kHz + 1 dB, -1.5 dB

0.1 Hz to 100 kHz + 1 dB, -6 dB

with a measurement uncertainty (re 10 kHz) of:

10 to 80 kHz $\pm$ 1.5 dB

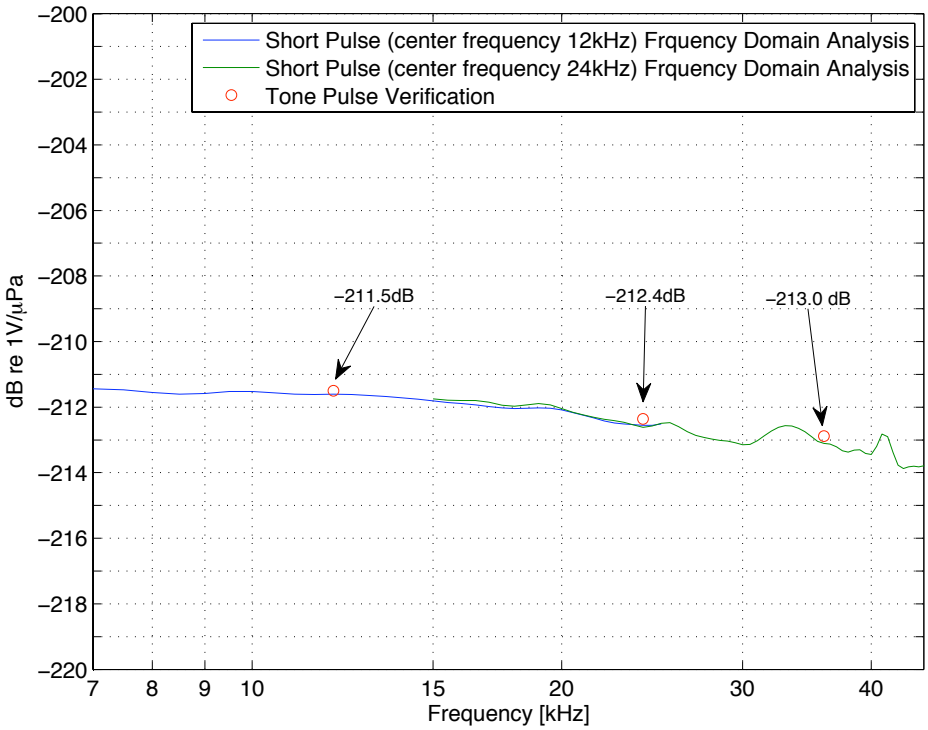

Figure 77: Frequency response of Brüel & Kjær 8103 (SN:2206083) hydrophone measured using a reciprocity calibration

It is seen that the sensitivity begins to deviate from its flat low frequency region at around 15 kHz and stays within 1 dB until approximately 23 kHz, whereafter, in the range studied here, it continues to decrease with increasing frequency. Higher frequency data was not taken in this study because it is not of interest. The sources used have a resonance frequency of around 13 kHz (see figure 32 in section 4.4.1.2) and so are not capable of producing significant sound pressure levels at frequencies outside the 7 - 45 kHz range. The main reason for doing this calibration is to allow an accurate measure of the peak sound pressure level in the array sound field which, due to the source characteristics, has most of its energy in the studied range.

The main source of uncertainty in the calibration conducted for this work is the distance between transducers.

A reciprocity check is also done. To be reciprocal, a transducer must be linear, passive, and reversible. If the system comprised of two transducers and the water medium and the surroundings is reciprocal then

$$\frac{E_{PT}}{I_P} = \frac{E_{TP}}{I_T} \tag{65}$$

These two ratios are plotted in the relevant frequency range and shown in figure 78. This is not an absolute method for confirming reciprocity because not all linear, passive and reversible transducers are reciprocal. However, it does indicate with a very high probability that the transducers are reciprocal [12]. Also, most conventional piezoelectric transducers are reciprocal at normal signal levels.

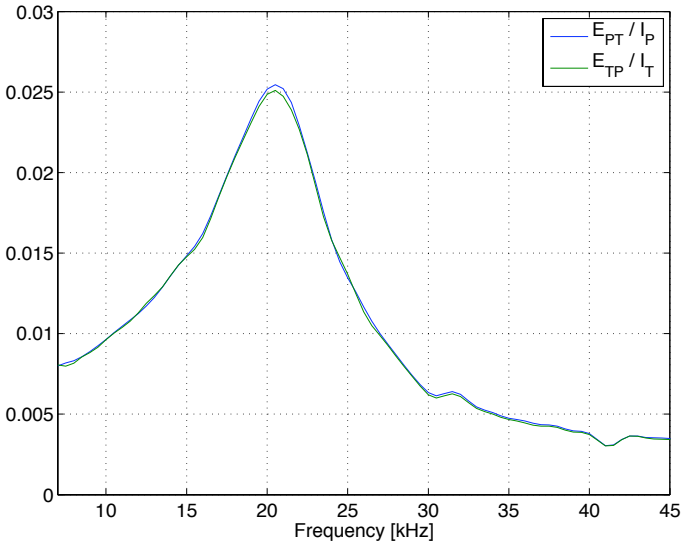

Figure 78: Plot showing reciprocity check for the reciprocity hydrophone calibration

D.2 Comparison Calibration for the Hydrophone: B&K 8100 (SN:1216465)

A comparison calibration is carried out for the B&K 8100 hydrophone using the previously calibrated B&K 8103 hydrophone as a calibrated standard. The frequency response plot is shown in figure 79. At 12 kHz the calibration is seen to be -206.1dB (59.5 μV/Pa). This curve also compares agreeably with the manufacturers calibration curve shown in figure 80.

D.3 Hydrophone Polarization

The voltage polarization of the hydrophones is an important consideration in this work. Under the vast majority of linear acoustic measurements it does not matter one way or the other, that is, whether a positive pressure in the field corresponds to a positive or negative voltage reading. However, the pressures produced at the focus of the array in this work reach and exceed the vapor pressure of the water and therefore it is likely that the water will cavitate. This issue is discussed in detail in section

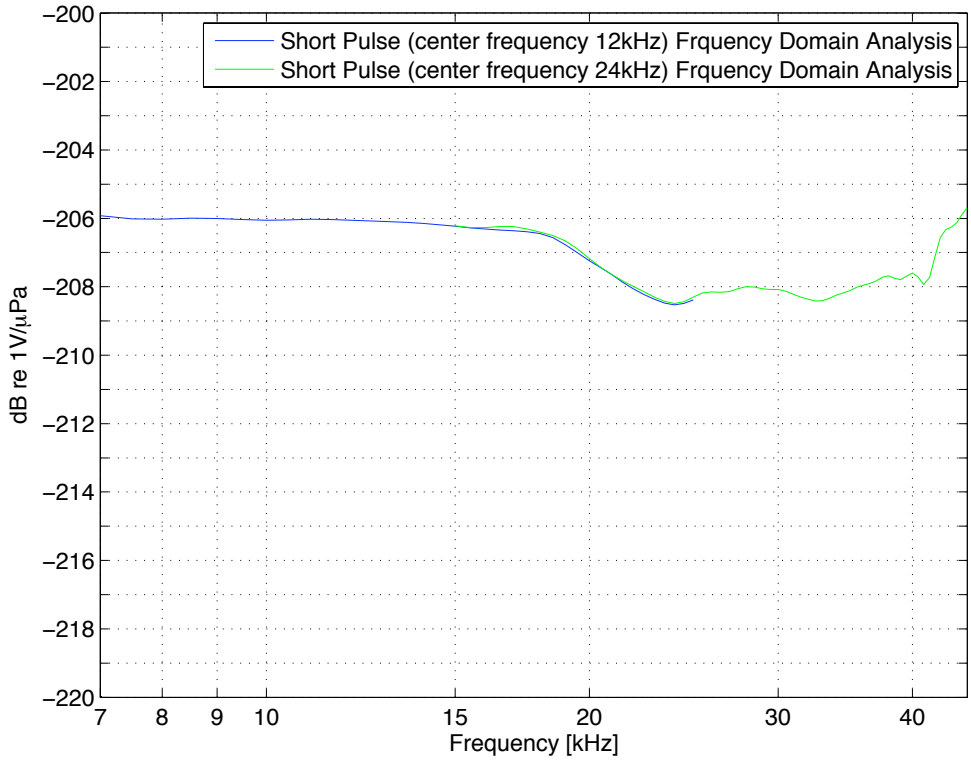

Figure 79: Frequency response of Brüel & Kjær 8100 (SN:1216465) hydrophone measured using a comparison calibration with the previously calibrated Brüel & Kjær 8103 (SN:2206083) hydrophone as the calibrated standard

4.4.6. In this situation the polarity of the pressure is important because it is only the negative acoustic pressures that cause cavitation.

Contrary to intuitive reasoning the polarity of the Brüel & Kjær hydrophones is negative so that a positive pressure gives a negative voltage reading. This has been determined by correspondence with the manufacturer, comparison with other hydrophones, and experiments conducted in the laboratory.

D.4 Hydrophone Calibration Curves Provided by the Manufacturer

Figures 80 and 81 show calibration curves provided by Brüel & Kjær for the hydrophones used in this work.

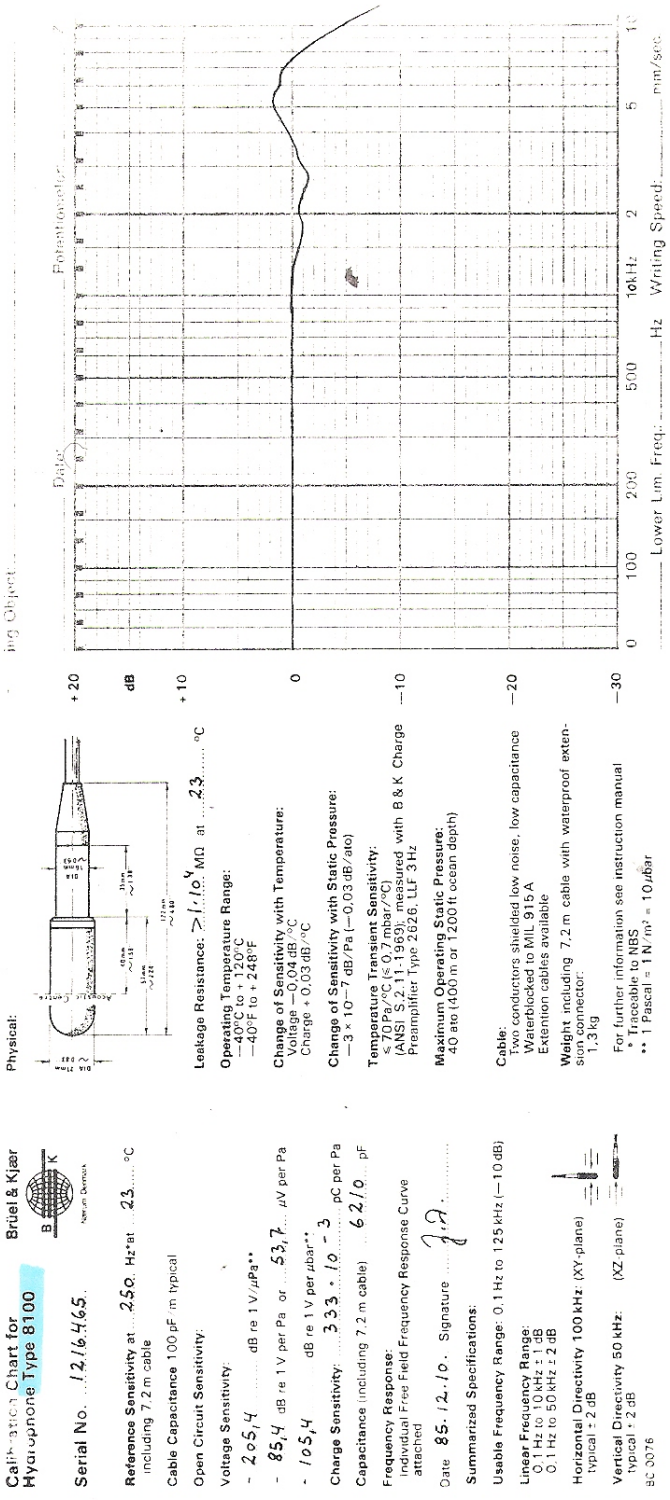

Figure 80: Frequency response of Brüel & Kjær 8100 (SN:1216465) hydrophone provided by the manufacturer

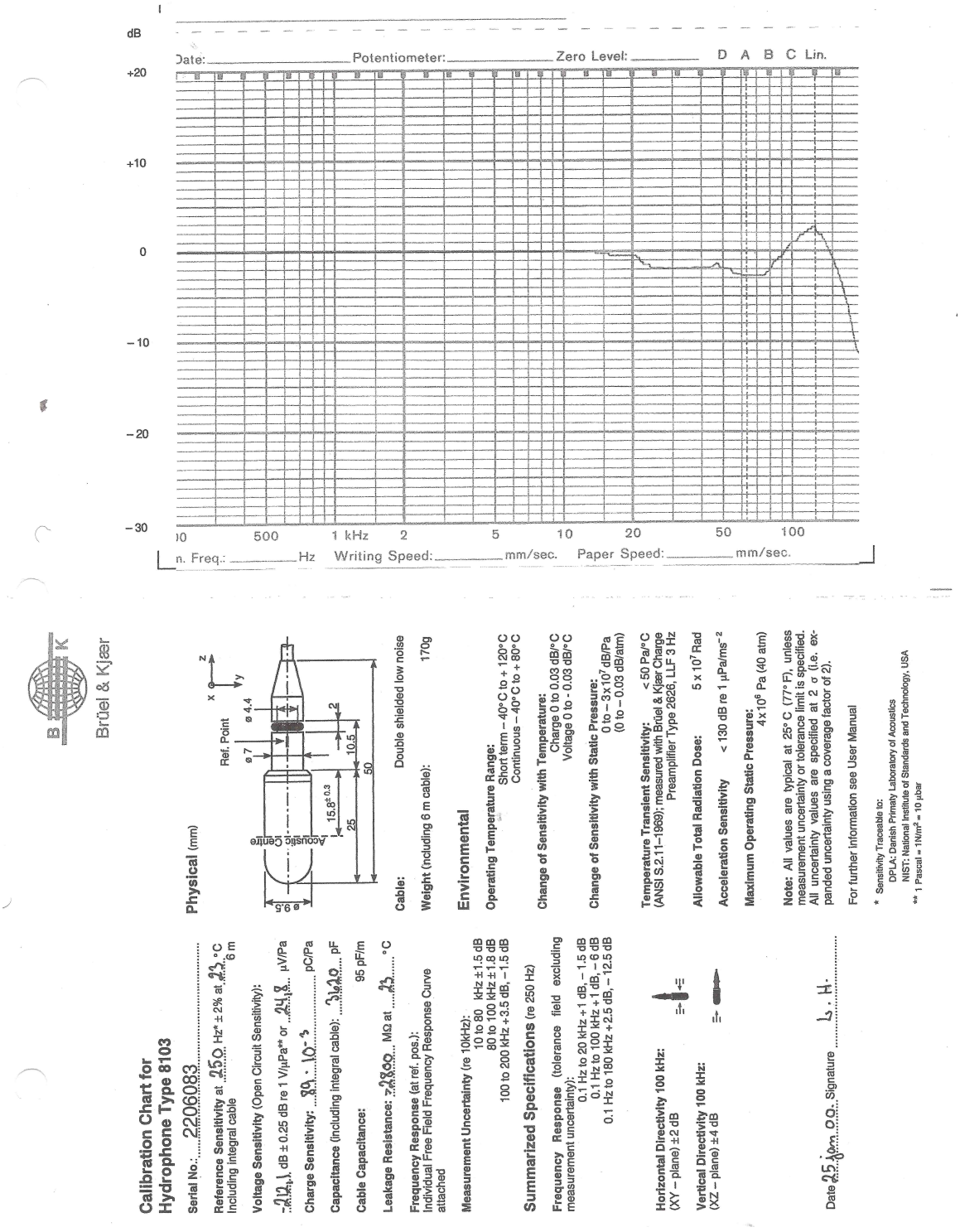

Figure 81: Frequency response of Brüel & Kjær 8103 (SN:2206083) hydrophone provided by the manufacturer

APPENDIX E

ITC 6135-1 TRANSDUCER TRANSMITTING VOLTAGE RESPONSE

Figure 82 shows a typical transmitting voltage response curve from International Transducer Corporation for an ITC-6135-1 transducer.

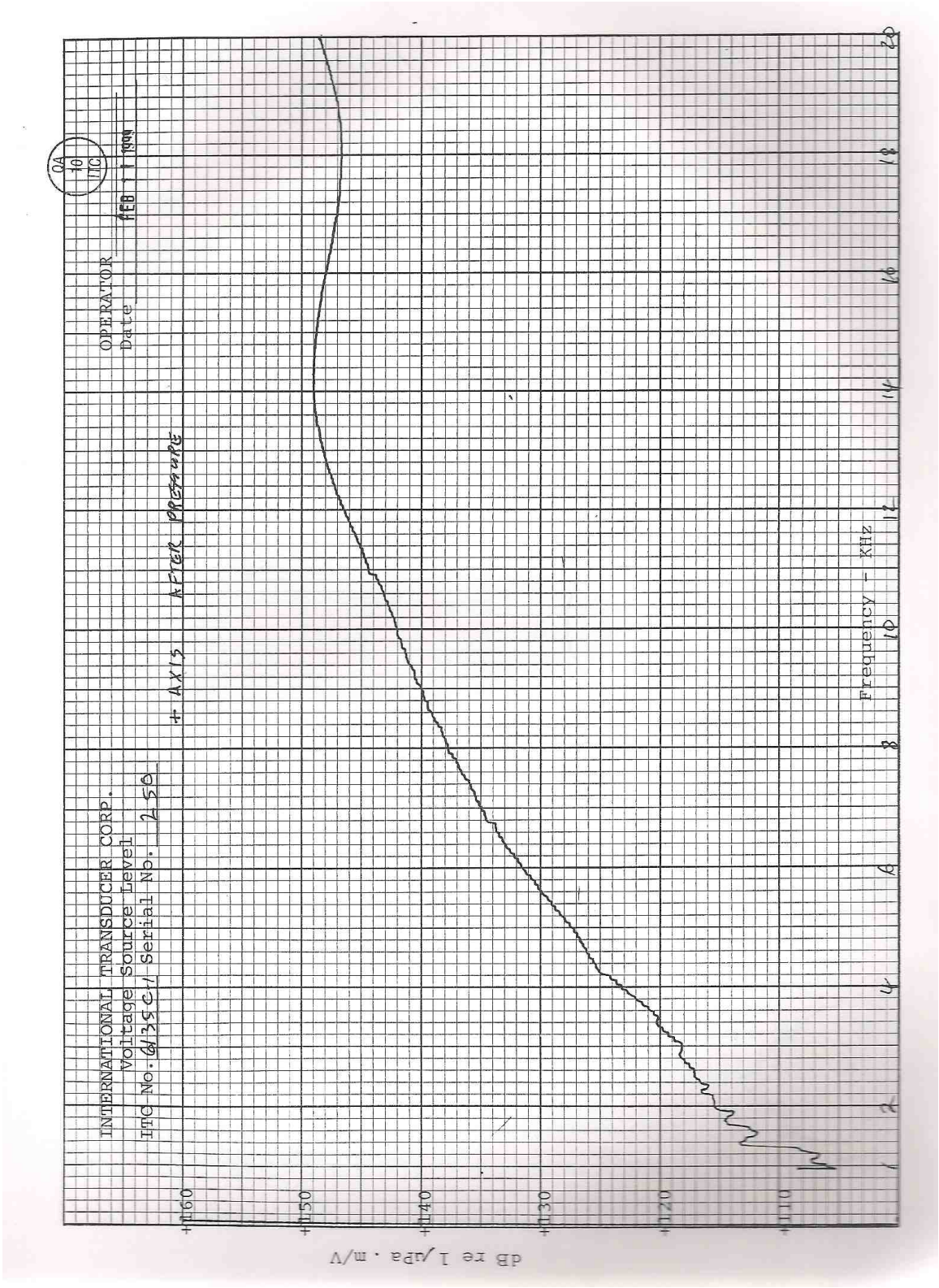

Figure 82: Transmitting voltage response curve from International Transducer Corporation for an ITC-6135-1 transducer

APPENDIX F

SAMPLE CONSECUTIVE FRAMES FROM A TYPICAL SHOT WITH NO IMPOSED ACOUSTIC PRESSURE

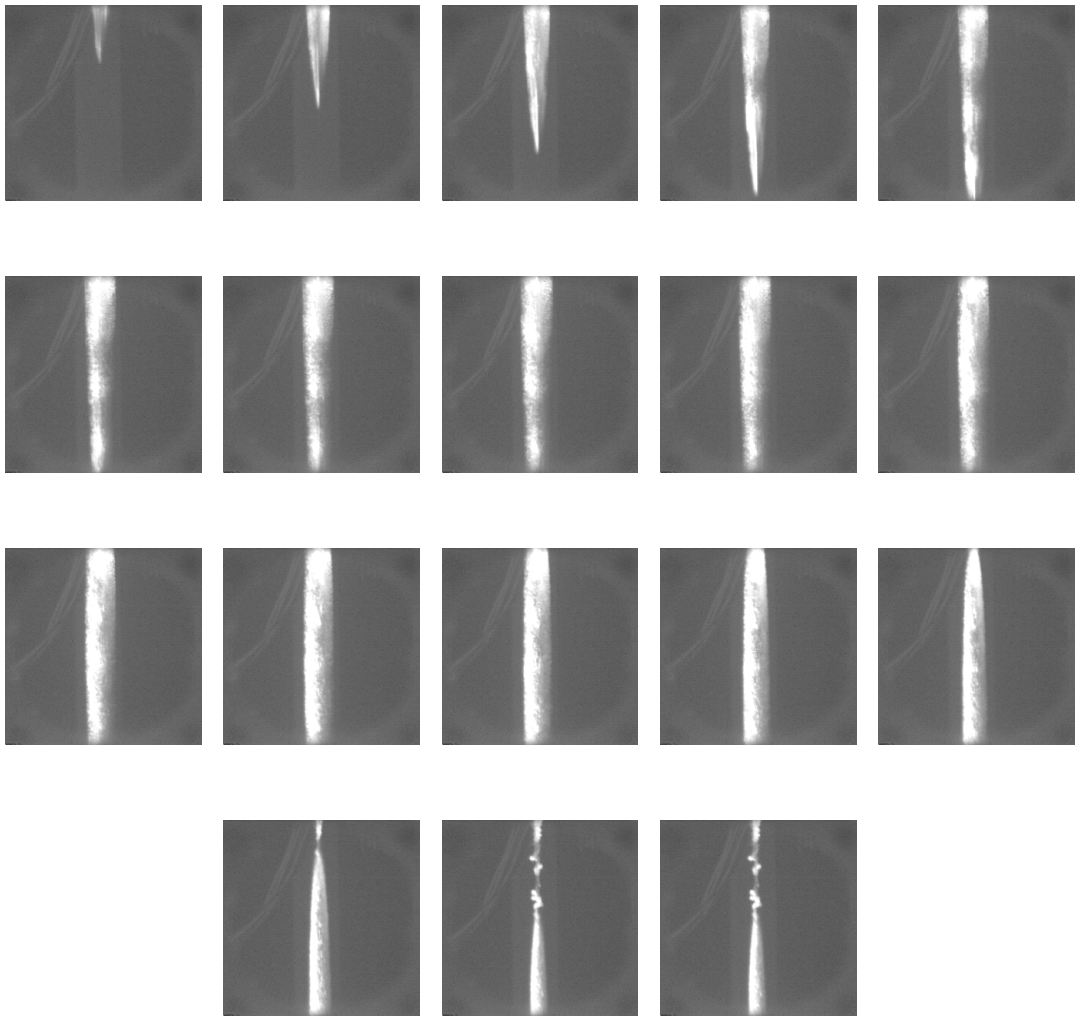

Figure 83: Sample consecutive frames from a typical shot with no imposed acoustic pressure

APPENDIX G

SAMPLE CONSECUTIVE FRAMES FROM A TYPICAL SHOT WITH AN IMPOSED ACOUSTIC PRESSURE

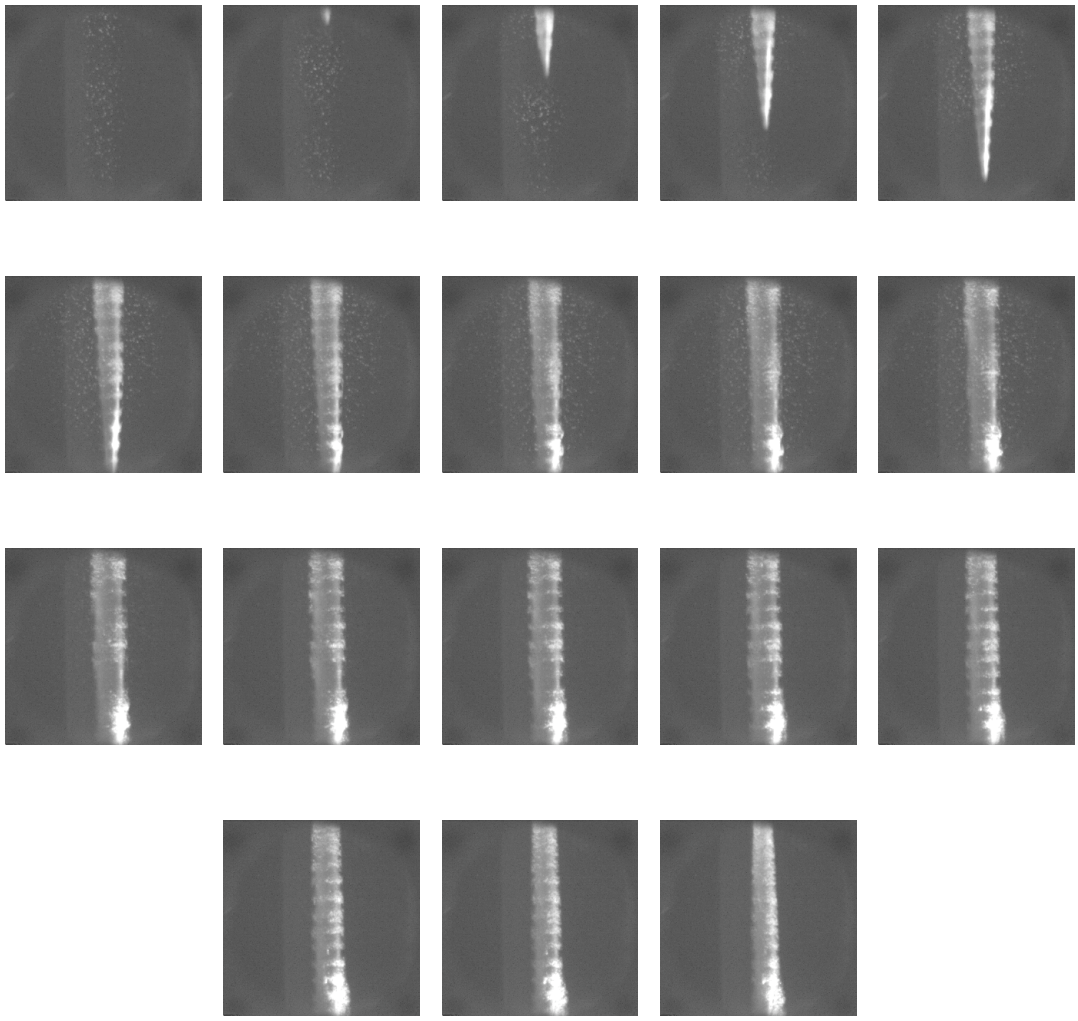

Figure 84: Sample consecutive frames from a typical shot with an imposed acoustic pressure

APPENDIX H

ACOUSTIC PRESSURE SIGNALS

Examples of typical acoustic pressure signals are presented for each pressure amplitude and signal frequency combination used in the experiments. For each experiment case there are three plots. One shows a measurement of the sound pressure at the array focus in the absence of a supercavity. The other two show measurements taken next to a model supercavity that was located at the array focus. The hydrophone locations were 2.3" (59 mm) aft of the cavity tip (where the tail of the projectile would have been inside the cavity) and at radial distances from the supercavity wall of 4.6 mm and 11.6 mm.

Figures 85, 86, and 87 show recordings for the 12 kHz signal at high, medium and low acoustic pressure amplitudes. Figures 88 and 89 show recordings for the 7.5 kHz signal at medium and low acoustic pressure amplitudes. Figures 90 and 91 show recordings for the 17.5 kHz signal at medium and low acoustic pressure amplitudes. Table 19 summarizes these figures.

Table 19: Summary of figures showing acoustic pressure signals.

	7.5 kHz Signal	12 kHz Signal	17.5 kHz Signal
High Amplitude		figure 85	
Medium Amplitude	figure 88	figure 86	figure 90
Low Amplitude	figure 89	figure 87	figure 91

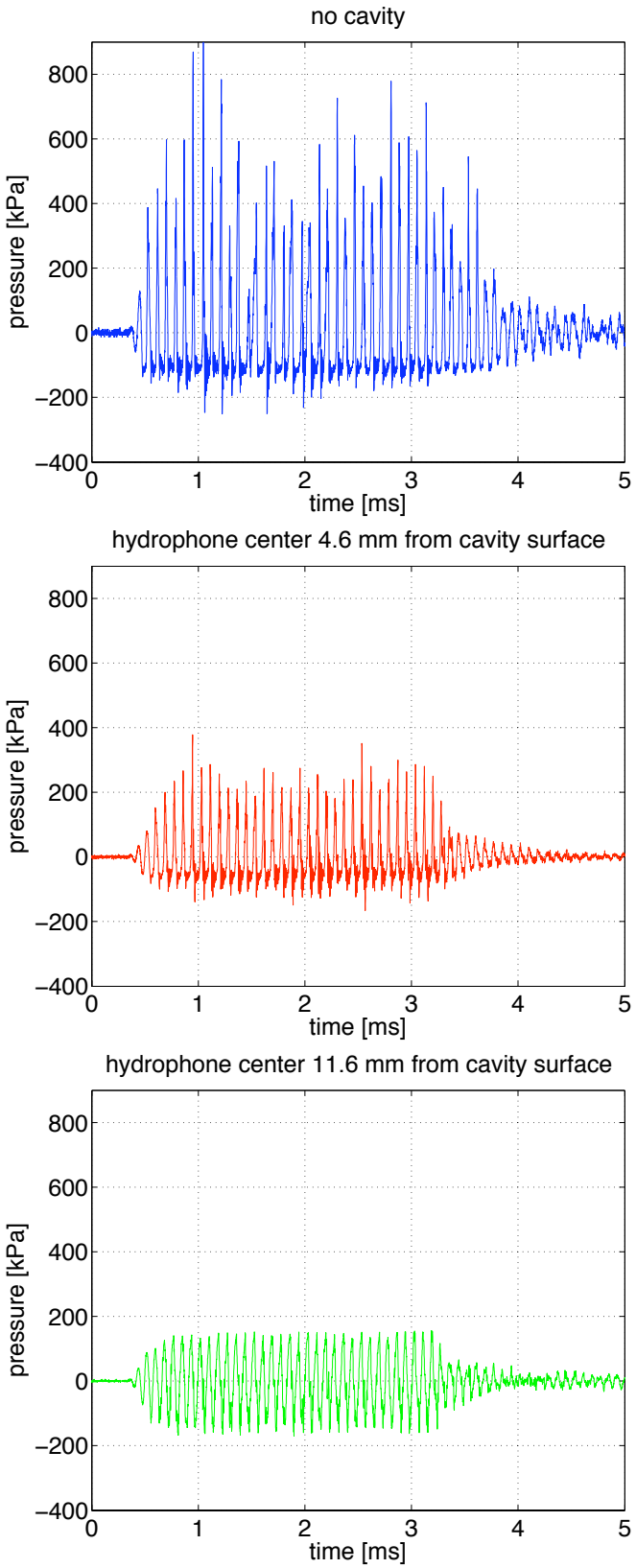

Figure 85: Example pressure signals for the case of high amplitude and 12 kHz

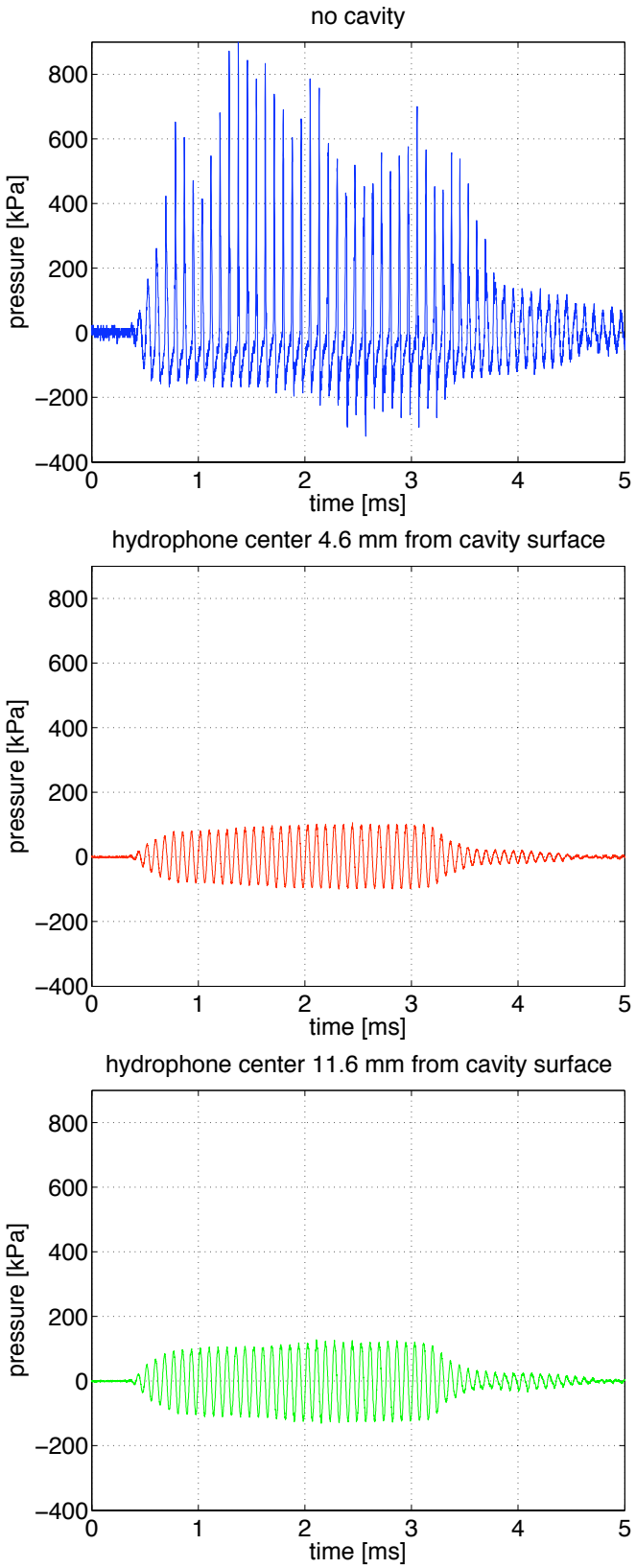

Figure 86: Example pressure signals for the case of medium amplitude and 12 kHz

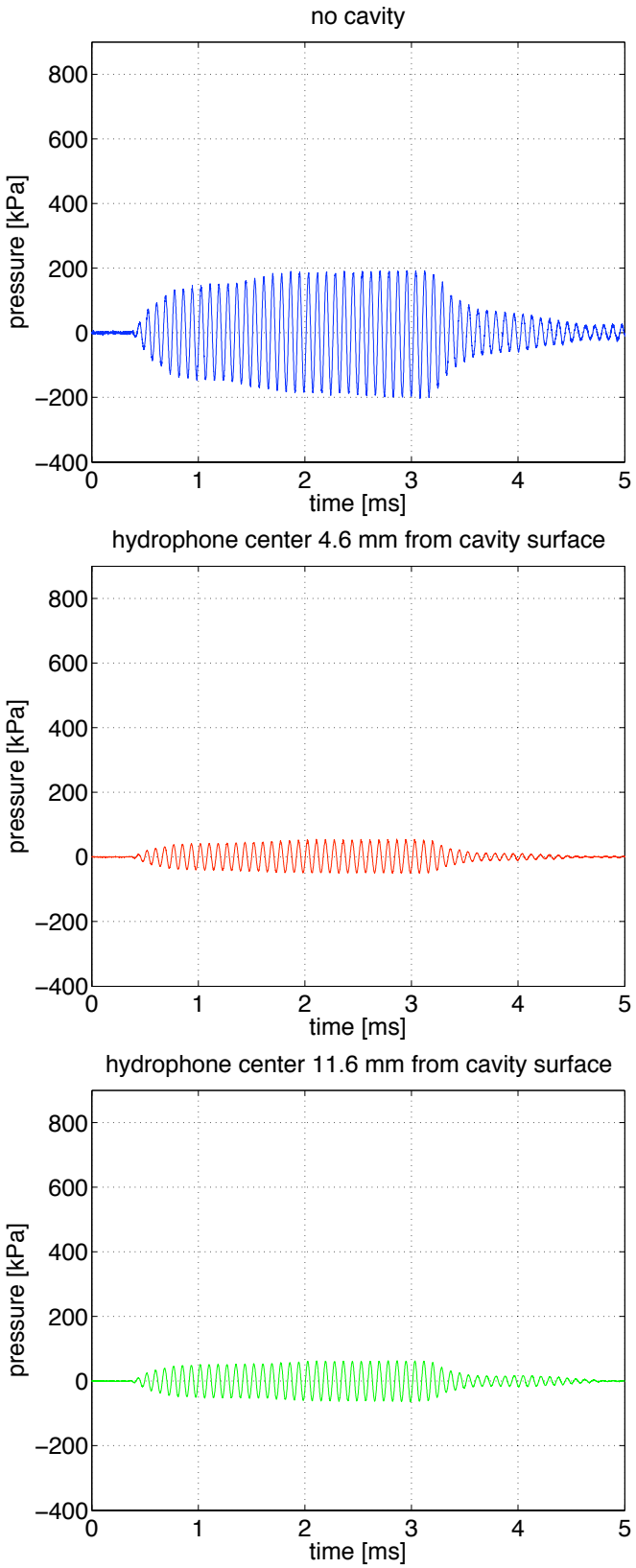

Figure 87: Example pressure signals for the case of low amplitude and 12 kHz

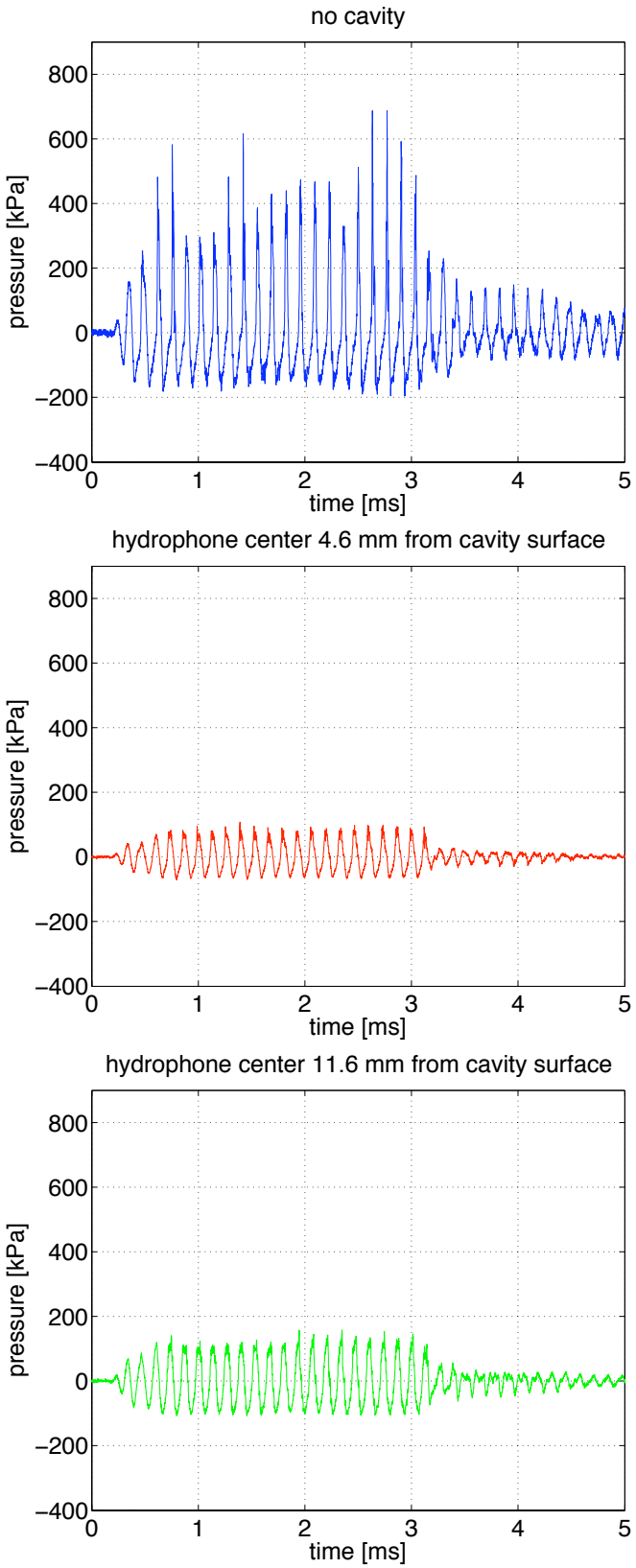

Figure 88: Example pressure signals for the case of medium amplitude and 7.5 kHz

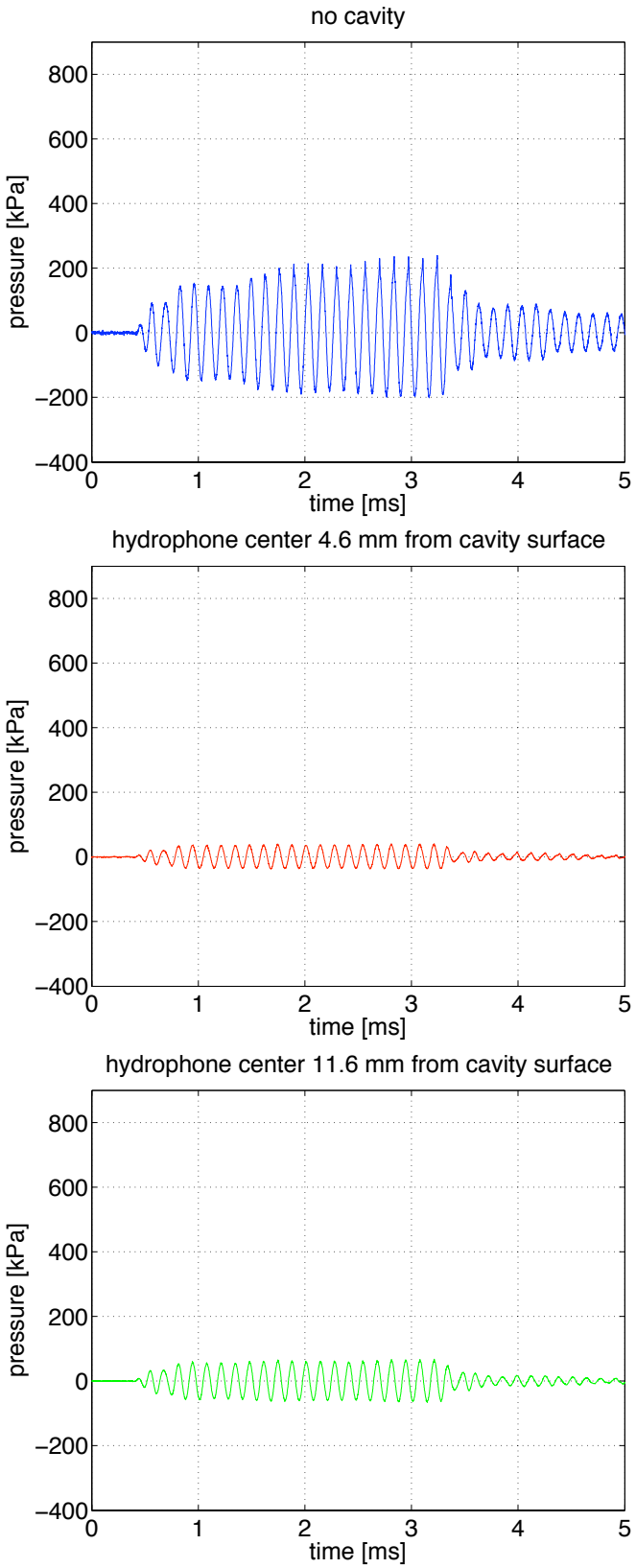

Figure 89: Example pressure signals for the case of low amplitude and 7.5 kHz

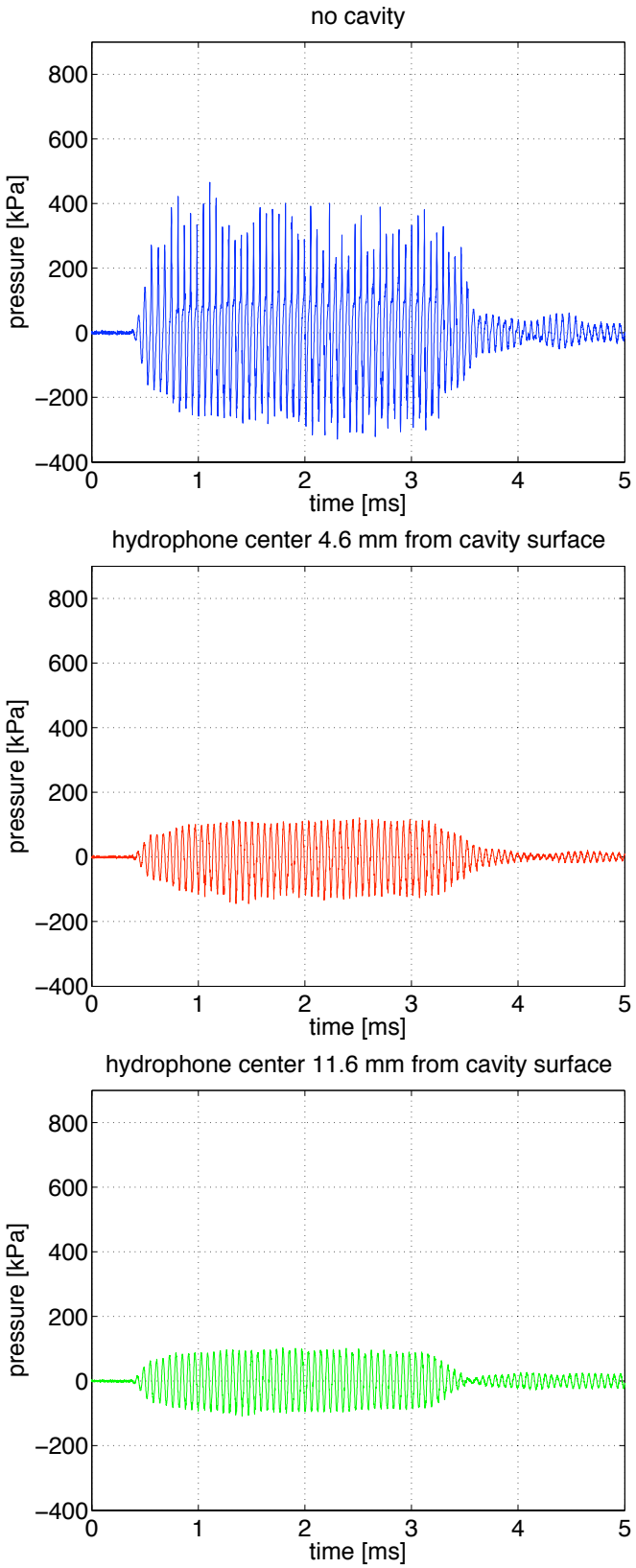

Figure 90: Example pressure signals for the case of medium amplitude and 17.5 kHz

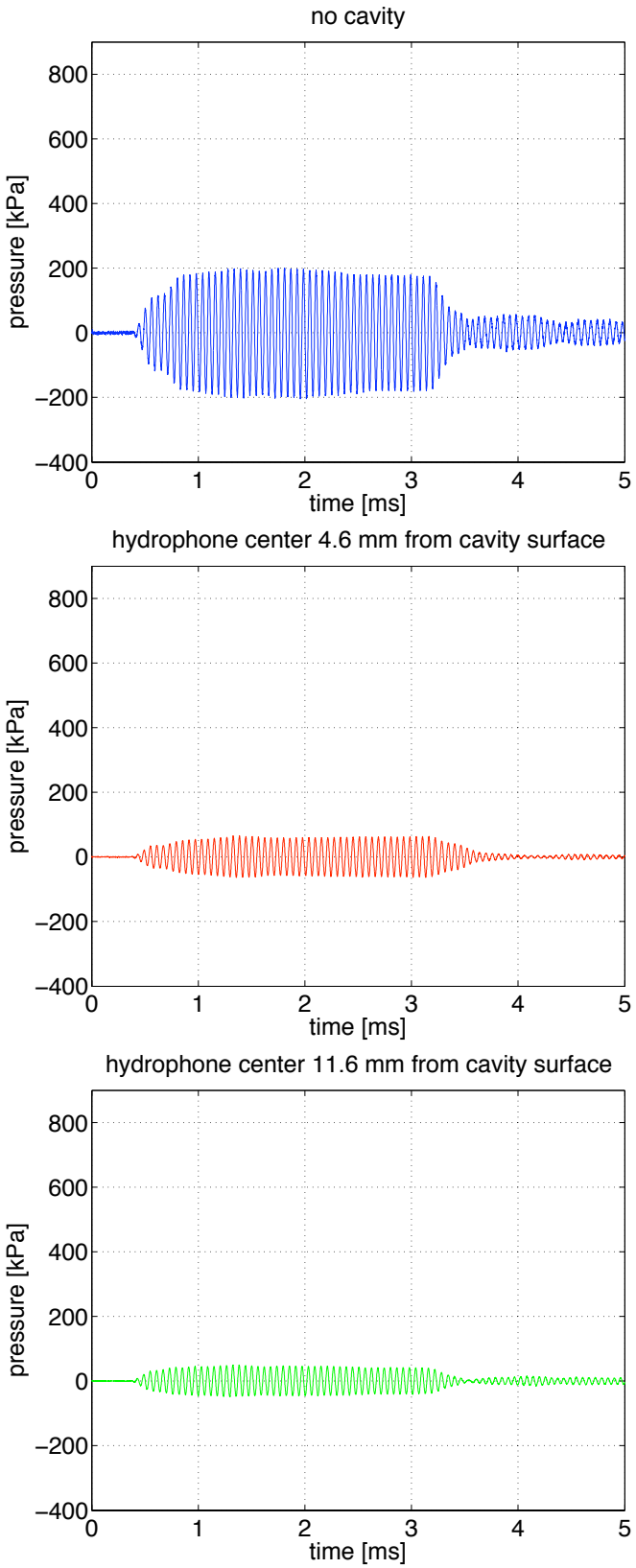

Figure 91: Example pressure signals for the case of low amplitude and 17.5 kHz

APPENDIX I

TARGET IMPACT LOCATIONS

Figure 92 shows the measured target impact locations for all of the experiment cases. In each plot the data centroid is normalized to the target center. Table 20 shows the layout of the plots in the figure. The asterisks correspond to experiments cases that were done. The top, middle and bottom rows in the figure show the high, medium and low amplitude cases respectively. The left, middle and right columns show the low, medium and high frequencies respectively.

Table 20: Summary of the experiment cases showing the layout of the plots in figure 92

	7.5 kHz	12 kHz	17.5 kHz
high amplitude		*	
medium amplitude	*	*	*
low amplitude	*	*	*

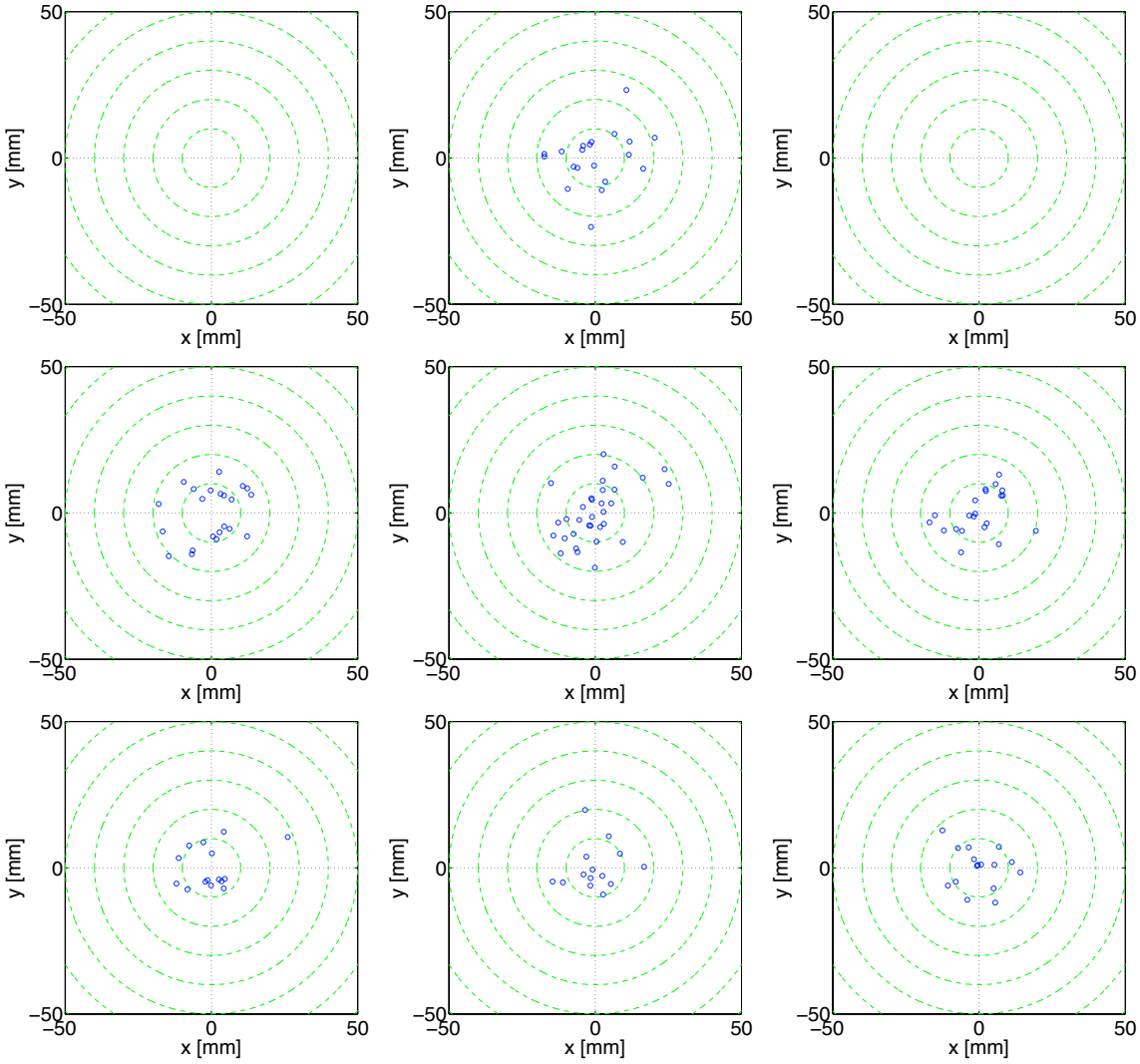

Figure 92: Target impact location plots. In each plot the data centroid is normalized to the target center.

REFERENCES

[1] Ahn, S. S., *An Integrated Approach to The Design of Supercavitating Underwater Vehicles*. Ph.d. dissertation, Georgia Institute of Technology, School of Aerospace Engineering, August 2007.

[2] Akulichev, V. A. and Il'ichev, V. I., "Acoustic cavitation threcholds of sea water in different regions of the world ocean," *Acoustical Physics*, vol. 51, no. 2, pp. 128–138, 2005.

[3] Anderson, J. D., *Fundamentals of Aerodynamics*. McGraw Hill, 3rd ed., 2001.

[4] ASME Design Engineering Technical Conferences, *Impact dynamics of a supercavitating underwater projectile*, (Sacramento CA), September 14-17 1997.

[5] Averkiou, M. A. and Cleveland, R. O., "Modeling of an electrohydraulic lithotripter with the KZK equation," *J. Acoust. Soc. Am.*, vol. 106, p. p102, July 1999.

[6] Balas, G. J., Bokor, J., Vanek, B., and Arndt, R. E. A., *Control of Uncertain Systems: Modelling, Approximation, and Design*, vol. 329/2006 of *Lecture Notes in Control and Information Sciences*. Springer Berlin / Heidelberg, 2006.

[7] Barger, J. E. and Hamblen, W. R., "The air gun impulsive underwater transducer," *J. Acoust. Soc. Am.*, vol. 68, October 1980.

[8] Bevington, P. R. and Robinson, D. K., *Data Reduction and Error Analysis for the Physical Sciences*. McGraw-Hill, 2nd ed., 1992.

[9] Beyer, R. T., *Nonlinear Acoustics*. Acoustical Society of America through the American Institute of Physics, 1997.

[10] Black, W. Z. and Hartley, J. G., *Thermodynamics*. Harper and Row, 1985.

[11] Blackstock, D. T., *Findamentals of Physical Acoustics*. John Wiley and Sons, Inc., 2000.

[12] Bobber, R. J., *Underwater Electroacoustic Measurements*. Naval Research Laboratory, 1970.

[13] Brüel & Kjær, *B&K hydrophone documentation*.

[14] Butler, S. C., Butler, J. L., Butler, A. L., and Cavanagh, G. H., "A low-frequency directional flextensional transducer and line array," *J. Acoust. Soc. Am.*, vol. 102, July 1997.

[15] Caflisch, R. E., Miksis, M. J., Papanicolaou, G. C., and Ting, L., "Effective equations for wave propagation in bubbly liquids," *J. Fluid Mech.*, vol. 153, pp. 259–273, 1985.

[16] Caflisch, R. E., Miksis, M. J., Papanicolaou, G. C., and Ting, L., "Wave propagation in bubbly liquids at finite volume fraction," *J. Fluid Mech.*, vol. 160, pp. 1–14, 1985.

[17] Cathignol, D. and Chapelon, J. Y., "High energy ultrasound therapy: Part II - shock waves and cavitation," in *Advances in Nonlinear Acoustics. 13th International Symposium on Nonlinear Acoustics.* (Hobaek, H., ed.), (Singapore), pp. 30–35, World Scientific, 28 June - 2 July 1993.

[18] Caupin, F. and Herbert, E., "Cavitation in water: a review," *C. R. Physique*, vol. 7, pp. 1000–1017, 2006.

[19] Chapelon, J. Y. and Cathignol, D., "High energy ultrasound therapy: Part I - high intensity focused ultrasound (HIFU)," in *Advances in Nonlinear Acoustics. 13th International Symposium on Nonlinear Acoustics.* (Hobaek, H., ed.), (Singapore), pp. 21–29, World Scientific, 28 June - 2 July 1993.

[20] Choi, J., Ruzzene, M., and Bauchau, O. A., "Dynamic analysis of flexible supercavitating vehicles using modal-based elements," *The Society for Modeling and Simulation International*, vol. 80, pp. 619–633, November 2004.

[21] Coleman, A. J., Choi, M. J., and Saunders, J. E., "Theoretical predictions of the acoustic pressure generated by a shock wave lithotripter," *Ultrasound in Med. & Biol.*, vol. 17, no. 3, pp. 245–255, 1991.

[22] Coleman, A. J. and Saunders, J. E., "A survey of the acoustic output of commercial extracorporeal shock wave lithotripters," *Ultrasound in Med. & Biol.*, vol. 15, no. 3, pp. 213–227, 1989.

[23] Coleman, A. J., Saunders, J. E., Crum, L. A., and Dyson, M., "Acoustic cavitation generated by an extracorporeal shockwave lithotripter," *Ultrasound in Med. & Biol.*, vol. 13, no. 2, pp. 69–76, 1987.

[24] Crown International, I., "Crown amplifier documentation ct-810." Manufacturer Web Page (http://www.crownaudio.com) accessed Sept. 04, 2008, 2000.

[25] Diehl BGT Defence, "Diehl bgt defence website, accessed september 2007."

[26] DuMond, J. W. M., Cohen, E. R., Panofsky, W. K. H., and Deeds, E., "A determination of the wave forms and laws of propagation and dissipation of ballistic shock waves," *J. Acoust. Soc. Am.*, vol. 18, pp. 97–118, July 1946.

[27] Duncan, R. C., Knapp, R. G., and Miller, M. C., *Introductory Biostatistics of the Health Sciences*. Delmar Publishers, Inc., second ed., 1983.

[28] Edmund Scientific, "Edmund scientific's 2006 catalog." Edmund Scientific's 2006 Catalog. Also see www.scientifics.com (accessed Jul. 03, 2007).

[29] Eller, A., "Growth of bubbles by rectified diffusion," *J. Acoust. Soc. Am.*, vol. 46, no. 5, pp. 1246–1250, 1969.

[30] Eller, A. and Flynn, H. G., "Rectified diffusion during nonlinear pulsations of cavitation bubbles," *J. Acoust. Soc. Am.*, vol. 37, pp. 493–503, March 1965.

[31] Fink, M., "Time reversal mirrors," in *Acoustical Imaging* (Jones, J. P., ed.), vol. 21, pp. 1–15, New York: Plenum, 1995.

[32] Fink, M., "Time reversed acoustics." Phys. Today, March 1997.

[33] Fowler, K. R., Sheeham, J., and Silver, S., "Simplified and inexpensive experimental set ups for studying supercavitation." Instrumentation and Measurement Technology Conference, Ottowa, Canada, May 17-19 2005.

[34] Franc, J. and Michel, J., *Fundamentals of Cavitation (Fluid Mechanics and Its Applications)*. Springer Publishing Company, 1st ed., 2004.

[35] Garabedian, P. R., "Calculation of axially symmetric cavities and jets," *Pac. J. Math.*, vol. 6, pp. 611–689, 1956.

[36] Germain, L. and Cheeke, J. D. N., "Generation and detection of high-order harmonics in liquids using scanning acoustic microscope," *J. Acoust. Soc. Am.*, vol. 83, March 1988.

[37] Grant, J. R. and Kirschner, I. N., "High-speed motion in bubbly flows." Fifth International Symposium on Cavitation (CAV2003), November 2003.

[38] Grant, J. R., Kirschner, I. N., and Uhlman, J. S., "Drag on a slender body moving at high speeds in a bubbly liquid." Sixth International Symposium on Cavitation (CAV2006), September 2006.

[39] GS Custom Bullets, "Website (http://gscustom.co.za), accessed march 2009."

[40] Hamilton, M. F. and Blackstock, D. T., eds., *Nonlinear Acoustics*. Academic Press, 1998.

[41] Hayman, G., Gelat, P. N., Moore, G. R., Wells, G. O., and Robinson, S. P., "A method for correcting the complex electrical impedance and open-circuit sensitivity of a hydrophone for the effect of added extension cable," *Measurement Science and Technology*, vol. 18, pp. N47–N52, 2007.

[42] Herbert, E., Balibar, S., and Caupin, F., "Cavitation pressure in water," *Physical Review E*, vol. 74, 2006.

[43] Hirose, A., Takahahsi, N., and Takahashi, S., "Spectral change in acoustic pressure and cavitation inception," *Jpn. J. Appl. Phys.*, vol. 36, pp. 3348–3349, May 1997.

[44] Hodgkiss, W. S., Song, H. C., and Kuperman, W. A., "A long-range and variable focus phase-conjugation experiment in shallow water," *J. Acoust. Soc. Am.*, vol. 105, p. p1597, March 1999.

[45] Holman, J. P., *Experimental Methods for Engineers*. McGraw Hill, 7th ed., 2001.

[46] Hrubes, J. D., "High-speed imaging of supercavitating underwater projectiles," *Experimental Fluids*, vol. 30, pp. 57–64, 2001.

[47] Jackson, D. R. and Dowling, D. R., "Phase conjugation in underwater acoustics," *J. Acoust. Soc. Am.*, vol. 89, pp. 171–181, January 1991.

[48] Jane's, "Va-111 shkval (russian federation)." Jane's Underwater Warfare Systems, April 2008.

[49] Jenkins, A. and Evans, T., "Sea mine neutralization using the an/aws-2 rapid airborne mine clearance system." IEEE Aerospace Conference Proceedings, 2004.

[50] Kiceniuk, T., "An experimental study of the hydrodynamic forces acting on a family of cavity-producing conical bodies of revolution inclined to the flow," tech. rep., Hydrodynamics Laboratory California Institute of Technology, Pasadena, CA, June 1954.

[51] Kirschner, I. N., "Results of selected experiments involving supercavitating flows." Paper presented at the RTO AVT lecture series on supercavitating flows at VKI, 2001.

[52] Kirschner, I. N., Fine, N. E., Uhlman, J. S., and Kring, D. C., "Numerical modeling of supercavitating flows." Paper presented at the RTO AVT lecture series on supercavitating flows at VKI, 2001.

[53] Kirschner, I. N., Fine, N. E., Uhlman, J. S., Kring, D. C., Rosenthal, B. J., Gieseke, T. A., Kuklinski, R., Varghese, A. N., Stinebring, D. R., Dzielski, J. E., Lindau, J. W., and Kunz, R. F., "Supercavitation research and development," 2001.

[54] Kirschner, I. N., Kring, D. C., Stokes, A. W., Fine, N. E., and Uhlman, J. S., "Control strategies for supercavitating vehicles," *Journal of Vibration and Control*, vol. 8, no. 2, pp. 219–242, 2002.

[55] Knapp, R., Daily, J., and Hammitt, F., *Cavitation*. McGraw-Hill, 1970.

[56] Kring, D. C., Fine, N. E., Uhlman, J. S., and Kirschner, I. N., "A time-domain cavitation model using a three-dimensional boundary-element method," *International Journal of Fluid Mechanics Research*, vol. 28, no. 5, 2001.

[57] Kulkarni, S. S. and Pratap, R., "Studies on the dynamics of a supercavitating projectile," *Applied Mathematical modeling*, vol. 24, pp. 113–129, 2000.

[58] Kuperman, W. A., Hodgkiss, W. S., and Song, H. C., "Phase conjugation in the ocean: Experimental demonstration of an acoustic time-reversal mirror," *J. Acoust. Soc. Am.*, vol. 103, p. p25, January 1998.

[59] Lamb, S. H., *Hydrodynamics*. New York Dover Publications, sixth edition ed., 1932.

[60] Larson, G. D., Rogers, P. H., and Munk, W., "State switched transducers: A new approach to high-power, low-frequency, underwater projectors," *J. Acoust. Soc. Am.*, vol. 103, p. p.1428, March 1998.

[61] Leighton, T. G., *The Acoustic Bubble*. San Diego, CA, 92101: Academic Press Inc., 1994.

[62] Lingevitch, J. F., Song, H. C., and Kuperman, W. A., "Time reversed reverberation focusing in a waveguide," *J. Acoust. Soc. Am.*, vol. 111, pp. 2609–2614, 2002.

[63] Logvinovich, G. V., "Some problems in planing surfaces [sic], translated from "nekotoryyi voprosy glissirovaniya i kavitatsii" [some problems in planing and cavitation]," *Trudy TsAGI 2052*, 1980.

[64] Louisnard, O. and Gomez, F., "Growth by rectified diffusion of strongly acoustically forced gas bubbles in nearly saturated liquids," *Physical Review E*, vol. 67, no. 3, 2003.

[65] May, A., "Water entry and the cavity-running behavior of missiles," tech. rep., NAVSEA Hydroballistics Advisory Committee, Silver Spring, MD (Reproduced by NTIS), 1975.

[66] Meyers, B., Cancilliere, F., and LaPointe, K., "Torpedoes and the next generation of undersea weapons." Undersea Warfare Magazine Winter/Spring 2002 (http://www.navy.mil).

[67] Morgenwelt Magazine. Morgenwelt Magazine, June 23 2005.

[68] Mostafa, N., Nayfeh, A., Vlachos, P., and Telionis, D., "Cavitating flow over a projectile." 39th Aerospace Sciences Meeting and Exhibit, Fluid Dynamics Conference, Reno, NV, January 8-11 2001.

[69] Neppiras, E. A., "Subharmonic and other low-frequency emission from bubbles in sound-irradiated liquids," *J. Acoust. Soc. Am.*, vol. 46, no. 3, pp. 587–601, 1968.

[70] Neppiras, E. A., "Acoustic cavitation," *Physical Reports (Rewiew Section of Physical Letters)*, vol. 61, no. 3, pp. 159–251, 1980.

[71] Owis, F. M. and Nayfeh, A. H., "Numerical simulation of super and partially cavitating flows over an axisymmetric projectile." 39th Aerospace Sciences Meeting and Exhibit, Reno, NV, January 8-11 2001.

[72] Owis, F. M. and Nayfeh, A. H., "A compressible multi-phase flow solver for the computation of the supercavitation over high speed torpedo." 40th AIAA Aerospace Sciences Meeting and Exhibit, Reno, NV, 14-17 January 2002.

[73] Owis, F. M. and Nayfeh, A. H., "Numerical simulation of 3-D incompressible, multi-phase flows over cavitating projectiles," , *European Journal of Mechanics B/Fluids*, vol. 23, pp. 39–351, 2004.

[74] Paryshev, E. V., "Mathematical modeling of unsteady cavity flows." Paper presented at the Fifth International Symposium on Cavitation (CAV2003), 2003.

[75] Paryshev, E. V., "Approximate mathematical model in high-speed hydrodynamics," *Journal of Engineering Mathematics*, vol. 55, pp. 41–64, 2006.

[76] Pierce, A. D., *Acoustics: An Introduction to Its Pyhsical Principles and Applications*. The Acoustical Society of America through the American Institute of Pysics, 1994.

[77] Pilkey, W. D., *Formulas for Stress, Strain, and Structural Matrices*. John Wiley and Sons, Inc., 1994.

[78] Przemieniecki, J. S., *Mathematical Methods in Defense Analyses*. American Institute of Aeronautics and Astronautics, Inc., third edition ed., 2000.

[79] Rolt, K. D., "History of the flextensional electoacoustic transducer," *J. Acoust. Soc. Am.*, vol. 87, March 1990.

[80] Root, J. A. and Rogers, P. H., "Performance of an underwater acoustic volume array using time-reversal focusing," *J. Acoust. Soc. Am.*, vol. 112, November 2002.

[81] Ruzzene, M., Kamada, R., Bottasso, C. L., and Scorcelletti, F., "Trajectory optimization strategies for supercavitating underwater vehicles," *Journal of Vibration and Control*, vol. 14, no. 5, pp. 611–644, 2008.

[82] Salvador, G. P. and Frankel, S. H., "Numerical modeling of cavitation using FLUENT: Validation and parametric studies." 34th AIAA Fluid Dynamics Conference and Exhibit, Portland, Oregon, 28 June - 1 July 2004.

[83] Savchenko, Y. N., "Motion in water at supercavitation speeds," *International Journal of Fluid Mechanics Research*, vol. 23, 1996.

[84] Savchenko, Y. N., "Experimental investigation of supercavitating motion of bodies." Paper presented at the RTO AVT lecture series on supercavitating flows at VKI, 2001.

[85] Schaffar, M., Rey, C., and Boeglen, G., "Behavior of supercavitating projectiles fired horizontally in a water tank: Theory and experiments. CFD computations with the OTi-HULL hydrocode." 35th AIAA Fluid Dynamics Conference and Exhibit, Toronto, Ontario Canada, June 6-9 2005.

[86] Schaffar, M. J., Rey, C. J., and Boeglen, G. S., "Comparision of two computational methods for high velocity cavitating flows around conical projectiles: OTi-HULL hydrocode and two phase flow method." Paper presented at the Fourth International Symposium on Cavitation (CAV2001), 2001.

[87] Schaffar, M. J., Rey, C. J., and Boeglen, G. S., "Experiments on supercavitating projectiles fired horizontally into water." Proceedings of ASME Fluids Engineering Division Summer Meeting, July 14-18 2002.

[88] Self, M. and Ripken, R. F., "Steady-state cavity studies in a free-jet water tunnel." St. Anthony Falls Hydr. Lab. Rep. 47, July 1955.

[89] Semenenko, V. N., "Dynamic processes of supercavitation and computer simulation." Paper presented at the RTO AVT lecture series on supercavitating flows at VKI, 2001.

[90] Singhal, A. K., Athavale, M. M., Li, H., and Jiang, Y., "Mathematical basis and validation of the full cavitation model," *Journal of Fluids Engineering*, vol. 124, pp. 617–624, 2002.

[91] Song, H. C., Kuperman, W. A., and Hodgkiss, W. S., "A time-reversal mirror with variable range focusing," *J. Acoust. Soc. Am.*, vol. 103, p. p3234, June 1998.

[92] Song, H. C., Kuperman, W. A., and Hodgkiss, W. S., "Iterative time reversal in the ocean," *J. Acoust. Soc. Am.*, vol. 105, p. p3176, June 1999.

[93] Stoughton, R., "Measurements of small-caliber ballistic shock waves in air," *J. Acoust. Soc. Am.*, vol. 102, pp. 781–787, August 1997.

[94] Taub, A. E. and Thomas, M. A., "Comparison of cep (circular probable error) estimators for elliptical normal errors," tech. rep., Naval Surface Weapons Center Dahlgren, Virginia, June 1983.

[95] Thuraisingham, R. A., "Sound speed in bubbly water at megahertz frequencies," *Ultrasonics*, vol. 36, pp. 767–773, 1998.

[96] Tulin, M. P., "Fifty years of supercavitating flow research in the united states: Personal recollections," *International Journal of Fluid Mechanics Research*, vol. 28, no. 5, 2001.

[97] Varghese, A. N., Uhlman, J. S., and Kirschner, I. N., "Numerical analysis of high-speed bodies in partially cavitating axisymmetric flow," *Journal of Fluids Engineering*, vol. 127, January 2005.

[98] Vasin, A. D., "Application of the slender body theory to investigation of the developed axially symmetric cavitation flows in a subsonic stream of compressible fluid," *International Journal of Fluid Mechanics Research*, vol. 28, no. 5, 2001.

[99] Vasin, A. D., "The principle of independence of the cavity sections expansion (logvinovich's principle) as the basis for investigation on cavitation flows." Paper presented at the RTO AVT lecture series on supercavitating flows at VKI, 2001.

[100] Vasin, A. D. and Paryshev, E. V., "Immersion of a cylinder in a fliud through a cylindrical free surface," *Fluid Dynamics*, vol. 36, no. 2, pp. 169–177, 2001.

[101] Vaughan, P. W., "Investigation of acoustic cavitation thresholds by observation of the first subharmonic," *J. Sound Vib.*, vol. 7, no. 2, pp. 236–246, 1968.

[102] Vlasenko, Y. D., "Experimental investigation of supercavitation flow regimes at subsonic and transonic speeds." Paper presented at the fifth international symposium on cavitation, CAV2003.

[103] Whitham, G. B., "The flow pattern of a supersonic projectile," *Communications on Pure and Applied Mathematics*, vol. 5, pp. 301–348, 1952.

[104] Wijngaarden, L. V., "One-dimensional flow of liquids containing small gas bubbles," *Annual Review of Fluid Mechanics*, vol. 4, pp. 369–396, 1972.

[105] Wosnik, M., Schauer, T. J., and Arndt, R. E. A., "Experimental study of a ventilated supercavitating vehicle." Fifth International Symposium on Cavitation, Osaka, Japan, November 1-4 2003.

[106] Wu, X. and Chahine, G., "Characterization of the content of the cavity behind a high-speed supercavitating body," *Journal of Fluids Engineering*, vol. 129, pp. 136 – 145, February 2007.